MANCHESTER 1824

The University of Manchester

The physics of pregnancy tests: a biophysical study of interfacial protein adsorption

A thesis submitted to The University of Manchester
for the degree of doctor of philosophy
in the faculty of Engineering and Physical Sciences

Benjamin James Cowsill

School of Physics and Astronomy
2012

CONTENTS

Final word count: 40,520

LIST OF FIGURES

LIST OF TABLES

ABSTRACT

Pregnancy tests and related immunoassays are heavily dependent on specific and non-specific protein adsorption. These interfacial processes are affected by many factors that influence the in situ conformations of interfacially immobilised antibodies. This thesis examines a number of representative features with dual polarisation interferometry (DPI) and neutron reflection (NR), thus combining real-time dynamic monitoring with high interfacial structural resolution.

Bovine serum albumin (BSA) was initially used as a model system to compare the surface coverage and thickness measurements of DPI and NR. The results show that DPI and NR provided similar surface coverage data but the measured thicknesses differed at BSA concentrations above 0.1 mg/ml. This discrepancy arose from the adoption of the uniform-layer model used by DPI for data analysis and the greater thickness sensitivity of NR.

A model pregnancy immunoassay was built in steps on a silica surface so that the adsorption of each protein could be accurately monitored. Both DPI and NR provided evidence of BSA insertion into the gaps on the surface between the antibody molecules. This suggests that BSA adsorption is an excellent method to block the non-specific adsorption of target antigens to the immunoassay test surface.

A magnetic tweezer system was designed and built in order to measure the specific antibody/antigen binding force. The antibodies and antigens were used to immuno-link magnetic beads to the experimental surface before the immuno-links were broken by increasing the attractive force between the magnetic tweezers and beads. The force per antibody/antigen immuno-link was estimated to lie between the values of 13.6 pN and 43.8 pN.

Immuno-link detachment as a function of time was investigated. It was found that the immuno-link comprised both a strong and a weak interaction. The dissociation constant of the strong antibody/antigen interaction was found to equal $(3 \pm 1) \times 10^{-4}\,\mathrm{s}^{-1}$ and had an interaction length of 0.06 ± 0.03 nm. The low population of beads bound by the second, weaker interaction meant that it was not possible to obtain accurate values of the dissociation constant and bond length of the second weaker interaction.

DECLARATION

The University of Manchester
PhD Candidate Declaration

Candidate Name: Benjamin James Cowsill

Faculty: Engineering and Physical Sciences

Thesis Title: The physics of pregnancy tests: a biophysical study of interfacial protein adsorption

Declaration to be completed by the candidate:

I declare that no portion of this work referred to in this thesis has been submitted in support of an application for another degree or qualification of this or any other university or other institute of learning.

Signed: Date: August 9, 2012

COPYRIGHT

[1] This excludes material already printed in academic journals, for which the copyright belongs to said journal and publisher. Pages for which the author does not own the copyright are numbered differently from the rest of the thesis.

ACKNOWLEDGEMENTS

First and foremost, I thank my supervisors Dr. Tom Waigh and Prof. Jian Lu for their invaluable help, advice and guidance over the course of my PhD.

A big thank you to my industrial supervisors, Robert Davies and Saji Eapen, for all of their help and constructive discussions.

I thank all of the members of the biological physics group for their help and for making the lab a fun place to be: Mohammed, Jon, Lisa, Faheem, Maria, Amy, Andrew, Pantelis, David, Dong Hui, Monica and Matthew. An extra thank you to Paul Coffey who took several weeks out of his own PhD to teach me how to use the DPI.

Thank you to Tim Butters and Jennifer Sanders for constructive drinking and Korean food and to Dick Steele for not being as good as me at Halo.

I'd like to thank the EPSRC and SPD Development Company Ltd. for funding my PhD and to the STFC for funding my neutron experiments.

A big thank you to Janice and Ian Anthonisz for putting up with me every weekend and for all of the trips to Sri Lanka and delicious chicken curries!

Thanks to Marie Anthonisz for always being there for me, for tolerating all my of PhD (and non-PhD) related bad moods. I could not have made it through the numerous low points of the PhD process without her support, love and black pork curry.

Finally a huge thank you to my parents, Janet and Nigel, for a great set of genes, a fantastic start to life and their continued love and support, particularly over the last year. I could not have done it without you!

NOMENCLATURE

A	Beads bound by species A
$A_i^{(n)}$	The ith order coefficient for the M Taylor series expansion of Φ
B	Beads bound by species B
D	Diffusion constant
F	Force
IS	Ionic strength
J	Protein molecular flux
K	Rate of deposition onto an empty surface via diffusion
L	Length
L_c	Length of car
M	Protein surface coverage
MW	Molecular weight
N	Beads remaining on surface
R	Distance from inlet pipe to waveguide surface
T	Temperature
V	Fluid velocity
X	Molecular attractive parameter
Y	Molecular repulsive parameter
ΔG	Change in the Gibbs energy
ΔH	Change in enthalpy
ΔS	Change in entropy
Φ	Uncovered surface fraction
η	Bond lifetime
κ^{-1}	Wavelength
λ	Wavelength
λ	Wavelength
$\mathbf{B}$	Magnetic field strength vector
$\mathbf{F}$	Magnetic force vector
μ	Permeability
ν	Molecular number density
ω	Energy
ψ_r	Phase of reference wave
ψ_s	Phase of sensing wave
ρ	Density
τ	Layer thickness
$\mathrm{d}n/\mathrm{d}c$	Refractive index increment
θ	Covered surface fraction
θ_c	Critical angle for total internal reflection
b	RSA constant
c_ν	Molecular concentration
c_b	Bulk protein concentration
d_f	Degrees of freedom
k_a	Chemical adsorption coefficient
k_b	Boltzmann's constant
k_d	Chemical desorption coefficient or dissociation constant
m_b	Buoyant mass
m_o	Mass of bead
n	Refractive index
q	Momentum transfer
r	Separation between molecules
r_e	Equilibrium separation
v	Volume
x	Fringe spacing
AFM	Atomic force microscopy
AgBC	Antigen binding capacity

Anti-α-hCG Antibody directed against the α epitope of hCG

Anti-β-hCG Antibody directed against the β epitope of hCG

BSA Bovine serum albumin

C8 Octyltrimethoxysilane

CCD Charge-coupled device

CMOS Complementary metal-oxide-semiconductor

DPI Dual polarisation interferometer

Fab Fragment antigen binding region

Fc Fragment crystallisable region

hCG Human Chorionic Gonadotrophin

HPLC High-performance liquid chromatography

HSA Human serum albumin

ILL Institut Laue-Langevin

LED Light emitting diode

NR Neutron reflectivity

PBS Phosphate buffered saline

RSA Random sequential adsorption

SPR Surface plasmon resonance

TE_0 Transverse electric polarisation

TIRF Total internal reflection fluorescence

TM_0 Transverse magnetic polarisation

UHQ Ultra-pure water

w/w Weight by weight

SUPPORTING PUBLICATIONS

Interfacial immobilization of monoclonal antibody and detection of human prostate-specific antigen

X. Zhao, F. Pan, B. Cowsill, J, R. Lu, L. Garcia-Gancedo, A. J. Flewitt, G. M. Ashley and J. Luo. *Langmuir*, 27 (12), 7654–7662. 2011

Measurement of the thickness of ultra-thin adsorbed globular protein layers with dual-polarisation interferometry: a comparison with neutron reflectivity

B. J. Cowsill, P. D. Coffey, M. Yaseen, T. A. Waigh, N. J. Freeman and J. R. Lu. *Soft matter*, 7, (16), 7223–7230. 2011

Biomedical coating characterization

M. Yaseen, B. J. Cowsill and J. R. Lu, (2012). In V. Hart (Eds.), *Coatings for biomedical applications*. Cambridge: Woodhead Publishing Ltd.

Interfacial structure and history dependent activity of immobilised antibodies in model pregnancy tests

B. J. Cowsill, T. A. Waigh, R. Davies, S. Eapen and J. R. Lu. *Soft matter*, Accepted

Interfacial structure of immobilized antibodies and deuterated HSA in model pregnancy tests measured with neutron reflectivity

B. J. Cowsill, T. A. Waigh, R. Davies, S. Eapen, M. Moulin, M.Haertlein and J. R. Lu. *In preparation*

CHAPTER

ONE

INTRODUCTION TO PROTEIN ADSORPTION AND ANTIBODY–ANTIGEN BINDING

1.1 Introduction

This thesis focuses on the interaction between proteins and surfaces, in particular protein adsorption and how it affects protein–protein interactions, such as antibody–antigen binding. Protein adsorption is the aggregation of protein molecules onto a surface and is vitally important to the development of biocompatible structures and devices, such as contact lenses, stents and breast implants [1–3] as well as biomedical devices such as immunoassays [4].

1.2 Proteins

Proteins are complex biological macromolecules that are made from linear chains of amino acids. Proteins are the building blocks of life and play a vital role in the processes that occur inside cells. When they act as enzymes, proteins speed up chemical reactions that, under physiological conditions, would not be fast enough to sustain life; as hormones they transmit information around an organism; and as antibodies they form a vital part of an organism's immune system. Despite their diverse range of functions all proteins are made up of different combinations of the same 20 amino acids (we will ignore the secondary effects of post-translational modifications). The huge diversity in protein function is primarily attributable to the wide range of structures that can be formed by the 20 amino acids. Peptide bonds link the carboxyl and amino groups of the individual amino acids into chains. Figure 1.1 shows the chemical structure of these amino acids.

The structure of a protein is divided into three groups, each of which determines how the protein folds and interacts with its surroundings [6].

- **Primary structure**: this determines the linear amino acid sequence.
- **Secondary structure**: this is defined by the pattern formed by the peptide bonds that link the protein's amino acids together into coils, helices and beta sheets.

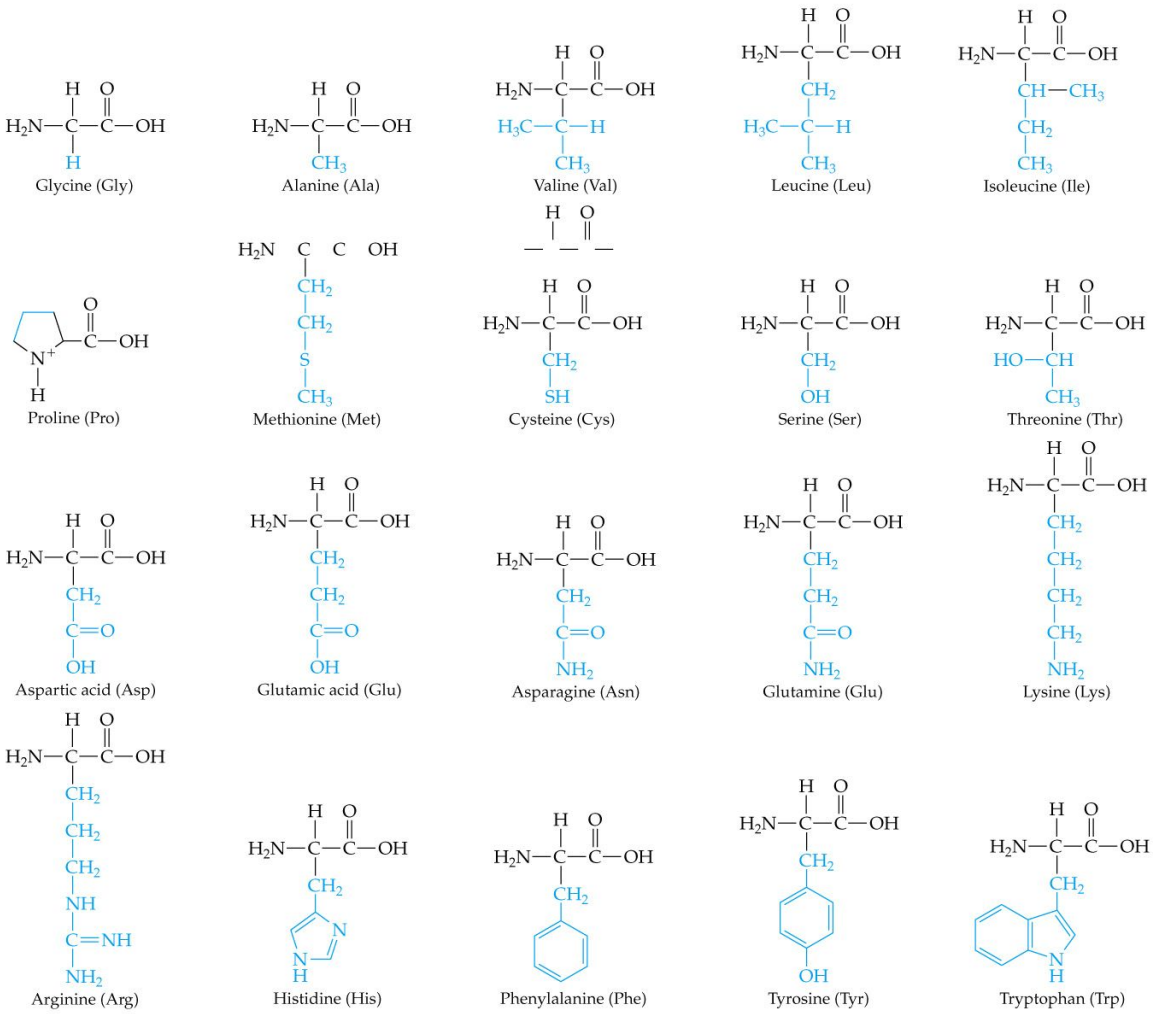

Figure 1.1: Chemical structure for the 20 amino acids that are found in all naturally occurring proteins [5].

- **Tertiary structure**: defines the global large scale structure of the protein e.g. the globular structure of most enzymes.

A protein can be further defined as one of three groups:

- Globular proteins, including albumin.
- Fibrous proteins, such as fibrinogen.
- Membrane proteins, including colicin A.

A protein's tertiary structure determines whether it is a globular, fibrous or membrane protein. All of the proteins used in the experiments described in this thesis are of the globular variety.

1.2.1 Proteins that will be studied

The three main types of proteins used for the experiments in this thesis are described here. These proteins are used in the production of human pregnancy tests, the operation of which is described in Section 1.4.2.

Bovine serum albumin

Bovine serum albumin (BSA) is a heart-shaped protein of approximate dimensions $40 \times 40 \times 140\,\text{Å}^3$ and has a molecular weight of 66,382 Da [7]. Although BSA does have a well defined overall shape, it is strongly pH, temperature and concentration dependent [8, 9] and can be considered to be composed of numerous wriggling parts [10]. Because of this, BSA is highly flexible and has been described as a "kicking and screaming stochastic" molecule [11].

Due to its low cost and ready availability (BSA is extracted from cow blood where it makes up between 60-70% of blood plasma [12]) BSA is extensively used as a blocking agent in commercial applications. For example, BSA is adsorbed to the sensing surface of pregnancy tests in order to reduce non-specific binding of other proteins to the surface of the test's sample stick.

Human serum albumin (HSA) was also used as blocking agent in the experiments described in Chapter 4. HSA is a similar size and weight as BSA [13]. HSA adsorbs in almost equal amounts as BSA and with the same conformation. Both albumins have their isoelectric point at pH 4.7 [14].

Human Chorionic Gonadotrophin

Human Chorionic Gonadotrophin (hCG) is a cigar-shaped antigen with two epitopes, α and β. The epitopes bind exclusively to their respective monoclonal antibodies: anti-α-hCG and anti-β-hCG. hCG has approximate dimensions of $75 \times 35 \times 30\,\text{Å}^3$ and a molecular weight of approximately 38,000 Da [15]. hCG is produced by the placenta during the initial stages of pregnancy. The concentration of hCG increases with the duration of time after insemination, thus the detection of hCG can be used as a test for pregnancy.

Antibodies

Two types of monoclonal antibodies were used for the experiments described here: anti-α-hCG and anti-β-hCG. Both antibodies have an approximate molecular weight of 150,000 Da and dimensions of $142 \times 85 \times 38\,\text{Å}^3$ [16]. The antibodies differed in their affinities to the epitopes of hCG. Anti-α-hCG has a high affinity to the α epitope of hCG while anti-β-hCG has a high affinity to the β epitope of hCG. Both antibodies have an isoelectric point between pH 5.5 and pH 6 [17].

1.2.2 Protein–surface interactions

Protein adsorption is the accumulation of protein molecules on a surface. It occurs along the interfacial region between an aqueous protein solution and a substrate [18]. When biomedical devices, such as stents or catheters, are implanted into the body they are exposed to proteins and cells that are present in the blood and other biological fluids.

Proteins are rapidly transported to the vicinity of the implant's surface via diffusion, where they adsorb to the surface and form a thin film.

As cells have a larger mass than proteins, they arrive at the implant surface after the proteins. Since the surface has been coated with a thin film of protein, a cell's response to the surface will be determined by protein–receptor interactions that occur through the cell membrane between the surface-adsorbed proteins and the intracellular proteins. Thus, the biocompatibility of a material is not determined by its constituent atoms but by the amount, conformation and species of protein that adsorb to it. Materials with poor biocompatibility may cause inflammation, infection or, if an immune response is triggered, be rejected by the host.

It is widely believed that the adsorption process consists of three stages:

1. The protein is transported from its solution to the solution/substrate interface via diffusion.

2. The protein becomes attached to the substrate.

3. The conformation of the adsorbed protein changes to optimise the protein/surface interaction. The extent of the conformation change depends on the forces between the protein and surface as well as the structure of the protein.

In thermal equilibrium protein adsorption can only occur if the Gibbs free energy of the system decreases. The change in the Gibbs energy, ΔG_{ads} is given by:

$$\Delta G_{ads} = \Delta H_{ads} - T\Delta S_{ads} < 0 \tag{1.2.1}$$

where ΔH_{ads} is the change in the enthalpy of the system, ΔS_{ads} is the change in entropy and T is the absolute temperature. Desorption of typical globular protein films on conventional surfaces takes much longer than adsorption (if desorption occurs at all) and often requires the use of detergents.

It has been shown that the non-specific binding of proteins to substrates depends on many variables including: the pH [19], salinity [20] and homogeneity of the buffer solution, the concentration of the protein solution [21] and the hydrophobicity of the substrate [22]. An extensive review by Haynes and Norde [23] showed that protein adsorption depends on a number of forces and effects, and is not dominated by any particular one. In particular van der Waals forces, electrostatic forces, the hydrophobic effect, hydrogen bond forces, depletion interactions, and both inter and intramolecular interactions can be important.

One of the most commonly used surfaces to investigate protein adsorption is silica (SiO_2). Silicon wafers are relatively cheap and easy to obtain due to the large quantities used in the manufacturing of electronic components. It is hydrophilic, easy to clean and it has been well characterised [24]. The most important forces that drive the adsorption of

proteins to silica are caused by electrostatic attraction and hydrogen bonding [25]. Electrostatic attraction describes the Coulombic attractions between charged surface groups and oppositely charged protein ions, while hydrogen bonding is a result of the attractive force between an electronegative atom, such as oxygen or nitrogen (hydrogen acceptor), and a hydrogen donor (usually a hydrogen atom that is covalently bound to another electronegative atom). The strength of a hydrogen bond can range from 1-155 kJ/mol and has an interaction length that is typically in the 100 pm range.

Another advantage of silica is that it can be reproducibly coated, allowing protein adsorption to be investigated on octyltrimethoxysilane (C8) [26] and other hydrophobic surfaces [27, 28] as well as surfaces such as poly(methylmethacrylate) (PMMA) [29].

1.3 Isoelectric point and pK_a theory

The Brønsted-Lowry theory states that an acid (HA) will donate a proton (H^+) when in the presence of a base (A^-),

$$\mathrm{HA} \rightleftharpoons \mathrm{A}^- + \mathrm{H}^+ \tag{1.3.1}$$

and an equilibrium occurs when the concentrations of the acid and base remain constant. A logarithmic acid dissociation constant (pK_a) is defined as

$$\mathrm{p}K_a = \log_{10} \frac{[\mathrm{HA}]}{[\mathrm{A}^-][\mathrm{H}^+]} \tag{1.3.2}$$

where [HA], [H^+] and [A^-] represent the molar concentrations of the acid, proton and base respectively. If the pK_a of a system and the concentrations of the acid and base are known, the pH of the solution can be calculated with the Henderson-Hasselbalch equation

$$\mathrm{pH} = \mathrm{p}K_a + \log\left(\frac{[\mathrm{A}^-]}{[\mathrm{HA}]}\right). \tag{1.3.3}$$

As well as calculating the pH of a solution, Equation (1.3.3) can also be used to calculate the charge of a substance at a given pH. Proteins contain various quantities of charged amino acids: glutamate, aspartate, histidine, lysine and arginine. The charge (Q) of a negatively charged amino acid (glutamate and aspartate), varies with solution pH as

$$Q = \frac{-n}{1 + 10^{\mathrm{p}K_a - \mathrm{pH}}} \tag{1.3.4}$$

and for a positively charged amino acid

$$Q = \frac{n}{1 + 10^{\mathrm{pH} - \mathrm{p}K_a}} \tag{1.3.5}$$

where n is the total number of each amino acid. The net charge of a protein is the total of all positive and negative charges. Figure 1.2 shows the net charge of a BSA molecule and

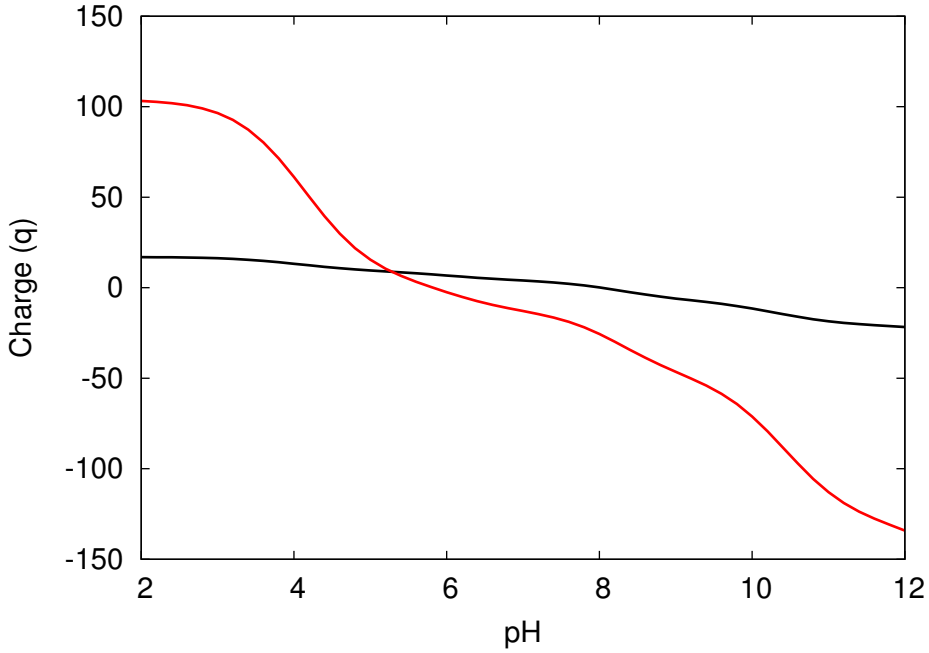

Figure 1.2: Calculated net electronic charge of BSA (red line) and hCG (black line) as a function of pH.

a hCG molecule as a function of pH.

The isoelectric point of a protein occurs when the net charge of the protein is zero. For BSA, the isoelectric point can be seen in Figure 1.2 to occur at pH 5.8. This calculated value differs from the experimental value as Equation (1.3.4) and Equation (1.3.5) do not take into account protein folding, which can internalise charged amino acids, or the interactions between neighbouring charges along a chain. In fact, the isoelectric point of BSA has been experimentally found to lie at pH 4.7 [14].

1.4 Immunoassays

Immunoassays are biomedical devices that use the specific recognition of antibody–antigen interactions to detect target antigens in a sample solution. Since 1959, when the first immunoassay for the detection of human antigens was developed [30], the global market for immunoassays has grown to approximately $7.7 bn [31]. Modern immunoassays have a wide range of applications, including the detection of: cancers [32], fertility [33], illegal drugs [34], viruses such as Hepatitis [35], and water and soil contaminants [36, 37].

1.4.1 Antibody–antigen interactions

Antibody–antigen interactions are a type of protein–protein interaction that are fundamental to the operation of many commercial immunoassays, such as human pregnancy tests [38] and blood tests. Antibodies are proteins that feature active binding sites to

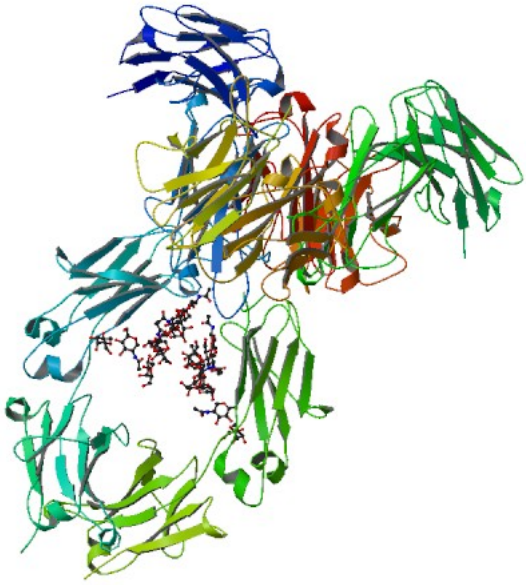

Figure 1.3: Crystal structure of human IgG B12 antibody. The Fabs protrude from the Fc to form a y-shape [39].

which only either a specific antigen may bind (monoclonal antibody) or several specific antigens (polyclonal antibody). These binding sites are found on regions known as fragment antigen binding (Fab) sites that are joined to a fragment crystallisable (Fc) region in such a way that they form a Y-shape. The crystal structure of an antibody, obtained with X-ray diffraction, can be seen in Figure 1.3. A typical immunoassay exploits this site-specific binding by immobilising monoclonal antibodies to a surface before exposing them to antigens in a solution. If the appropriate antigens are present in the sample solution they will bind to the antibody Fabs, whereas other antigens will not. The antigen binding capacity (AgBC) of an antibody determines the effectiveness of the Fabs at capturing antigens. The maximum AgBC of an antibody is two, i.e. one antigen is bound to each of the two antibody Fabs.

1.4.2 Pregnancy tests

The modern human pregnancy test is one of the most commonly used immunoassays. It is the product of hundreds of thousands of pounds of research and is capable of detecting pregnancy several days before the user experiences a missed period. Indeed, one television commercial described the advertised pregnancy test as ‘The most advanced piece of technology you will ever pee on’. Previous generations of pregnancy tests were less advanced. A papyrus from Egypt, dated ca 1350–1200 BC instructs a woman to urinate on a mixture of wheat and barley seeds [40]. If the woman was pregnant one type of seed would germinate and the type of seed that germinated was thought to predict the sex of the unborn child. The ancient Egyptian test was reproduced in 1963 and found to correctly detect pregnancy in 70% of cases, although it could not predict the sex of the

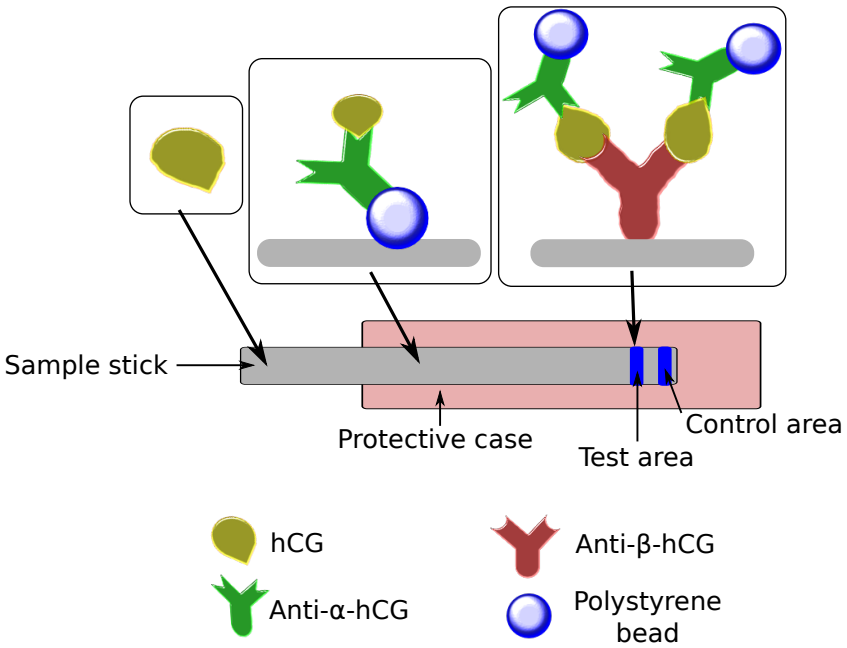

Figure 1.4: Schematic diagram of a pregnancy immunoassay. The uncovered end of the sample stick is exposed to a sample solution of urine. If hCG is present in the sample, it will form a complex with the antibodies. The complex is then washed to the test area where the other epitope of the hCG molecule binds to the surface adsorbed antibody. For clarity, BSA blocking molecules are not shown on the sample stick or polystyrene beads, although they are necessary for the immunoassay to function correctly.

child [41].

Modern pregnancy tests use antibody binding to test for the presence of the hCG antigen, which is produced in greater amounts during pregnancy. A schematic diagram of a commercial pregnancy test that can be performed at home is shown in Figure 1.4. The pregnancy test is manufactured by the sequential adsorption of anti-α-hCG and BSA onto latex beads that are several microns in diameter. The coated beads are then allowed to settle onto one end of a BSA-coated porous nitrocellulose sample stick before they are dried. At the other end of the sample stick a test area is formed by the sequential adsorption of anti-β-hCG and BSA along a small strip. Typical antibody and BSA bulk concentrations are in the region of 5 mg/ml.

The anti-α-hCG end of the sample stick is then exposed to a urine sample. If there are hCG molecules in the urine, a proportion of them will specifically bind to the anti-α-hCG antibodies to form a complex. Non-specific adsorption of hCG to the sample stick is prevented by the BSA adsorption step, which blocks available surface binding sites. The capilliary action of the porous foam forces the urine and anti-α-hCG/hCG complex coated beads towards the test area end of the stick. At the test area, the β epitope of the hCG becomes specifically bound to the surface-immobilised anti-β-hCG antibodies. Thus, the polystyrene beads are anchored to the test area by the anti-α-hCG/hCG/anti-β-hCG complex. The latex beads are dyed blue to give them a distinctive colour. Although the latex beads are only several microns in diameter, once a sufficient number of beads have become immobilised at the test surface a blue strip can be seen by eye. This indicates

Table 1.1: Percentage effectiveness of a Clearblue DIGITAL pregnancy test

Number of days before period is due	**Effectiveness of test (%)**
1	98
2	97
3	86
4	55

a pregnant result.

If there is no hCG present in the sample urine the anti-α-hCG-coated beads will pass the test area without becoming immobilised. In this case no blue line will form on the test area and a not-pregnant result will be given.

The pregnancy test also features a control area in which anti-β-hCG/hCG complexes are pre-adsorbed onto the surface. Any anti-α-hCG coated beads that are washed past the test area become bound to the complexes on the control area and form a blue line. The control area is used to test that the immunoassay is functioning correctly.

Different brands of pregnancy tests use different types of beads and each type of bead has its own distinctive colour. For example, colloidal gold and colloidal selenium both create red test areas. Phosphor particles and the bioluminescent protein aequorin have also been used for immunoassay labelling [4].

1.4.3 Effectiveness of pregnancy tests

Commercial pregnancy tests are often quoted to be 99% effective, i.e. they can correctly diagnose pregnancy 99% of the time. However, the quoted effectiveness is typically for the day of the user's missed period and the effectiveness sharply declines prior to this date, as shown in Table 1.1. The reduced effectiveness of the test before the day of the period is due to the lower concentration of hCG in the urine, which increases rapidly after conception, as shown in Figure 1.5. Four days before the period the hCG concentration is approximately 0.5 μg/l, too low to produce a reliable signal. The hCG concentration rapidly increases until it is approximately 10 μg/l on the day of the period. This concentration is sufficient to saturate all of the binding sites of the antibodies and the effectiveness of the test will not increase beyond this concentration.

Modern pregnancy tests are simple and quick to use and can be operated without the assistance of medical professionals. Indeed, a systematic review found that the effectiveness of home pregnancy tests were high regardless of whether they were operated

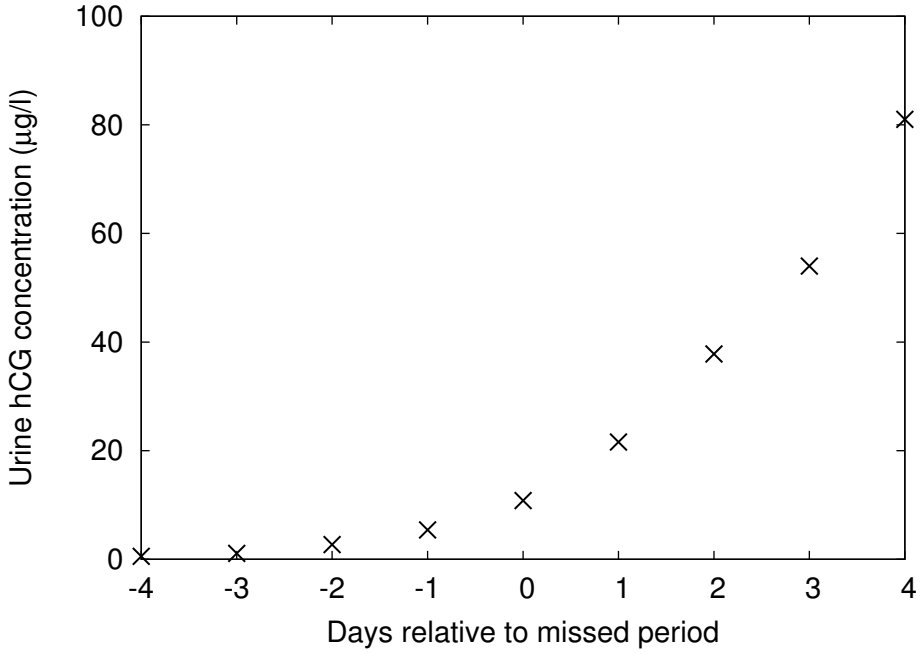

Figure 1.5: Concentration of hCG in urine as a function of time before period.

Figure 1.6: Photograph of a Clearblue DIGITAL pregnancy test. The dark blue cover is removed to expose the sample stick, which is dipped in the sample urine. Light from an LED is reflected from the test area and monitored by a photo diode. The intensity of the reflected beam is proportional to the number of polystyrene beads that are immobilised at the test area, which in turn is proportional to the urine hCG concentration. A liquid crystal display informs the user whether they are pregnant and how many days ago conception occurred (calculated from the urine hCG concentration).

by consumers or experienced technicians [42]. A photograph of a Clearblue DIGITAL home pregnancy test is shown in Figure 1.6. The test is able to give a diagnosis within 3 minutes of exposure to the sample. The test is manufactured by Swiss Precision Diagnostics Gmbh, Geneva, Switzerland and is sold globally.

1.4.4 Antigen binding capacity

As previously mentioned, the maximum antigen binding capacity (AgBC) is two, one antigen binds to each Fab of an antibody. Unfortunately, the AgBC of an immobilised protein is reduced and is often lower than 0.1. Currently, there are two different factors which are thought to explain the reduction in AgBC: the surface packing density of the adsorbed antibodies and their orientation on the substrate surface.

The surface packing density has been investigated by Herron et al [43] and Xu et al [44, 45]. Their results show that the AgBC is inversely proportional to the density of antibodies adsorbed at the solid/liquid interface. Numerous other experiments have been

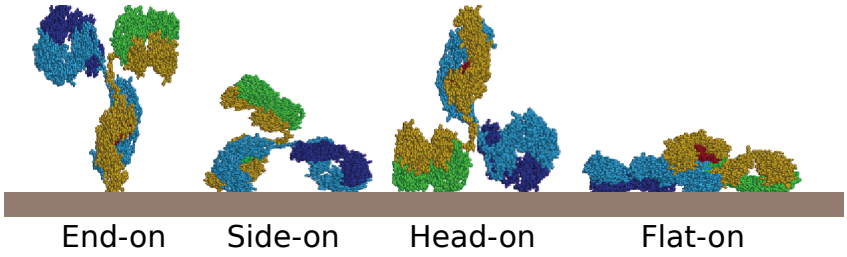

Figure 1.7: Different orientations adopted by antibodies adsorbed to a solid surface. Adapted from [44].

carried out to investigate the effect that the interfacial orientation of antibodies has on their AgBC [45–47]. It is believed that certain orientations inhibit antigen binding because of steric effects, for example, an antigen would be unable to reach the binding site of an hCG antibody adsorbed with its Fabs flat against the substrate surface in an inverted Y-shape. Xu et al [45] showed that the most common orientation of adsorbed hCG antibodies is the 'flat-on' position, where the Fc and both Fabs lie flat on the surface of the substrate, as shown in Figure 1.7. The steric hindrance associated with this position may help to explain the reduced AgBC of adsorbed antibodies.

The conditions necessary for the optimum binding of hCG antibodies to their antigens have not been widely researched, although Albertorio et al [48] have demonstrated that it is possible to measure antibody–antigen interactions when the antibody is immobilised on a lipopolymer. Their results show that the AgBC of an antibody is higher when immobilised on a lipopolymer instead of a hydrophilic substrate. A deeper understanding of the factors that cause the reduced AgBC of immobilised antibodies will increase the sensitivity of future immunoassays. This will greatly improve the diagnosis rates of life-threatening viruses and cancers.

1.4.5 Pregnancy tests and non-specific adsorption

For pregnancy tests and other immunoassays, it is vitally important to prevent the unwanted non-specific adsorption of antibodies and antigens to the sample surface. Failure to do so will result in incorrect diagnoses. For example, if the sample surface is insufficiently blocked, hCG antigen will become adsorbed on the surface. This will reduce the number of bulk hCG molecules. In extreme cases, the bulk hCG concentration will be reduced lower than the threshold necessary to produce a positive result. This will lead to a false negative result. Similarly, if the test area is insufficiently blocked, the anti-α-hCG coated beads will become non-specifically bound to the test area, whether or not there is hCG present in the urine. This will lead to a false positive result.

During the manufacturing process a control experiment is performed on a sample of the pregnancy tests. It is found that a significant proportion of the pregnancy tests fail and as such cannot be relied upon to give accurate results. This is likely due to the effect of unwanted non-specific adsorption of antibodies or antigens on the nitrocellulose sample

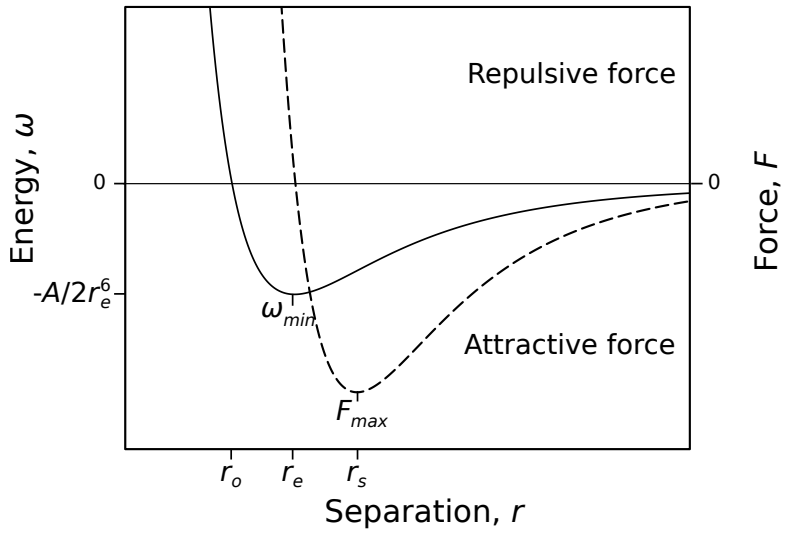

Figure 1.8: Energy and force as a function of the separation between two molecules of neutral charge. The attractive force between the molecules can be seen to be a maximum at r_s.

stick.

A better understanding of the non-specific binding of proteins to surfaces will enable more effective and more reliable pregnancy tests, and other immunoassays, to be produced.

1.5 Dynamic single molecule adhesion

Single molecule investigations into antibody–antigen binding forces have helped to provide further information about antibody–antigen interactions. Izrailev et al [49] studied the unbinding of avidin from biotin. However, the binding force between hCG and its antibodies has so far not been ascertained. It is known that antibody–antigen binding forces are typically of the order 1–100 pN [50].

The intermolecular force, F between two neutral molecules separated by a distance, r, can be approximated with the following equation

$$F = -\mathrm{d}\omega/\mathrm{d}r \tag{1.5.1}$$

where ω is the energy and is given by the van der Waals interaction pair potential:

$$\omega(r) = -X/r^6 + Y/r^{12} \tag{1.5.2}$$

where X and Y are the respective attractive and repulsive parameters inherent to the molecules and r is the molecular separation. From Figure 1.8 it can be seen that the force is zero at r_e, the equilibrium separation. At this point, the attractive and repulsive forces are balanced and the energy is at its minimum value. In order to separate the two molecules a force of F_{max} is needed. F_{max} occurs at r_s on Figure 1.8.

F_{max} is a simplistic approximation and does not account for the effects of temperature or time. For any temperature above 0 K the bound molecules will continuously vibrate and will also be struck by other vibrating molecules. At temperature T the energy of each collision will have a mean thermal energy of k_bT. Even if the depth of ω_{min} is far greater than the mean energy imparted to the bound molecule by a collision, given enough time a collision with sufficient energy to overcome the energy barrier will occur. Therefore, the force required to separate the molecules will be reduced. The Bell equation [51] can be used to calculate the reduced force:

$$F(t) = \frac{k_bT\ln(\tau/t)}{r_0} \tag{1.5.3}$$

where r_0 is the length of the bond and τ is the lifetime of the bond under zero force. For a system with average time between collisions, τ_0, the mean lifetime of a bond will be given by:

$$\tau = \tau_0 e^{-\omega_{min}/k_bT}. \tag{1.5.4}$$

For two molecules that are anchored together by multiple bonds, the separation force does not scale linearly with the number of bonds. This is because numerous attachments and detachments will occur over a given time. Instead, the Jarzynski equation [52] must be used:

$$\langle e^{W/k_bT}\rangle \xrightarrow[n=\infty]{} e^{-\omega_{min}/k_bT}. \tag{1.5.5}$$

where n is the number of rupture experiments performed on the bond and W is the work done, which is equal to Fr_0. The Jarzynski equation is required because some of the bonds will require an energy greater than ω_{min} to rupture [53].

1.6 Protein adsorption models

Numerous protein adsorption models have been developed in an attempt to predict adsorption. The accumulation over time, t, of protein mass per unit area, M, on a surface can be described by

$$\frac{\mathrm{d}M}{\mathrm{d}t} = k_ac_b\Phi(t,M) - k_d(t,M)M \tag{1.6.1}$$

where c_b is the protein concentration in the bulk, $\Phi(t,M)$ is the uncovered surface fraction, and k_a and k_d are the chemical adsorption and desorption coefficients respectively. The factors that influence the chemical adsorption coefficient include the diffusivity, of the protein, the protein-surface separation, and the interaction potential, which is the sum of the Van der Waals, electrostatic and electron donor-acceptor interactions. Thus, the value of k_a depends on the surface and solvent conditions such as, pH, ionic strength and temperature [54]. For most models, k_a is assumed to remain constant for all values of Φ.

The determination of Φ with respect to time is model dependent. Two of the most commonly used models, Langmuir adsorption and random sequential adsorption (RSA),

are described here.

1.6.1 Langmuir adsorption

Langmuir adsorption is a simple model that assumes that proteins are adsorbed irreversibly onto surface sites, that the molecules are not altered on adsorption, and that there are no interactions between the adsorbed molecules. The rate of deposition of molecules per unit area, ν, onto a surface is given by

$$\frac{\partial \nu(t)}{\partial t} = J c_\nu \Phi(t) \tag{1.6.2}$$

where $\nu(t)$ is the number density of molecules on the surface at time t, c_ν is the molecular concentration in the bulk, and J is the protein molecular flux at the empty surface. Because the Langmuir model assumes that there are no interactions between the adsorbed molecules, the uncovered surface fraction is given simply by

$$\Phi(t) = 1 - \theta(t) \tag{1.6.3}$$

where $\theta(t)$ is the fraction of the surface covered by proteins.

1.6.2 Random sequential adsorption

The random sequential adsorption (RSA) model also predicts that the rate of deposition is given by Equation (1.6.2). However, RSA takes into account the interaction between adsorbed particles. The model proposes that an adsorbed protein will produce an exclusion zone in which further proteins are prohibited from adsorbing. Figure 1.9 shows an example of this. Further protein adsorption can only occur at the available site between the adsorbed proteins' exclusion zones. The uncovered surface fraction for RSA, $\Phi(t)$, is approximated using [55, 56]:

$$\Phi = 1 - 4\theta + \frac{6\sqrt{3}}{\pi}\theta^2 + b\theta^3. \tag{1.6.4}$$

where b is a constant.

At long adsorption times the protein exclusion zones reduce the available surface fraction to the extent that further adsorption is not possible. This is known as the jamming limit. At the approach to the jamming limit there are numerous processes occurring, for example: adsorbed proteins may rearrange themselves on the surface or adsorbed proteins may leave the surface to be replaced by other proteins. At this point the system becomes too complex to be analytically solved. However, simulations have predicted that the rate of adsorption follows a t^{-1/d_f} trend [57],

$$\nu_\infty - \nu \sim t^{-1/d_f} \tag{1.6.5}$$

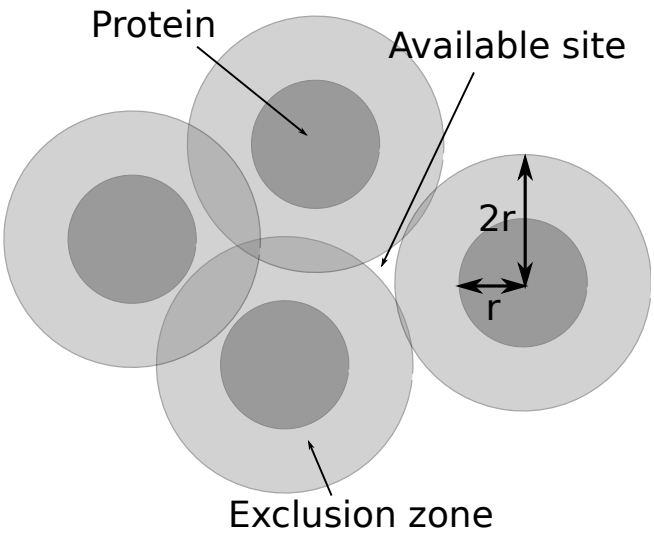

Figure 1.9: Top down view of proteins adsorbed on to a 2-dimensional surface. The RSA model assumes that adsorbed proteins generate an exclusion zone in which the adsorption of further proteins is forbidden.

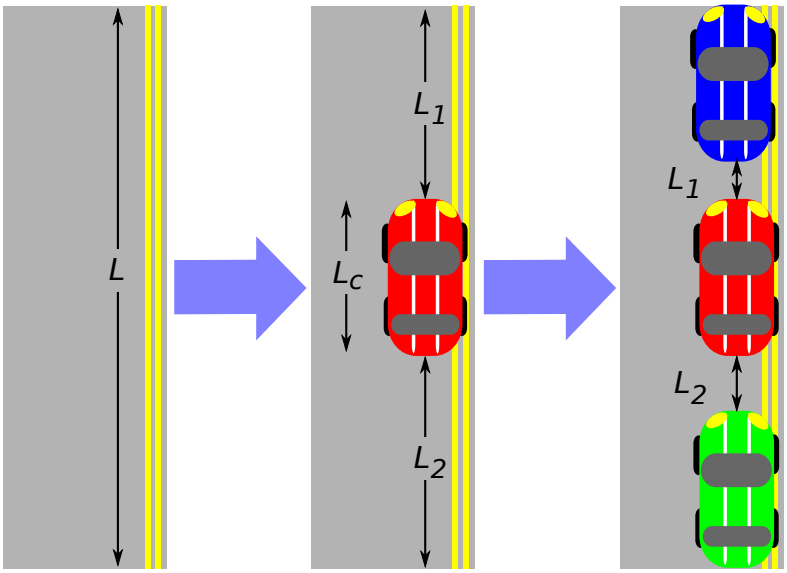

Figure 1.10: Approach to the jamming limit for a 1-dimensional system.

where d_f is the number of degrees of freedom of the system. At the jamming limit, Φ will be non-zero. This is because there are still uncovered areas on the surface but the exclusion zones of the adsorbed particles prevent further adsorption.

Figure 1.10 is a cartoon to demonstrate the approach to the jamming limit for a 1-dimensional system: cars that are sequentially parked at random points along the side of a road. Initially, the street is empty and cars are able to park along the entire length of the street, L. At this point Φ is equal to 1. If a car, of length L_c then parks, the total length available for other cars will be reduced to $L - L_c$ and Φ will be reduced to $(L - L_c)/L$. However, because the cars are parked at random, the available parking length will not necessarily be contiguous. For the example given in Figure 1.10, the car is parked so that the parking length is split into two parts, L_1 and L_2. At the jamming limit, the uncovered surface fraction, Φ, becomes small but non-zero: there are still unfilled lengths between

the cars but each unfilled length is smaller than L_c and further parking is prevented.

Adamczyk et al recently used Equation (1.6.5) to predict the adsorption of fibrinogen onto hydrophillic surfaces [58] but, so far, there has been little experimental verification of Equation (1.6.5). However, Ramsden [59] investigated the approach to the jamming limit for transferrin with the optical waveguide lightmode spectroscopy (OWLS) technique. He found that the experimental data closely followed the trend predicted by Equation (1.6.5).

1.6.3 History dependence

Calonder et al [60] have proposed that the adsorption kinetics of multi-step experiments can be used to quantify the history dependence of an adsorbed protein film. Their results show that the rate of protein adsorption is increased if the adsorbate has a previously adsorbed protein layer, when compared to a bare adsorbate. For adsorption onto a bare surface Φ in Equation (1.6.1) can be expanded as a power series of M [55] so that

$$\Phi = A + BM + CM^2 + \cdots \tag{1.6.6}$$

where A, B and C are non-zero coefficients. To second order, Equation (1.6.1) becomes

$$\left(\frac{\mathrm{d}M}{\mathrm{d}t}\right) = k_a c_b[A + BM] - k_d M \tag{1.6.7}$$

where A and B are the first and second order coefficients from the power series. A is equal to 1 for adsorption onto a bare surface [54]. For a multi-step experiment a protein solution is initially exposed to the surface (step 1) before it is replaced with a protein-free buffer solution to rinse reversibly adsorbed proteins from the surface. Another adsorption step is then performed (step 2). The experiment consists of n steps and the adsorption rate for the nth step is given by

$$\left(\frac{\mathrm{d}M}{\mathrm{d}t}\right)_n = k_a c_b[A_n + B_n(M_n - M_{(n-1)})] - k_d(M_n - M_{(n-1)}) \tag{1.6.8}$$

where A_n may differ from 1 due to the presence of the pre-adsorbed proteins [60]. $M_{(n-1)}$ is the surface coverage prior to the nth adsorption step.

1.6.4 Behaviour of real proteins

The models described in Section 1.6 incorrectly assume that the adsorbed protein molecules are rigid. In reality, the interaction forces between a protein molecule and the surface can lead to a change in the conformation or denaturation of the protein. The extent of the conformational change can be investigated with a plot of area per surface adsorbed molecule as a function of bulk protein concentration [61].

Ramsden's investigation of transferrin [59] revealed a decrease in the area per molecule with increased bulk concentration, which implies that the conformation of the adsorbed

proteins is dependent on the surface and intermolecular forces. A neutron reflectivity study by Su et al [19] showed that, at low bulk concentrations, the area per adsorbed BSA molecule was less than the short axis of BSA. Su's results suggest that denaturation of the BSA molecules had occurred.

A model developed by Van Tassel et al [62] includes the effect of proteins spreading over the surface over a finite amount of time. The model provided an excellent fit to Ramsden's transferrin adsorption data. More recently, a series of papers by Rabe et al describes a sophisticated model to describe the surface-induced spreading of protein clusters [63–65].

1.7 Research motivations

The study of proteins at the solid/liquid interface is of vital importance to numerous areas, such as the production of biocompatible materials and immunoassays. Numerous techniques for analysing the interfacial structure of adsorbed proteins exist [66], but it is often difficult to directly compare results from different studies due to different experimental conditions. Even slight changes in the surface chemistry, buffer properties or the inadvertent presence of fatty acids and other mixtures can hugely alter the adsorbed amount and thickness of an adsorbed protein layer [67]. Multiple techniques to make interfacial measurements, where the experimental conditions are kept constant, are therefore needed. As well as providing information on adsorbed protein layers, the results can also be used to directly compare the techniques employed.

Interfacial adsorption is of particular interest to the makers of immunoassays. The binding capacity of adsorbed antibodies is massively reduced compared to antibodies in solution. Although the binding capacity of the anti-β-hCG antibody has been investigated with ellipsometry [44], it has been difficult to obtain reliable thickness measurements in real-time. Obtaining the thickness of the adsorbed antibody layer would help to determine the orientation of the antibody, blocking agent and antigen. A combined ellipsometry, neutron reflection (NR) and dual polarisation interferometry (DPI) approach was successfully used to investigate the binding capacity of the PSA antigen [68] but the dynamics of the adsorption were not investigated. A study of the kinetics will allow further information to be obtained, such as determining at what surface coverage do intermolecular interactions dominate and whether the time between each adsorption step is important.

In addition, the adsorption of the blocking agent has largely been overlooked. The blocking agent is vital in preventing unwanted molecules from reaching the immunoassay surface where they may create false positive results. It is useful to know whether the blocking molecules slot between the antibodies and reduce the adsorption of unwanted molecules or if they sit on top of the antibody layer and reduce the antigen binding capacity.

1.8 Outline of thesis

Chapter 1 was designed to give the reader an introduction to protein adsorption and antibody–antigen binding. The operation of a typical pregnancy immunoassay was described in order to illustrate the applications of antibody–antigen binding. Interactions between proteins and surfaces as well as between proteins and proteins were discussed.

Chapter 2 will describe the operation of dual polarisation interferometry (DPI), neutron reflection (NR) and magnetic tweezers. DPI and NR can be used to determine the interfacial structure of adsorbed protein layers while magnetic tweezers investigate force changes that give indications of dynamic binding processes. The experimental method for each technique will be described in detail.

Chapter 3 BSA is widely used as a blocking agent in immunoassays. The detailed kinetics of its adsorption are thus important to optimise blocking and prevent non-specific adsorption of the target antigen. The near real-time resolution of DPI will be used to investigate the Langmuir and random sequential adsorption (RSA) protein adsorption models for BSA adsorbed at the silica/water interface. In addition, BSA adsorption at the silica/water interface will be used as a model system to explore DPI measurements and compare with the more established technique of neutron reflection.

Chapter 4 will describe how a model pregnancy test can be built on a silica surface in order to measure the interfacial structure of the adsorbed proteins with DPI and NR. DPI will also be used to investigate the adsorption kinetics of the proteins.

Chapter 5 will explain how a set of magnetic tweezers were designed and built in order to investigate the interaction between the hCG antigen and its antibodies. The design process will be given in detail. The completed magnetic tweezer system will be used to estimate the binding force between the hCG antigen and its antibodies as well as the effective bond length and dissociation constant.

Chapter 6 will summarise the thesis and offer ideas for future work.

CHAPTER
TWO

EXPERIMENTAL TECHNIQUES

2.1 Dual polarisation interferometry

2.1.1 Overview of dual polarisation interferometry

The Farfield Analight Bio200 Dual Polarisation Interferometer (DPI) is able to bridge the resolution gap between neutron reflectivity (NR) and ellipsometry. DPI can probe the interfacial structure of a protein layer with a depth resolution of several angstroms and it can do so in real time.

The DPI uses an illuminated slab waveguide interferometer to produce interference patterns that vary with the thickness and refractive index of adsorbed biological films. True to its name, the DPI simultaneously resolves two orthogonal polarisations of light: the transverse electric (TE_0) mode and the transverse magnetic (TM_0) mode. A mathematical analysis of the interference patterns produced by the two modes yields quantitative values of refractive index, thickness and density for an adsorbed biological film.

2.1.2 Total internal reflection and evanescent waves

The phenomenon of total internal reflection occurs when electromagnetic radiation, such as light, that is traveling through a material of high refractive index, n_1, is reflected from the interface formed by the high refractive index material and a second material of lower refractive index, n_2, as shown in part A of Figure 2.1. The simple ray model (Snell's law) can be used to show that a ray will be entirely reflected from the interface if it is incident at an angle greater than the critical angle θ_c, which is given by:

$$\theta_c = \sin^{-1} \frac{n_2}{n_1}. \tag{2.1.1}$$

If the incident angle is less than θ_c the ray will become split. Part of the ray will be reflected from the interface, but part will be refracted. Total internal reflection is commonly used to confine light to waveguides and fibre optic cables.

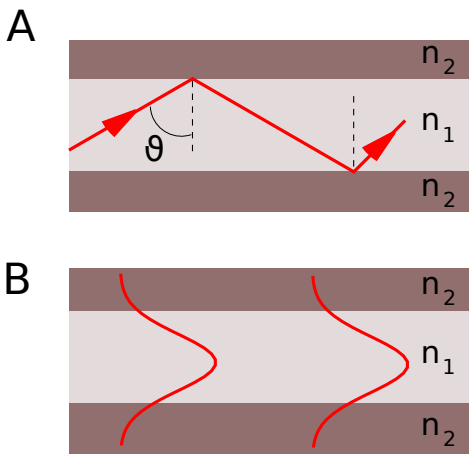

Figure 2.1: A) Ray diagram of an optical beam propagating through a waveguide. The beam is confined to the layer of high refractive index (n_1) and undergoes total internal reflection at the interfaces with the cladding layers. B) Plane wave model of the beam propagating through the waveguide. Although the wave is confined to the core layer, an evanescent field extends into the cladding layers.

In reality, light is better described as a wave than a ray. The simple ray model is therefore unable to fully describe the propagation of light, instead the plane wave model can be used to give a more accurate description. Part B of Figure 2.1 shows the amplitude of two wavefronts propagating through the waveguide. It can be seen that the amplitude of the wavefronts extends into the cladding layer, this is known as an evanescent wave. DPI makes use of this phenomenon to obtain structural data of adsorbed protein layers. The amplitude of the evanescent wave decays exponentially perpendicularly to the interface, which places an upper limit (< 100 nm) on the size of objects that may be measured with DPI.

2.1.3 Optical waveguide theory

A waveguide is formed by a core region of refractive index n_1 that is surrounded by a cladding layer of refractive index n_2, where $n_1 > n_2$. Light that is coupled to the waveguide is confined to the core region by total internal reflection, provided that $\theta > \theta_c$. A schematic diagram of a slab waveguide is shown in Figure 2.2.

Maxwell's equations describe how the magnetic and electric fields propagate in a given medium, they also state that electric and magnetic fields go hand in hand: a time-dependent electric field will generate a time-dependent magnetic field and vice versa. Maxwell's equations for the time-dependent propagation of magnetic and electric fields can be written as

$$\nabla \times \mathbf{E} = -\mu \frac{\partial \mathbf{H}}{\partial t} \tag{2.1.2}$$

and

$$\nabla \times \mathbf{H} = \epsilon \frac{\partial \mathbf{E}}{\partial t} \tag{2.1.3}$$

where $\mathbf{E}$ is the electric field vector and $\mathbf{H}$ is the magnetic field vector. ϵ is the dielectric

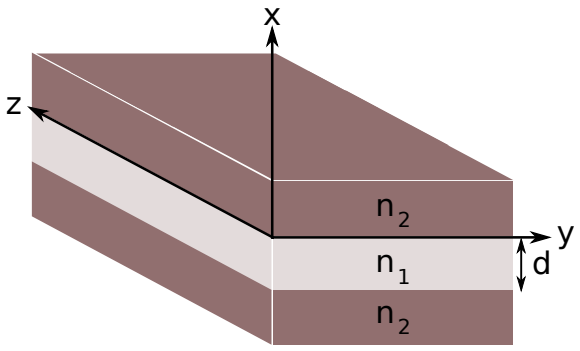

Figure 2.2: Schematic diagram of a dielectric slab waveguide. A layer of thickness d and refractive index n_1 is surrounded by cladding layers with refractive index n_2.

permittivity and is calculated from

$$\epsilon = \epsilon_0 n^2. \tag{2.1.4}$$

Since this thesis only considers non-magnetic waveguides, the magnetic permeability of the waveguide can be assumed to be

$$\mu = \mu_0 \tag{2.1.5}$$

where μ_0 is the magnetic permeability of a vacuum. For an electromagnetic plane wave of angular frequency, ω, the $\mathbf{E}$ and $\mathbf{H}$ fields will vary with time (t). For plane waves that propagate along the z axis, $\mathbf{E}$ is given by

$$\mathbf{E}(t) = \mathbf{E}_{(x,y)} e^{i(\beta z - \omega t)} \tag{2.1.6}$$

where β is the propagation constant in the z direction. Similarly for the magnetic field vector

$$\mathbf{H}(t) = \mathbf{H}_{(x,y)} e^{i(\beta z - \omega t)}. \tag{2.1.7}$$

The two Maxwell equations (Equations (2.1.2) and (2.1.3)) and Equations (2.1.6) and (2.1.7) can be combined to give

$$\frac{\partial E_z}{\partial y} - i\beta E_y = i\mu\omega H_x \tag{2.1.8}$$

$$i\beta E_x - \frac{\partial E_z}{\partial x} = i\mu\omega H_y \tag{2.1.9}$$

$$\frac{\partial E_y}{\partial x} - \frac{\partial E_x}{\partial y} = i\mu\omega H_z \tag{2.1.10}$$

and

$$\frac{\partial H_Z}{\partial y} - i\beta H_y = -i\omega\epsilon E_x \tag{2.1.11}$$

$$i\beta H_x - \frac{\partial H_z}{\partial x} = -i\omega\epsilon E_y \tag{2.1.12}$$

$$\frac{\partial H_y}{\partial x} - \frac{\partial H_x}{\partial y} = -i\omega\epsilon E_z. \tag{2.1.13}$$

The factor $e^{i(\beta z-\omega t)}$ is common to the right hand side of Equations (2.1.8) to (2.1.13), but is omitted for conciseness.

2.1.4 TE mode analysis

By definition the TE mode has no component of the electric field in the direction of wave propagation:

$$E_x = E_z = H_y = 0, \tag{2.1.14}$$

therefore it is possible to rearrange Equation (2.1.8) and Equation (2.1.10) to obtain the **H** components in terms of E_y

$$H_x = -\left(\frac{\beta}{\omega\mu}\right) E_y \tag{2.1.15}$$

$$H_z = \left(\frac{-i}{\omega\mu}\right) \frac{\partial E_y}{\partial x} \tag{2.1.16}$$

which are both substituted into Equation (2.1.12) to obtain the one-dimensional wave equation for the TE mode:

$$\frac{\mathrm{d}^2 E_y}{\mathrm{d}x^2} + (k^2 n^2 - \beta^2) E_y = 0 \tag{2.1.17}$$

where

$$k^2 = \omega^2 \epsilon_0 \mu_0 = \left(\frac{2\pi}{\lambda}\right)^2. \tag{2.1.18}$$

E_y can be separated into two plane waves where one propagates along the positive x axis and the other along the negative x axis in order to obtain the general solution for Equation (2.1.17). Thus, Equation (2.1.19) satisfies Equation (2.1.17)

$$E_y(x, z, t) = \left(ae^{-ik_x x} + be^{ik_x x}\right) e^{i(\beta z-\omega t)} \tag{2.1.19}$$

where a and b are field amplitude coefficients for the plane waves and $k_x = (k^2 - \beta^2)^{1/2}$. For the magnetic field, Equation (2.1.19) can be substituted into Equation (2.1.16) so that

$$H_z(x, z, t) = \frac{-k_x}{\mu\omega} \left(ae^{-ik_x x} - be^{ik_x x}\right) e^{i(\beta z-\omega t)}. \tag{2.1.20}$$

H_x is omitted as only the field components tangential to the layer interfaces are needed.

For a slab waveguide with N layers there are $N - 1$ interfaces. The tangential com-

ponents of the electric and magnetic fields must be continuous at each of these interfaces. For the first layer ($l = 1$) the following boundary conditions are required to let the evanescent field decay therefore, the coefficient a_1 should equal zero. The matching condition for E_y is

$$b_1 e^{ik_{x,1}x_1} = a_2 e^{-ik_{x,2}x_1} + b_2 e^{ik_{x,2}x_1} \tag{2.1.21}$$

and for H_z

$$\frac{-k_{x,1}}{\mu_1} b_1 e^{ik_x x} = \frac{k_{x,2}}{\mu_2} \left(a_2 e^{-ik_{x,2}x_1} - b_2 e^{ik_{x,2}x_1} \right) \tag{2.1.22}$$

where the subscripts represent the layer number. As ω and β are constant throughout each layer, the $e^{i(\beta z - \omega t)}$ term is omitted. For all layers where $2 \leq l \leq N - 2$ the matching conditions at each interface are

$$a_l e^{-ik_{x,l}x_l} + b_l e^{ik_{x,l}x_l} = a_{l+1} e^{-ik_{x,l+1}x_l} + b_{l+1} e^{ik_{x,l+1}x_l} \tag{2.1.23}$$

$$\frac{k_{x,l}}{\mu_l} \left(a_l e^{-ik_{x,l}x_l} - b_l e^{ik_{x,l}x_l} \right) = \frac{k_{x,l+1}}{\mu_{l+1}} \left(a_{l+1} e^{-ik_{x,l+1}x_l} - b_{l+1} e^{ik_{x,l+1}x_l} \right). \tag{2.1.24}$$

For the final interface, between layers $l = N$ and $l = N - 1$, the evanescent field must decay, which means that $b_N = 0$

$$a_{N-1} e^{-ik_{x,N-1}x_{N-1}} + b_{N-1} e^{ik_{x,N-1}x_{N-1}} = a_N e^{-ik_{x,N}x_{N-1}} \tag{2.1.25}$$

$$\frac{k_{x,N-1}}{\mu_{N-1}} \left(a_{N-1} e^{-ik_{x,N-1}x_{N-1}} - b_{N-1} e^{ik_{x,N-1}x_{N-1}} \right) = \frac{k_{x,N}}{\mu_N} a_N e^{-ik_{x,N}x_{N-1}}. \tag{2.1.26}$$

2.1.5 TM mode analysis

The TM mode has no component of the magnetic field along the axis of propagation, and has the field components H_y, E_x and E_z. Equation (2.1.11) and Equation (2.1.13) can be rearranged in terms of H_y and substituted into Equation (2.1.9) to give

$$\left(k^2 n^2 - \beta^2 \right) H_y + \frac{\partial^2 H_y}{\partial x^2} = 0 \tag{2.1.27}$$

which is the one-dimensional wave equation for the H_y component. The general solution for Equation (2.1.27) is

$$H_y(x, z, t) = \left(a e^{-ik_x x} + b e^{ik_x x} \right) e^{i(\beta z - \omega t)}. \tag{2.1.28}$$

As only the tangential components are required, E_x can be omitted and the general solution for E_z is given by

$$E_z = \frac{k_x}{\omega\epsilon}\left(-ae^{-ik_x x} + be^{ik_x x}\right)e^{i(\beta z - \omega t)}. \tag{2.1.29}$$

For the TM mode, the boundary conditions are required to be continuous at the interfaces for the H_y and E_z components. a_1 is set to zero for the first interface so that the evanescent wave can decay in the first layer:

$$b_1 e^{ik_{x,1}x_1} = a_2 e^{-ik_{x,2}x_1} + b_2 e^{ik_{x,2}x_1} \tag{2.1.30}$$

$$\frac{k_{x,1}}{\omega\epsilon_1}\left(b_1 e^{ik_{x,1}x_1}\right) = \frac{k_{x,2}}{\omega\epsilon_2}\left(-a_2 e^{-ik_{x,2}x_1} + b_2 e^{ik_{x,2}x_1}\right). \tag{2.1.31}$$

For the layers $2 \leq l \leq N-2$ the matching conditions at each interface are

$$a_l e^{-ik_{x,l}x_l} + b_l e^{ik_{x,l}x_l} = a_{l+1}e^{-ik_{x,l+1}x_l} + b_{l+1}e^{ik_{x,l+1}x_l} \tag{2.1.32}$$

for the H_y component and

$$\frac{k_{x,l}}{\omega\epsilon_l}\left(-a_l e^{-ik_{x,l}x_l} + b_l e^{ik_{x,l}x_l}\right) = \frac{k_{x,l+1}}{\omega\epsilon_l + 1}\left(-a_{l+1}e^{-ik_{x,l+1}x_l} + b_{l+1}e^{ik_{x,l+1}x_l}\right) \tag{2.1.33}$$

for the E_z component. At the final interface b_N must be zero in order for the evanescent wave to decay in the final layer

$$a_{N-1}e^{-ik_{x,N-1}x_{N-1}} + b_{N-1}e^{ik_{x,N-1}x_{N-1}} = a_N e^{-ik_{x,N}x_{N-1}} \tag{2.1.34}$$

$$\frac{k_{x,N-1}}{\omega\epsilon_{N-1}}\left(-a_{N-1}e^{-ik_{x,N-1}x_{N-1}} + b_{N-1}e^{ik_{x,N-1}x_{N-1}}\right) = \frac{k_{x,N}}{\omega\epsilon_N}\left(-a_N e^{-ik_{x,N}x_{N-1}}\right). \tag{2.1.35}$$

The matching conditions for the TE and TM modes can be used to calculate the propagation constant along the x direction, k_x, and the thickness, x, for a given layer by use of Equation (2.1.36)

$$\mathbf{M}(\beta^2)\begin{pmatrix} b_1 \\ a_2 \\ b_2 \\ a_3 \\ \vdots \\ a_N \end{pmatrix} = 0 \tag{2.1.36}$$

where $\mathbf{M}$ is a matrix. Each mode will have its own value of β. Equation (2.1.36) can be solved iteratively once β is known, as discussed in Section 2.1.6.

2.1.6 DPI theory

The DPI uses a CMOS camera to monitor the interference fringes produced by light emitted from two layers of a slab waveguide. The slab waveguide is made from two silicon oxynitride layers, known as the sensing and reference layers, that are separated by a silicon oxynitride cladding layer of thickness, d, as shown in figure (2.3).

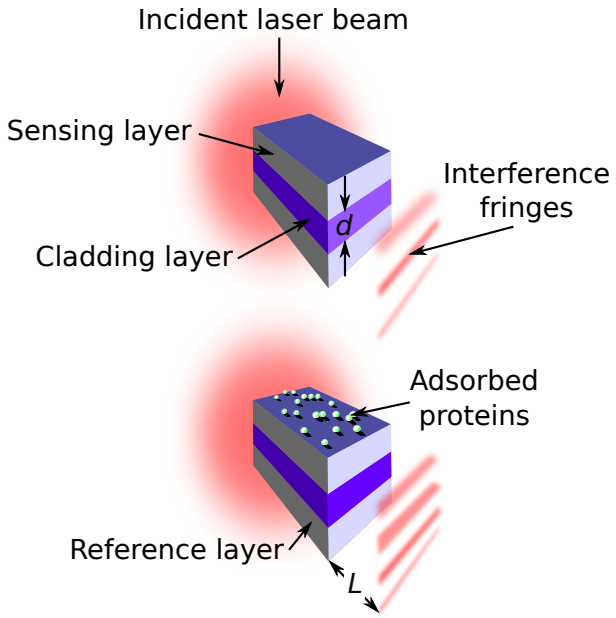

Figure 2.3: A schematic diagram of the DPI sensing system geometry. Top: The sensing surface is not exposed to protein. Bottom: The interference fringes are vertically shifted by protein adsorption on the sensing surface. A CMOS camera is positioned a distance, L, from the end of the waveguide in order to monitor the interference fringes.

The waveguide layers are made of silicon oxynitride. The refractive index of a layer is proportional to its nitrogen content, which is controlled in order that light will be confined to and propagate through the sensing and reference layers when the waveguide is illuminated at its end facet. The refractive index and thickness of each waveguide layer is given in Table 2.1. A helium-neon laser (λ = 632.8 nm) is coupled to one facet of the waveguide. Both TE_0 and TM_0 modes of the incident light propagate through the sensing and reference layers before exiting from the opposite facet. The CMOS camera is positioned in the far field region, $L >> d$, which means that the light emitted from the sensing and reference layers can be considered as two point sources. Thus, the setup resembles Young's double slit experiment and interference fringes form in the far field region. In the far field region, constructive interference occurs where the two light sources are in phase,

$$\psi_s + \psi_r = \frac{2\pi dx}{\lambda L} = 2\pi m \tag{2.1.37}$$

where ψ_s and ψ_r represent the respective phases of the sensing and reference waves, m is an integer and x is the fringe spacing.

Light that undergoes total internal reflection at the interface between two media of

Table 2.1: Optogeometrical parameters for the slab waveguide layers.

Layer	Refractive index, n	Thickness (nm)
Sensing	1.520	1000
Cladding	1.470	3000
Reference	1.520	1000
Cladding	1.485	2000

different refractive indices will create an evanescent field. An evanescent field will exponentially decay perpendicularly from this interface and can interact with the electrons of the media in which it is present. The result of this is a change in the propagation constant, β, of the mode:

$$\beta = \sqrt{\omega^2 n^2 \mu - k_x^2} \tag{2.1.38}$$

where n is the refractive index of the medium [69]. Thus, a mode propagating in the medium has a propagation constant that is dependent on the refractive index of the medium as well as that of the material that interacts with the evanescent field. DPI makes use of this phenomenon by exposing the surface of the sensing layer to different sample materials. The samples interact with the evanescent field and the propagation constant of the mode in the sensing layer is altered. Meanwhile, the propagation constant of the reference mode will remain constant, because its evanescent field decays in the cladding layer. Figure 2.4 shows how an evanescent field extends from both the sensing and reference waveguides.

The resulting change in the propagation constant of the mode in the sensing layer leads to a phase difference, $\Delta\psi$, between the light that leaves the reference and sensing layers. This phase difference causes the interference fringes to be vertically shifted by Δx,

$$\Delta x = \frac{\lambda L}{2\pi d}\Delta\psi = \frac{x\Delta\psi}{2\pi d}. \tag{2.1.39}$$

The fringe shift is recorded by the CMOS camera so that the change in the propagation constant of the sensing waveguide ($\Delta\beta$) can be calculated

$$\Delta\psi = \Delta\beta l \tag{2.1.40}$$

where l is the length of the sensing waveguide that is exposed to the sample [70]. From the propagation constant of each polarisation it is possible to calculate the thickness and refractive index of the layer adsorbed on the sensing waveguide with Equation (2.1.36).

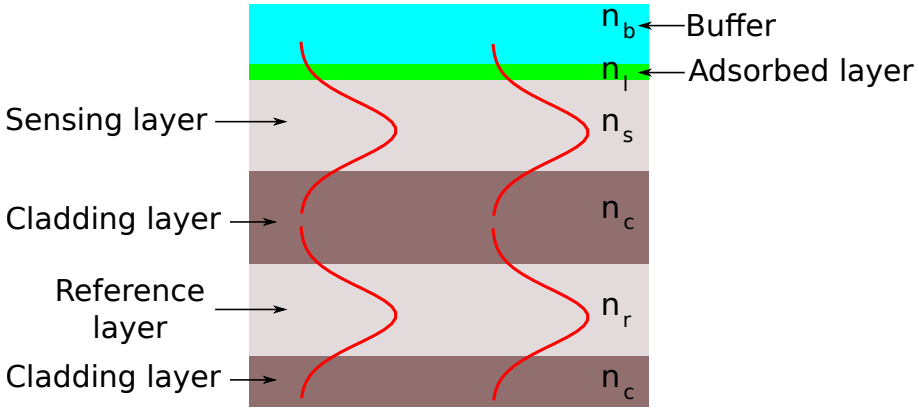

Figure 2.4: The slab waveguide is composed of sensing, reference and cladding layers that have respective refractive indices n_s, n_r and n_c. An evanescent field extends from the reference layer into the cladding layers above and below. Thus, the propagation constant of the reference mode is dependent on n_r and n_c, and can be considered to be a constant. The propagation constant of the sensing layer is dependent on n_s and n_c as well as the refractive indices of the adsorbed layer (n_l) and buffer (n_b) above.

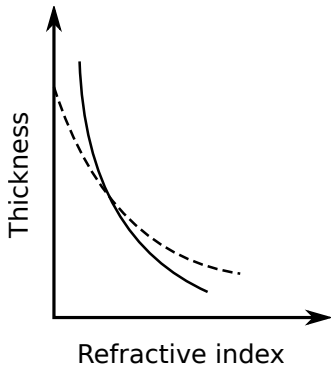

Figure 2.5: Graph to show the possible combinations of thickness and refractive index values that will satisfy Maxwell's equations for a given sample. The dotted line represents the possible values for the TE_0 polarisation and the solid line the TM_0 polarisation. The lines intersect at the point where the values simultaneously satisfy the equations for both polarisations.

As the refractive indices of the sensing layer and bulk solution are determined from calibration steps, only the matching conditions for the adsorbed layer are missing. These are calculated iteratively and for each polarisation there will be a continuous range of layer refractive index and thickness values for the adsorbed layer that will satisfy the equations. However, for an isotropic homogeneous model, there will only be one combination that is able to satisfy the equations for both polarisations simultaneously, as shown in Figure 2.5.

For an adsorbed layer with refractive index n_l and thickness $\mathrm{d}x$ in a buffer of refractive index n_b the measured change in optical path length will be

$$[n_l(x) - n_b]\mathrm{d}x. \tag{2.1.41}$$

If the adsorbed layer has an inhomogeneous refractive index along the x direction then

the change in path length will be

$$\int_0^\infty [n_l(x) - n_b]\mathrm{d}x. \tag{2.1.42}$$

McCrackin and Colson showed that a weighted average layer refractive index, $\overline{n}_l$, can be calculated from an adsorbed layer of thickness $\mathrm{d}x$ that alters the optical path length as described in Equation (2.1.41) by [71]

$$\overline{n}_l = \frac{\int_0^\infty n_l(x)[n_l(x) - n_b]\mathrm{d}x}{\int_0^\infty [n_l(x) - n_b]\mathrm{d}x} \tag{2.1.43}$$

and for the average thickness, $\overline{x}$,

$$\overline{x} = \frac{\int_0^\infty [n_l(x) - n_b]\mathrm{d}x}{\overline{n}_l - n_b}. \tag{2.1.44}$$

Equation (2.1.43) and Equation (2.1.44) were extended by De Feijter et al in order that the adsorbed mass per unit area, or surface coverage, M, could be calculated. The surface coverage is proportional to the excess concentration of protein in the adsorbed layer, $\Delta c_l(x)$

$$M = \int_0^\infty \Delta c_l(x)\mathrm{d}x \tag{2.1.45}$$

where

$$\Delta c_l(x) = c_l(x) - c_b \tag{2.1.46}$$

and c_l is the absolute concentration of protein in the adsorbed layer and c_b is the bulk protein concentration [72]. If n_l depends linearly on the protein concentration then

$$n_l = n_b + (\mathrm{d}n/\mathrm{d}c)\,\Delta c_b \tag{2.1.47}$$

where $\mathrm{d}n/\mathrm{d}c$ is the gradient of a linear fit applied to the refractive index of a protein solution as a function of its protein concentration. Equations (2.1.43) to (2.1.45) and (2.1.47) can be combined to give the De Feijter equation [72]

$$M = \frac{\overline{x}(\overline{n}_l - n_b)}{\mathrm{d}n/\mathrm{d}c} \tag{2.1.48}$$

so that M can be calculated.

The layer thickness and refractive index obtained by DPI is calculated from the assumption that the adsorbed layer has a uniform thickness (x_{avg}) and refractive index (n_{avg}). Thus, the DPI obtained value for Equation (2.1.42) will be

$$[n_{avg} - n_b]x_{avg}. \tag{2.1.49}$$

However, it has been shown that the integral for an inhomogeneous film and the homoge-

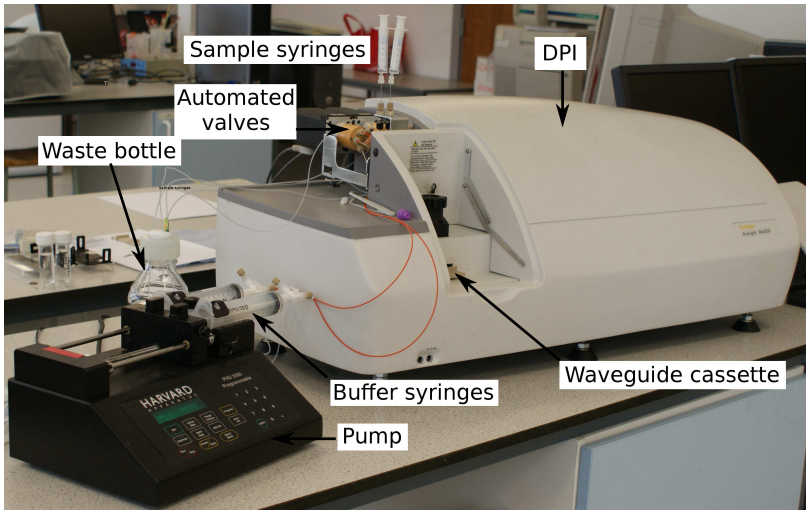

Figure 2.6: Photograph of an Analight Bio200 DPI and associated equipment.

neous DPI equivalent are in good agreement [70]. The De Feijter equation can therefore be used to obtain surface coverage from DPI data, where $\overline{x}$ and $\overline{n}_l$ in Equation (2.1.48) are substituted for the DPI equivalents:

$$M = \frac{x_{avg}(n_{avg} - n_b)}{\mathrm{d}n/\mathrm{d}c}. \tag{2.1.50}$$

2.1.7 Experimental method for DPI

A photograph of the DPI is shown in Figure 2.6. Samples and cleaning agents were injected into the valves with the sample syringes. A PHD2000 (Harvard Apparatus Ltd., Kent, UK) pump was then used to flow buffer, samples or cleaning agents over the waveguide surface.

The DPI fluidic system was thoroughly cleaned prior to each experiment in order to remove trace amounts of proteins or surfactants that may have been present in the flow tubes and valves. The sample valves were loaded with 5% (w/w) Decon 90 solution and left to soak for 25 minutes. 30 ml of the Decon 90 solution was then loaded into the buffer syringes and an automated cleaning script was set to run. The script pumped the Decon in the buffer syringes through the fluidic system at various flow rates and the sample valves alternated between the open and closed positions. This ensured that both the flow tubes and the sample valves were cleaned. After all of the Decon had been pumped through the DPI the same script and procedure were performed with 50% ethanol solution (w/w) in the buffer syringes and sample valves. This step was designed to remove Decon solution from the fluidic system. Finally, the procedure was repeated with buffer solution in the sample valves and buffer syringes in order to remove the ethanol solution.

After prolonged use of the DPI it was found that additional cleaning steps were required. Over time, the glass window that covers the CMOS camera accumulated dirt. This made the interference fringes appear less well defined. The CMOS window was cleaned with an ethanol-soaked lens tissue wrapped around a cotton swab. The lens tis-

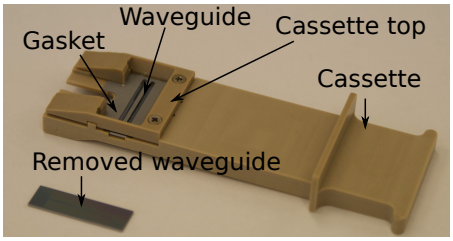

Figure 2.7: Photograph of a cassette-mounted waveguide and gasket. An unmounted waveguide is shown next to the cassette.

sue was wiped across the window once and was then discarded. This was repeated until the definition of the fringes was improved. In addition, a polyether ether ketone (PEEK) block, that was placed on top of the waveguide to create sample channels, required cleaning after 5-10 days of DPI experiments. The block was cleaned with an ethanol-soaked lens tissue before it was dried with nitrogen.

Before each experiment it was necessary to thoroughly clean the removable waveguide. The waveguide was removed from the DPI and scrubbed with lens tissue in a 5% solution of Decon 90 for several minutes. The waveguide was then rinsed with copious amounts of ultra-pure water (UHQ) in order to ensure that all of the Decon solution was removed from the waveguide surface. Excess water was removed from the waveguide by blowing with nitrogen gas before the waveguide was placed onto its cassette. A gasket, made from Kalrez®, was cleaned and dried in the same way as the waveguide before it was placed on top of the waveguide. The gasket was used to form two channels, each with a volume of 0.4 ml. The waveguide and gasket were then firmly attached to the cassette by screwing the cassette top into place. The cassette, waveguide and gasket are shown in Figure 2.7. The cassette-mounted waveguide and gasket were then reinserted into the DPI.

In order to check that the waveguide had been adequately cleaned, repeated samples of water and ethanol were passed over the waveguide surface. If the phase was observed to remain constant to within 0.1 radians before and after the ethanol injections then it was deduced that nothing had been added to or removed from the surface of the waveguide.

Since the waveguide was removable, it was necessary to calibrate it prior to each experiment. The calibration was performed by measuring the phase difference between a sample of 80% ethanol/water (w/w) and pure water.

Sample solutions were introduced to the waveguide surface at a flow rate of 10 μl/min and adsorbed for 10 minutes before the pump was stopped and the sample was allowed to equilibrate. After enough data had been obtained, the adsorbed samples were washed from the waveguide with at least three 0.7 ml injections of Decon 90 at a flow rate of 100 μl/min. After the Decon clean the phase was observed to be less than before the sample had been introduced. Repeated 0.7 ml ethanol injections were used to remove all traces of the Decon. Because the Decon may have etched away a thin layer of the waveguide surface, it was necessary to repeat the calibration procedure before further

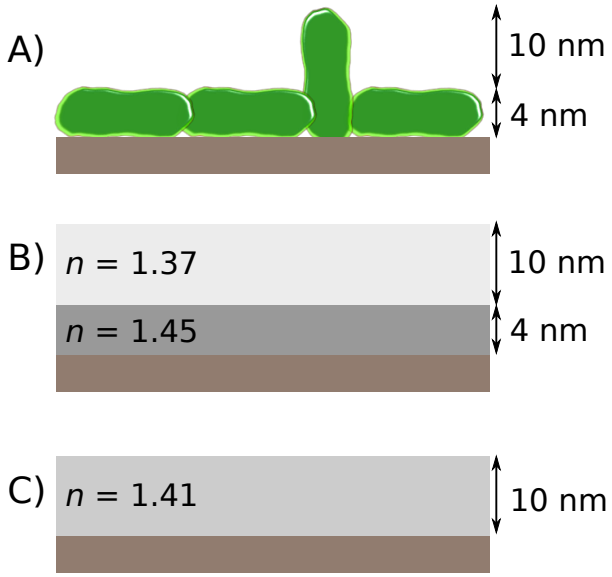

Figure 2.8: Panel A: BSA (green blobs) adsorbed on a substrate (dark grey). The adsorbed BSA can be split into two equivalent homogeneous layers: an inner layer of high density (refractive index) and low thickness and a diffuse but thicker outer layer, as seen in panel B. Panel C: As the DPI uses a single layer fit, it measures an homogeneous layer that is a weighted average of the two layers seen in panel B.

samples were adsorbed.

DPI data analysis was performed using the Analight Explorer software. The software used the measured phase data and Maxwell's equations to calculate the thickness and refractive index of the adsorbed samples, as described in Section 2.1.6.

2.1.8 Limitations of DPI

The uniform layer approximation of DPI means that information about the density profile perpendicular to the surface can be lost. Panel A of Figure 2.8 shows an adsorbed BSA layer. The majority of the BSA molecules adsorb in the side-on orientation so that their short axis of 4 nm is perpendicular to the surface (this is discussed further in Chapter 3). However, one molecule has adsorbed so that its long axis is perpendicular to the surface. This complex structure can be approximated as two equivalent homogeneous layers, as shown in panel B. The inner layer (closest to the substrate) is thinner but more dense than the outer layer and therefore has a correspondingly higher refractive index of 1.45. The outer layer is thicker but more diffuse. Because the refractive index of protein is higher than the surrounding buffer, the refractive index of the layer is proportional to the layer density. Therefore the outer, diffuse layer has a lower refractive index than the inner layer. The DPI measured layer is shown in panel C and is a weighted average of the two layers shown in panel B.

The effect of perpendicular density distribution was investigated with the DPI DOS Resolver software (Farfield group, Ltd., Manchester). The software enables the phase change from a given interfacial structure to be calculated and was used to calculate the

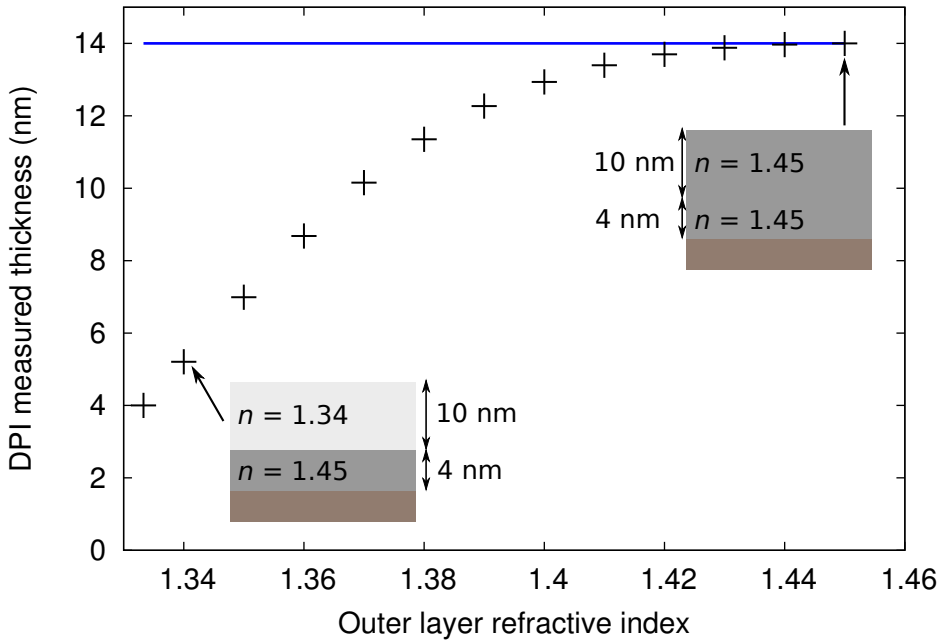

Figure 2.9: Theoretical DPI-measured thickness as a function of the refractive index of the outer layer (black crosses). The blue line indicates the actual combined thickness of the inner and outer layers.

expected phase change produced by BSA adsorbed in the structure shown in panel A of Figure 2.8. A simulated buffer with a refractive index of 1.333 was used for all calculations. The thickness and refractive index of the inner layer were kept constant at 4 nm and 1.45 respectively. For the outer layer, only the refractive index was varied, the thickness was kept constant at 10 nm. The refractive index of the outer layer was varied between 1.45 and 1.334. An outer layer refractive index of 1.45 simulated a BSA layer where all the molecules had adsorbed in the end-on position to create a single, close-packed layer of 14 nm. An outer layer refractive index of 1.334 meant that the outer layer was almost entirely composed of buffer. The chip parameters used for the calculations are shown in Table 2.1.

Figure 2.9 shows that the DPI measured thickness of the average layer increased with the refractive index of the outer layer. As the outer layer became more diffuse, the DPI measured thickness dropped significantly. The DPI-measured average refractive index of the two layers is shown as a function of the outer layer refractive index in Figure 2.10. The average refractive index as measured by the DPI can be seen to decrease

Propagation through a waveguide can be investigated by splitting the length of the waveguide into discrete steps and evaluating the optical constants at each interface between each step [73]. This method provides a useful way to investigate how DPI measures the thickness of diffuse layers. The DPI waveguide can be divided into arbitrary lengths and each length can either have adsorbed protein on its surface (filled) or not (empty). The phase of modes that propagate through the waveguide will be retarded along filled lengths when compared to the empty lengths. The total phase change experienced by

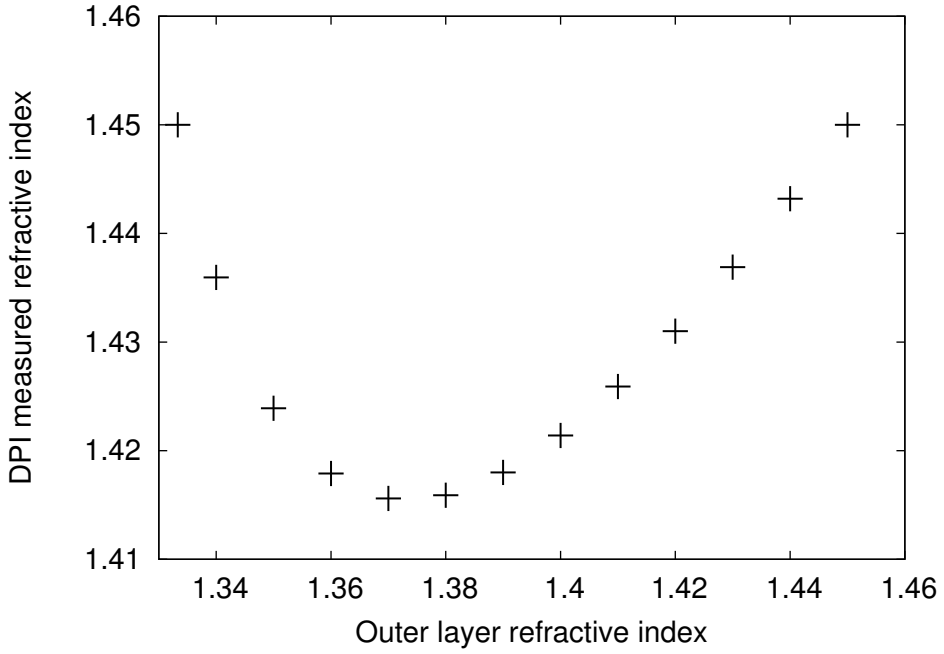

Figure 2.10: Theoretical DPI measured refractive index as a function of the outer layer refractive index.

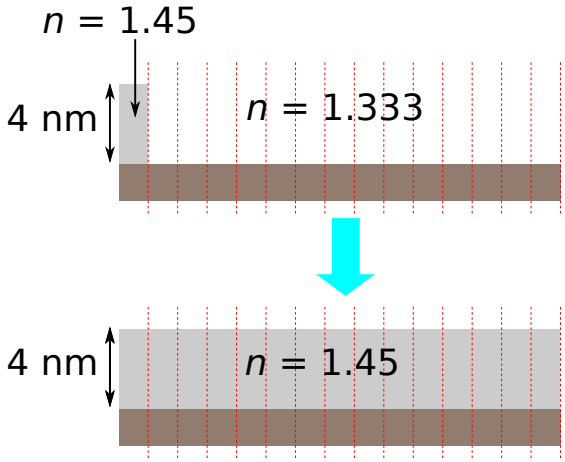

Figure 2.11: Schematic diagram to show how the waveguide has been divided into 15 1 mm lengths (not to scale). Top: the first length has an adsorbed protein block 4 nm thick and with a refractive index of 1.45. The other lengths have no adsorbed blocks and have a refractive index equal to the buffer. Bottom: the lengths were then sequentially filled with protein blocks until the entire waveguide was full.

the modes in the waveguide will be equal to the sum of the phase of each length. To enable the waveguide to be modelled in this way with the DPI DOS Resolver software, the waveguide was split into 15 1 mm lengths, as shown in Figure 2.11. Each length had either an adsorbed "block" of protein or was empty.

The phase change experienced by the TE and TM modes was calculated as a function of the number of protein blocks on the surface, as shown in Figure 2.12. A single filled length was modelled by calculating the phase change for a 4 nm thick block with a refractive index of 1.45 on a 1 mm waveguide. A single block had a phase change of 0.5413312

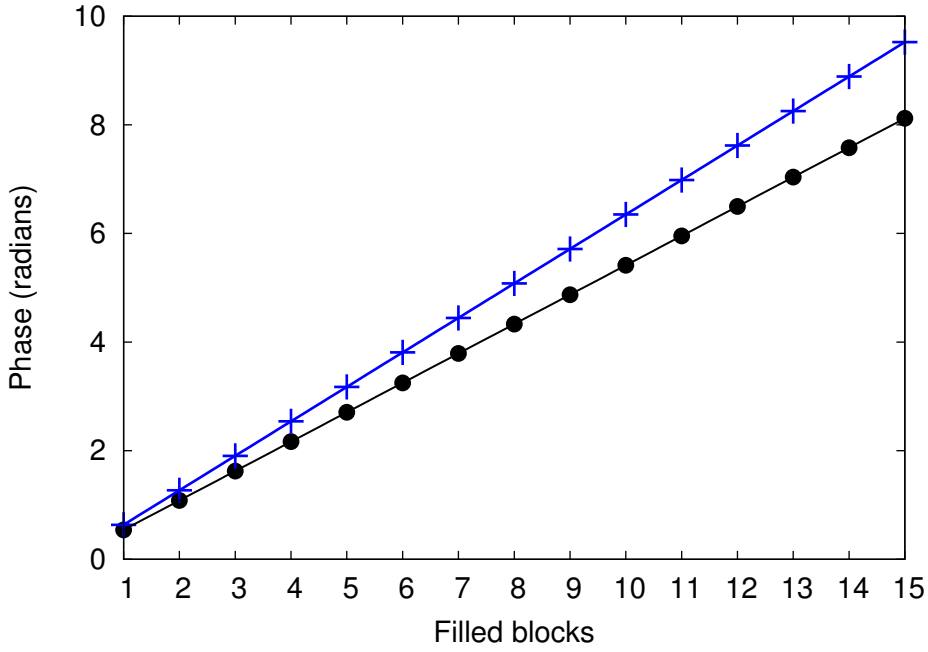

Figure 2.12: TE (black circles) and TM (blue crosses) phase as a function of the number of filled protein blocks. The solid lines represent linear fits to the data.

and 0.6349201 for the TE and TM modes respectively, while an empty length offered no phase change. The phase change of N blocks was calculated by modelling the same layer on an N mm waveguide. The phase change increased linearly with the number of filled blocks.

The phase change for N blocks was then put into the resolver software for a 15 mm waveguide, so that the thickness and refractive index of the equivalent homogeneous layer could be calculated, as seen in Figure 2.13. Both the thickness and refractive index of the equivalent homogeneous layer can be seen to increase linearly with the number of filled protein blocks. Only when all of the blocks are filled are the correct thickness and refractive index measured. Although real protein adsorption does not occur in 1 mm blocks, the results of this crude simulation show that the thickness of a diffuse layer is underestimated by DPI.

Another limitation of DPI is that different interfacial structures may appear to have the same thickness. For example, instead of protein blocks filling the surface laterally, they can also be stacked on top of each other in such a way that the average layer thickness of n stacked blocks is similar to the average layer thickness of n blocks adsorbed laterally. Figure 2.14 shows two stacked blocks. Stacked blocks can be used to simulate end-on adsorbed proteins or multilayers.

The phase change was calculated for a 1 mm waveguide with stacked blocks of 4 nm thickness and a refractive index of 1.45, results are shown in Figure 2.15. Linear fits were applied to the phase data of each mode. Although the phase initially increased linearly, the data no longer followed a linear trend after the fourth block had been added. A linear fit was applied to the first three data points of each mode and is shown in Figure 2.15 so

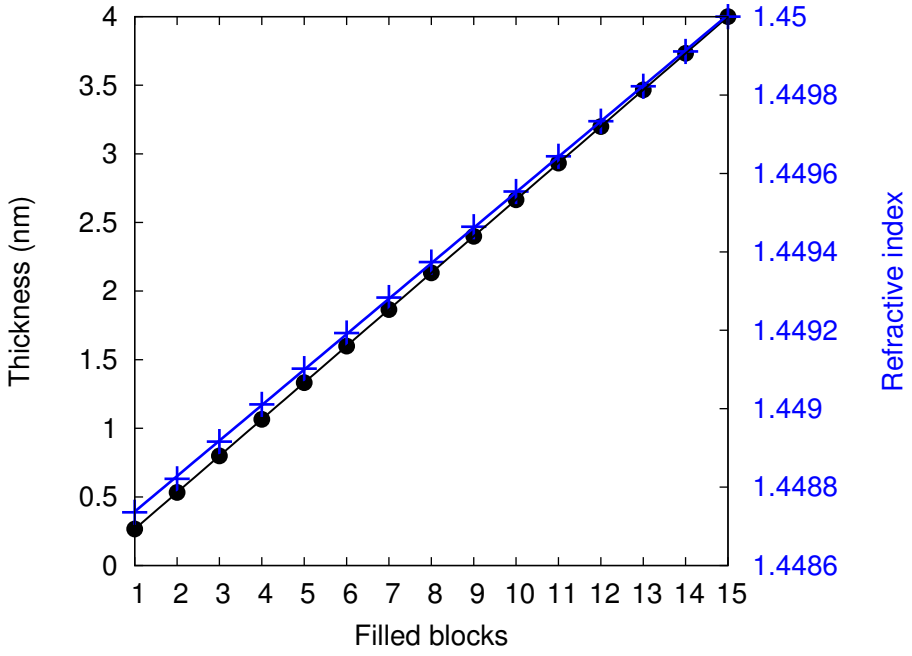

Figure 2.13: Thickness (black circles, left axis) and refractive index (blue crosses, right axis) as a function of the number of filled protein blocks. The solid lines represent linear fits to the data.

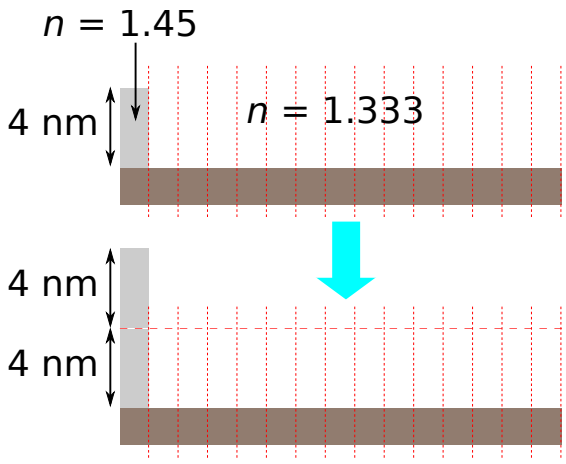

Figure 2.14: Schematic diagram to show a second protein block stacked on top of the first.

that deviations from the linear fit can be seen clearly. As the phase change above four blocks (16 nm) is less than predicted by the linear fit, it is likely that this is a result of the decay of the evanescent field.

The thickness and refractive index of an equivalent homogeneous layer were then calculated from each phase change resolved on a 15 mm waveguide, results are shown in Figure 2.16. It can be seen that the thickness of the equivalent homogeneous layer initially increased linearly with the number of stacked blocks before it began to increase more slowly than predicted by the linear fit. Meanwhile, the refractive index decreased as the number of stacked blocks increased.

A stack of two blocks produced an equivalent homogeneous layer with a thickness of

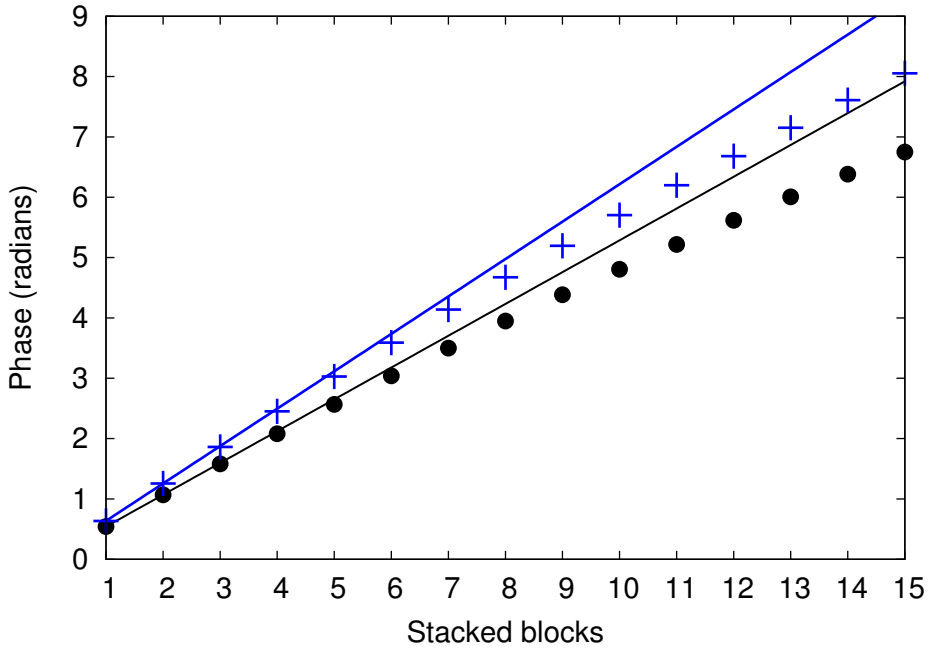

Figure 2.15: TE (black circles) and TM (blue crosses) phase as a function of the number of stacked protein blocks. A linear fit was applied to the first three data points of each mode (solid lines).

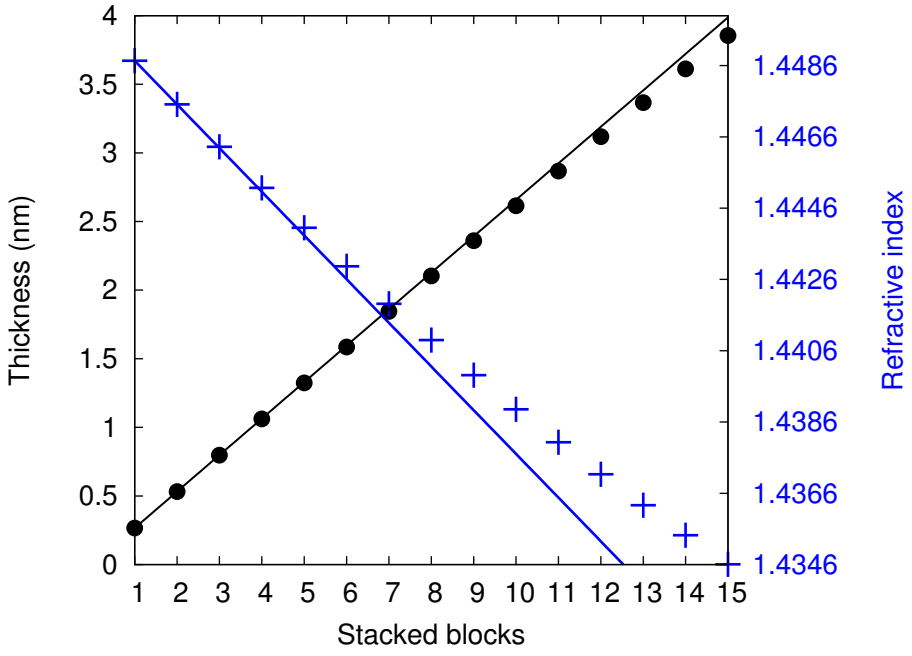

Figure 2.16: Thickness (black circles, left axis) and refractive index (blue crosses, right axis) as a function of the number of stacked protein blocks. A linear fit was applied to the first three data points for both thickness and refractive index (solid lines).

0.532 nm, equal to the 0.532 nm thickness of the equivalent homogeneous layer created by two blocks adsorbed side by side. Figure 2.13 and Figure 2.16 show that the equivalent homogeneous layer thickness for N lateral blocks is approximately equal to that of N stacked blocks. This result further highlights how care must be taken when measuring the thickness of adsorbed layers with non-uniform density distributions with DPI and other waveguide-based instruments.

2.2 Neutron reflection

2.2.1 Overview of neutron reflection

Neutron reflection is a useful technique to reveal structural information of ultra-thin films at the solid-liquid and air-liquid interfaces. The resolution of neutron reflection experiments depends on the neutron wavelength. Neutrons of wavelength 0.5-13 Å are typically selected for reflection experiments as they give a resolution of 2-3 Å when investigating the interfacial thickness of an adsorbed protein layer. This wavelength range is much lower than that of visible light and means that NR can resolve smaller structural details than diffraction-limited optical techniques. The non-ionising nature of neutron radiation means that biological samples are not damaged, unlike for X-ray diffraction.

All NR experiments described in this thesis were performed at the ISIS Neutron Facility (Rutherford Appleton Laboratory, Chilton, Didcot, UK) on the SURF medium flux reflectometer and the D17 reflectometer at the Institut Laue-Langevin (ILL), Grenoble, France.

2.2.2 Neutron production

ISIS uses a spallation source to generate neutrons. Initially, an ion source is used to provide a linear accelerator with H^- atoms. The linear accelerator increases the kinetic energy of the H^- beam to 70 MeV before feeding it into a 52 m diameter synchrotron. Once inside the synchrotron, the beam collides with an aluminium oxide foil in order to strip the H^- atoms of their electrons. After 10,000 orbits of the synchrotron the proton beam is accelerated to 800 MeV (84 percent of the speed of light) and is directed on to a tantalum target where the collision is of sufficient energy to force neutrons from their nuclei. Approximately 12 neutrons are released for every proton that collides with the target. This process is repeated 50 times per second.

At the ILL, neutrons are generated by a nuclear fission reactor. The reaction is optimised to produce neutrons for research rather than to provide electricity.

The kinetic energy of the neutrons produced at ISIS and the ILL is too high for them to be used experimentally. In order to reduce the kinetic energy of the neutrons, the beam is passed through a series of neutron moderator tanks; The tanks are filled with water, liquid methane or liquid hydrogen. The various reflectivity and scattering experiments at

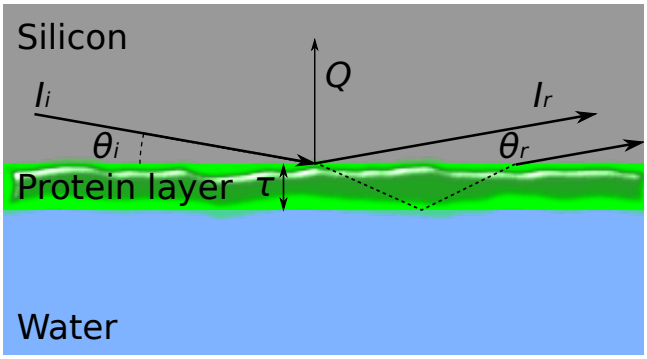

Figure 2.17: Schematic diagram of a NR experiment. Neutrons undergo reflection at the interfaces of the different media.

ISIS and the ILL are positioned along the axis of the moderated beam. By-products of the fission reaction or spallation, such as muons and γ-rays, are used by other instruments.

2.2.3 Theory of neutron reflection

Thanks to their wave-particle duality, neutrons can be reflected from interfaces in the same way as photons. Figure 2.17 shows that the experimental setup for a NR experiment is similar to that of an optical technique, such as ellipsometry. In the solid/liquid NR experiments described in this thesis, an incident neutron beam of known intensity is reflected from a silica/protein interface into a neutron detector. The neutron detector measures the reflected beam intensity. Because the beam is also refracted at each interface, there will be a difference between the incident and reflected intensities. The ratio between the incident and reflected beam intensities for specular reflection (incident angle is equal to the reflected angle) is known as the reflectivity, R.

Reflectivity is usually calculated as a function of the momentum transfer, q, and scattering length density, ρ:

$$R(q) = \frac{16\pi^2}{q_z^2}|\rho(q)|^2 \tag{2.2.1}$$

where q_z is the momentum transfer perpendicular to the interface. The momentum transfer function is used to describe the change in momentum of a neutron reflected at an angle of θ. The momentum transfer also depends on the wavelength, λ, of the reflected neutrons:

$$q = \frac{4\pi}{\lambda}\sin\theta. \tag{2.2.2}$$

The scattering length density is a function of the number density, n, of an element, i, with scattering length, b

$$\rho = \sum b_i n_i. \tag{2.2.3}$$

The scattering length density of a species is determined experimentally and can have a positive, negative or zero value. Table 2.2 lists the scattering lengths and scattering length densities of some typical materials that are used in NR experiments.

Table 2.2: Scattering lengths and scattering length densities for typical species used in NR experiments.

Species	**Scattering length** ($\times 10^5$ Å^{-1})	**Scattering length density** ($\times 10^6$ Å^{-2})
D_2O	19.2	6.4
H_2O	-1.7	-0.6
SiO_2	15.9	3.4
lysozyme (in H_2O)	3377.4	2.0

In a protein adsorption experiment, the sample is allowed to adsorb before the reflectivity is measured as a function of the momentum transfer. A model is then fitted to the experimental data. NR models are typically based on the optical matrix method [74], which assumes that the adsorbed protein film can be split into any number of stacked parallel layers. Each of the model layers is assumed to be a region of homogeneous thickness and scattering length density. However, each layer is composed of a mixture of scattering species, therefore the total volume of an adsorbed protein layer can be split into a protein fraction and a solvent fraction. The volume fraction of the protein is calculated with

$$\phi_p = \frac{\rho_l - \rho_s}{\rho_p - \rho_s} \tag{2.2.4}$$

where ρ_l, ρ_s and ρ_p are the scattering length densities of the layer (as estimated from the model), pure solvent and pure protein respectively. The protein volume fraction and layer thickness, τ, can then be used to calculate the area, a, of the substrate that is occupied by a single protein molecule

$$a = \frac{V_p}{\tau \phi_p} \tag{2.2.5}$$

where V_p is the molecular volume of protein. Finally, the surface coverage can be calculated with

$$M = \frac{M_W}{N_A a} \tag{2.2.6}$$

where M_W is the molecular weight of the protein and N_A is the Avogadro constant.

It is often necessary to calculate the volume fraction of a protein (y) that has adsorbed on a surface that has been pre-coated with another protein (x), as for the model immunoassays described in Chapter 4. In this case, the volume fraction of protein y, ϕ_y, is given by

$$\phi_y = \frac{\rho_{l(x+y)} - \rho_{lx}}{\rho_y - \rho_s} \tag{2.2.7}$$

where $\rho_{l(x+y)}$ is the scattering length density of the mixed protein layer and ρ_{lx} is the scattering length density of the pre-adsorbed protein layer.

The model that is chosen for the experimental data is the one that provides the best fit with the least number of parameters. However, in some cases, multiple models may provide good fits to the same experimental data, adding ambiguity to the structure of the sample layers. Fortunately, one of the major advantages of NR is that the scattering length density contrast between the sample and solvent can be easily varied with isotopic substitution. As can be seen from Table 2.2, there is a large difference between the scattering length densities of H_2O and D_2O, which are both readily available solvents. Thus, parallel experiments can be performed in D_2O, H_2O, or a mixture of the two. It is likely that only one model will fit the experimental data for multiple contrasts. Isotopic substitution has little effect on the chemistry of the experiment, but it does affect the scattering length density of the studied protein. Protein scattering length densities are different in H_2O compared to D_2O due to the exchange of the protein's labile hydrogen atoms with the hydrogen in the solvent.

2.2.4 Experimental method for neutron reflection

NR experiments were performed on the surface of a <111> silicon block. Prior to the experiments, the block was initially polished with various-sized diamond particles before a final polish with 0.1 μm alumina colloids. The polished block was then immersed in pH neutral Decon 90 for 30 minutes before it was washed with UHQ and ethanol. In order to maximise its surface hydrophilicity, the block was immersed for 2 minutes in Piranha solution (6:1 98% H_2SO_4 to 25% H_2O_2) at $90°$C. The Piranha solution was then rinsed from the block surface with running water. The treated block was then scrubbed in Decon 90 solution with a lens tissue before it was rinsed clean with UHQ and dried with nitrogen. A UVISEL ellipsometer (Horiba Jobin Yvon) measured the oxide layer on at least five places on the surface of the block to be 15 ± 3 Å.

A custom-built perspex trough was clamped to the prepared block surface as shown in Figure 2.18. The trough had a volume of $\sim$3 ml and featured entrance and exit tubes so that solvents and samples could be introduced to and removed from the block surface. Before use, the trough and tubes were immersed in Decon 90 and cleaned with a lens tissue. The trough was then thoroughly rinsed with UHQ and dried with nitrogen. Screws on the clamps were used to form a tight seal between the block surface and the trough. Care was taken to not over-tighten the screws, as this could have bent the block surface.

Samples and solvents were pumped slowly into the trough with either a syringe or a HPLC pump. The top clamp had a window so that bubbles on the experimental surface could be seen and removed.

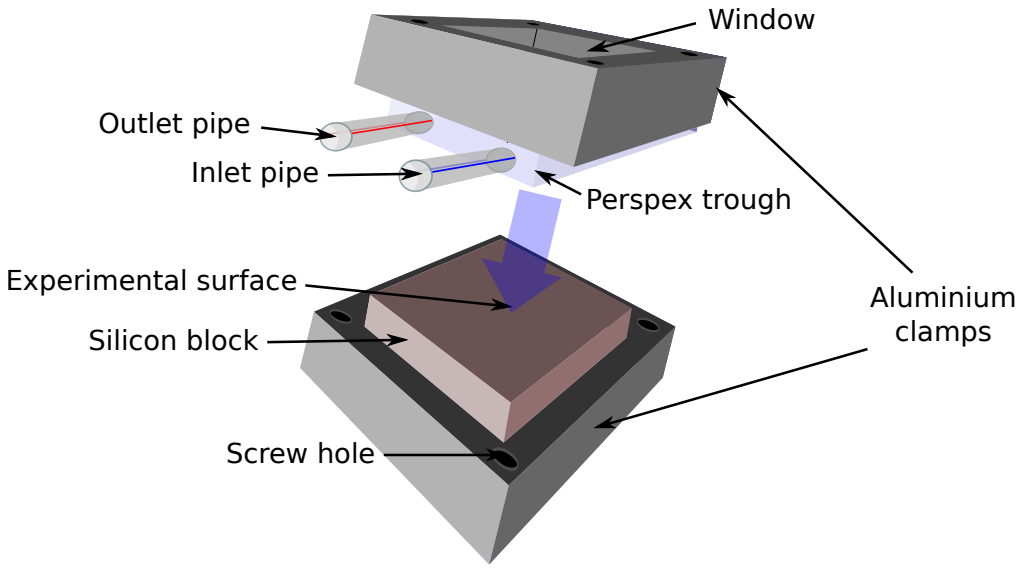

Figure 2.18: A schematic diagram of the NR block, trough and clamps. The silicon block and trough are sandwiched between the aluminium clamps to form a tight seal. Solvents and samples are introduced to and removed from the experimental surface via the inlet and outlet tubes. Screws are used on each corner of the clamp to prevent the system from leaking.

The exchange of the cell was measured by first filling the cell with H_2O and then pumping D_2O into the cell 2 ml at a time, via an HPLC pump. After each 2 ml injection the reflectivity was measured, as shown in Figure 2.19. As the D_2O content of the trough increased the critical edge that is characteristic of D_2O reflection began to emerge. After 10 ml of D_2O had been pumped through the cell the critical edge was well defined (Figure 2.19 blue triangles). This indicated that the original H_2O had been completely replaced with D_2O.

The block was mounted on a computer controlled goniometer and aligned along the axis of the neutron beam. A coarse alignment was initially performed with a laser before the neutron beam was used for fine alignment. The block was positioned so that the neutron beam passed through the small face of the block and was reflected from the solid/liquid interface. The experimental surface of the block was illuminated with a neutron beam with a footprint of 40 mm $\times$ 20 mm. The height and angle of the block were adjusted in iterative steps to maximise the reflectivity from the interface. Horizontal and vertical slits were used to collimate the beam and define the size of the beam footprint on the block surface. An additional set of horizontal and vertical slits were used to reduce the background neutron radiation at the detector. A chopper was used to select neutrons of wavelengths between 0.5 Å and 13 Å for experimental use.

Prior to the actual experiment, the reflectivity of the block surface was measured so that the SiO_2 layer could be accurately included in the models that were fitted to the sample reflectivity profiles. Reflectivity measurements were performed at incident beam angles of 0.35°, 0.8° and 1.8° to give a q range of 0.012 $Å^{-1}$ to 0.7 $Å^{-1}$. The reflectivity

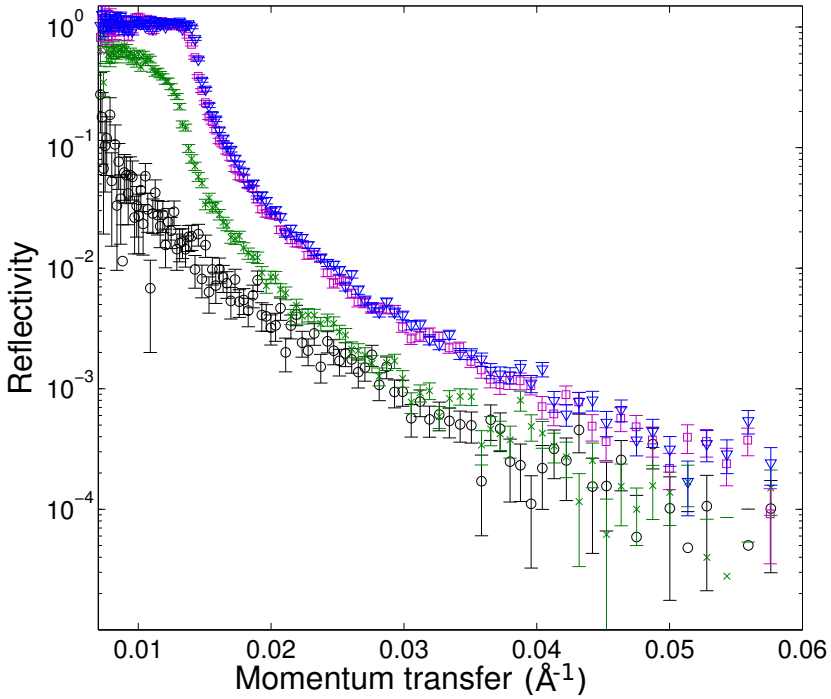

Figure 2.19: Graph to show the reflectivity of the silica surface of the silicon block after pure H_2O (black circles) was replaced with D_2O in steps of 2 ml. The green crosses represent 4 ml of D_2O, purple squares represent 8 ml and blue triangles 10 ml. The characteristic critical edge of D_2O reflection can be seen to emerge after D_2O is pumped into the cell.

below this range was assumed to be unity and a scaling factor was added to the final plots to account for this. The background reflectivity was estimated from an average of the reflectivity between q values 0.25 $Å^{-1}$ and 0.6 $Å^{-1}$. The background was then subtracted from the measured reflectivity and was typically less than 2×10^{-6} for measurements performed in D_2O. The block and sample were left in the beam until enough neutrons had been reflected into the detector. The number of neutrons required was dependent on the incident beam angle. Less neutrons were required at small angles than large angles as it was easier to determine the reflected neutrons from the background level of neutrons at small angles, as seen in Figure 2.20. A typical experiment in a D_2O buffer took 90 minutes on the Surf reflectometer and only 30 minutes on the D17 reflectometer due to the higher neutron flux available on the D17 reflectometer.

Datafit, FRESNEL and MOTOFIT [75] programs were used to analyse the reflectivity curves. The programs used slab models based on the Abeles matrix approach where the thickness and scattering length density of the slab layers were the fitted parameters. Analysis was performed in iterative steps until the calculated reflectivity profile provided a suitable fit to the experimental reflectivity profile.

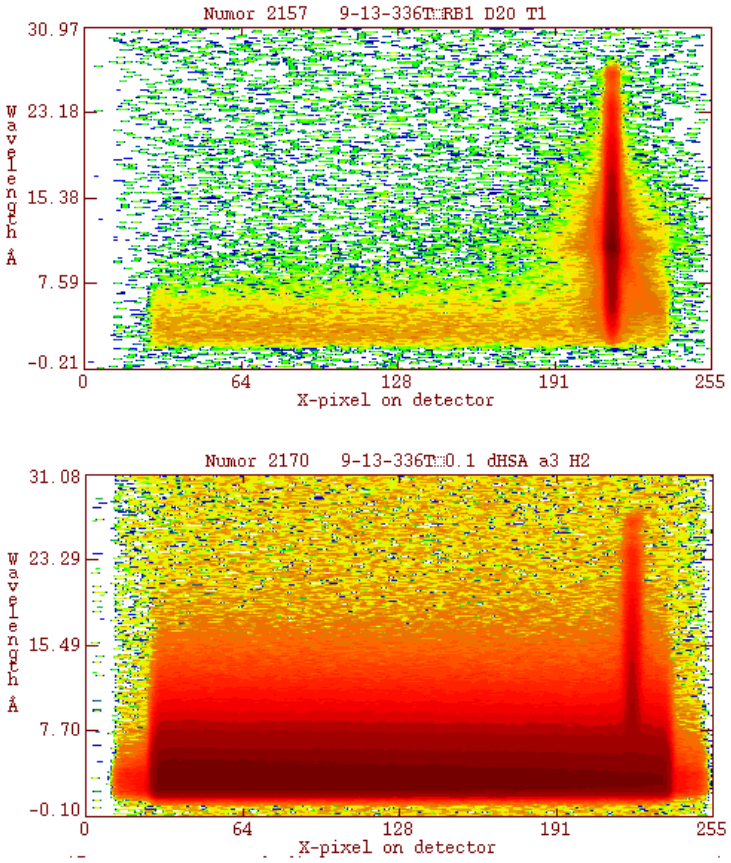

Figure 2.20: Comparison of neutron detector counts at small (top) and large (bottom) incident beam angles from the D17 reflectometer. Blue means few neutrons were recorded by that pixel of the detector while red means many neutrons were detected by the pixel. At small angles the reflected neutron beam is a dark red peak that can be clearly distinguished from the background. At larger angles the reflected beam is more difficult to see.

2.3 Magnetic tweezers

2.3.1 Overview of magnetic tweezers

A magnetic tweezer system exploits a magnetic field gradient in order to exert precise forces upon magnetic particles. Biological samples are attached to the magnetic particles so that force spectroscopy and rheology experiments can be performed on the sample [76–78].

2.3.2 Magnetism

According to classical atomic theory, electrons orbit their respective nucleus in a circular motion. It is known that magnetic fields are produced by moving charges; therefore all electrons must generate a magnetic dipole moment [79]. However the net magnetic

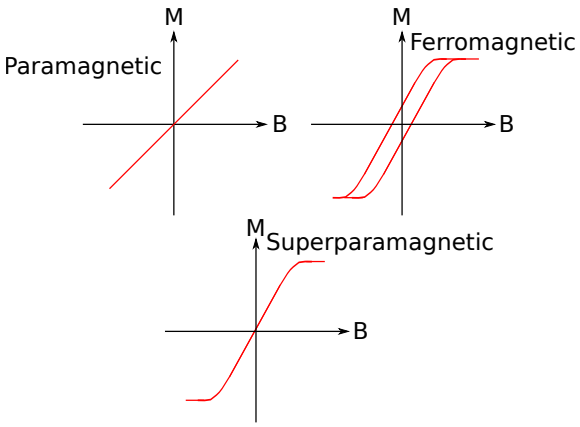

Figure 2.21: Magnetisation response ($\mathbf{M}$) of paramagnetic, ferromagnetic and superparamagnetic materials in an external magnetic field ($\mathbf{B}$).

dipole moment of an atom will depend on the overall alignment of the individual dipole moments of all of its constituent electrons. If, for example, the dipole moments of the electrons in a helium atom are anti-parallel, then the atom will have a net magnetisation of zero. An atom will acquire an induced magnetisation in the presence of an external magnetic field, because the magnetic dipoles of its electrons seek to align themselves parallel to the field. The intrinsic magnetisation of an atom and the extent to which its magnetic dipoles align themselves with an external field determine its magnetic behaviour. There are three types of magnetic behaviour relevant to the magnetic tweezers system described in this thesis: *paramagnetism*, *ferromagnetism* and *superparamagnetism*.

The atoms of paramagnetic materials feature permanent magnetic dipole moments [80]. These dipoles usually experience a coupling force that causes neighbouring dipoles to align in the same direction. However, the thermal energy, at room temperature, is sufficient to overcome the coupling force in a paramagnet. This results in the random alignment of the dipoles meaning that a macroscopic sample of a paramagnetic material will have zero net magnetisation. The low magnetic susceptibility, characteristic of paramagnetic materials, means that the magnetisation induced in the presence of an external magnetic field will be low. The magnetic dipoles will revert back to their randomised state when the material is removed from the field. Figure 2.21 depicts how the magnetisation of a paramagnetic material depends on the strength of an external magnetic field.

Ferromagnetic materials also contain atoms with permanent magnetic dipole moments. Unlike paramagnets however, the magnetic atomic dipoles of a ferromagnet tend to align themselves together in macroscopic domains as the coupling force is more prominent than the effects caused by thermal energy. Generally, the alignment of the magnetic domains in a ferromagnet will be random. When an external magnetic field is introduced, the magnetic domains whose alignment matches that of the field will increase in size whilst the domains of opposed magnetic alignment will contract. A ferromagnet will therefore become strongly magnetised in the presence of even a weak magnetic field. Stronger fields increase the re-alignment rate of the magnetic domains. A ferromagnet is said to be saturated when all of its magnetic domains are aligned with the external field,

the magnetisation will remain constant once saturation has occurred, hence the plateau observed in Figure 2.21. The majority of magnetic domains will remain aligned when the external field is removed. Thus, the magnetisation of a ferromagnet will depend on its magnetic history [81]. A hysteresis effect is observed in ferromagnets due to the tendency for the domains to remain aligned.

Superparamagnetic materials are composed of numerous ferromagnetic particles that are separated by dielectric regions [81]. The ferromagnetic particles are typically 1–10 nm in size. For superparamagnetic behaviour to occur, the thermal energy must be insufficient to overcome the coupling force between atoms but sufficient to change the alignment of the ferromagnetic particles. Thus, the ferromagnetic particles form magnetic domains, but the alignment of the domains is randomised, thereby causing the average magnetisation to be zero. Such behaviour means that a superparamagnet will respond to an external magnetic field in a similar manner to a ferromagnet except that magnetisation and demagnetisation occur rapidly with no hysteresis. The ferromagnetic domains rapidly align towards a field and quickly become randomly oriented upon removal of the field.

Commercially available superparamagnetic beads include Dynabeads, manufactured by Invitrogen. Dynabeads are formed from superparamagnetic Maghemite ($\gamma-Fe_2O_3$) particles of 8 nm diameter that are evenly distributed within a polymer shell.

2.3.3 Magnetic tweezer systems

One of the first magnetic tweezer systems was designed by Crick and Hughes in 1949 [82]. Their system lacked the high magnification optics and computer integration typical of modern tweezer systems, which meant that useful results were difficult to obtain. However, modern magnetic tweezer systems operate in the same way as Crick and Hughes' original system: an external magnetic field is used to exert a force on a magnetic particle, or particles. Current magnetic tweezer systems operate in the following way:

- The sample is attached to magnetic beads that are placed in a buffer.
- An electromagnet or permanent magnet is used to produce a magnetic field.
- A microscope is coupled with a camera in order to obtain images of the magnetic beads.
- The force on the magnetic beads is varied.
- The recorded images are passed to a computer ready for analysis.

The force, $\mathbf{F}$ on a magnetic bead depends on the strength of an external magnetic field $\mathbf{B}$ as well as the gradient of the external magnetic field [83]:

$$\mathbf{F} = \rho V \nabla(\mathbf{M}_0 \cdot \mathbf{B}) + \frac{\chi_{bead} V}{\mu_0}(\mathbf{B} \cdot \nabla)\mathbf{B} \tag{2.3.1}$$

where ρ, V and $\mathbf{M}_0$ are the density, volume and initial magnetisation of the bead, respectively. The initial magnetic susceptibility of the bead is χ_{bead} and μ_0 is the permeability of free space. Two common techniques exist to vary the magnetic field gradient, and hence the force, experienced by a magnetic bead. The most common method is to use an electromagnet to generate the external magnetic field and vary the current (I) in the coil [77]. The magnetic field produced by an electromagnetic of length L is proportional to the current

$$B = \frac{\mu N I}{L} \tag{2.3.2}$$

where N is the number of turns in the coil and μ is the permeability of the electromagnet's core.

The force exerted on magnetic beads can also be varied when using a permanent magnet of constant magnetic field strength. In this case, the distance between the beads and magnet is varied. The magnetic field strength and gradient tend to be larger nearer to the pole of the magnet. Typically, the beads are stationary and the magnet is mounted on a travelling stage [84].

A comparison of magnetic tweezers with the popular single-molecule force spectroscopy techniques of atomic force microscopy (AFM) and optical tweezers is given in Table 2.3 [78].

Table 2.3: A comparison of single-molecule force spectroscopy techniques.

	Magnetic tweezers	**Optical tweezers**	**AFM**
Spatial resolution (nm)	5-10	0.1-2	0.5-1
Temporal resolution (s)	10^{-1}-10^{-2}	10^{-4}	10^{-3}
Stiffness (pN/mm)	10^{-3}-10^{-6}	0.005-1	10-10^{5}
Force range (pN)	10^{-3}-10^{2}	0.1-100	10-10^{4}
Displacement range (nm)	5-10^{4}	0.1-10^{5}	0.5-10^{4}
Limitations	Force hysteresis	Photo-damage	High stiffness

2.3.4 Experimental method for magnetic tweezers

The magnetic tweezers were set up as shown in Figure 2.22. A stack of NdFeB permanent magnets were poled and mounted on to a ThorLabs LTS150 linear travelling stage (Thorlabs Ltd., Ely, UK). Sample beads were placed into uncoated Ibidi μ-slides (Ibidi

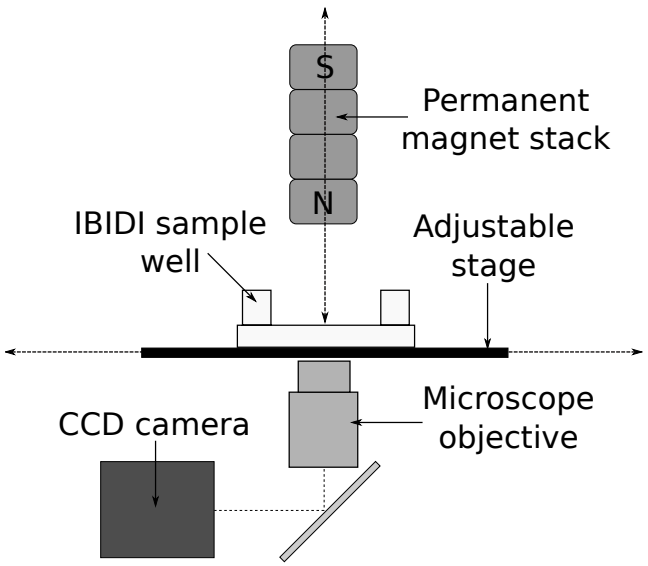

Figure 2.22: Schematic diagram of the magnetic tweezer and optical set-up. The stack of permanent magnets was mounted on a travelling stage and was moved towards the lens in order to increase the force on the magnetic beads in the Ibidi capillary. Each Ibidi device had 6 capillaries which could be used separately by moving an x-y-adjustable stage.

GmbH, Martinsried, Germany) and viewed with the $10\times$ lens of an Olympus IX71 inverted microscope that was operated in epi-illumination mode. A blue light emitting diode (LED) was used to illuminate the sample. Images of the sample beads were captured by a Photron Fastcam 1024 PCI CCD camera (Photron Europe Ltd., West Wycombe, UK).

The force on the magnetic beads was perpendicular to the experimental surface and was increased by moving the permanent magnet stack closer to the beads. After each increase in force, the beads were given 1 minute to equilibrate before an image was recorded with the CCD camera. ImageJ counting software [85] was used to count the number of beads and measure the average area of the beads in each image. The number of beads in each image can be seen to decrease with increased force in Figure 2.23. The attractive force between the beads and surfaces plus the weight of the beads could therefore be measured.

A bead in a liquid requires less force to lift from a surface than a bead in air due to buoyancy. The effective mass of a buoyant bead (m_b) is given by:

$$m_b = m_o(1 - \frac{\rho_f}{\rho_o}) \tag{2.3.3}$$

where m_o is the mass of the bead, ρ_f is the density of the fluid and ρ_o is the density of the bead. M270 Carboxylic acid Dynabeads (Life Technologies Ltd., Paisley, UK) were used for all experiments described in Chapter 5. The M270 beads had a density of 1400 kg/m^{-3} and a mass of 1.54 $\times 10^{-14}$ kg, therefore in the PBS buffer of density 1000 kg/m^{-3} the force required to lift an M270 bead from the experimental surface was 0.04 pN.

The concentration of beads was adjusted so that between 500 and 700 beads were

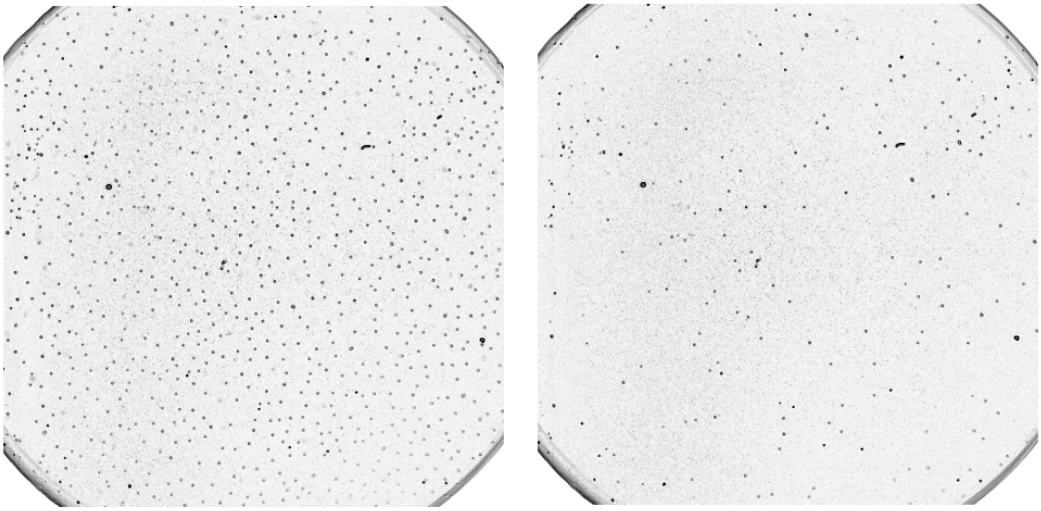

Figure 2.23: Example photographs of M270 beads on the surface of an Ibidi μ-slide. The left photo was taken at a low force while the right was taken of the same beads at a high force. The high force removed beads from the surface.

imaged at a time. This enabled a large number of experiments to be performed in parallel, which reduced the need for repeat experiments. Although it was possible to image more beads, it was found that the magnetic attraction between the beads was sufficient to cause them to group together in high magnet field strengths when >1000 beads were present. Grouped beads were equivalent to a single bead with a larger volume and so experienced a greater attractive force towards the magnet stack.

The Debye screening length (κ^{-1}) for a monovalent salt was approximated to estimate the effects of electrostatic interactions between the beads [53],

$$\kappa^{-1} = \frac{0.304}{\sqrt{I_S}} \tag{2.3.4}$$

where I_S is the ionic strength of the buffer. κ^{-1} was calculated to be 0.8 nm for beads placed in a buffer of 150 mM ionic strength while the beads were typically spaced a minimum of 10 μm apart. Electrostatic interactions between the beads were therefore considered to be negligible. Interactions between the surface and bead were investigated and are discussed in Section 5.4.

The M270 beads required washing prior to use. The beads were prepared by diluting them in 3 ml of PBS (pH 5 20 mM ionic strength). The bead solution was then left to mix in an Eppendorf tube for 20 minutes on a rotating platform. A NdFeB permanent magnet was then used to pellet the beads so that they could be separated from the supernatant with a pipette before another 3 ml of PBS was added to the beads. This washing procedure was repeated 3 times in order to remove the surfactant that the beads were stored in. Washed beads were then coated with either BSA or antibody. The coating procedure is described in detail in Section 5.4.

CHAPTER

THREE

BSA ADSORPTION

3.1 Overview

BSA is widely used as a blocking agent in antigen binding assays. The detailed kinetics of its adsorption are thus important to optimise blocking in pregnancy tests. BSA adsorption at the silica/water interface was used as a model system to explore DPI measurements and compare with the more established technique of neutron reflection. Although the surface coverage results were similar for both techniques, differences in the measured thicknesses were found. The differences were investigated and are discussed further.

In addition, the near real-time DPI data was used to investigate the Langmuir and random sequential adsorption (RSA) protein adsorption models. The models work well in dilute and concentrated regimes respectively.

3.2 Introduction

As previously discussed, protein adsorption at the solid/liquid interface is of great importance in many applications. For example, understanding how proteins interact with the surfaces of medical implants will further the development of biocompatible materials [86, 87]. The majority of these applications require that the adsorbed amount and structural conformation of the adsorbed protein are able to be controlled. Thus, experiments are necessary to probe the phenomenon of adsorption.

Currently, there are many experimental techniques that are able to investigate protein adsorption. Popular techniques include ellipsometry [88, 89], quartz crystal microbalance [90], surface plasmon resonance (SPR) [91] and neutron reflection [92, 93]. Each technique has its own advantages and disadvantages.

Thanks to its rapid sampling rate, ellipsometry is an excellent technique for investigating adsorption dynamics. However, for very thin layers (< 50 nm) ellipsometry cannot reliably distinguish a thick layer of low refractive index from a thin layer of high refractive index [94].

Neutron reflectivity (NR) is a particularly powerful technique that has been used to investigate the adsorption of a wide range of proteins [95]. Due to the small wavelengths of neutrons, NR is able to probe the interfacial structure of an adsorbed protein film with a resolution of 2-3 Å. Unfortunately, in a typical experiment, it may take over one hour for the detector to obtain the required number of reflected neutrons necessary to produce an adequate reflectivity plot. Because of this, NR is only suitable for investigating the equilibrium adsorbed amount and conformation of a system. Adsorption dynamics generally cannot be explored with NR.

Dual-polarisation interferometry (DPI) is a relatively new technique that attempts to bridge the resolution gap between NR and ellipsometry. As previously mentioned, it is a bench-top technique that is able to offer an unambiguous interfacial depth resolution of several angstroms at a time resolution of 100 ms. Recent DPI studies [96–100] have shown that DPI is able to reliably and reproducibly measure the adsorbed mass and thickness of proteins such as lysozyme and BSA. Although the DPI measured results have been compared with results from other techniques, there are often differences in the surface chemistry, buffer conditions (i.e. pH and ionic strength) and the lot numbers of the proteins (which introduces a degree of chemical variability). This means that there are very few direct comparisons between DPI and other techniques. A comparison between DPI and NR is of particular interest as this would allow DPI to complement the more expensive NR experiments. For this reason, a direct comparison of layer thickness and surface coverage of adsorbed BSA was made between DPI and NR.

3.3 Experimental method

3.3.1 Sample preparation

PBS solution was made by dissolving a combination of NaH_2PO_4 and Na_2HPO_4 in either UHQ, for the DPI experiments, or D_2O, for the NR experiments. The BSA (Proliant BSA 6870, lot: BB62010101) was dissolved into the PBS solutions to form a stock solution that was diluted with further PBS to obtain the desired BSA concentration.

An Abbe refractometer was used to check the refractive index increment, $\mathrm{d}n/\mathrm{d}c$, of BSA at a wavelength of 632.8 nm. The gradient of Figure 3.1 revealed that the $\mathrm{d}n/\mathrm{d}c$ of BSA in PBS with 20 mM ionic strength and a pH of 5 was 0.181 ± 0.005 ml/mg. This value was used by the DPI analysis software to calculate the surface coverage from the measured phase changes, as shown in Equation (2.1.48).

3.3.2 DPI

All DPI experiments were performed on the same waveguide. Before use, the waveguide was soaked in 5% (w/w) Decon 90 solution while the surface was repeatedly wiped with a lens tissue. The Decon was then washed off with approximately 50 ml of UHQ

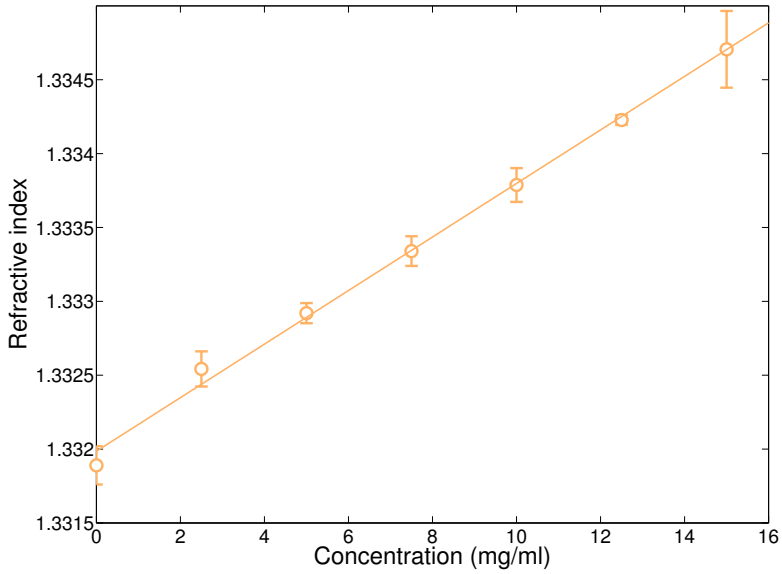

Figure 3.1: Refractive index increment of BSA at $\lambda = 632.8$ nm, measured with an Abbe refractometer.

water before the waveguide was dried with nitrogen. The waveguide gasket was cleaned in the same way.

The cleaned waveguide was placed into the DPI. PBS, which was used as a running buffer throughout the DPI experiments, was then passed over the waveguide surface. The calibration procedure began when the phase reached a baseline that was constant to within 0.1 radians over 10 minutes. To ensure that the waveguide was sufficiently clean, 80% ethanol/water (w/w) was injected onto the waveguide surface for 2 minutes before reverting back to PBS. This was repeated twice and the phase was seen to remain constant before and after each ethanol injection had been completed. The constant phase implied that no impurities had been removed from the waveguide surface by the ethanol, thus the waveguide was deemed sufficiently clean. The calibration was performed by measuring the phase difference between 80% ethanol and UHQ as well as the phase difference between the PBS buffer and UHQ. The bulk refractive index of the PBS buffer was found to be 1.333 ± 0.001.

BSA samples were introduced to the waveguide surface at a flow rate of 10 μl/min for 10 minutes before the pump was stopped and the protein allowed to equilibrate. After the phase change had reached a plateau, the sample was cleaned from the waveguide with 3 injections of Decon 90 followed by 3 injections of ethanol at 100 μl/min. The calibration procedure described above was repeated before each BSA sample.

A Peltier stage was used to keep the instrument temperature at 20.000 ± 0.002°C throughout the experiment.

3.3.3 Neutron reflection

All NR experiments were performed on the silica surface of a <111> silicon block that was prepared as described in Section 2.2.4.

A perspex trough was clamped to the block surface and a syringe was used to insert the BSA samples between the block surface and trough. Each BSA sample was adsorbed for 30 minutes before the neutron reflectivity of the sample was measured. Reflectivity was measured at incidence angles of 0.35, 0.8 and 1.8° in order to maximise the probed wave vector range. The data was then normalised and the background reflectivity, which was measured from the 1.8° angle, was subtracted.

The block and trough were thoroughly cleaned with Decon 90 and UHQ water after each sample had been measured.

NR experiments were performed at the medium flux SURF reflectometer at the ISIS Neutron Facility, Rutherford Appleton Laboratory, Didcot, UK.

3.4 Results and discussion

3.4.1 BSA adsorption kinetics

The surface coverage and thickness of an adsorbed BSA layer have been shown to vary with BSA concentration by several techniques [18, 21]. This same effect was investigated with DPI. The BSA solutions were made in PBS buffer of 20 mM ionic strength at pH 5. These buffer conditions were chosen as they were found to produce easily repeatable results, presumably due to the strong adsorption due to the isoelectric point of BSA being close to 5 pH units.

Figure 3.2 shows how the surface excess increases with concentration. The surface coverage asymptotes towards an equilibrium value, M_∞ after a period of time that decreases with increased BSA concentration. The existence of M_∞ means that the adsorbed BSA does not form a multilayer [59]. The value of M_∞ can be seen to increase with concentration.

Although other techniques, such as ellipsometry, are able to determine the surface excess of thin layers, few are capable of providing accurate thickness measurements. Due to its use of both TE_0 and TM_0 polarisations, DPI is one technique that is able to unambiguously determine the thickness of an adsorbed layer. Figure 3.3 shows how the thickness of an adsorbed BSA layer varies with time for 3 example concentrations. As per the surface excess in Figure 3.2, the thickness can be seen to reach a maximum value that increases with concentration. The time taken to reach the maximum thickness is inversely proportional to the BSA concentration.

Langmuir and RSA models were fitted to the DPI measured surface coverage data. The best fitting Langmuir and RSA models are shown for 3 bulk concentrations of BSA in Figure 3.4. It was found that the Langmuir adsorption model provided the best fit for BSA

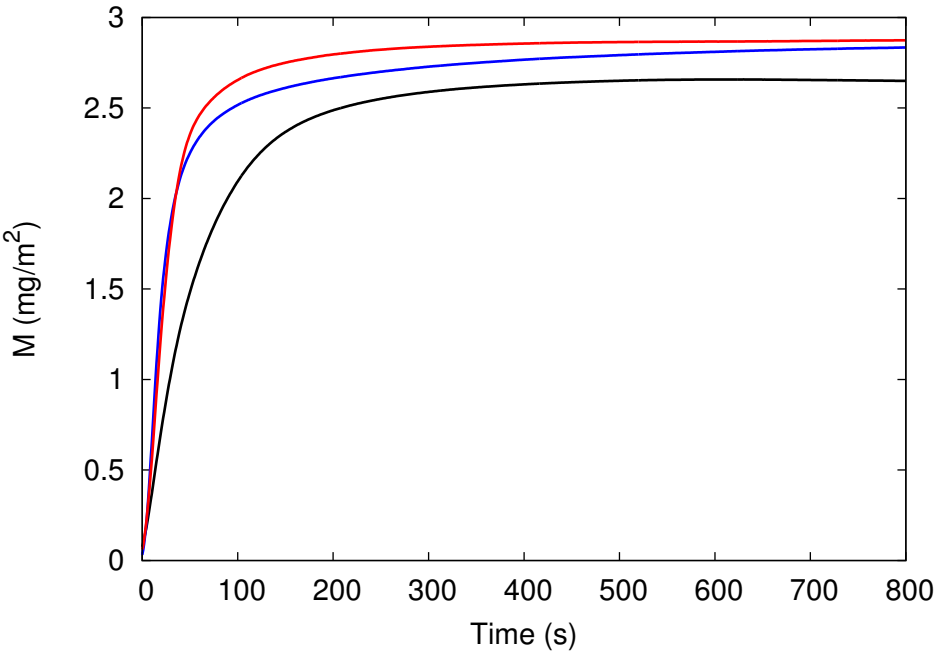

Figure 3.2: DPI measured increase of surface coverage with time for three bulk concentrations of BSA: 1 mg/ml (red line), 0.5 mg/ml (blue line) and 0.25 mg/ml (black line).

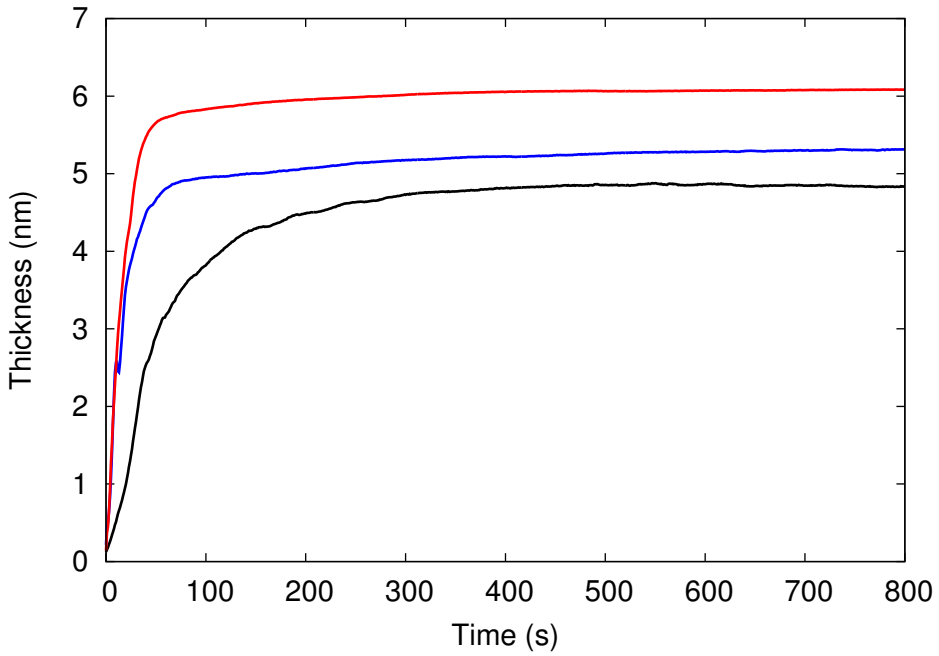

Figure 3.3: Increase of layer thickness with time for three bulk concentrations of BSA: 1 mg/ml (red line), 0.5 mg/ml (blue line) and 0.25 mg/ml (black line).

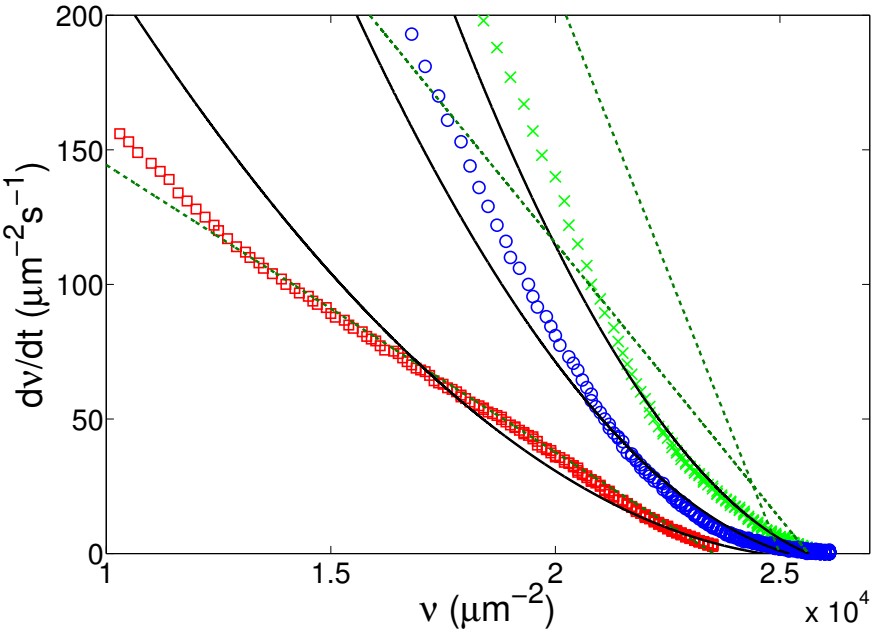

Figure 3.4: Plots of deposition rate as a function of molecules per unit area for the BSA bulk concentrations shown in Figure 3.2 (red squares 0.25 mg/ml, blue circles 0.5 mg/ml and green crosses 1 mg/ml). The best fitting Langmuir model for each concentration is given by the dashed green lines. The solid black lines represent the best fitting RSA models.

concentrations equal to or less than 0.25 mg/ml, presumably because the gaps between the adsorbed molecules were sufficiently large that interactions between the adsorbed molecules were not significant. Above BSA bulk concentrations of 0.25 mg/ml the RSA model provided the best fit. This suggests that interaction effects between the adsorbed molecules only become significant above BSA bulk concentrations of 0.25 mg/ml.

The fitted parameters for each concentration of BSA are shown in Table 3.1. The area per adsorbed BSA molecule can be seen to decrease from a maximum of 91 nm^2 at a concentration of 0.025 mg/ml to a minimum of 15.1 nm^2 at 2 mg/ml. The same trend of increased area per adsorbed molecule with decreased BSA concentration was observed for BSA with NR by Su et al [19]. Su's results suggest that the area per adsorbed BSA molecule is larger than the maximum calculated area of 44 nm^2, based on the ellipsoidal dimensions of BSA in aqueous solution. This is likely due to the reduced lateral repulsion of the adsorbed molecules at low BSA bulk concentrations, which would enable the molecules to spread out over the surface and increase their footprint.

The RSA model predicts that the time dependent approach to the jamming limit, as described by Equation (1.6.5), should have a $t^{-1/2}$ relationship for proteins that are approximately spherical, such as BSA [101]. This was investigated by monitoring long-time BSA adsorption over a 16 hour period. Since the surface coverage, M, is proportional to the number density of adsorbed molecules, ν, Equation (1.6.5) can be rewritten as

$$M_\infty - M = \xi t^{-\frac{1}{2}} \tag{3.4.1}$$

Table 3.1: Fitted model parameters for the adsorbed BSA films.

BSA concentration, c_b (mg/ml)	Area per adsorbed molecule, a (nm^2)	J (μm nmol^{-1} s^{-1})	Model
0.025	91	70	Langmuir
0.05	60	60	Langmuir
0.1	47	70	Langmuir
0.25	42.5	67	Langmuir
0.5	17.5	145	RSA
1	17.2	105	RSA
2	15.1	120	RSA

where ξ is a scaling factor. When investigating power laws, such as Equation (3.4.1), the natural logarithm of the dependent variable is typically plotted as a function of the natural logarithm of the independent variable [102, 103]. Therefore, the natural logarithm of time was plotted against the natural logarithm of $M_\infty - M$, the results are shown in Figure 3.5, where the gradient of the line of best fit is equal to the exponent of Equation (3.4.1). The exponent for BSA was found to equal -0.5048 ± 0.0007 over 3 logarithms in time, in agreement with the predicted value of -0.5. The same experiment was performed with transferrin (Sigma Life Sciences human transferrin T3309, lot: 049K12572), another protein that is approximately spherical at pH 5 [104]. The exponent was found to be -0.4968 ± 0.0006 over 4 logarithms in time, again in agreement with the predicted value. Both proteins were made at a bulk concentration of 0.5 mg/ml in PBS buffer of pH 5 and an ionic strength of 20 mM.

In addition, the rate of deposition onto an empty surface via convective diffusion (K) can be found by substituting J and c_ν in Equation (1.6.2). The following equation, devised by Ramsden, can be used to estimate K for BSA molecules in a fluid that passes through the narrow DPI flow chamber [59]

$$K = \left(\frac{9}{2}\right)^{2/3} \left[\frac{1}{\Gamma\left(\frac{1}{3}\right)}\right] D^{2/3} \left(\frac{V}{Rz}\right)^{1/3} c_b \tag{3.4.2}$$

where D is the diffusion coefficient, $6.0 \pm 0.1 \times 10^{-7}$ cm^{2}s^{-1} [105], V is the fluid velocity, which was 0.5 mms^{-1} and z is the depth of the channel formed by the gasket (0.5 mm). In Ramsden's investigation of Equation (3.4.2), the value of R was defined as the point at

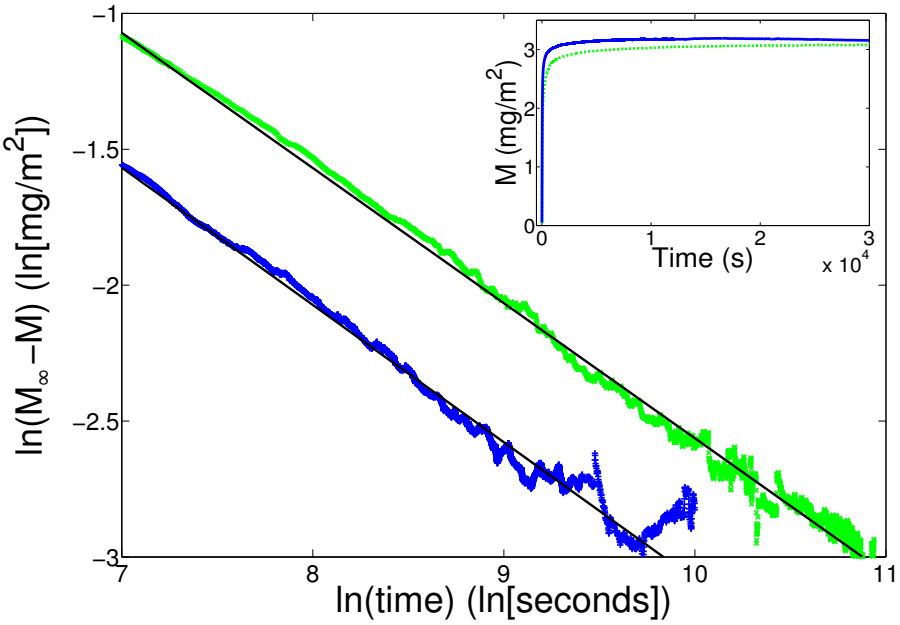

Figure 3.5: Late time surface coverage data for BSA (blue crosses) and transferrin (green crosses). Linear fits (least squares) are shown by the solid lines. Adsorption curves of surface coverage as a function of time are included in the subplot with a linear scale, where the solid blue line represents BSA and the dashed green line transferrin.

which the laser beam impinged on the surface of his OWLS waveguide. Since the DPI's evanescent wave extends along the surface of the sensing waveguide, R was defined here as the midpoint between the DPI outlet and inlet pipe: $R = 3\,\text{mm}$. Figure 3.6 shows how R was defined for OWLS and DPI.

The validity of Equation (3.4.2) was investigated for BSA. The calculated and measured values of K are shown in Figure 3.7. Although there is a difference between the theoretical and experimental K values it can be seen that they both increase linearly. This implies that Equation (3.4.2) is correctly describing the relevant physical phenomena, but that there is a missing scale factor. This may be due to the non-ideal boundary conditions in the DPI flow chamber. Due to the finite length the evanescent field propagates along the waveguide, R can be varied between 0 mm and 15 mm (which would yield K values at the inlet and outlet pipes respectively). However, varying this length between these values did little to improve the fit of Equation (3.4.2), as shown in Figure 3.7.

As well as providing information on the kinetics of BSA adsorption, the DPI results show that the surface coverage of BSA increases with BSA bulk concentration. Other techniques, such as ellipsometry and total internal reflection fluorescence (TIRF) [106], are capable of providing this information, but DPI is one of the few techniques that can also provide reliable thickness data. For example, AFM may compress the protein layer [107] and SPR and ellipsometry cannot distinguish between thin, dense layers and thick, diffuse layers. TIRF requires that the molecules are labeled with fluorophores, which may alter the adsorption dynamics and interfacial structure of an adsorbed layer. Therefore, NR is one of the few techniques that is able to produce reliable and reproducible thickness measurements at the molecular level. The DPI results are compared with NR results in

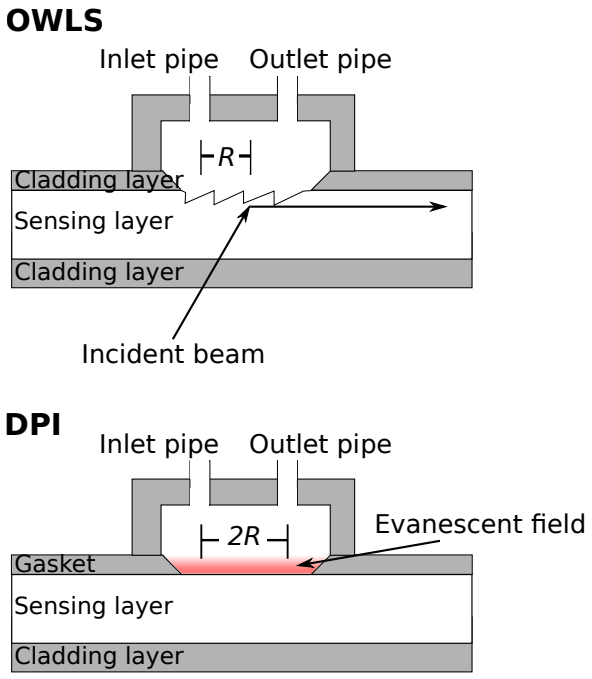

Figure 3.6: Schematic diagram to show R for OWLS and DPI. For OWLS, R is the point at which the incident beam impinges, while for DPI a value of K could be calculated for any point along the evanescent field between the inlet and outlet pipes. R was defined as the midpoint between the pipes for DPI.

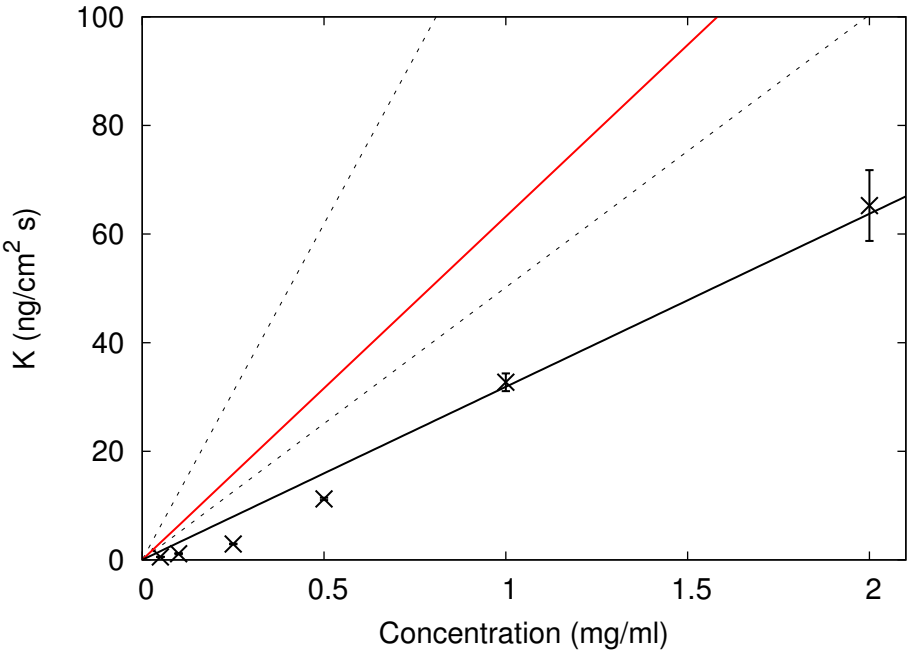

Figure 3.7: The dotted lines show the upper (R=1 mm) and lower (R=15 mm) limits of the calculated deposition rates onto an empty surface (K values). The red line shows the calculated K values at the centre of the waveguide (R=7.5 mm). The measured values are displayed as black crosses and the solid black line is a linear fit to the measured data.

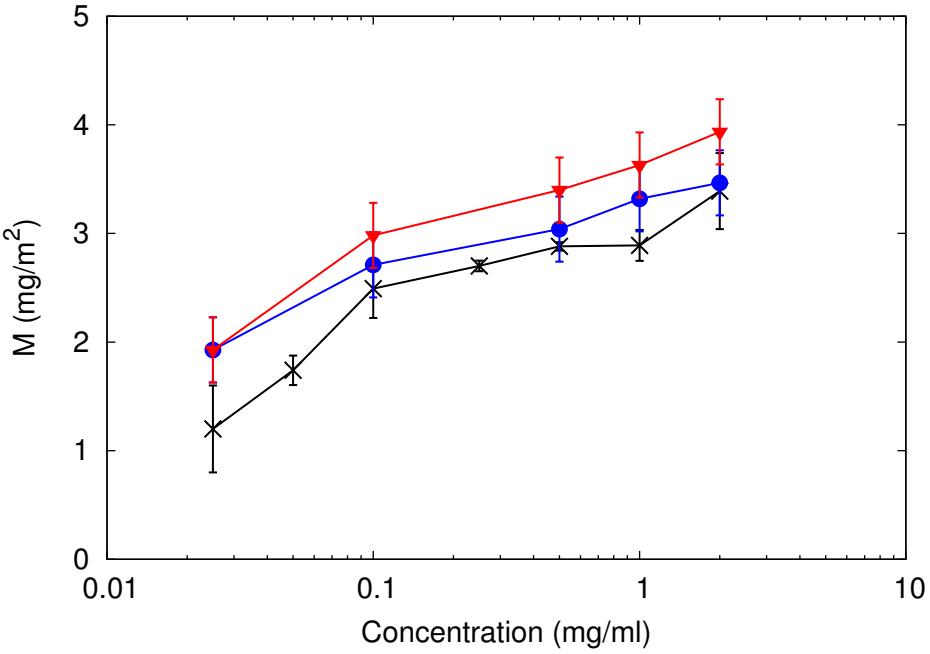

Figure 3.8: Surface coverage as a function of concentration for BSA, as measured by DPI and NR. The crosses represent DPI data, blue circles the uniform layer NR data, and red triangles the two-layer NR data.

the following section.

3.4.2 Comparison with NR

The equilibrated surface coverage as a function of bulk BSA concentration and bulk pH in comparison with NR results is shown in Figure 3.8 and Figure 3.18 respectively. Error bars were calculated from the standard deviation of at least 4 repeated experiments for DPI and estimated for NR from a repeat of the 0.1 mg/ml BSA sample.

The experiments were performed under almost identical conditions. The only differences were in the experimental surfaces. The DPI waveguide surface was made from silicon-oxynitride and had a roughness (measured with AFM) of 50-80 Å while the smoother NR surface had a 15 ± 3 Å layer of silica. However, both surfaces were strongly hydrophilic with contact angles of below 20°. It was not possible to perform both DPI and NR experiments on the DPI waveguide, so that the substrates would be consistent, due to the geometry of the waveguide. The sensing surface of the DPI waveguide had an area of approximately 1 mm $\times$ 15 mm on a 6 mm $\times$ 22 mm silicon-oxynitride surface of different refractive index, therefore it would not have been possible to tell whether the neutron beam was consistently aligned on this sensing area as opposed to the surrounding silicon-oxynitride. The neutron beam alignment procedure simply reveals where the reflected signal is at a maximum, it would not be able to differentiate between the sensing region and the cladding region. In addition, it was not possible to focus the neutron beam onto an area as small as the sensing region. Similarly, the DPI experiments could not have been carried out on a bare silica surface. The sensing surface of the DPI waveguide re-

quires doping with nitrogen in order to create the necessary difference in refractive index between the waveguide layers. Without this difference it would not be possible to create the interference fringes that are necessary to obtain measurements. DPI waveguides with un-doped silica sensing surfaces do not exist. Despite the differences in the surfaces and the physical principles used by the two techniques, Figure 3.8 shows good agreement between DPI and NR.

Although the volumes and sensing areas of DPI and NR are different, both systems had a Reynold's number that was less than one. Laminar flow therefore occurred for buffers and protein solutions that passed over the substrate surfaces of DPI and NR.

Figure 3.8 shows that both DPI and NR measured an increase in surface coverage with bulk BSA concentration. This trend has been observed by various techniques [9, 18, 108, 109], including NR [19] but the absolute values differ between the studies due to the different experimental conditions.

In order to obtain surface coverage and layer thickness data, NR and DPI both rely on model fitting. The DPI fitting model assumes that the adsorbed proteins form a single homogeneous layer of constant thickness and density. This is in contrast to the optical matrix method used to analyse NR data, which assumes that the measured reflectivity is produced by any number of equivalent homogeneous layers, each of which is a region of constant thickness and scattering length density. To compare the DPI and NR results a single-layer model was initially used to describe the NR data. Figure 3.9 shows that this single-layer NR model proved a poor fit for the reflectivity profile produced by a BSA concentration of 0.1 mg/ml. This implies that at 0.1 mg/ml, the protein film had a non-uniform SLD distribution perpendicular to the substrate. It can also be seen that a two-layer model, which accounts for a non-uniform scattering length density distribution, better fitted the reflectivity data. The two-layer model revealed an inner layer with a scattering length density of $4.85 \pm 0.05 \times 10^{-6}$ Å^{-2} and an outer layer of $6.00 \pm 0.05 \times 10^{-6}$ Å^{-2}, which correspond to volume fractions of 0.50 ± 0.05 and 0.12 ± 0.01 respectively.

Lu et al [110] have shown that the measured surface coverage is largely independent of the NR model. This is true of the obtained NR data: it can be seen from Figure 3.8 that the differences between the single- and two-layer model results are small. This model independence is not true of the measured thickness, as shown in Figure 3.10.

Figure 3.10 compares the adsorbed BSA film thickness as measured by NR and DPI. Although the single-layer NR data is in good agreement with the DPI data, a two-layer NR model was required for BSA concentrations of 0.1 mg/ml and above, as previously discussed. Unlike for surface coverage, the adoption of the two-layer model can be seen to increase the measured thickness to almost double that of the DPI data. Despite the differences in absolute values, DPI and both NR fits show a definite trend of increased film thickness with increased BSA bulk concentration. All results obtained from the two-layer NR fit are displayed in Table 3.2.

The DPI and NR data allow the conformation of the adsorbed BSA molecules to be

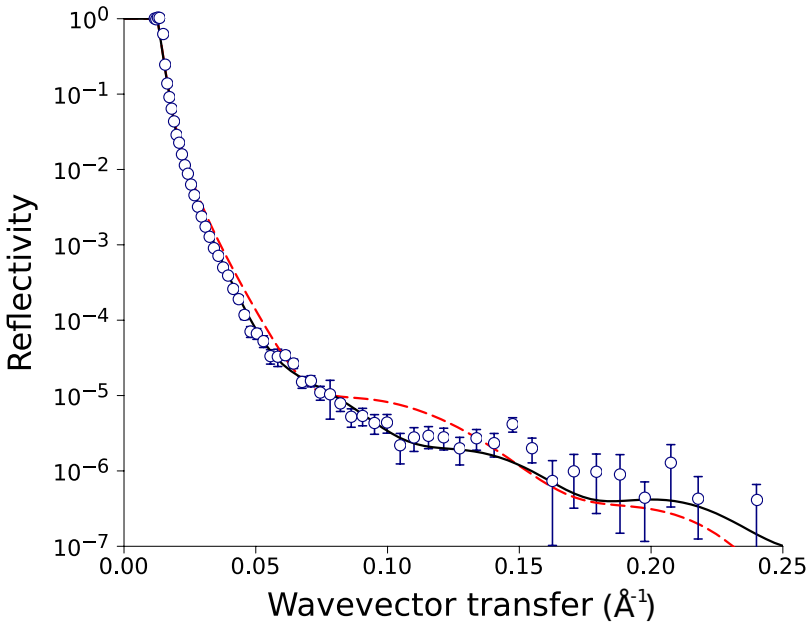

Figure 3.9: Neutron reflection data for 0.1 mg/ml of BSA. A one-layer model (broken red line) provides a poor fit for the data. A two-layer model (solid black line) is therefore required.

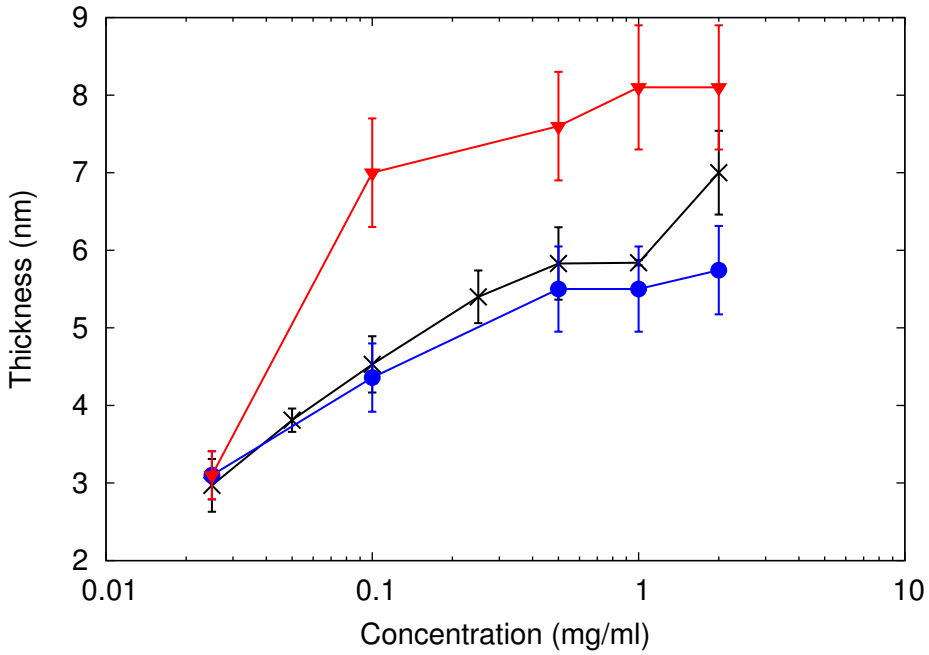

Figure 3.10: Total protein film thickness plotted against bulk BSA concentration. The crosses represent DPI data, blue circles the single-layer NR data and red triangles the two-layer NR data. The two-layer NR model shows a higher layer thickness than the single-layer fits from NR and DPI.

Table 3.2: Parameters extracted from NR data using a two-layer model and the optical matrix method.

BSA concentration, c_b (mg/ml)	**Layer number**	**Thickness (nm)**	**Surface coverage, M (mg/m^2)**	**Volume fraction, ϕ_P**	**Area per molecule, a (nm^2)**
0.025	1	3.1 ± 0.3	1.9 ± 0.3	0.45 ± 0.05	57 ± 5
0.1	1	3.5 ± 0.4	2.4 ± 0.3	0.50 ± 0.05	46 ± 5
	2	3.5 ± 0.4	0.6 ± 0.3	0.12 ± 0.01	200 ± 20
0.5	1	4.0 ± 0.4	2.5 ± 0.3	0.45 ± 0.05	44 ± 5
	2	3.6 ± 0.4	0.9 ± 0.3	0.18 ± 0.02	120 ± 10
1	1	4.1 ± 0.4	2.6 ± 0.3	0.45 ± 0.05	43 ± 5
	2	4.0 ± 0.4	1.0 ± 0.3	0.19 ± 0.02	110 ± 10
2	1	4.1 ± 0.4	2.7 ± 0.3	0.48 ± 0.05	40 ± 5
	2	4.0 ± 0.4	1.2 ± 0.3	0.22 ± 0.02	92 ± 10

investigated as a function of bulk BSA concentration. Both techniques show that the film thickness increased with surface coverage. For the 0.025 mg/ml BSA sample, both NR and DPI measured the film thickness to be 3 nm: less than the 4 nm short axis of BSA. Also, the average surface area of each adsorbed BSA molecule was measured to be 57 nm^2 by NR and 91 nm^2 by DPI: larger than the maximum area of 44 nm^2 of BSA in aqueous solution. For a BSA concentration of 0.025 mg/ml, the thickness and surface area measurements suggest that the lateral repulsion between the adsorbed molecules was weak enough to allow the molecules to adsorb in the side-on orientation. At pH 5, BSA molecules have no net charge and the lack of lateral repulsion between the adsorbed molecules would allow them to spread over the surface. This would account for the increased surface area per molecule and would also result in a reduction in the thickness of the film to below the 4 nm short axis of BSA.

In theory, the lateral repulsion between the adsorbed molecules will increase with surface coverage. Therefore, at higher bulk BSA concentrations, the BSA molecules will adopt an end-on orientation that would increase the film thickness. Molecules adsorbed in this orientation would also experience less exposure to surface forces, so would therefore be less likely to become flattened. The DPI and NR results support this theory: the film thickness can be clearly seen to increase with BSA concentration while the area per molecule is reduced. NR identified a dense inner layer and a more diffuse outer layer at concentrations above 0.1 mg/ml. This arrangement could be explained by multilayer formation, where BSA molecules become attached to the inner adsorbed layer. However, the DPI results presented in Figure 3.2 show that, for each concentration, the surface reached a maximum value and therefore exclude multilayer formation [67]. A more plausible explanation is that the molecules adsorbed in a combination of end-on and side-on orientations, as shown in Figure 3.11. Figure 3.11 is a schematic diagram to show how the conformation of adsorbed BSA molecules changes with bulk BSA concentration. At high surface coverages the majority of BSA molecules adopt a side-on orientation that form a dense layer close to the surface with a small number of end on aligned molecules that protrude from the inner layer to create a diffuse outer layer. At low surface coverages all of the molecules remain in the side-on orientation, and their high exposure to the surface and lack of lateral repulsion cause the molecules to become spread out on the surface.

As previously discussed in Section 2.1.8, for adsorbed layers with non-uniform density distributions, the DPI-measured thickness and refractive index of an adsorbed film will be strongly dependent on the layer density. A previous experiment investigated the adsorption of polystyrene nanospheres with DPI [111]. At low surface coverage the measured thickness was less than the 30 nm diameter of the spheres. As the surface coverage was increased, the measured thickness increased linearly before a plateau was reached at $\approx$30 nm. This effect was a result of the adsorbed layer not being homogeneous at low surface coverage. Instead, the adsorbed layer had a lateral density profile where the surface was composed of adsorbed spheres and empty spaces. As the surface coverage increased,

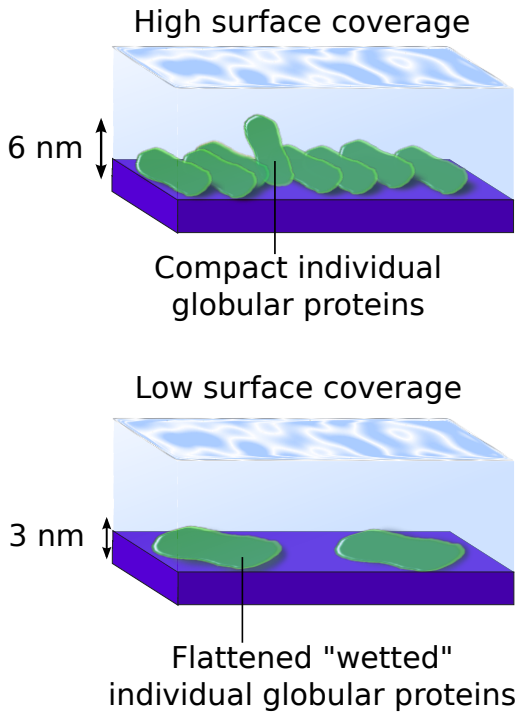

Figure 3.11: Schematic diagram to depict the increase of the equilibrium surface coverage with BSA concentration and its impact on the structural conformation. a) At high surface coverage globular proteins overlap, but adopt compact structures, b) at low surface coverage the globular protein structure collapses wetting the oppositely charged substrate.

the empty spaces on the surface were filled by the spheres. When enough spheres had filled the surface, the equivalent homogeneous layer assumption was valid and the DPI correctly measured the thickness of the adsorbed spheres, as predicted by the calculated results shown in Figure 2.13.

The dependence of DPI-measured thickness on the density of the adsorbed layer could explain why the thickness of the adsorbed BSA was less than the BSA short axis at low surface coverage. However, NR, which is more sensitive to non-uniform density distributions, also measured the thickness to be less than 4 nm. Therefore, spreading of the BSA molecules seems more likely.

Figure 3.12 shows how the thickness and refractive index of adsorbed BSA varied with BSA surface coverage. The experiment was carried out in the same PBS buffer of pH 5 and 20 mM ionic strength. The DPI-measured thickness can be seen to increase with the surface coverage of the BSA, as seen for the nanospheres. However, a plateau that corresponded to the length of a BSA molecule was not reached. The lack of a thickness plateau could be due to BSA molecules becoming stacked on top of each other, instead of adsorbing to the surface. This would increase the thickness beyond 4 nm but would also result in a decrease of the refractive index, as seen in Figure 2.16. This is not seen in Figure 3.12. Thus, it seems most likely that at higher surface coverage, the BSA molecules

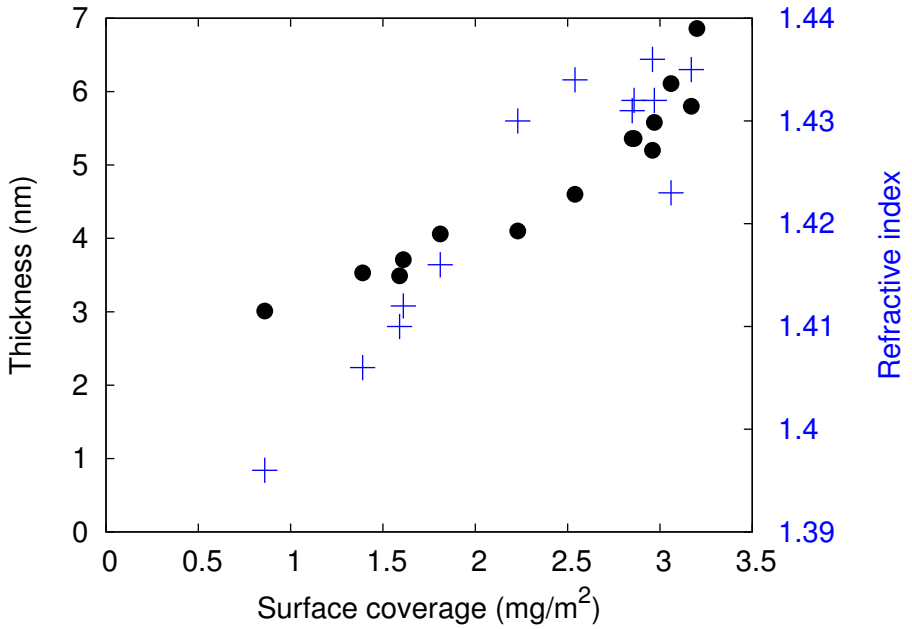

Figure 3.12: DPI-measured thickness (black circles) and refractive index (blue crosses) of adsorbed BSA as a function of BSA surface coverage.

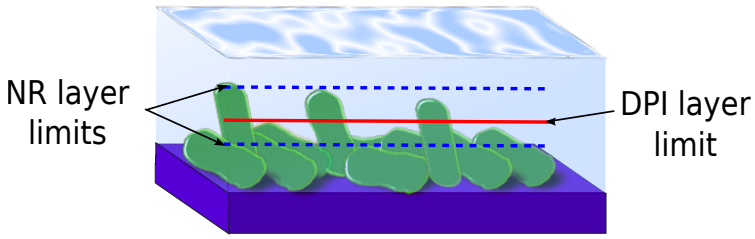

Figure 3.13: Schematic diagram to show how the model layers are defined by NR and DPI for a thin film with a non-uniform density distribution.

began to adopt an end-on aligned formation, and therefore increased the thickness of the layer beyond the 4 nm short axis.

The fact that DPI uses a uniform-layer model, as opposed to the two-layer model used by NR, may account for the large discrepancies between the measured thicknesses. Figure 3.13 shows how NR and DPI define their model's layer boundaries for adsorbed BSA molecules that have formed a non-uniform density distribution perpendicular to the surface normal. Two equivalent homogeneous layers can be seen: an inner dense layer that is composed of the side-on molecules and an outer layer that is made from the protruding end-on aligned molecules. The two-layer NR model is able to define layer boundaries that form two layers of different scattering length density, while the DPI uniform-layer model is a weighted average of the two layers [112]. This implies that DPI is less sensitive to the diffuse layer and would therefore measure the total film thickness to be less than the NR measured thickness. In order to test this hypothesis, TE_0 and TM_0 phase changes were estimated from the two-layer NR thickness measurements with analysis

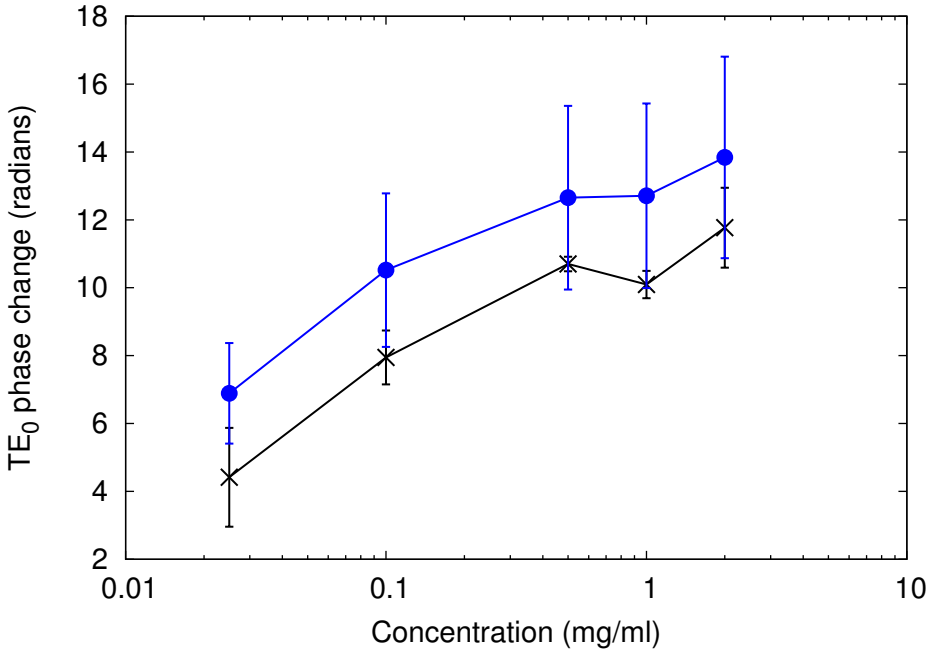

Figure 3.14: TE_0 phase change as measured by DPI (crosses) and calculated from NR thickness and refractive index values (blue circles).

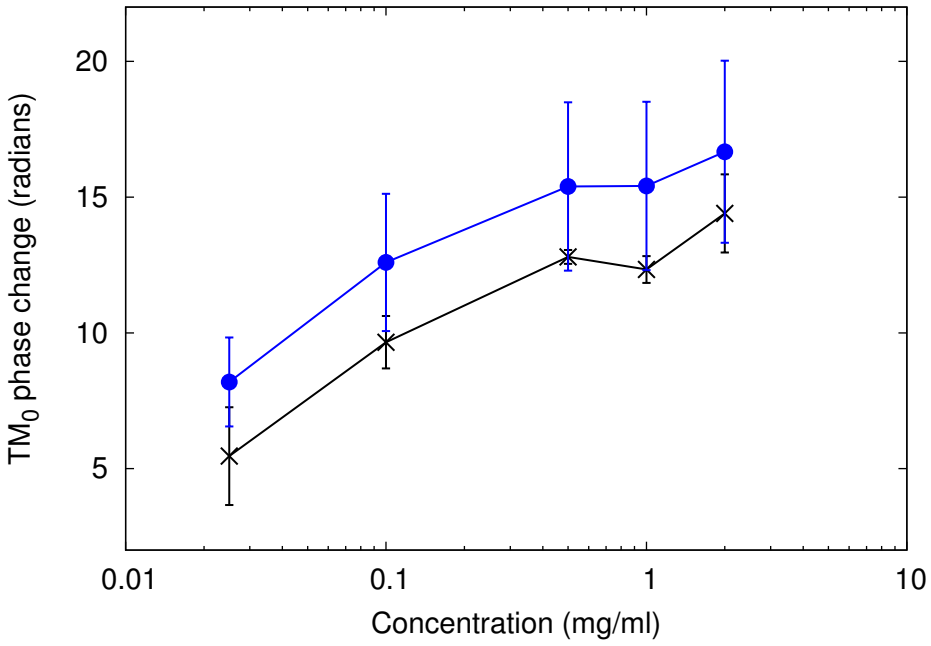

Figure 3.15: TM_0 phase change as measured by DPI (crosses) and calculated from NR thickness and refractive index values (blue circles).

software [29] that performed the DPI analysis equations in reverse. In other words, instead of the phase change being used to calculate the layer thickness and refractive index, the thickness and scattering length density were used to calculate a phase change. The calculated phase changes from the TE_0 and TM_0 polarisations are shown in Figure 3.14 and Figure 3.15 respectively. The results show that the raw phase signals measured by the two techniques are in good agreement.

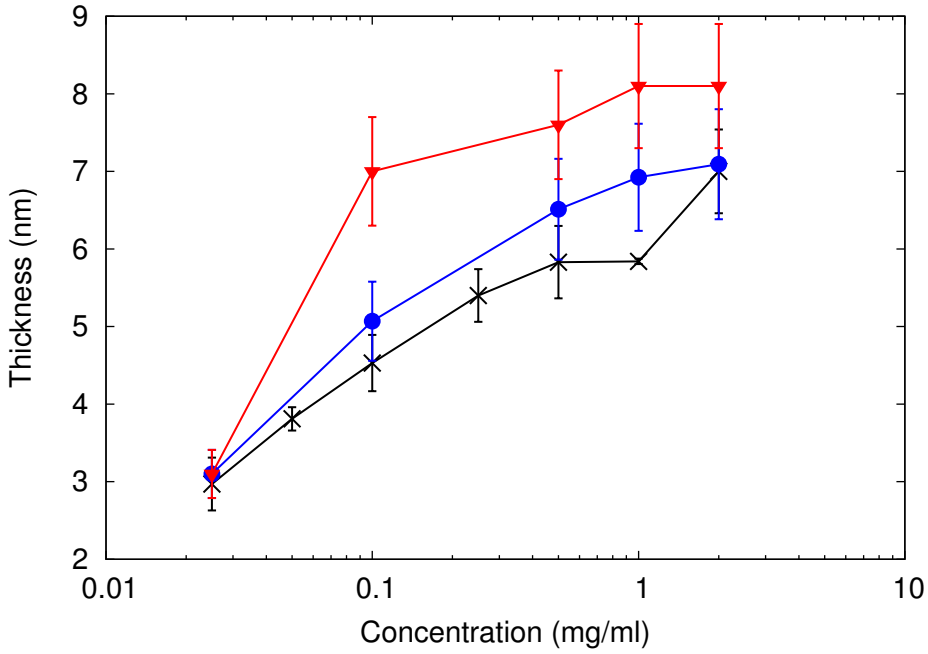

Figure 3.16: Phase-derived NR thickness compared with the thickness measured directly using two-layer NR and DPI. The crosses represent DPI data, red triangles the two-layer NR data, and blue circles the phase-derived NR data.

The estimated TE_0 and TM_0 phase changes were then put back into the uniform-layer DPI model in order to calculate a uniform-layer thickness and refractive index for each concentration of BSA. The calculated thickness results are compared with the DPI and two-layer NR results in Figure 3.16. Figure 3.16 shows that the phase-derived NR thicknesses are in close agreement with the DPI results. This agreement strongly suggests that the discrepancy in the measured film thicknesses between the two techniques is a result of the differences in the way NR and DPI measure the thickness of layers with non-uniform density distributions.

Although the DPI-measured thickness seems to be less sensitive to low density layers than NR, the fact that the DPI-measured thickness does not depend on a user-defined number of layers will likely mean that DPI will give more consistent results. For example, Su et al's [19] NR data for BSA adsorption at pH 5 shows a sudden jump in the total BSA film thickness of 4 nm between BSA concentrations 0.5 mg/ml and 1 mg/ml, as seen in Figure 3.17. This sudden and unrealistic increase was due to the adoption of a two-layer model at BSA concentrations above 0.5 mg/ml. DPI could therefore be used to complement NR results by validating the adoption of multi-layer models.

3.4.3 The effect of buffer pH

The effect of buffer pH on the surface excess and thickness of an adsorbed BSA film was also investigated with DPI and NR. For the pH values of 3, 5 and 7 a BSA concentration of 0.1 mg/ml in PBS buffer with an ionic strength of 20 mM was used. Figure 3.18 shows that the surface excess was measured by DPI and NR to be at a maximum at pH

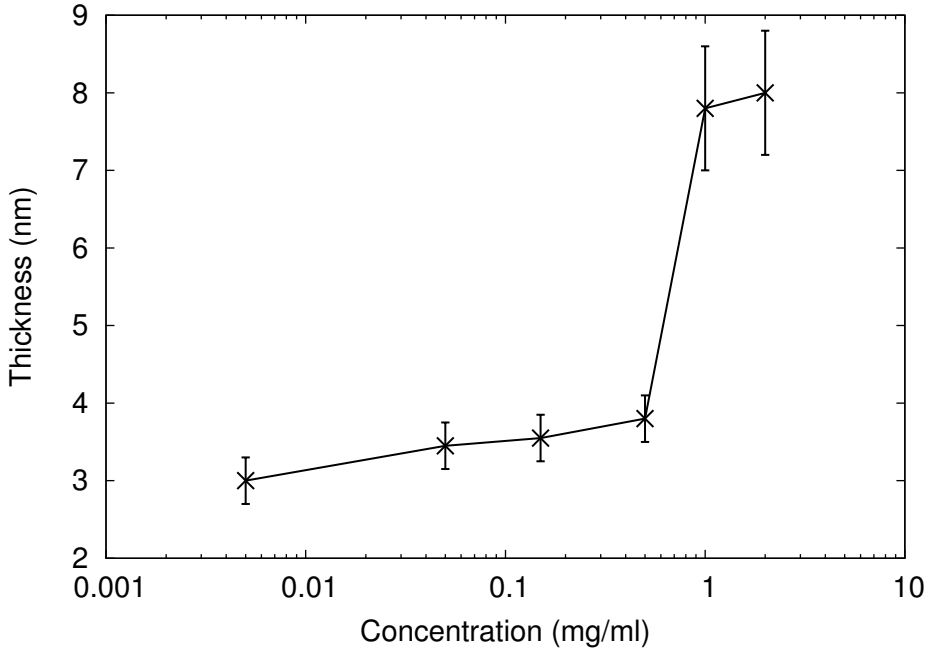

Figure 3.17: Su et al's NR results for BSA thickness as a function of bulk BSA concentration. The experimental buffer was set to pH 5 and 20 mM ionic strength.

5, close to the pH 4.7 isoelectric point of BSA. The equilibrium surface coverage can be seen to decrease as the pH is shifted away from pH 5. The same effect was observed by Kondo et al [21] and Norde and Favier [108] who performed extensive studies on the effect of pH on BSA adsorption. Kondo obtained adsorption isotherms for pH 2.6, 5, 6, 7 and 10 at a range of concentrations, the maximum surface coverage was found to occur at pH 5. Both studies measured the adsorption of BSA on to ultra-fine silica particles with circular dichroism.

The conformation of serum albumin, in solution [101] and adsorbed on a substrate [113], has been shown to be pH dependent. At neutral pH the BSA molecule is in its normal "N" form, which is approximately spherical. Below pH 4.3 the conformation of the BSA molecule changes to the more elongated fast "F" form. At extremely low pH (< pH 2.7) the molecule becomes even more elongated and adopts the extended "E" form. The three forms of serum alumin are shown in Figure 3.19. This structural transition may explain why the surface coverage was so low at pH 3. At low pH the BSA molecules adopt the "F" form, which has a greater aspect ratio than that of molecules in the "N" form. Viot et al's [115] theoretical models show that the jamming limit decreased for molecules with increased aspect ratio, which would lead to a reduction in the surface coverage as less BSA molecules would be able to adsorb to the surface. However, there is also a large difference between the surface coverage at pH 5 (2.5 mg/m^2 for DPI and 3.0 mg/m^2 for NR) and at pH 7 (1.0 mg/m^2 for DPI and 1.3 mg/m^2 for NR) and BSA adopts the normal form for both pH 5 and pH 7. Thus pH dependent structural transitions alone cannot account for all of the observed surface coverage differences over the studied pH range. For this reason the electrostatic interactions between the protein molecules and

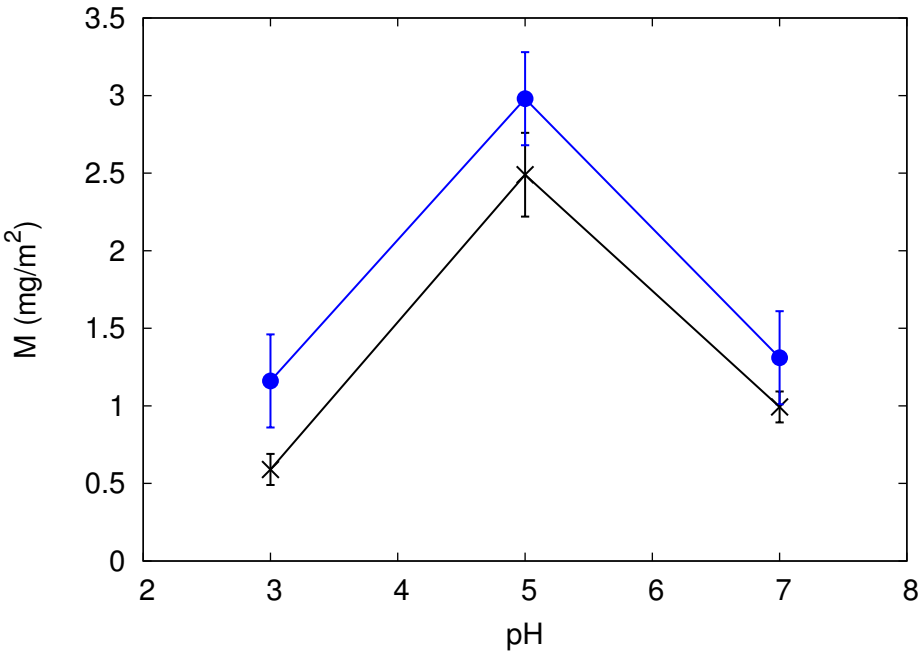

Figure 3.18: Surface coverage as a function of pH for 0.1 mg/ml bulk BSA concentration, as measured by DPI (black crosses) and NR (blue circles).

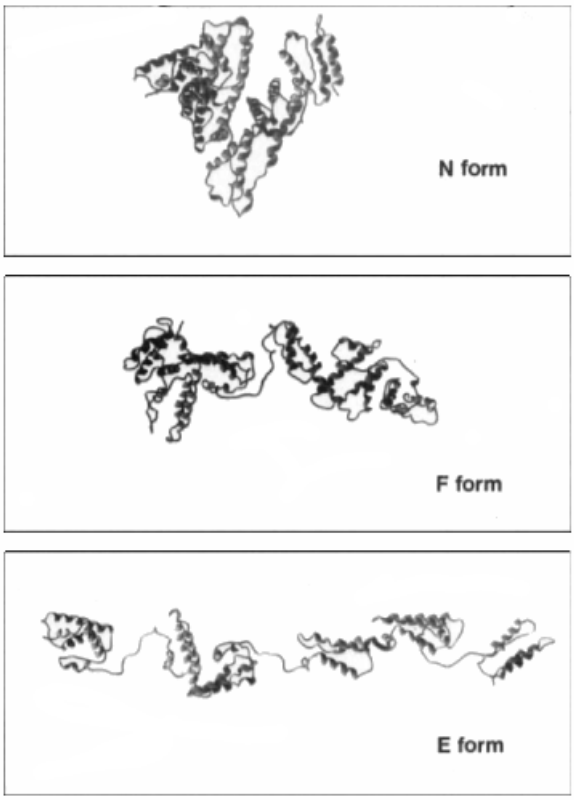

Figure 3.19: Ribbon diagram of serum albumin in "N", "E" and "F" forms [114].

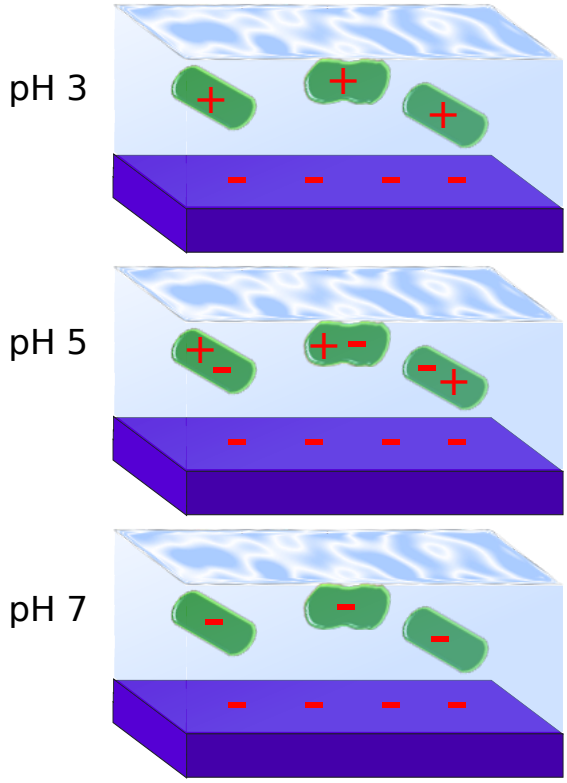

Figure 3.20: Net charge of BSA molecules at pH 3, pH 5 and pH 7. The silica surface remained negatively charged over the studied pH range.

the surface were considered.

The surface is assumed to be silica for both NR and DPI (in reality the DPI surface contains a small amount of nitrogen). Previous work shows strong agreement between the measured surface coverage of BSA on silica and silicon-oxynitride [70], which suggests that the surfaces are similar. The isoelectric point of silica is thought to occur below pH 2 [116], therefore the experimental surfaces had a net negative charge over the pH range studied (pH > 2). Previous work has shown that the net negative charge of silica increases over the pH range 3–8 [117]. The isoelectric point of BSA is pH 5. Thus, BSA has a net positive charge at pH 3, neutral net charge at pH 5 and negative net charge at pH 7, as shown in Figure 3.20.

Both DPI and NR show that the surface coverage was at a minimum at pH 3, despite the favourable electrostatic attraction between the BSA molecules and the surface. This could suggest that either electrostatic repulsion between adsorbed positively charged BSA molecules reduced further adsorption at long times, or the conformational "N" to "F" transition reduced the adsorption due to the more extended form of the BSA molecules. Electrostatic screening from ions in the buffer would have been present for each pH. However, screening was constant and weak for each buffer, as the ionic strength was 20 mM. The Debye screening length was calculated with Equation (2.3.4) to be 2.3 nm for each buffer.

pH 7 also showed low surface coverage. This is likely due to electrostatic repulsion between the negatively charged proteins and the negatively charged surface. The con-

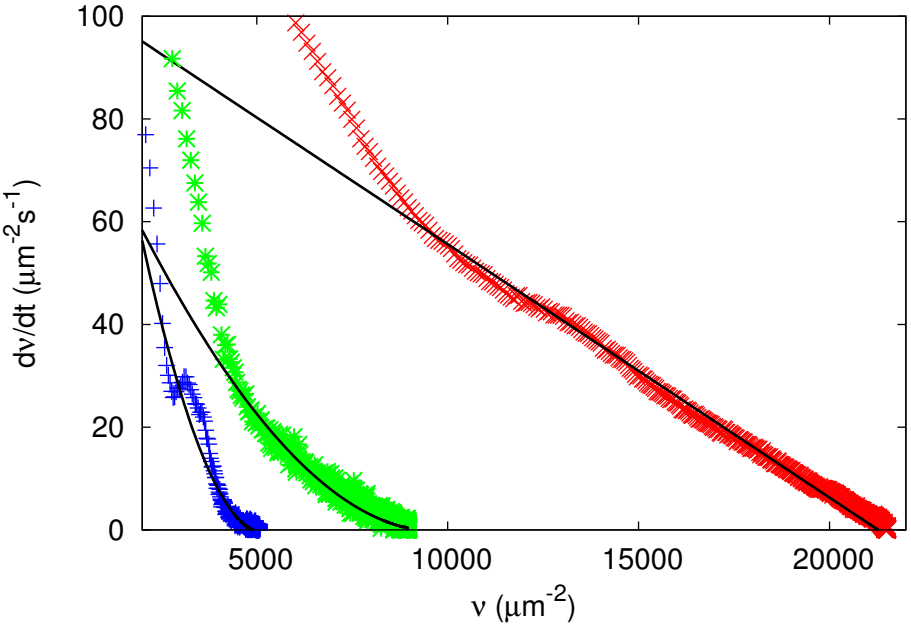

Figure 3.21: Plots of the deposition rate as a function of molecules per unit area for BSA in buffer of pH 3 (blue), pH 5 (red) and pH 7 (green). The best fitting adsorption model for each pH is given by the solid lines and was found to be Langmuir for pH 5, and RSA for pH 3 and pH 7.

formational transition of the BSA is absent in this case i.e. BSA continues to be in the compact "N" form.

The highest surface coverage was found at pH 5. At pH 5 the BSA molecules have no net charge and will experience weak electrostatic forces between the surface and the protein, and between adjacent protein molecules. However the BSA is in the more compact "N" form and small positive charged patches on the protein can still make strong electrostatic bonds with the surface, once they are sufficiently close to it.

The high adsorption for the proteins that have zero net charge at pH 5, as opposed to the low adsorption for charged proteins, suggests that protein-protein interactions rather than protein-surface interactions are the dominant factor. One way to investigate this is to look at the adsorption rate ($d\nu/dt$) as a function of adsorbed molecules per unit area (ν). From Figure 3.21 the rate of adsorption for pH 5 can be seen to follow the linear Langmuir model. This model assumes that there are no interactions between the adsorbed molecules. The Langmuir model did not fit the adsorption curves for pH 3 and pH 7. Instead, for pH 3 and pH 7 the rate of adsorption more closely followed the concave shape that is characteristic of RSA. RSA assumes that adsorbed molecules are surrounded by an exclusion zone, in which further adsorption is prevented.

We have shown in Section 3.4.1 that the RSA model was previously only required at pH 5 for high BSA concentrations as the effect of protein-protein interactions only became significant once ν had increased to over 25,000 molecules/μm^2. At pH 3 and pH 7 protein-protein interactions became significant at much lower values of ν (5,000 and 8,000 molecules/μm^2 respectively). This is likely due to the greater electrostatic repul-

Table 3.3: Fitted model parameters for the adsorbed BSA films at pH 3, pH 5 and pH 7.

Buffer pH	Area per adsorbed molecule, a (nm^2)	J (μm nmol^{-1} s^{-1})	Model
3	90	95	RSA
5	47	70	Langmuir
7	48	60	RSA

sion between the charged BSA molecules, which increases the size of the exclusion zone around each adsorbed molecule. This acts to reduce the number of molecules that can fit on the surface.

The parameters obtained from the model fits to the kinetic data are shown in Table 3.3. The fitted parameters reveal that J, the protein flux at the surface, is highest at pH 3 and decreases with increasing pH. This suggests that the electrostatic forces between the protein and surface drive the initial adsorption: the protein flux is highest when the protein and surface are oppositely charged and lowest when they are both negatively charged. The reduction in J (10 μm nmol^{-1} s^{-1}) at pH 7 compared to pH 5 is of lower magnitude than the increase in J (25 μm nmol^{-1} s^{-1}) at pH 3 compared to pH 7. This could be a result of the differences in the magnitude of the net BSA charge; at pH 3 and pH 7 BSA was calculated to have a net charge of +95 q and -18 q respectively, as shown in Figure 1.2.

The area per adsorbed molecule (a) was almost twice as large at pH 3 (90 nm^2) than at pH 5 and pH 7 (47 nm^2 and 48 nm^2 respectively). This increase in area at pH 3 is likely a result of the adoption of the "F" form and the strong attractive force between the negatively charged surface and positively charged protein, which may cause the protein to become denatured and spread out over the surface. This conformation would further reduce the number of protein molecules able to adsorb to the surface.

The variation of thickness with pH is shown in Figure 3.22. A single-layer model was used to fit the pH 3 NR data, but a two-layer model was required to fit the non-uniform scattering length density distributions found at pH 5 and pH 7. As for the thickness as a function of concentration data (Figure 3.10), large differences between the DPI and NR thickness results occur when a two-layer NR model is used.

At pH 3 both techniques show that the thickness of the BSA layer was less than the 4 nm short axis of a BSA molecule. This implies that the adsorbed protein molecules had become flattened against the surface, as would be expected for a BSA molecule in the "F" form. This also supports the high area per molecule revealed by the kinetic analysis at pH 3.

The thickness increased at pH 5. Both techniques show that the layer was thicker than

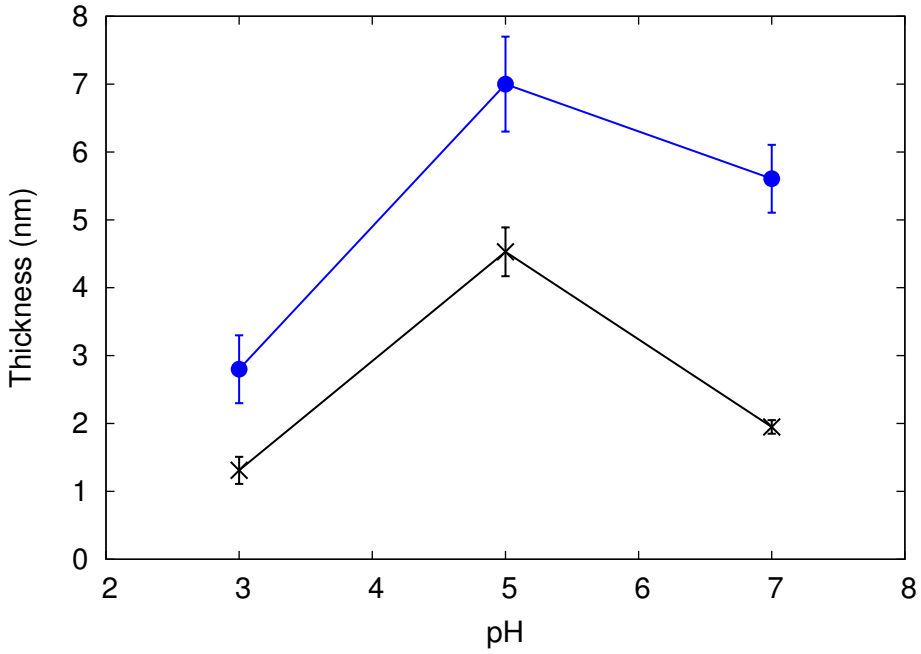

Figure 3.22: Thickness against pH for 0.1 mg/ml of BSA as measured by DPI (black crosses) and NR (blue circles).

the short axis, which suggests that some of the BSA molecules were aligned in the end-on orientation, which would result in an increased layer thickness. This orientation was likely a result of the high number of protein molecules on the surface which reduce the size of available adsorption sites so that BSA molecules must be tilted in order to fit on the surface.

At pH 7 NR measured a thickness of 5.6 nm while DPI measured only 2.0 nm. As DPI measures an average thickness, the result, when compared to the higher NR measured thickness, implies that the protein molecules are sparsely populated on the surface, which results in a low average thickness. This is supported by the low surface coverage (1.0 mg/m^2). The 5.6 nm thickness measured by NR is longer than the short axis of BSA and may be a result of the electrostatic repulsion between BSA and the surface. This repulsion would limit which region of the molecule could bind to the surface. For example, strongly negatively charged regions would be unable to bind, while regions with a net neutral charge would be able to bind. The result would be a molecule that was tilted away from the side-on orientation.

A diagram to show the orientation of BSA adsorbed at the studied buffer pHs is shown in Figure 3.23. At pH 3 the negatively charged surface exerts a strong electrostatic force on the positively charged proteins. The force causes the proteins to flatten on the surface so that they have a large area. This results in a low layer thickness. The electrostatic force between the charged proteins combined with their elongated "F" form excludes large amounts of the surface from further adsorption events.

Weak electrostatic forces between surface and proteins occur at pH 5. The proteins are able to pack together in large numbers meaning that the surface coverage is high.

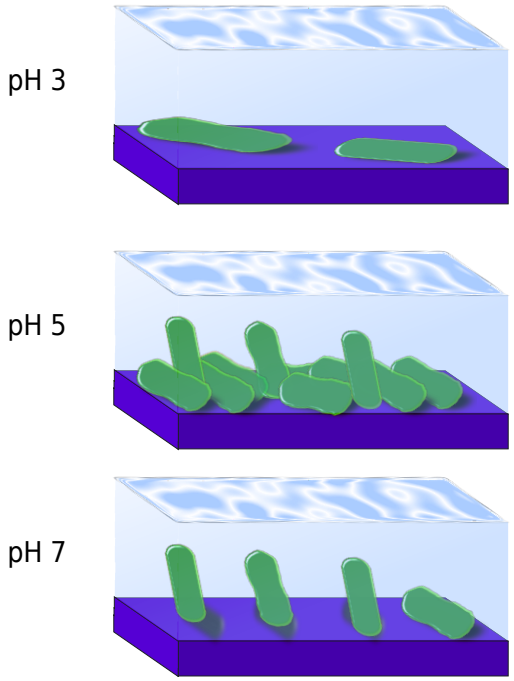

Figure 3.23: Schematic diagram to show the orientation of adsorbed BSA molecules at pH 3, pH 5 and pH 7.

When the space between the molecules is small, further molecules can adsorb by tilting towards the end-on orientation. This creates an inner layer of high density and an outer diffuse layer. DPI is less sensitive to this non-uniform density distribution than NR and so measures a lower thickness than NR.

At pH 7 the negatively charged proteins repel each other. This results in a lower surface coverage than at pH 5. The negatively charged surface causes the adsorbed proteins to be projected towards the end-on orientation. This creates a diffuse layer that DPI is largely insensitive to, which results in a large discrepancy between the NR and DPI measured thickness.

3.5 Conclusions

The effects of concentration and pH on BSA adsorption were investigated with DPI and NR. It was found from both techniques that the adsorbed layer thickness and surface coverage increased with concentration. The layer thickness and surface excess was shown to reach a maximum at pH 5, the isoelectric point of BSA. The further the pH was from the isoelectric point the lower the surface coverage.

The two techniques provided similar surface coverage data, even when using a two-layer model to fit the NR data. Thus DPI, a relatively inexpensive bench-top technique, can provide reliable protein surface coverage measurements that can be used to complement more expensive NR studies.

The main advantage of DPI over most other techniques is that it can also provide

reliable thickness measurements for thin films. DPI measured thicknesses were compared with NR results that were analysed with both single- and two-layer models. Although the DPI measured thicknesses were close to those obtained by the single-layer NR model, large differences were observed between the DPI and two-layer NR measured thicknesses. Two-layer models were fitted to the NR data as it was found increasingly difficult to fit single-layer models to the reflectivity profiles from concentrations above 0.1 mg/ml. DPI was observed to be less sensitive to low density regions than NR.

DPI measured kinetic data were used to investigate the Langmuir and RSA adsorption models. The Langmuir model was found to fit BSA concentrations of 0.25 mg/ml or less, where the interactions between the adsorbed proteins were insignificant. Above 0.25 mg/ml the surface coverage was high enough for interactions between the adsorbed molecules to limit the adsorption rate of further proteins. Thus the RSA model proved the better fit to the data above concentrations of 0.25 mg/ml.

The approach to the jamming limit, as predicted by RSA, was also investigated. For the approximately spherical proteins of BSA and transferrin it was found that their approach to the jamming limit had relationships of $t^{-0.5048\pm0.0007}$ and $t^{-0.4968\pm0.0006}$, in excellent agreement with the predicted value of $t^{-0.5}$. The RSA model could therefore be used to optimise the adsorption times of spherical blocking proteins that are used in immunoassays. This could reduce the production costs of commercial immunoassays.

A combination of NR and DPI measurements were used to investigate the effect of pH on the adsorption of BSA. It was thought that pH dependent structural transitions and electrostatic repulsion between adsorbed molecules accounted for the differences in surface coverage and thickness.

CHAPTER

FOUR

ANTIBODY BINDING

4.1 Overview

A model pregnancy test was investigated using a combination of DPI and NR. The model test was built up in stages so that each component could be investigated in detail. Although both techniques were able to investigate the interfacial structure of the adsorbed proteins, DPI was also able to provide data on the adsorption kinetics of each of the adsorbed proteins.

4.2 Introduction

Specific binding between antibodies and antigens is used in many biosensors and other biomedical devices, such as pregnancy tests [4], in the detection of viral Hepatitis [118] and the diagnosis of prostate cancer [119]. In the majority of these applications the antibody is immobilised onto a solid support, such as nitro-cellulose or polystyrene, before the target antigen is introduced in solution. The antibody and antigen form a complex which is then used to infer a positive result, as described in Section 1.4.

Immunoassays need to be extremely sensitive as the amount of target antigen in the sample solution is often in the picomolar range. In addition, the solution itself is often urine, saliva or blood, all of which contain a range of additional antigens, proteins and other molecules that may interfere with the immunoassay. The sensitivity of the immunoassay is dependent on the antigen binding capacity (AgBC) of the immobilised antibodies. In theory, the maximum AgBC of an antibody is two, one antigen per Fab. However, in reality, the AgBC of immobilised antibodies is markedly lower: typical AgBCs for commercial immunoassays are less than 0.1. As yet, it is not understood what causes the diminished AgBC of immobilised antibodies, although it has been shown that the antibody orientation [44] and the molecular density of the adsorbed antibodies [17] have an effect. This is likely due to the fact that antigens are unable to reach the binding sites of the antibody Fabs, since the Fabs have become blocked by the surface or by other antibodies. A better understanding of the reasons behind the reduced AgBC

of immobilised antibodies will improve the sensitivity of future immunoassays, thereby improving the diagnosis rates of viruses and cancers.

In addition to antibody immobilisation and its effect on the AgBC, the adsorption of a blocking agent and its interaction with the surface-adsorbed antibodies must be considered. Commercial immunoassays employ a wide range of blocking agents to prevent the non-specific adsorption of antigen molecules onto the support surface. Typically, the blocking agent is introduced to the surface after the antibodies have been allowed to adsorb. The blocking agent is then thought to either adsorb in the gaps on the surface that were not filled by the antibody adsorption step or cover the antibody layer in such a way that further molecular access to the surface is prevented. In practice, the surface is never completely blocked and the antigen can become non-specifically bound to the surface. This reduces the accuracy of the immunoassay and false positive results can occur.

Commercial immunoassays require blocking agents to have a high affinity for the support surface, to be soluble and to be as cheap as possible. Example blocking agents include surfactants such as Tween and proteins such as lysozyme and BSA.

Previous studies have used ellipsometry [17] and optical reflectometry [46] to investigate model immunoassays. Although these techniques were able to provide informative surface coverage data for the adsorption of antibodies, blocking agents and antigens, they could not provide thickness or density measurements. As such it was not possible to investigate the orientation of the adsorbed antibodies or ascertain whether the blocking agents slotted between the antibodies or sat on top of the antibodies. For this reason, DPI and NR, two techniques that are capable of obtaining thickness and density measurements in addition to surface coverage, were used to explore the specific and non-specific binding of proteins in a model pregnancy test.

4.3 Experimental method

DPI measurements were performed on a clean silicon-oxynitride waveguide (Farfield Group Ltd., Manchester, UK). The surface of the waveguide was wiped clean in detergent (Decon 90 5% solution) before it was rinsed with large quantities of ultra-pure water (UHQ). The DPI valve system was used to alternate between injected samples, cleaning agents and buffer.

PBS solution was used as a running buffer throughout the experiments. The PBS had an ionic strength of 20 mM at pH 5 and was made from NaH_2PO_4 and Na_2HPO_4 dissolved in UHQ. The bulk refractive index of the PBS was measured to be 1.333 ± 0.001 by the DPI and was calculated from the phase difference between the PBS and UHQ. The antibody, BSA and hCG samples were all prepared in the same PBS buffer.

To ensure that the waveguide had been adequately cleaned the phase was observed to return to a baseline before and after repeated 80% (w/w) ethanol/water injections. Since a change in the waveguide surface is manifested as a phase change, this step proved that

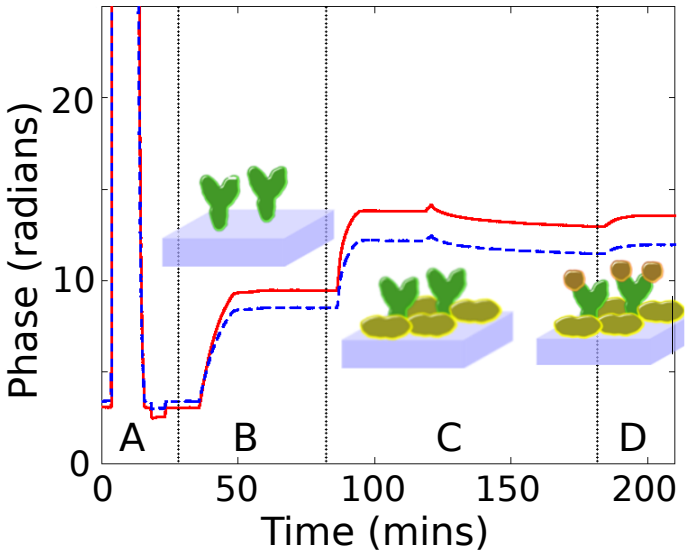

Figure 4.1: Region A is the ethanol to water calibration, B is the antibody adsorption and wash, C is the BSA adsorption and wash, and D is the antigen binding and wash.

the surface of the waveguide had remained constant. The waveguide was calibrated from the measured phase difference between UHQ and the 80% ethanol solution.

Once the waveguide had been cleaned and calibrated, 0.7 ml of antibody solution was injected and allowed to adsorb. After the required antibody surface coverage (M) had been reached, a buffer wash of 25 μl/min was used to remove reversibly adsorbed molecules from the waveguide. This was then repeated for a 0.025 mg/ml BSA solution in order to block any non-specific adsorption sites on the waveguide. The BSA solution was introduced at a flow rate of 10 μl/min. After 10 minutes the flow was stopped and the BSA was allowed to adsorb for a further 10 minutes in order to ensure it had equilibrated. Buffer was pumped over the antibody/BSA layer at a flow rate of 25 μl/min until any excess protein was removed from the system and the phase reached a constant level. Finally, hCG was introduced to the waveguide at a concentration of 0.002 mg/ml. Figure 4.1 shows the adsorption process and the subsequent phase change observed by the DPI. The increase in phase seen in regions B and C was due to the antibody and BSA molecules non-specifically binding to the waveguide surface respectively. The phase increase seen in region D was directly attributable to the specific binding of hCG and its antibody, since the BSA had effectively blocked any remaining non-specific adsorption sites on the waveguide surface.

The adsorption and binding of BSA and hCG was investigated at different antibody surface coverages. The surface coverage of the adsorbed antibody was varied by changing its concentration in solution and by altering the time the sample was allowed to adsorb.

Three control experiments were performed to ensure that the hCG was bound only to the antibody. Figure 4.2 shows surface coverage over time for the adsorption of 0.025 mg/ml of BSA and subsequent buffer wash followed by the introduction of 0.002 mg/ml of hCG. This experiment was performed in order to determine whether hCG could become

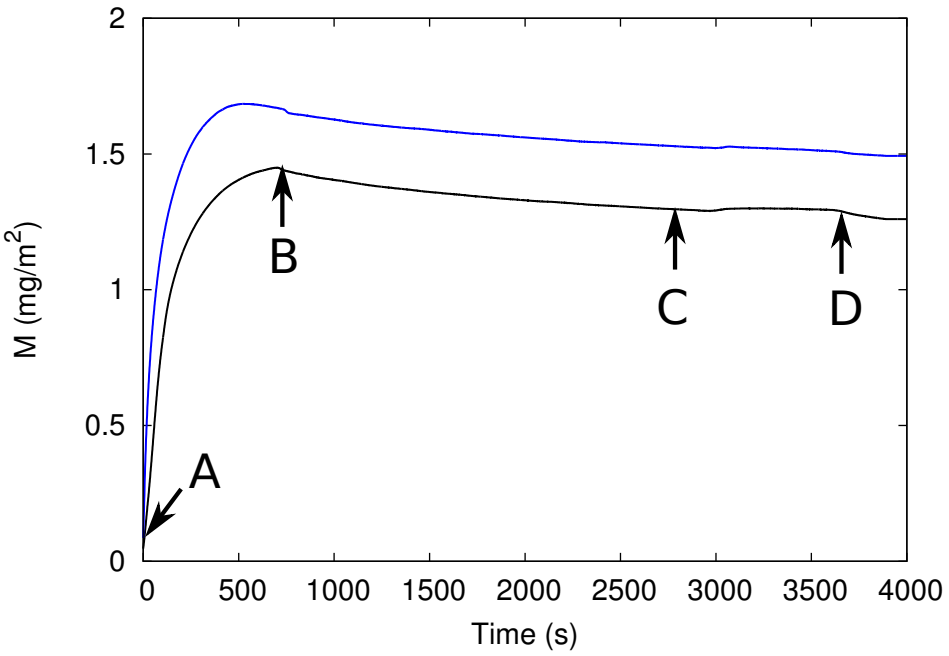

Figure 4.2: Surface coverage as a function of time for a control experiment of 0.025 mg/ml of BSA (adsorbed at step A and washed at step B) followed by 0.002 mg/ml of hCG (adsorbed at step C and washed at step D). The two lines represent data from the two experimental DPI channels.

bound to an adsorbed BSA layer. It can be seen that, within error, the introduction of hCG does not increase the surface coverage. This implies that no appreciable amount of hCG will bind to an adsorbed BSA layer.

To determine the amount of BSA required to block the hCG from the surface a further control experiment was performed. Solutions of 0.002 mg/ml of hCG were introduced to a waveguide that had been coated with BSA concentrations of either 0 mg/ml, 0.005 mg/ml, 0.025 mg/ml or 0.05 mg/ml, after any reversibly adsorbed BSA was removed by a buffer wash. The results are shown in Figure 4.3 which shows that a concentration of 0.025 mg/ml was sufficient to reduce hCG non-specific adsorption to a negligible amount.

The final control experiment was performed to ensure that the adsorbed anti-α-hCG would only specifically bind to its hCG antigen. Figure 4.4 depicts the surface coverage as a function of time for 0.01 mg/ml of anti-α-hCG and buffer wash followed by a 0.025 mg/ml BSA adsorption step and buffer wash. 0.025 mg/ml of HSA (blue line) or 0.025 mg/ml of lysozyme (black line) were then introduced. The results show that neither HSA nor lysozyme were able to bind to the anti-α-hCG antibody layer.

The instrument temperature was maintained at 20.000 ± 0.002°C throughout the experiments by use of a Peltier stage.

NR experiments were also performed on a clean silica surface of a silicon block, as described in Section 2.2.4. The immunoassay was constructed in stages, the antibody was introduced to the surface and allowed to adsorb before reversibly adsorbed molecules were washed from the surface with buffer. The duration of the adsorption was used to

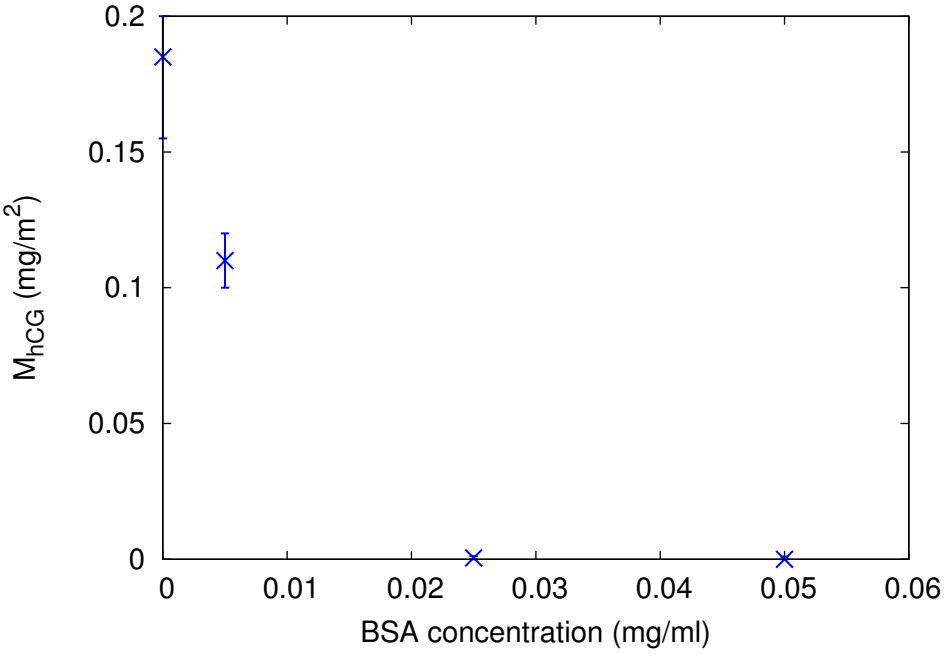

Figure 4.3: Non-specifically adsorbed hCG surface coverage as a function of pre-adsorbed BSA surface coverage, as measured by DPI.

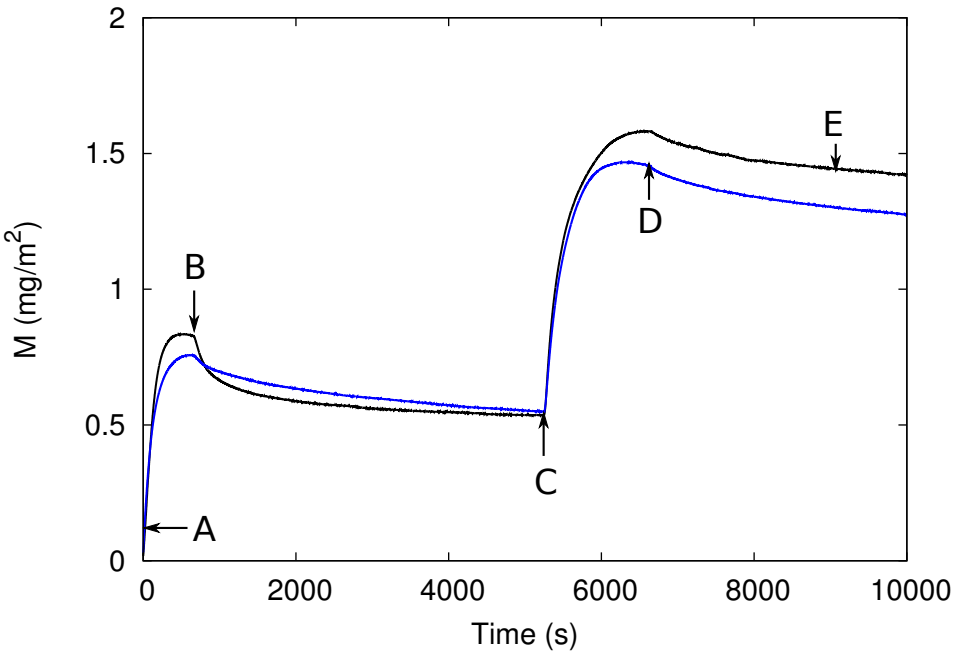

Figure 4.4: Surface coverage as a function of time for a control experiment of 0.01 mg/ml of anti-α-hCG (step A), followed by a buffer wash (step B), and 0.025 mg/ml of BSA (step C). After the BSA adsorption step and wash (step D), 0.025 mg/ml of HSA (blue line) or 0.025 mg/ml of lysozyme (black line) were introduced (step E).

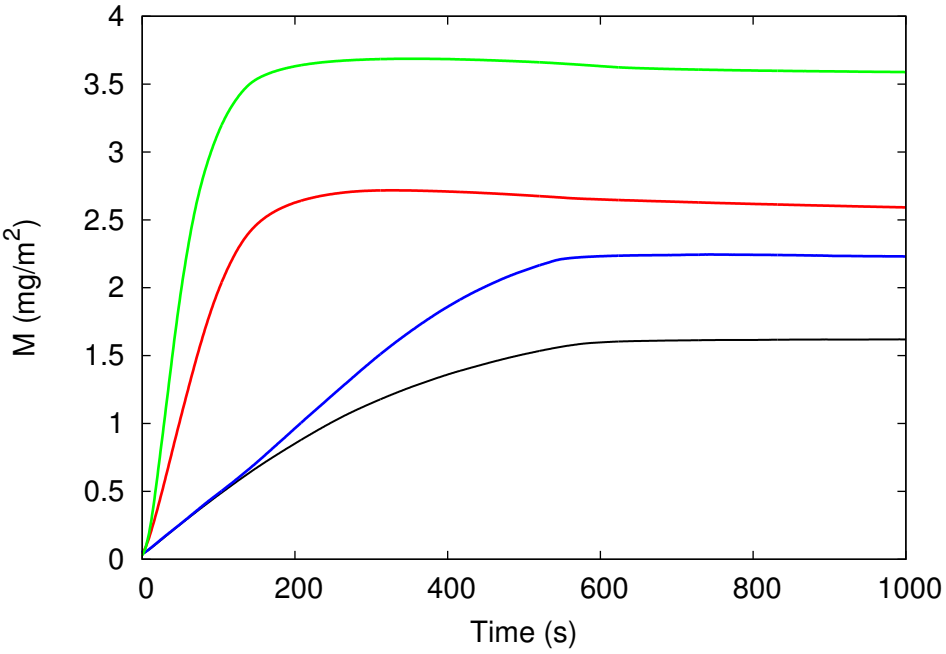

Figure 4.5: Time dependent surface coverage for four concentrations of anti-α-hCG. Green represents 0.1 mg/ml, red 0.05 mg/ml, blue 0.025 mg/ml and black 0.01 mg/ml.

vary the antibody surface coverage, and longer adsorption times resulted in higher surface coverages. After the antibody adsorption, 0.025 mg/ml of blocking protein (either HSA or deuterated HSA) was adsorbed and washed. Finally, 0.002 mg/ml of antigen was introduced to the surface of the block and washed after an adsorption time of 1 hour. Reflectivity profiles were obtained after each buffer wash step in order to determine the thickness and scattering length density of each adsorbed sample. Samples and buffers were introduced to the block with either a syringe or an HPLC pump.

Identical buffers were used for the NR and DPI experiments, however the NR buffers were made in either D_2O or H_2O.

NR experiments were performed at the medium flux SURF reflectometer at the ISIS Neutron Facility, Rutherford Appleton Laboratory, Didcot, UK and the D17 reflectometer at the Institut Laue-Langevin, Grenoble, France.

4.4 Results and discussion

4.4.1 Antibody adsorption dynamics

The antibody surface coverage and film thickness were investigated with DPI. Previous studies have used ellipsometry and NR to show that the surface coverage and thickness of an antibody layer vary with bulk antibody concentration [44] [120] [46]. Figure 4.5 shows the time dependent surface coverage for four anti-α-hCG bulk concentrations while Figure 4.6 shows the time dependent film thickness for the same antibody bulk concentrations. Each plot is an average of at least four repeats.

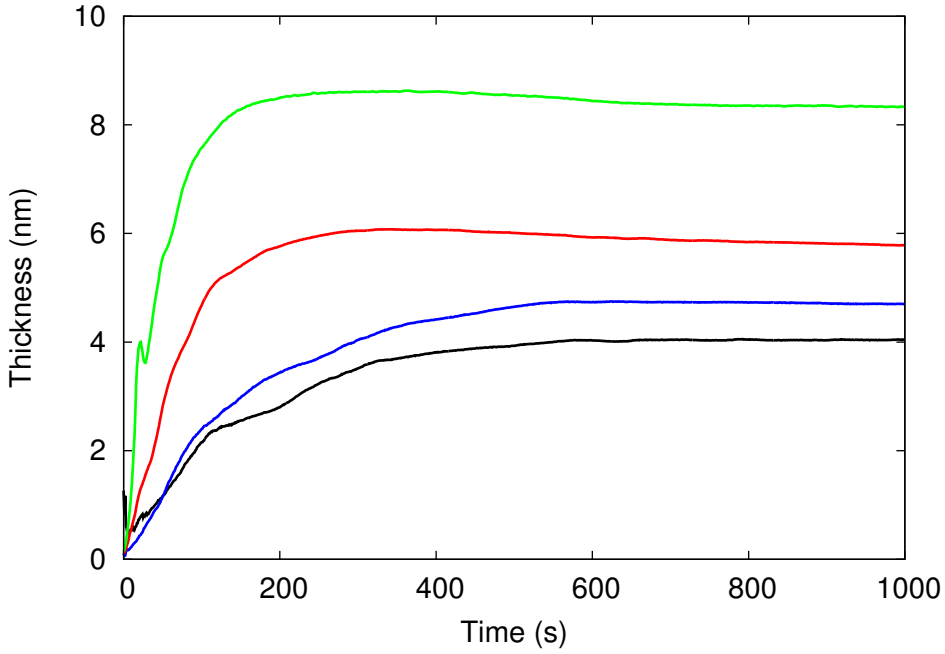

Figure 4.6: Time dependent film thickness for four concentrations of anti-α-hCG. Green represents 0.1 mg/ml, red 0.05 mg/ml, blue 0.025 mg/ml and black 0.01 mg/ml.

Figure 4.5 and Figure 4.6 show that the surface coverage and thickness asymptotically approached peak values that increased with bulk concentration. The data also show that the time taken to reach the peak values decreased at higher bulk concentrations. This has been observed by Xu et al [44] and Höök et al [121]. The reduction in the time taken to reach the peak thickness and surface coverage values with increased bulk concentration can be explained by the increase in the antibody molecular flux at the surface for increased concentrations. Because there are more molecules at the surface, the probability of an adsorption event is higher and the surface will become filled more rapidly. The higher adsorption probability will also influence the relaxation of adsorbed molecules on the surface: an adsorbed molecule may be prevented from spreading on the surface if other molecules adsorb nearby [59]. This would act to increase the surface coverage as more molecules will be able to adsorb per unit area. High surface coverages also imply that the film thickness will be increased: the oblate antibody molecules will be oriented perpendicularly to the surface if there is insufficient room for them to adsorb in a flat-on orientation. This effect can be seen from the data. At a concentration of 0.01 mg/ml the peak surface coverage is 1.5 mg/m^2 and the film thickness corresponds to the thickness of an antibody adsorbed in the flat-on orientation: 4 nm. When the concentration is increased to 0.1 mg/ml the surface coverage is increased to 3.6 mg/m^2 and the film thickness to 8.2 nm. The increased film thickness suggests that more molecules have become oriented perpendicularly to the surface. However, the thickness is still less than the long-axis of the antibody molecule ($\approx$ 14 nm).

Plots of deposition rate as a function of adsorbed molecules per unit area are given in Figure 4.7. Because the deposition rates decreased linearly with molecular areal den-

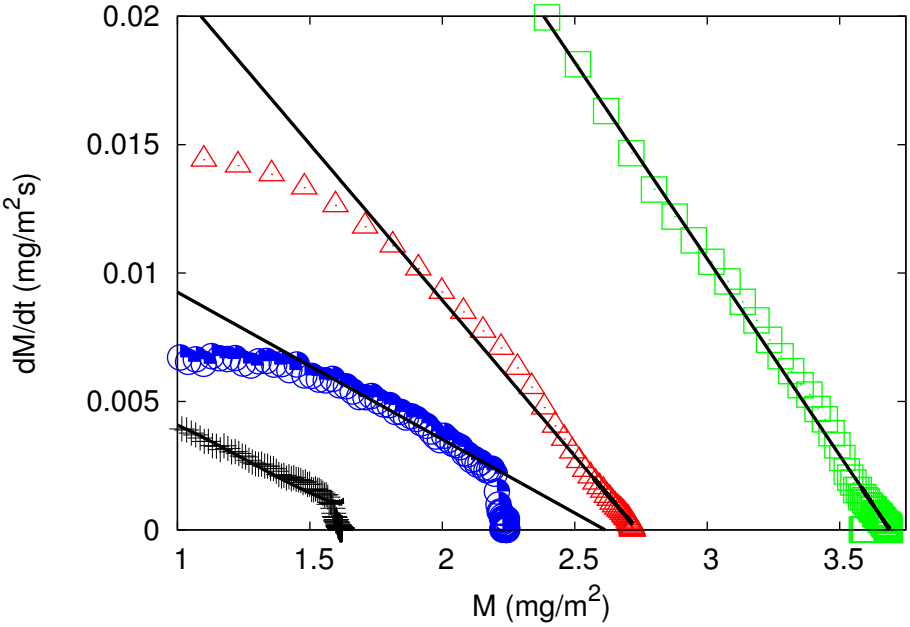

Figure 4.7: Deposition rates as a function of antibody surface coverage for antibody bulk concentrations of 0.01 mg/ml (black crosses), 0.025 mg/ml (blue circles), 0.05 mg/ml (red triangles) and 0.1 mg/ml (green squares). The solid lines represent the best fitting Langmuir adsorption model. The deposition rate values (y-axis) are multiplied by two for the 0.01 mg/ml and 0.025 mg/ml concentrations to make them clearly visible on the chosen axes. Every tenth data point is shown for each concentration.

sity, the RSA model was rejected in favour of the more simple Langmuir model (Equation (1.6.2)). The Langmuir model provided an excellent fit to the experimental data for all of the studied concentrations. At low molecular areal density the experimental data deviates from the linear Langmuir model for all bulk concentrations. This was due to the finite time taken for the antibody molecules in the bulk to reach the waveguide surface. Thus, at early times the bulk antibody concentration at the waveguide surface was less than the average bulk antibody concentration of the sample and an adsorption model was not applied in this region.

4.4.2 Antibody history dependence

It has been shown that the rate of adsorption of a protein can be used to accurately probe its history dependence [54, 60]. In order to measure the degree of history dependence a second, third or ith adsorption step is performed on a surface that has previously undergone protein adsorption, as described in Section 1.6.3. Thus, the BSA adsorption step, used to prevent the non-specific adsorption of hCG on to the waveguide surface, can be used to measure the degree of history dependence of anti-α-hCG adsorption.

The surface coverage as a function of time for 0.025 mg/ml of BSA onto an empty surface is shown in Figure 4.8. Changes to the surface topology on a scale approximately equal to the size of a BSA molecule will result in a different adsorption curve to that

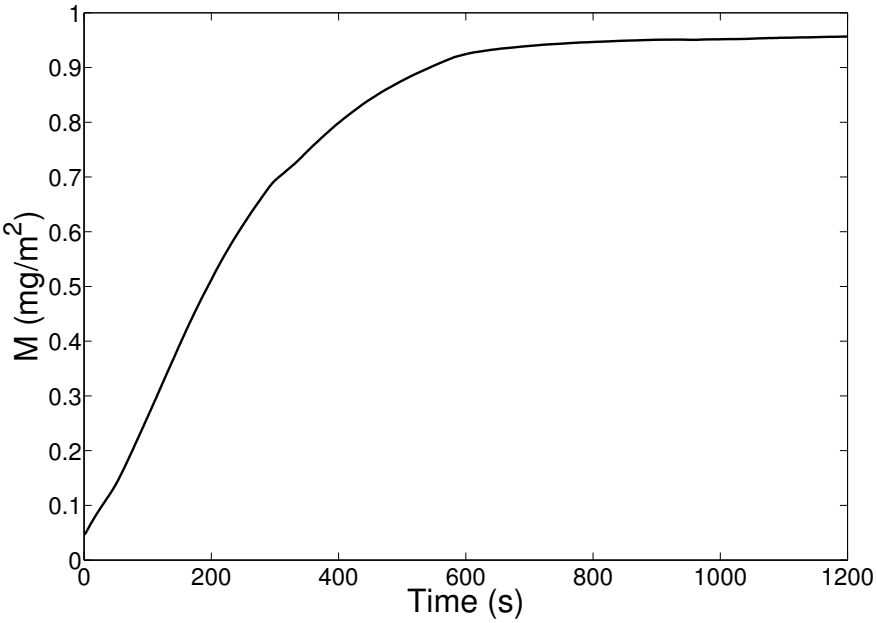

Figure 4.8: Surface coverage as a function of time for 0.025 mg/ml of BSA on an empty waveguide. The experimental buffer was set to pH 5 and 20 mM ionic strength.

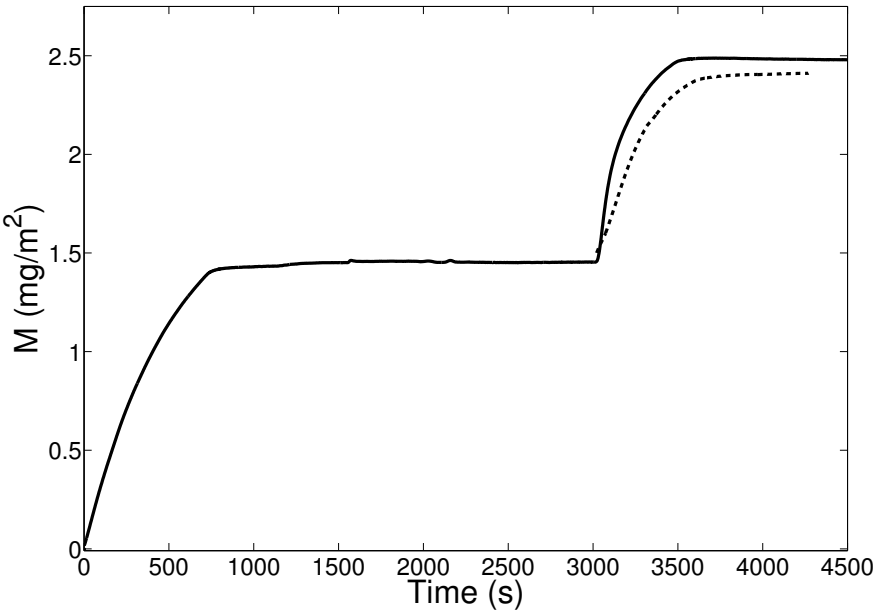

Figure 4.9: Surface coverage as a function of time for 0.01 mg/ml of anti-α-hCG followed by 0.025 mg/ml of BSA. The adsorption of BSA onto an empty surface (dotted line) is overlayed on the BSA adsorption step. The experimental buffer was set to pH 5 and 20 mM ionic strength.

shown in Figure 4.8. To allow a comparison, Figure 4.8 is shifted in time and initial surface coverage to match the BSA adsorption step performed after the initial adsorption of 0.01 mg/ml of anti-α-hCG in Figure 4.9. A detailed comparison of the two adsorption curves shows that both steps reach an approximate surface coverage of 2.5 mg/m^2, but the amount of time taken to reach this surface coverage is different. Although this is to be expected due to the different surfaces (one is empty and the other has an adsorbed antibody layer) the rate of adsorption for the BSA onto the antibody coated surface can

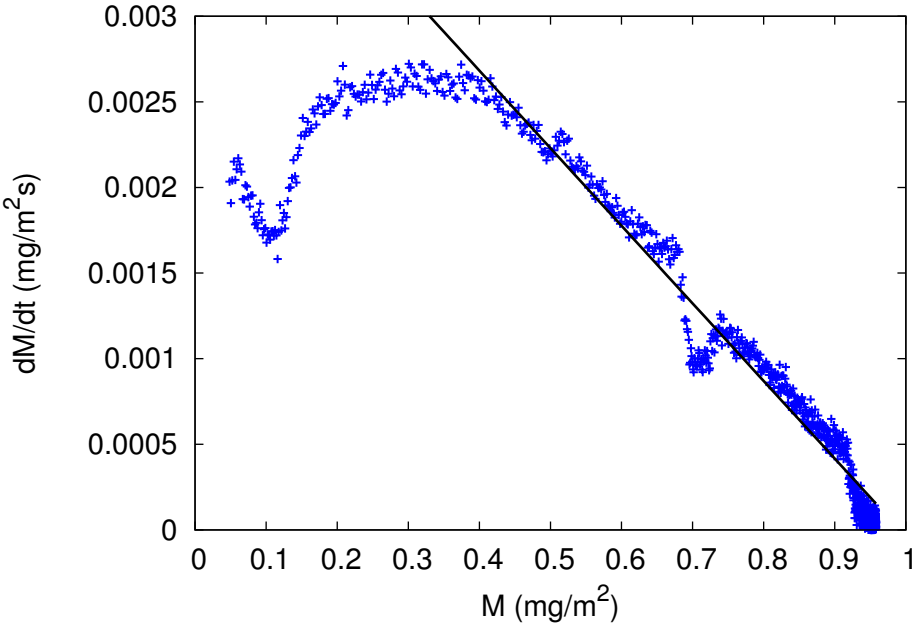

Figure 4.10: Adsorption rate as a function of surface coverage for 0.025 mg/ml of BSA onto an empty surface. A linear fit (solid line) is applied to the data.

be seen to be greater than the rate of adsorption of BSA onto the empty surface. This can be seen in greater detail by looking at how the rate of adsorption varies with surface coverage, where Equation (1.6.8) can be rewritten in the form $y = mx + c$ as

$$\left(\frac{\mathrm{d}M}{\mathrm{d}t}\right)_{\alpha} = k_a c_b B_\alpha M + k_a c_b A_\alpha \tag{4.4.1}$$

for the antibody adsorption step and

$$\left(\frac{\mathrm{d}M}{\mathrm{d}t}\right)_{BSA} = k_a c_b B_{BSA}(M_\alpha - M) + k_a c_b A_{BSA} \tag{4.4.2}$$

for the BSA adsorption step, where α and BSA subscripts are used to indicate the antibody and BSA adsorption steps. A and B represent the respective first and second order coefficients from the power series expansion of Φ, as shown in Equation (1.6.6). A is equal to one for the antibody adsorption step described by Equation (4.4.1). A is assumed to equal 1 for the BSA adsorption step despite the presence of the previously adsorbed antibody molecules. M_α is the antibody surface coverage prior to the BSA co-adsorption step, for example, $M_\alpha = 1.49\,\mathrm{mg/m^2}$ in Figure 4.9. Equation (4.4.1) and Equation (4.4.2) predict that linear regions will exist outside of the transport-limited regime for the antibody and BSA adsorption steps respectively.

The adsorption rate as a function of surface coverage for 0.025 mg/ml of BSA on to an empty surface and onto an antibody coated surface are shown in Figure 4.10 and Figure 4.11 respectively. Linear fits were applied to the surface-limited regime of both sets of data and the gradients were measured to be different; $-0.00650 \pm 0.00005\,\mathrm{s^{-1}}$

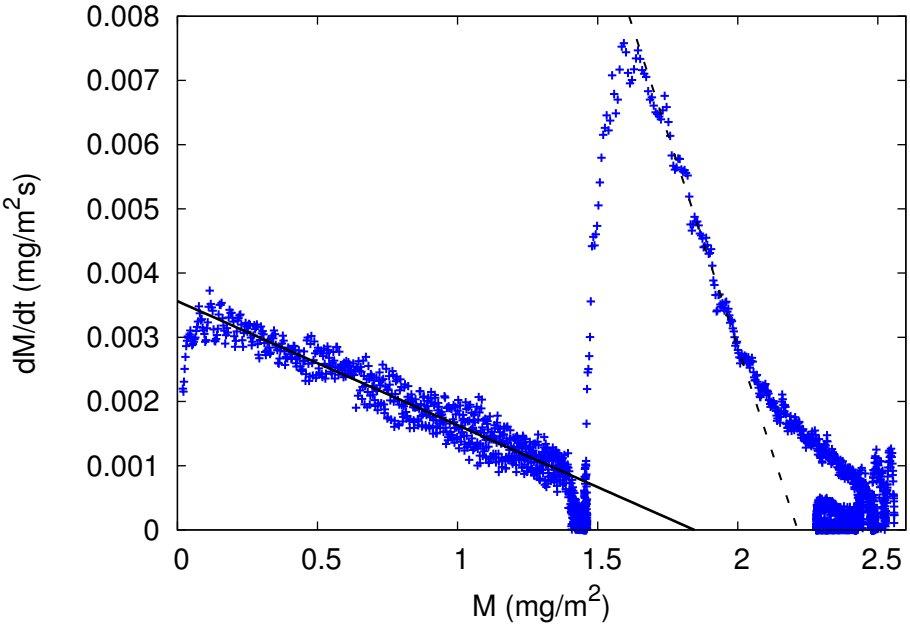

Figure 4.11: Adsorption rate as a function of surface coverage for an empty surface coated with 0.01 mg/ml of antibody followed by 0.025 mg/ml of BSA (same data as in Figure 4.9). Linear fits were applied to the antibody adsorption step (solid line) and the BSA adsorption step (broken line).

for the empty surface and $-0.0120 \pm 0.0001\,\mathrm{s}^{-1}$ for the BSA adsorbed on the antibody coated surface.

Calonder et al [60] observed a similar phenomenon for two different proteins: fibronectin and cytochrome c. They attributed the accelerated adsorption rate of readsorbed proteins to the irreversible formation of protein clusters on the surface. Protein clustering has previously been observed for lysozyme [122] and ferritin [123], measured with transmission electron microscopy and scanning tunneling microscopy respectively. Furthermore, protein clustering has been predicted by an adsorption model, developed by Ravichandran and Talbot [124], where lysozyme molecules were transported to the surface via Brownian motion.

Since protein clustering would likely be time dependent, as the adsorbed proteins would require a finite amount of time to rearrange themselves on the surface, the adsorption rate of BSA onto the empty surface was compared to the adsorption rates for BSA adsorbed onto antibody coated surfaces, where the antibody had been allowed to adsorb for different amounts of time. The results are displayed in Figure 4.12. Linear fits were applied to the BSA adsorption rates, as shown in Figure 4.11, in order to calculate the gradient of the BSA adsorption rate. This was done in order to investigate the effect of time on the conformation of the antibody layer. Figure 4.12 shows that the adsorption rate is time dependent, which implies that the surface-adsorbed antibodies form irreversible clusters when given enough time before the BSA adsorption step. Xu et al [17] previously measured anti-β-hCG antibodies on a silica surface with AFM and found that the antibodies formed clusters of between 2 and 15 molecules.

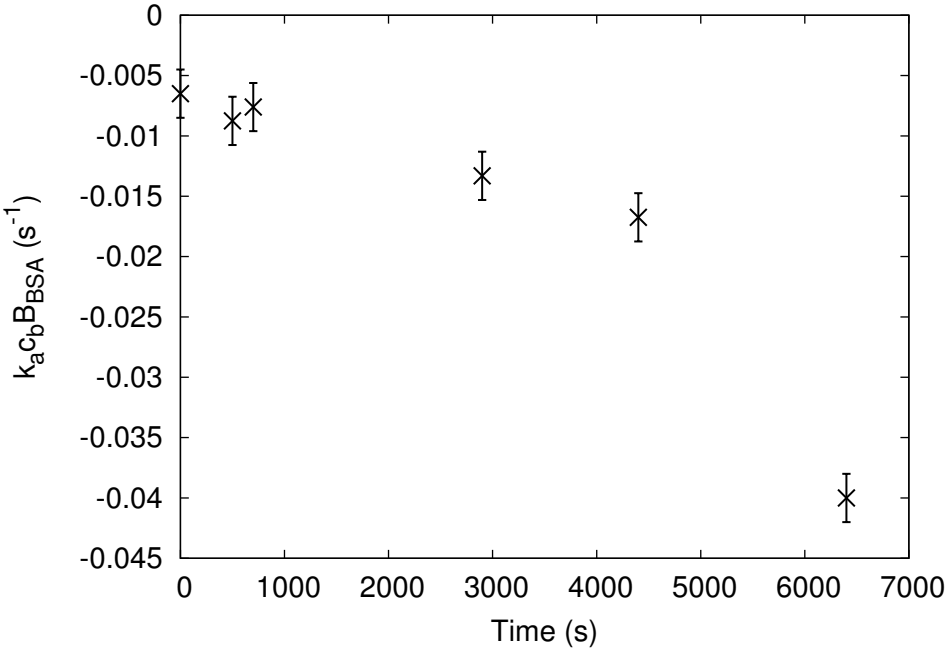

Figure 4.12: BSA adsorption rate gradients as a function of antibody total adsorption and desorption time.

Protein clustering could be a result of interactions between the adsorbed molecules or surface inhomogeneities, which would cause the attractive force between protein and surface to vary at different points on the surface. To test for surface heterogeneity, the apparent adsorption rate constant, k_a was calculated from the intercept of a linear fit applied to the adsorption rate data, as seen in Figure 4.11. In theory, the value of k_a is a property of the adsorbate-adsorbent system [54] and is dependent on the surface chemistry and solvent pH and ionic strength, as well as temperature and pressure. Thus, the value of k_a should remain approximately constant between experiments. Figure 4.13 shows that k_a remained approximately constant for the BSA adsorption steps. Differences between the values of k_a are likely due to the coefficient A_{BSA} differing from unity, due to the previous antibody adsorption step. Similarly, the values of k_a for the initial antibody adsorption step remained approximately constant. This suggests that it is protein clustering and not surface heterogeneity that is responsible for the increased BSA adsorption rate on a pre-coated surface.

Although the adsorption of antibody was seen to closely follow the Langmuir adsorption model, which assumes that there are no interactions between adsorbed molecules, clustering becomes apparent only after time-scales of between 1000 and 3000 seconds. At these timescales the rate of adsorption is close to zero, as seen in Figure 4.6, and the corresponding data do not follow the linear relationship predicted by the Langmuir model. The adsorption of antibody can therefore be split into three distinct regimes. The initial regime shows Langmuir-like adsorption that lasts for between 50 seconds and 600 seconds. After the rate of adsorption has become zero, post-adsorption processes occur that result in interactions between the adsorbed molecules. This regime lasts for between 1000 seconds

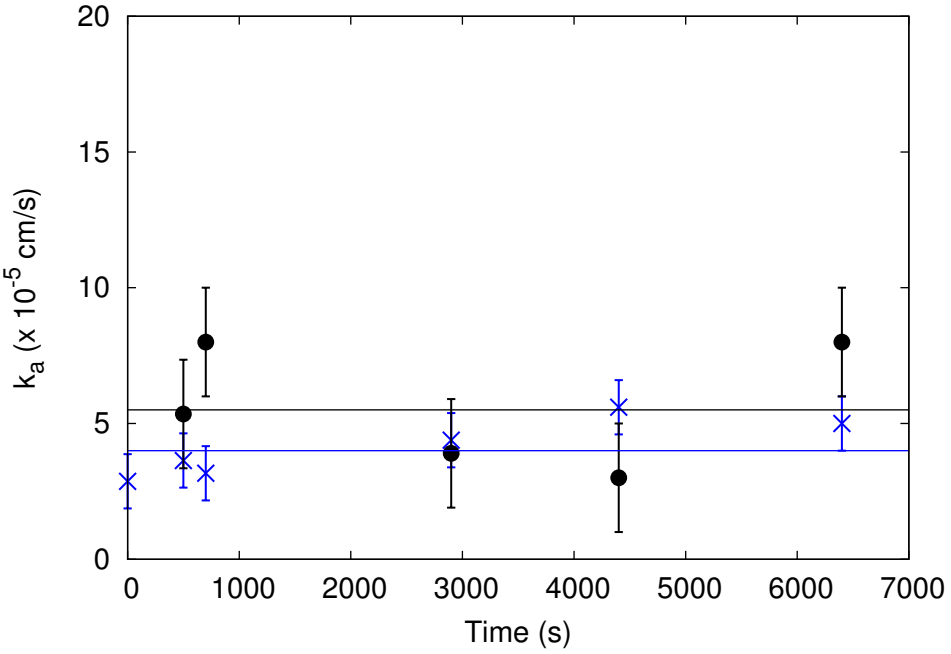

Figure 4.13: Apparent adsorption rate constant (k_a) as a function of antibody total adsorption and desorption time. The black circles are for k_a for the initial antibody adsorption onto an empty surface and the blue crosses are for k_a BSA adsorbed onto the pre-coated antibody surface.

and 3000 seconds. The final regime occurs when the interactions between the adsorbed antibodies are sufficient to cause protein clustering.

Further information about the co-adsorbed BSA can be obtained from the BSA desorption step, which was obtained by rinsing the mixed layer with buffer prior to the hCG adsorption. Figure 4.14 shows the negative BSA desorption as a function of anti-α-hCG surface coverage for a typical BSA buffer rinse step. The desorption constant k_d is an average of any number of desorption constants. Figure 4.14 shows that two linear regimes were present in a typical BSA desorption step. The initial and steepest region is defined as having a desorption rate constant of k_{d1} and applies to a population of weakly adsorbed BSA molecules that are rapidly removed from the surface by the buffer rinse, which will be referred to as population 1. At lower anti-α-hCG surface coverage, a second linear regime can be seen and had a desorption rate constant of k_{d2}. BSA molecules removed in this region were rinsed from the surface at a slower rate than those in the initial region. The more slowly removed molecules will be referred to as population 2. A third population of adsorbed BSA molecules exists: those that are irreversibly adsorbed.

Figure 4.15 shows how the magnitudes of k_{d1} and k_{d2} varied as a function of anti-α-hCG surface coverage. Although k_{d2} remained approximately constant over the studied surface coverage, k_{d1} can be seen to increase rapidly with increased anti-α-hCG surface coverage. The high values of k_{d1} imply that BSA molecules in population 1 were less strongly adsorbed than those in population 2. Since the buffer and substrate conditions were identical for each population, this suggests that molecules in population 1 had less area in contact with the surface than those in population 2. This is likely a result of

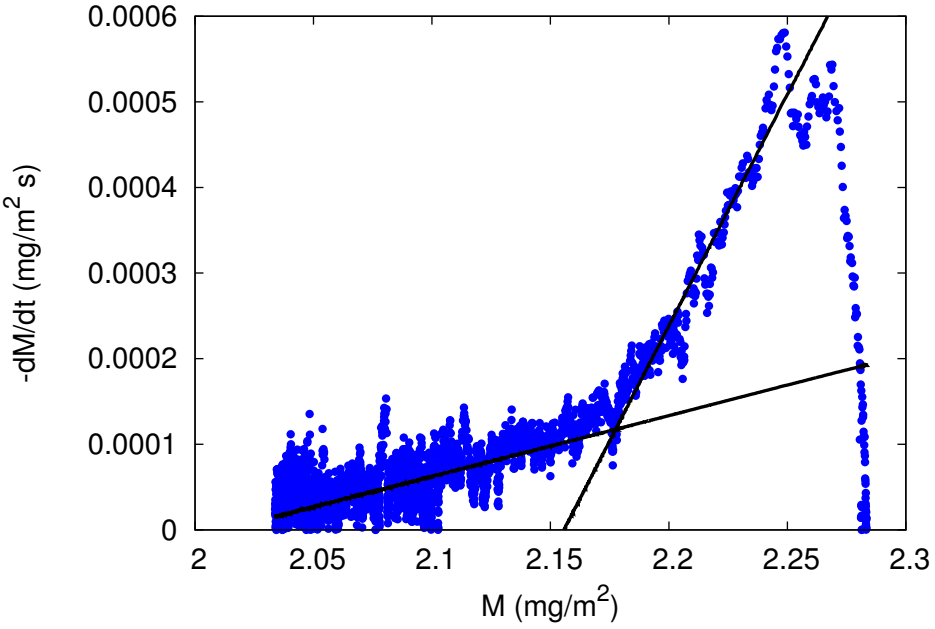

Figure 4.14: Negative of the BSA desorption rate as a function of anti-α-hCG surface coverage. Linear fits were applied to two regions: the initial, steeper rate of desorption (k_{d1}) and the final rate of desorption (k_{d2}). Both fits are represented by the solid lines.

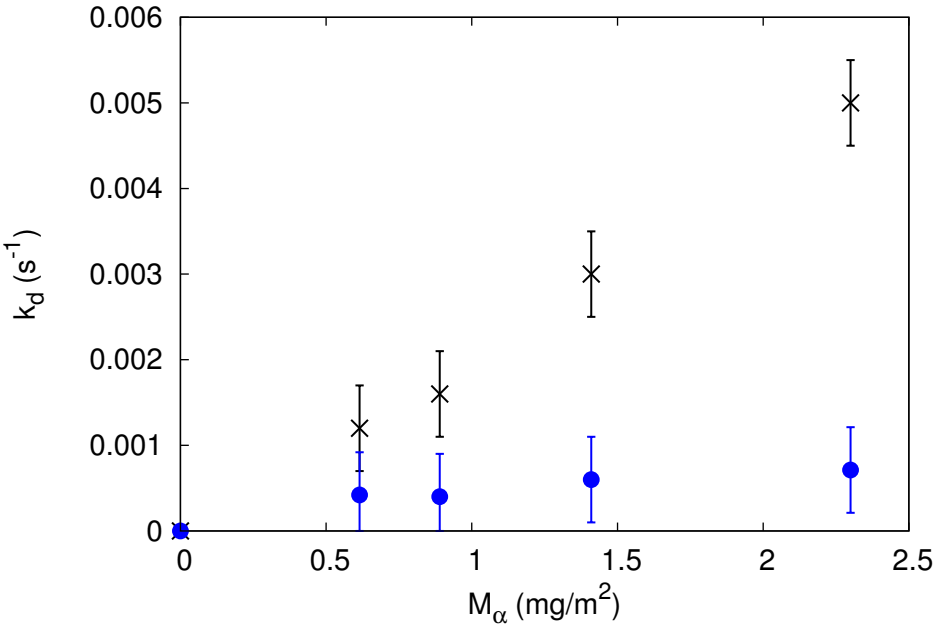

Figure 4.15: Desorbed BSA k_{d1} (black crosses) and k_{d2} (blue circles) values as a function of anti-α-hCG surface coverage. For 0.025 mg/ml of BSA adsorbed onto a bare surface ($M_\alpha = 0$) there was no measurable desorption.

molecular crowding on the surface, which would have prevented some BSA molecules from adsorbing in the side-on orientation and increased the number of end-on oriented BSA molecules. As the anti-α-hCG surface coverage increased so did the magnitudes of k_{d1}, which implies that the increased molecular crowding further reduced the surface-adsorbed area per molecule of BSA molecules in population 1.

4.4.3 Interfacial structure

The interfacial structure of antibody/blocker/hCG immunoassays were probed with DPI and NR. The DPI results are discussed first.

DPI results

Figure 4.16 shows experimental data for an anti-α-hCG/hCG binding curve with low antibody surface coverage. Antibody was adsorbed until it reached the required surface coverage, which was 0.8 mg/m^2 in this case. The average thickness of the adsorbed antibodies was 2.8 nm, less than the 3.8 nm short axis of the antibody. This suggests that either the antibody molecules adsorbed in the flat-on position and, due to the low lateral repulsion between the molecules, became spread across the surface, or that the antibody layer was too diffuse for the DPI to accurately determine the layer thickness. A similar effect was observed for low surface coverage BSA films, as described in Chapter 3. The surface coverage, thickness and density remained constant throughout the buffer wash.

Upon adsorption, BSA was seen to create a new, mixed antibody/BSA film of increased surface coverage, density and thickness. The new layer had a thickness of 4.1 nm, approximately the length of the short axis of a BSA molecule. This suggests that the BSA became non-specifically adsorbed to vacant spaces on the substrate that were not filled by the antibody adsorption step. As the BSA filled the gaps between the antibodies, the DPI-measured layer thickness would have increased. Although BSA stacked on top of the antibodies would have also increased the thickness it would not account for the increased density of the layer. The addition of BSA can be seen to increase the film density from approximately 0.30 g/cm^3 to 0.45 g/cm^3. This provides further evidence that the BSA molecules adsorbed on the waveguide surface between the antibody molecules. In effect, the gaps between the antibodies were filled by BSA to create a more dense layer. If the BSA molecules were to adsorb on top of the antibodies then the density would be expected to remain constant or decrease. A minor reduction in the thickness, density and surface coverage of the mixed layer occurred during the buffer wash. It is assumed that only BSA molecules were removed by the buffer wash as any reversibly adsorbed antibodies should have been removed by the antibody buffer wash prior to BSA adsorption.

Finally, 0.002 mg/ml of hCG antigen was added to the antibody/BSA film. Figure 4.16 shows that the hCG caused the surface coverage to increase by a small amount. Since the antibody/BSA layer had blocked the non-specific binding sites on the surface, the

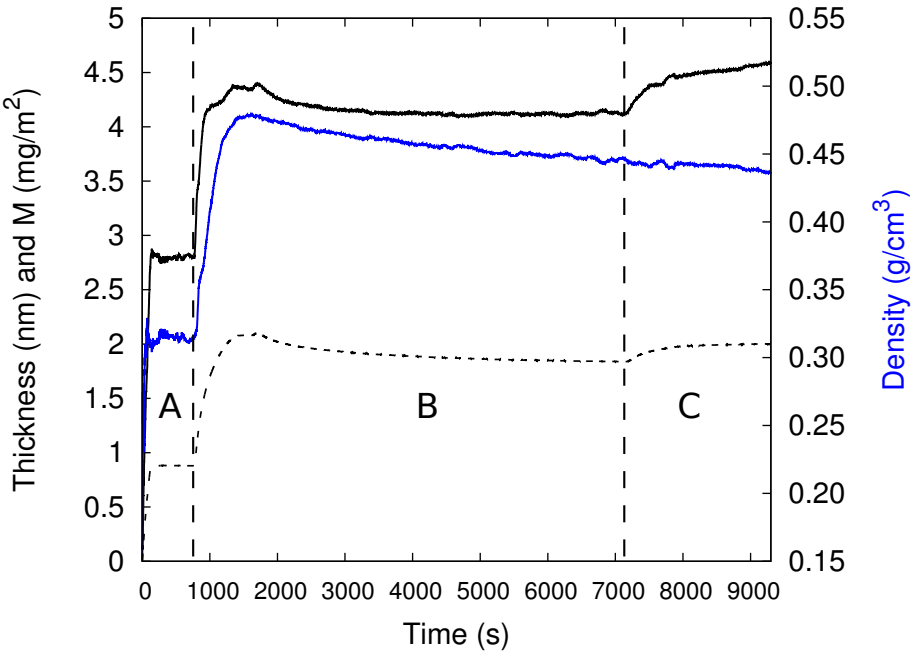

Figure 4.16: DPI measured surface coverage (broken line), thickness (solid line) and density (blue line) of low surface coverage antibody/BSA/hCG binding curve as functions of time. Region A is the antibody adsorption and wash, region B is the BSA adsorption and wash and region C is the hCG adsorption and wash.

hCG must have specifically bound to the antibody Fabs. The increase in the total surface coverage suggests that only a small number of Fabs were available for the hCG molecules to bind to. After the hCG was introduced, the thickness increased by 0.5 nm while the density remained approximately constant at 0.44 g/cm^3. As the increase in thickness is less than the short axis of hCG, it can be inferred that the hCG molecules bound to Fabs inside the antibody/BSA layer, and increased the layer density, while part of the hCG molecules protruded from the layer to form a region of reduced density. Thus, the average density of the film would have remained approximately constant.

Figure 4.17 shows how the thickness, surface coverage and density vary with time for a higher bulk concentration of antibody. The antibody surface coverage reached a peak of 2.9 mg/m^2 before it was reduced to 2.6 mg/m^2 by the buffer wash. At its peak, the antibody layer had a thickness of approximately 6.0 nm, which could be achieved by a double layer of flat-on adsorbed antibodies or a combination of flat-on, side-on and end-on aligned molecules. The former is unlikely as the surface coverage and thickness reached a maximum and then plateaued, which discredits multilayer formation. At such high surface coverage it is likely that many of the adsorbed antibody molecules had only a small area in contact with the surface and the shear force of the wash was sufficient to remove them. The fact that the layer thickness was reduced to 5.4 nm after the wash also suggests that some of the perpendicularly oriented molecules were washed from the surface, due to their small area of contact with the surface.

The addition of BSA to the antibody layer resulted in an increase in the surface coverage, thickness and density of the layer. However, the magnitude of the increase was

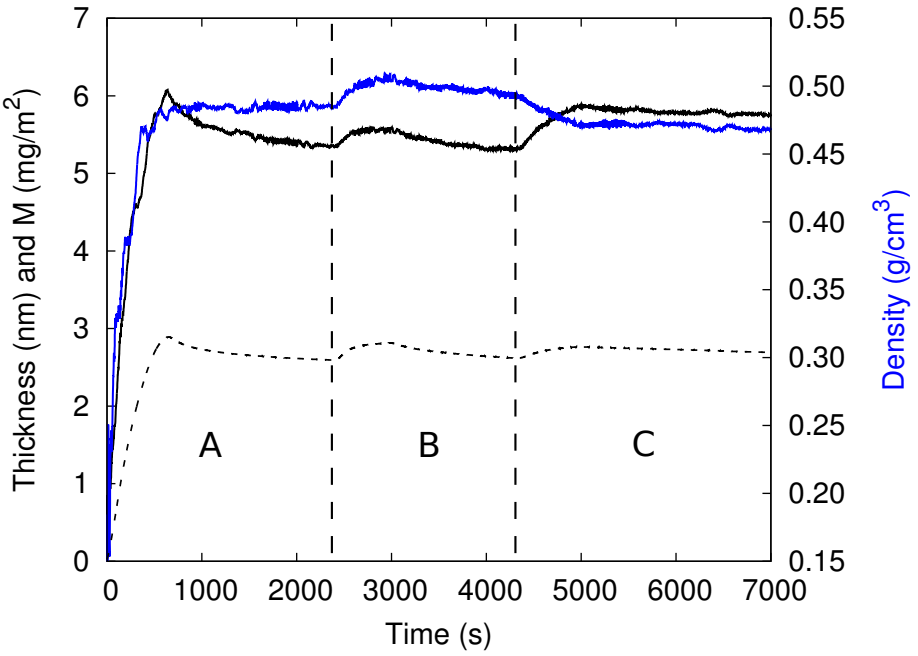

Figure 4.17: Time dependent surface coverage (broken line), thickness (solid line) and density (blue line) of high surface coverage antibody/BSA/hCG binding curve as measured by DPI. Region A is the antibody adsorption and wash, region B is the BSA adsorption and wash, and region C is the hCG adsorption and wash.

less than for the BSA shown in Figure 4.16. For the high antibody surface coverage, the buffer wash after the BSA adsorption reduced the total surface coverage to 2.6 mg/m^2, the same level as before the BSA was introduced. The total layer thickness was equal to the thickness prior to the introduction of BSA: 5.4 nm. The density increased marginally from 0.49 g/cm^3 to 0.50 g/cm^3 after the buffer wash. The increase in surface coverage and density and the reduction in thickness after the BSA step imply that few BSA molecules became adsorbed to the surface, but those that did were adsorbed in the spaces between the antibody molecules.

Figure 4.18 shows the adsorbed BSA density as a function of antibody density. The BSA density was calculated by subtracting the antibody density from the combined antibody/BSA layer density. The BSA density can be seen to decrease linearly with increasing antibody density. This suggests that the available surface adsorption sites for BSA are reduced when antibodies are adsorbed. BSA adsorption is completely prevented at an approximate antibody density of 0.5 g/cm^3. This provides further evidence that BSA adsorbs to the surface between the antibody molecules. When the antibody density is sufficiently high there are no more spaces on the surface that are large enough for the BSA molecules to adsorb to.

Figure 4.18 suggests that commercial pregnancy tests, where the sample substrate is coated with a high concentration (> 3 mg/ml) of antibodies, may not require a BSA adsorption step to block the substrate surface. However, the substrate of commercial tests is typically a porous foam that has a much higher surface area than the DPI waveguide. Thus, even a concentration of 3 mg/ml of antibody may leave gaps on the porous foam

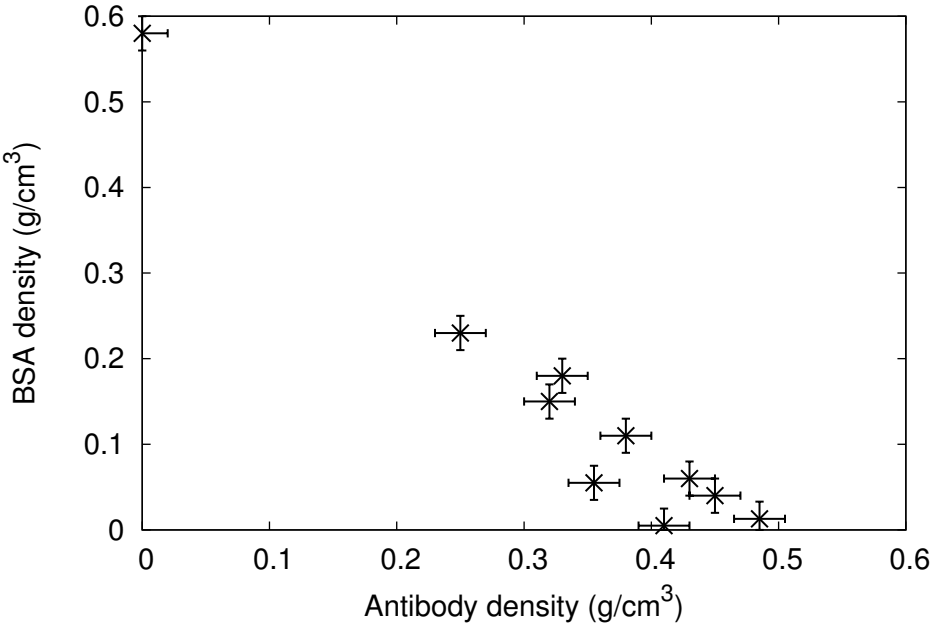

Figure 4.18: DPI measured density of adsorbed BSA as a function of the density of a pre-adsorbed antibody layer.

surface.

Neutron reflection

Due to its ability to obtain precise thickness and density measurements of thin films, NR was used to investigate the interfacial structure of the immunoassay. As previously discussed, parallel NR experiments can be performed with solvents of different scattering length densities. This method is known as contrast matching. There are two advantages to contrast matching, the first is that the number of theoretical models that will fit the data, and thus the ambiguity of which model is most appropriate, is reduced. Secondly, deuterium labelling can be used to highlight samples in order to distinguish them from the substrate, solvent or other samples. This technique is particularly useful for multiple component systems, such as the immunoassay described in this chapter.

To take advantage of contrast matching, deuterated human serum albumin (d-HSA) was used instead of BSA as a blocking agent. The scattering length density of d-HSA was calculated to be 7.9×10^{-6} Å^{-2} in D_2O and 6.4×10^{-6} Å^{-2} in H_2O. Thus, the signal produced by d-HSA in H_2O was large and it was possible to more accurately determine the structure of the adsorbed d-HSA. Deuterated BSA was not available, however, HSA and BSA are structurally similar and adsorb in similar amounts [10, 114]. As deuterated BSA was not available, it was thought that standard, hydrogenated HSA would make a better comparison between the hydrogenated HSA and the d-HSA NR measurements.

NR measurements were performed on an anti-α-hCG/HSA/hCG immunoassay. Measurements were taken after each protein had been adsorbed and washed. Figure 4.19 shows the reflectivity profile produced by anti-α-hCG adsorbed onto a bare silica surface.

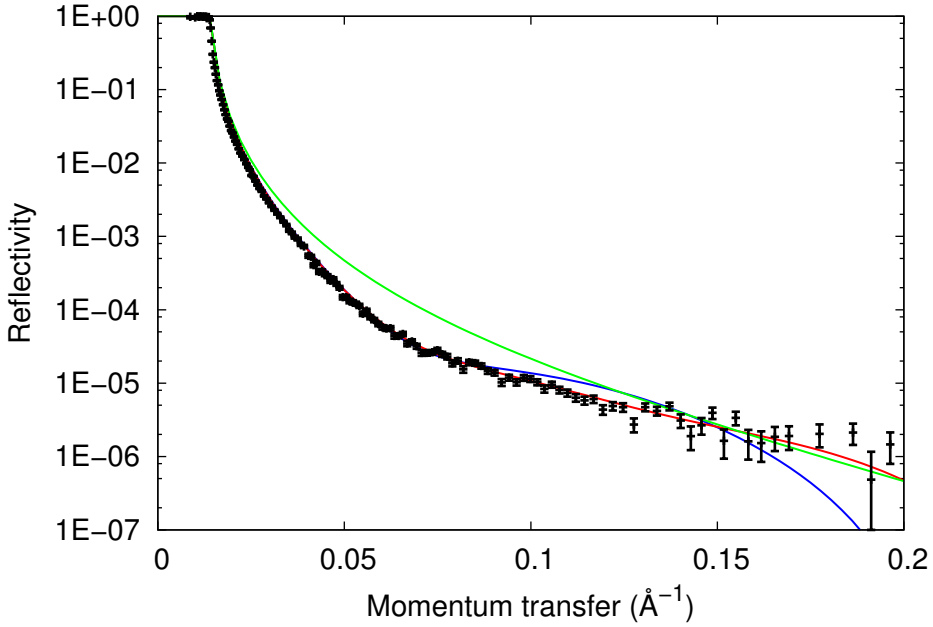

Figure 4.19: Reflectivity profile for anti-α-hCG adsorbed onto a silica surface. The red line represents the best fitting double-layer model and the blue line represents the best fitting uniform-layer model. The green line is the best fit for the measured silica layer.

The silica surface was previously measured and the best fit to the experimental data is shown as the green line in Figure 4.19. The experimental data clearly shows that the antibody adsorbed to the surface: a marked deviation from the bare silica surface can be seen. The simplest fit, a uniform-layer, shown as the blue line in Figure 4.19, provided a poor fit to the experimental data in the momentum transfer range 0.1 Å^{-1} to 0.2 Å^{-1}. This implied that the adsorbed antibody film featured regions of different scattering length densities and that multiple layers were needed to fit the data.

A two-layer model (red line) provided a closer fit to the experimental data than the uniform-layer model. The two-layer model measured an inner layer (in contact with the silica layer) of thickness 3.5 nm and volume fraction 0.36 and an outer layer of thickness 2.5 nm and volume fraction 0.10. A complete list of the parameters extracted from the NR data are shown in Table 4.1. The thickness of the inner layer is close to the 3.8 nm length of the short axis of the antibody. This suggests that the inner layer is composed of a large number of antibody molecules that have adsorbed in the flat-on orientation where their short axes are perpendicular to the silica surface. Previous studies have shown that the flat-on orientation is the preferred orientation for antibodies adsorbed on silica surfaces [44, 68]. The preference for the flat-on orientation can be explained by the electrostatic interaction between the surface and antibody, which has a maximum contact area with the surface in this orientation. The diffuse outer layer identified by the two-layer model is likely due to antibodies that adsorb mainly in the flat-on orientation but overlap other antibodies. A diagram to depict this is shown in Figure 4.20.

As the two-layer model provided a superior fit to the uniform-layer model, the two-

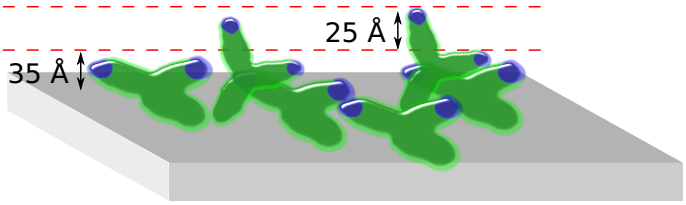

Figure 4.20: Antibody molecular arrangement described by the NR fit. The green Y-shapes are the antibodies and the blue patches represent their Fabs. The majority of the antibody molecules adsorb in the flat-on orientation to form an inner layer of 35 Å. Some molecules overlap the flat-on oriented molecules to produce a less dense 25 Å outer layer.

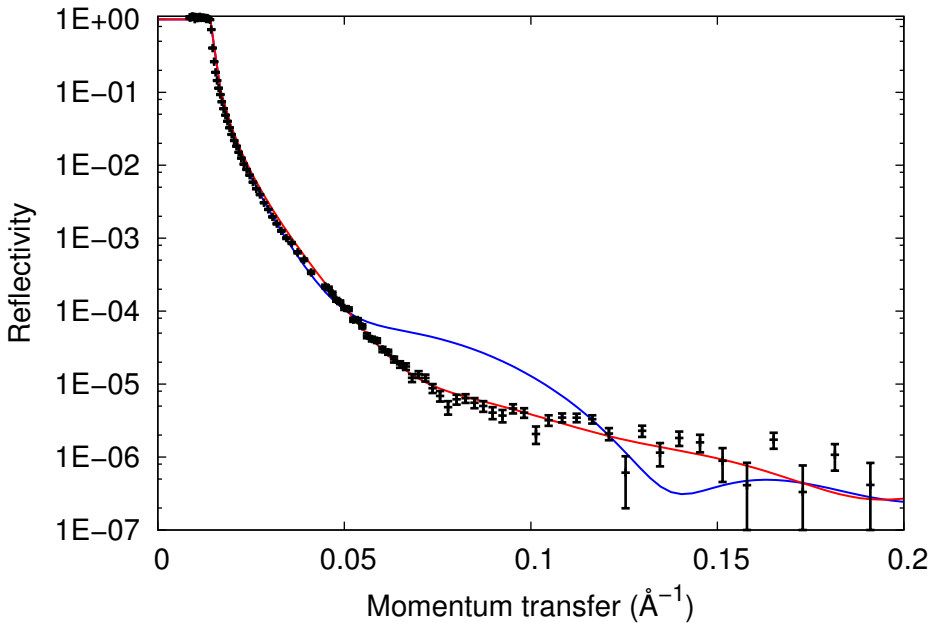

Figure 4.21: Reflectivity profile for HSA adsorbed onto the pre-adsorbed anti-α-hCG film. The red line represents the best fitting model where the parameters of either antibody layer can be adjusted. The blue line represents the best fitting model based on HSA molecules that are only inserted in the upper layer of the pre-adsorbed anti-α-hCG film.

layer model was used as a base for all subsequent measurements.

Hydrogenated HSA was then introduced to the antibody coated surface and allowed to adsorb for 1 hour before any reversibly adsorbed HSA molecules were rinsed from the surface with buffer. This created a mixed antibody/HSA film on the silica substrate. The reflectivity profile for the mixed antibody/HSA film is shown in Figure 4.21.

The HSA was thought to be inserted into the antibody film in two ways. The first way is represented by the blue line and assumes that HSA molecules are inserted only into the outer diffuse antibody layer. In effect, the HSA molecules settle on top of the adsorbed antibody molecules and increase the volume fraction of the outer layer, whereas the inner layer remains mostly constant. Figure 4.22 is a diagram to show how HSA molecules could be inserted into the outer layer only.

The second way for the HSA molecules to co-adsorb with the antibody molecules is for the HSA molecules to adsorb to areas on the surface that were not covered by antibody

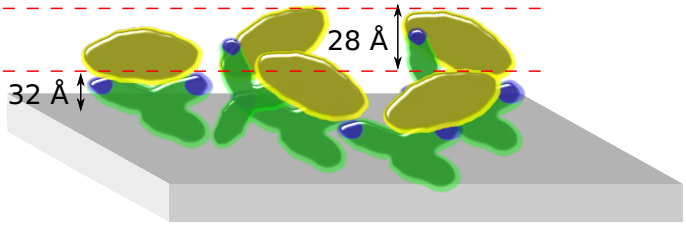

Figure 4.22: Schematic diagram to show how HSA (yellow spheres) could settle on top of the antibody layer. The diagram assumes that the HSA molecules form a layer of 28 Å as used to obtain the blue line in Figure 4.21.

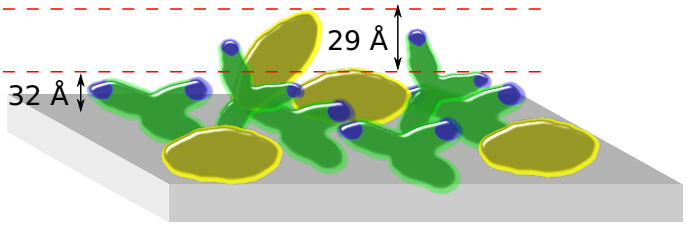

Figure 4.23: The HSA molecules (yellow spheres) adsorb into the spaces between the antibodies on the substrate surface and increases the density of the inner layer. The HSA is also present in the outer layer. This may be due to HSA molecules that partially overlap pre-adsorbed molecules, so that the long axis of the HSA molecules are directed perpendicularly to the substrate surface.

molecules. This would result in an increase in the volume fraction of the inner layer, and, if the HSA molecules were oriented so that their long axes were perpendicular to the surface, a slight increase in the volume fraction of the outer layer. This method of HSA insertion is shown in Figure 4.23 and its best-fitting model is displayed as the red line in Figure 4.21.

From Figure 4.21 it can be seen that the red line, based on HSA molecules that are predominantly inserted into the inner layer, provides the most suitable fit to the experimental data. The model states that 0.53 mg/m^2 of HSA was inserted into the inner layer to increase the volume fraction by 0.12. The thickness of the inner layer was reduced to 3.2 nm, within error of the previous value of 3.5 nm and approximately equal to the short axis of HSA. Therefore the majority of the HSA molecules were adsorbed in the flat-on orientation in the inner layer of the antibody film.

In addition, the model shows that the introduction of HSA increased the volume fraction and surface coverage of the outer layer by a small amount, 0.02 and 0.08 mg/m^2 respectively. This increase could be caused by the adsorption of end-on oriented HSA molecules in the inner layer that overlapped other adsorbed molecules so that part of their volume extended into the outer layer. Such an orientation can be explained by the fact that some empty areas on the surface may have been so small as to permit only part of the HSA molecule to adsorb. The remainder of the HSA molecule would then overlap other adsorbed molecules.

Finally, 0.002 mg/ml hCG antigen was introduced to the antibody/HSA film. The reflectivity profile for the antibody/HSA/hCG film is shown in Figure 4.24 and the fitted

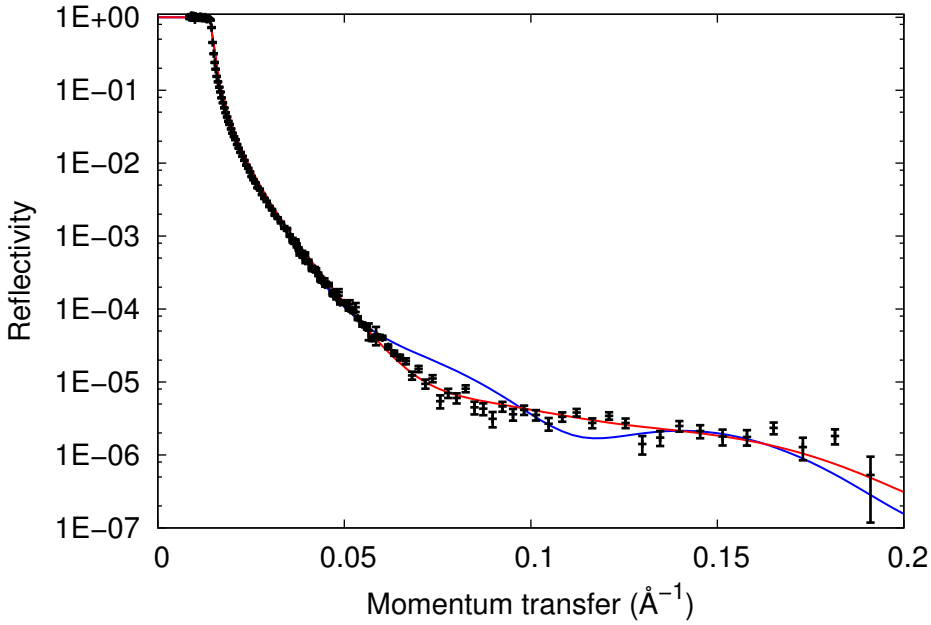

Figure 4.24: Reflectivity profile for hCG introduced to the pre-adsorbed anti-α-hCG/HSA film. The red line represents the best fitting model and the blue line represents the best fitting model based on hCG molecules that adsorb only in the upper layer of the pre-adsorbed mixed film.

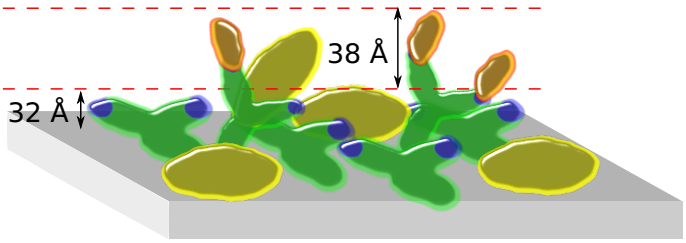

Figure 4.25: Diagram to illustrate hCG molecules that bind exclusively to the Fabs of the antibodies in the outer layer. This results in an increased outer layer thickness and volume fraction.

models were based on the best fitting model from the HSA data. As before, two different models of hCG insertion were tested. The blue line is based on hCG molecules that are inserted exclusively into the outer antibody/HSA layer. A diagram of this is shown in Figure 4.25 and is based on the idea that antibody Fabs in the outer layer are available for the hCG molecules to bind to, whereas antibody Fabs in the inner layer are not, possibly due to the Fabs being obstructed by other molecules.

The alternative model (red line) assumes that the hCG molecules may bind to antibody Fabs in either layer. Non-specific adsorption of hCG molecules to the silica surface is not considered for either model. This is due to the control experiment, described in Section 4.3, that shows that non-specific adsorption of hCG is negligible when the surface has been blocked with 0.025 mg/ml of albumin.

It can be seen from Figure 4.24 that only one model was able to adequately fit the experimental data: the model that allowed for hCG molecules to bind to antibody Fabs

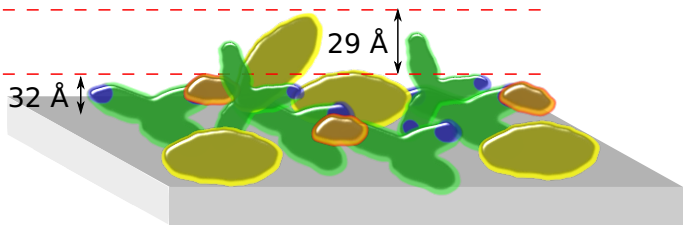

Figure 4.26: The hCG molecules bind to the Fabs of the antibodies in the inner layer and increase the volume fraction of the layer. The hCG molecules are bound to antibody Fabs in the inner layer as there are few Fabs present in the outer layer.

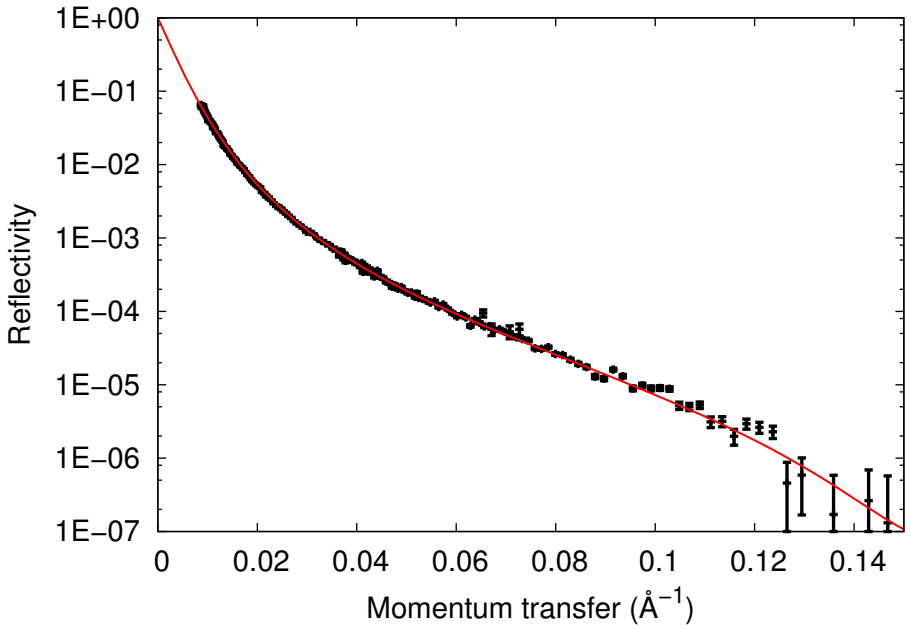

Figure 4.27: Reflectivity profile for 0.025 mg/ml d-HSA. The red line represents the best fitting uniform-layer model.

in the inner layer. Since non-specific hCG adsorption is negligible, this implies that the antibody Fabs in the inner layer were more active than those in the outer layer, perhaps because there were insufficient antibody Fabs in the outer layer for a detectable amount of hCG to bind to. A diagram of the molecular arrangement described by the model is shown in Figure 4.26.

The optimal structural parameters obtained from the best fits to the experimental NR data for the antibody/HSA/hCG film are shown in Table 4.1.

In order to obtain additional information about the interfacial structure of the adsorbed blocking agent, d-HSA was added to a pre-adsorbed antibody layer. NR measurements were performed in D_2O and H_2O, where the large difference between the scattering length densities of H_2O (-0.56 $\times 10^{-6}$ Å^{-2}) and d-HSA (6.4 $\times 10^{-6}$ Å^{-2}) produced a large signal. Since d-HSA had not previously been studied with NR, the adsorption of 0.025 mg/ml of d-HSA onto a silica surface was first investigated with NR. The reflectivity profile is shown in Figure 4.27. The parameters used to obtain the best fit (red line in Figure 4.27) are listed in Table 4.2 along with the parameters obtained for 0.025 mg/ml BSA (as de-

Table 4.1: Parameters extracted from NR data using the best fitting model and the optical matrix method.

Sample	Layer no.	Thickness, τ (nm)	SLD, ρ ($\times 10^{-6}$Å^{-2})	Volume fraction, $\phi_\alpha, \phi_{\text{HSA}}, \phi_{\text{hCG}}$ ± 0.01	Surface coverage, $M_\alpha, M_{\text{HSA}}, M_{\text{hCG}}$ (± 0.05 mg/m^2)	Total surface coverage, M_{total} (± 0.05 mg/m^2)
α	1	3.5 ± 0.4	5.26 ± 0.05	0.36, 0, 0	1.91, 0, 0	2.27
	2	2.5 ± 0.4	6.06 ± 0.05	0.10, 0, 0	0.36, 0, 0	
α, HSA	1	3.2 ± 0.4	4.90 ± 0.05	0.36, 0.12, 0	1.91, 0.53, 0	2.88
	2	2.9 ± 0.4	6.00 ± 0.05	0.10, 0.02, 0	0.36, 0.08, 0	
α, HSA, hCG	1	3.2 ± 0.4	4.70 ± 0.05	0.36, 0.12, 0.07	1.91, 0.53, 0.17	3.05
	2	2.9 ± 0.4	6.00 ± 0.05	0.10, 0.02, 0	0.36, 0.08, 0	

Table 4.2: Parameters extracted from NR data using the optical matrix method. The parameters are for 0.025 mg/ml BSA, measured in D_2O, and 0.025 mg/ml d-HSA, measured in H_2O.

Sample	Thickness, τ (nm)	Surface coverage, M (mg/m^2)	Volume fraction, ϕ_P	Area per molecule, a (nm^2)
BSA	3.1 ± 0.3	1.9 ± 0.3	0.45 ± 0.05	57 ± 5
d-HSA	2.6 ± 0.5	1.2 ± 0.5	0.32 ± 0.05	96 ± 10

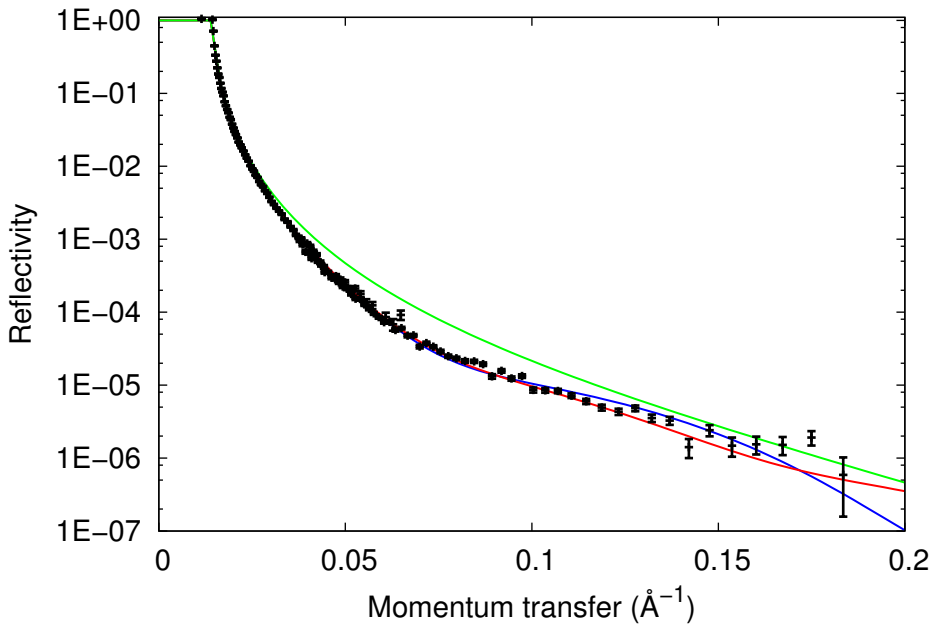

Figure 4.28: Reflectivity profile for anti-α-hCG adsorbed on to a bare silica surface. The red line represents the best fitting two-layer model and the blue line represents the best fitting uniform-layer model.

scribed in Chapter 3). The surface coverage and thickness of the adsorbed d-HSA layer can be seen to be lower than the equivalent BSA layer. However, the differences are small and are almost within error. Unpublished NR data has also been reported that shows that d-HSA adsorbs in lower amounts than for hydrogenated HSA [125]. d-HSA was assumed to adsorb in similar amounts and orientations as hydrogenated HSA.

Antibody was then introduced to a cleaned NR block with a silica layer of 12 ± 5 Å. After a buffer wash, a reflectivity profile was obtained in D_2O and is shown in Figure 4.28. Although a uniform-layer fit (blue line) almost fits the reflectivity profile shown in Figure 4.28, it can be seen to diverge from the experimental data at momentum transfer values greater than 0.1 Å^{-1}. The two-layer fit (red line) provided a closer fit to the experimental data.

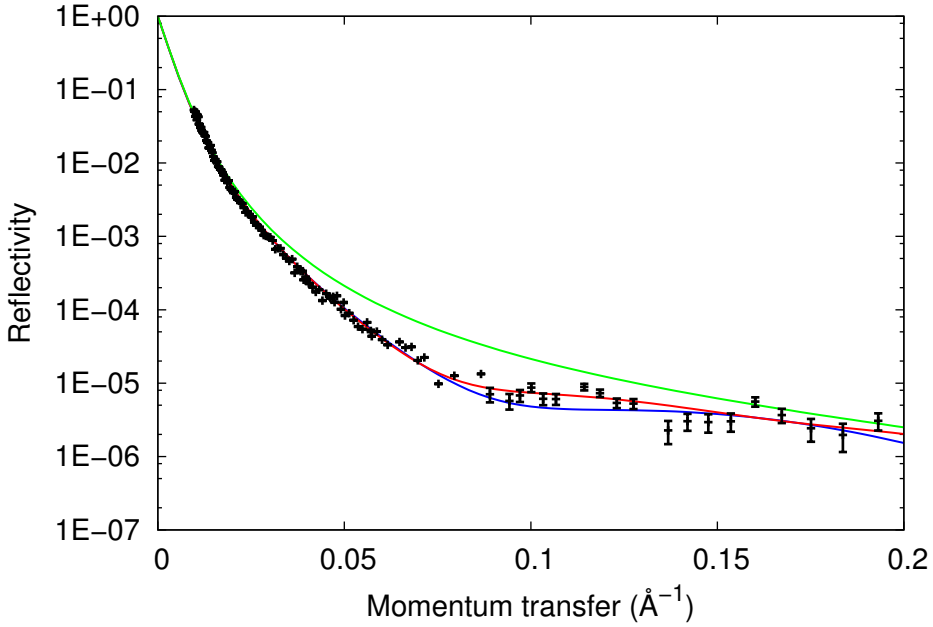

Figure 4.29: Reflectivity profile for anti-α-hCG adsorbed on to a bare silica surface. The red line represents the best fitting two-layer model and the blue line represents the best fitting uniform-layer model. The green line is a reflectivity profile from a bare silica layer of 12 Å.

Parallel reflectivity curves were obtained in different contrasts in order to reduce the ambiguity of the fitted models. Figure 4.29 shows the reflectivity profile for the same antibody sample as measured in H_2O. The reflectivity profile of the experimental data can be seen to deviate from the silica layer (green line), meaning that the antibody had adsorbed to the surface. Although a uniform-layer fit (blue line) provided a reasonable fit to the experimental data, it can be seen to slightly under-fit the data in the momentum transfer range 0.1 Å^{-1} to 0.15 Å^{-1}. The two-layer fit (red line) was able to better fit the experimental data and the parameters extracted from the fit were in excellent agreement with those from the D_2O run, as shown in Table 4.3.

The total surface coverage of the adsorbed antibody film was measured to be 1.71 mg/m^2 in D_2O and 1.69 mg/m^2 in H_2O. The two-layer models for both solvents revealed a denser inner layer (volume fraction 0.32 for D_2O and 0.24 for H_2O) and a more diffuse outer layer (volume fraction 0.12 and 0.11 for D_2O and H_2O respectively). Thus, the antibody arrangement was similar to that of the antibody/HSA/hCG experiment shown in Figure 4.20: most antibodies adsorbed in the flat-on orientation with some molecular overlapping to create a dense inner layer and a diffuse outer layer. The two-layer models for each solvent were used as the basis for the models of the subsequent samples.

0.025 mg/ml of d-HSA was then introduced to the antibody-coated surface and allowed to adsorb before being rinsed with buffer. The reflectivity profiles for the D_2O and H_2O runs are shown in Figure 4.30 and Figure 4.31 respectively. In the same way as for the hydrogenated HSA experiment, two different models were examined to determine where and in which orientation the d-HSA was inserted into the antibody layers.

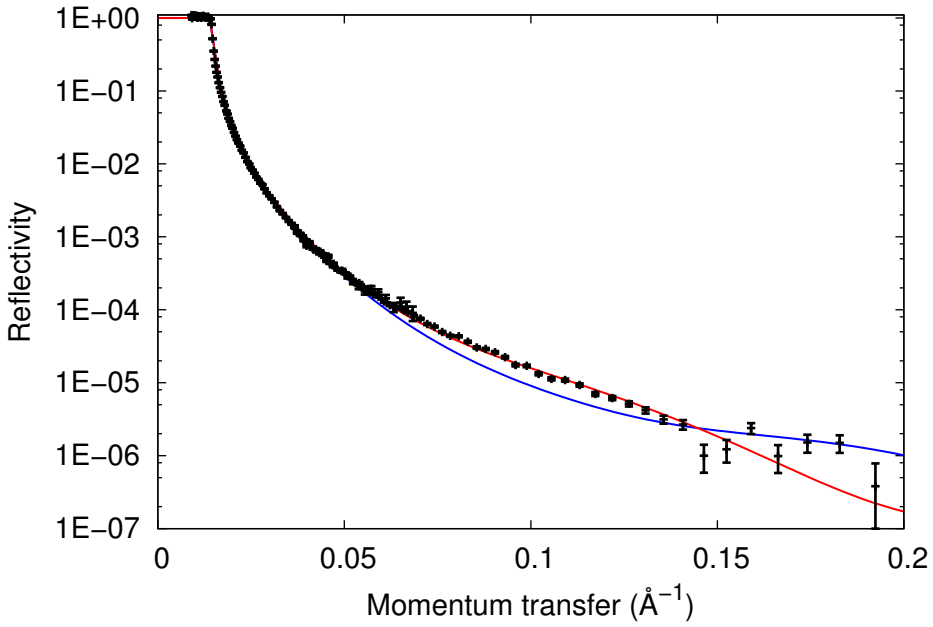

Figure 4.30: Reflectivity profile for d-HSA introduced to the pre-adsorbed anti-α-hCG film. The red line represents the best fitting model where the d-HSA is present in both the inner and outer layers, and the blue line represents the best fitting model where the d-HSA is present in the outer layer only.

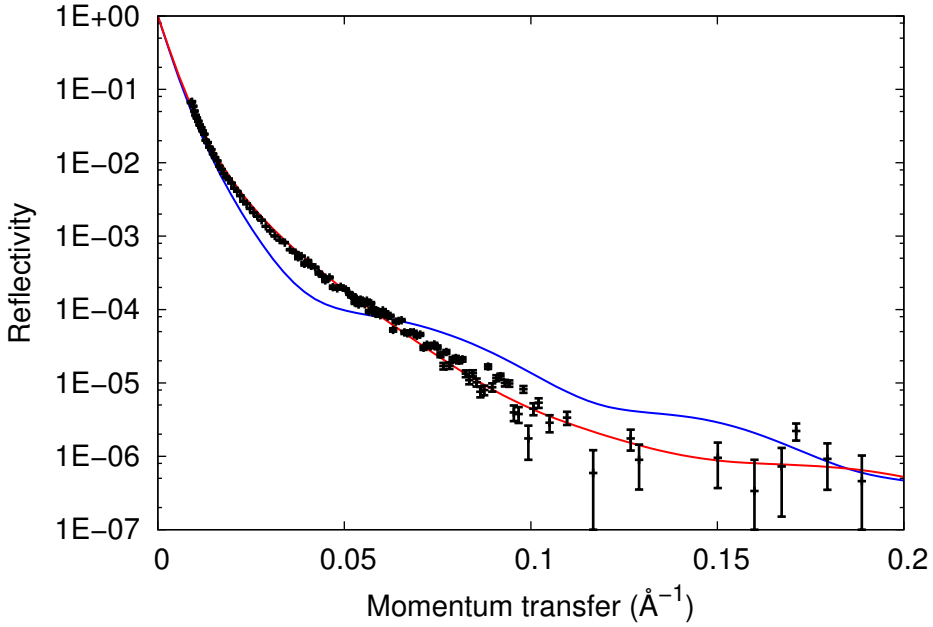

Figure 4.31: Reflectivity profile for d-HSA introduced to the pre-adsorbed anti-α-hCG film. The red line represents the best fitting model where the d-HSA is present in both the inner and outer layers, and the blue line represents the best fitting model where the d-HSA is exclusively present in the outer layer.

The blue lines show the best fit for d-HSA inserted exclusively into the outer layer, as depicted in Figure 4.22, while the red lines are the best fit for d-HSA molecules inserted into both antibody layers, as shown in Figure 4.23. Once again, the model based on the d-HSA molecules being inserted into both antibody layers provided the closest fit to the experimental data. The best-fitting model for both solvents revealed that approximately 1 mg/m^2 of d-HSA was inserted into the inner layer and approximately 0.1 mg/m^2 into the outer layer. This increased the volume fraction of the inner layer by 0.33 and 0.22 for the D_2O and H_2O runs respectively, while the volume fraction of the outer layer increased by 0.02 and 0.03.

The addition of d-HSA resulted in a decrease in the thickness of the inner layer from 2.8 nm to 2.4 nm for the D_2O and from 3.8 nm to 2.8 nm for the H_2O run. However, the combined thickness of the inner and outer layers remained approximately constant for each solvent, the D_2O run saw a decrease from 5.0 nm to 4.7 nm and the H_2O run a decrease from 5.8 nm to 5.5 nm. These thicknesses are close to the length of the short axis of albumin, therefore it would appear that the d-HSA molecules also adsorb in the flat-on orientation between the flat-on adsorbed antibodies to create a thin layer of high volume fraction. Where the spaces between the antibody molecules are of insufficient size for the d-HSA molecules to adsorb, only part of the d-HSA molecule may adsorb to the surface, while the rest of the molecule overlaps the other d-HSA and antibody molecules to create an outer layer of low volume fraction.

It is worth noting that the addition of d-HSA to the antibody layer caused the scattering length density for the D_2O run to increase, from 5.40 $\times 10^{-6}$ Å^{-2} to 5.90 $\times 10^{-6}$ Å^{-2} for the inner layer and from 6.00 $\times 10^{-6}$ Å^{-2} to 6.03 $\times 10^{-6}$ Å^{-2} for the outer layer. Typically, for D_2O runs, an increase in the scattering length density that is towards the scattering length density of D_2O (6.25 $\times 10^{-6}$ Å^{-2}) would suggest that the adsorbed sample had been removed from the surface and replaced with pure D_2O. However, the scattering length density of the d-HSA was higher than D_2O and would have caused the scattering length density of the layer to increase if d-HSA was inserted into the layer. The insertion of d-HSA was confirmed by the H_2O run, which detected an increase in the scattering length density of the layer (away from the negative scattering length density of H_2O) when d-HSA was added to the antibody-coated block.

Figure 4.32 shows how the surface coverage of the blocking albumin (BSA for the DPI experiments and either HSA or d-HSA for the NR experiments) varied with antibody surface coverage when measured by NR and DPI. Both techniques revealed that the surface coverage of the albumin decreased with increased antibody surface coverage. If the albumin settled on the antibody, as in Figure 4.22, then the albumin surface coverage would not be expected to show this trend. The reduction in albumin surface coverage at higher antibody surface coverage suggests that antibody molecules occupied the silica surface at the expense of albumin molecules. Thus, the trend shown in Figure 4.32 provides further evidence that albumin slots into the spaces on the surface between the

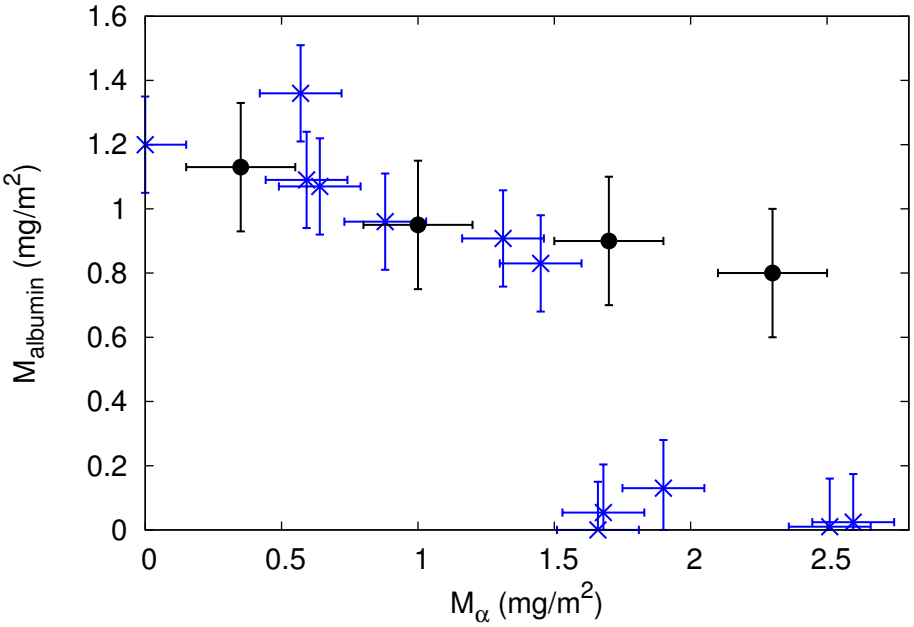

Figure 4.32: Adsorbed albumin surface coverage as a function of antibody surface coverage as measured by DPI (blue crosses) and NR (black circles).

antibody molecules, as shown in Figure 4.23.

Although the same trend was observed by DPI and NR, Figure 4.32 shows that the reduction in albumin surface coverage was substantially larger when measured by DPI, instead of NR, for antibody surface coverages greater than 1.5 mg/m^2. One possible explanation for this is that the duration of the buffer wash was significantly longer for the DPI experiments than the NR experiments: 10 minutes for NR and typically more than 30 minutes for DPI. The increased duration of the buffer wash may have removed more of the adsorbed BSA molecules, particularly the molecules that had a small footprint, and consequently small binding force, on the surface.

After the d-HSA measurements, 0.002 mg/ml of hCG was introduced and allowed to settle for 1 hour before a buffer wash was performed. Reflectivity profiles for the D_2O and H_2O runs are shown in Figure 4.33 and Figure 4.34 respectively. The blue lines are for a model that assumes that hCG is bound exclusively to antibody Fabs in the outer layer and the red lines for a model that allows for hCG to bind to antibody Fabs in either the inner or outer layer. For both solvents the latter model, with similar parameters, was the only one able to adequately fit the experimental data.

Unlike the antibody/HSA/hCG assay, which showed that hCG was inserted into the inner layer only, the best fitting model for the antibody/d-HSA/hCG assay revealed that hCG was inserted into both the inner layer and the outer layer. After the introduction of hCG, the D_2O and H_2O runs both saw an increase in the surface coverage of approximately 0.2 mg/m^2 that was evenly distributed between the inner and outer layers. This interfacial structure would result from either; hCG binding to antibody Fabs in either layer, or that the hCG molecules bind to antibody Fabs in the inner layer and are aligned

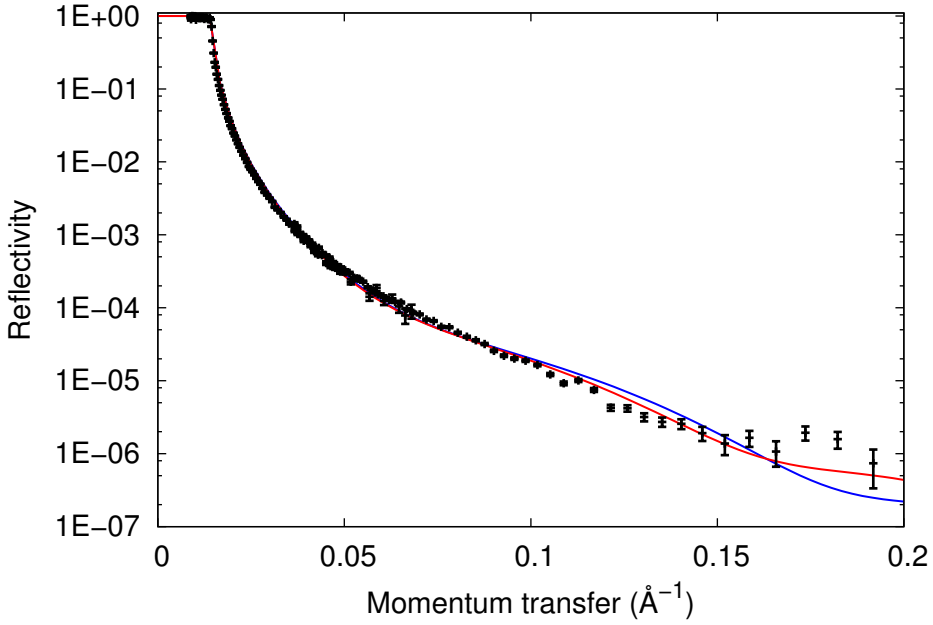

Figure 4.33: Reflectivity profile for hCG introduced to the pre-adsorbed anti-α-hCG/d-HSA mixed film. The red line represents the best fitting model where the hCG is present in both the inner and outer layers, and the blue line represents the best fitting model where the hCG is only present in the outer layer.

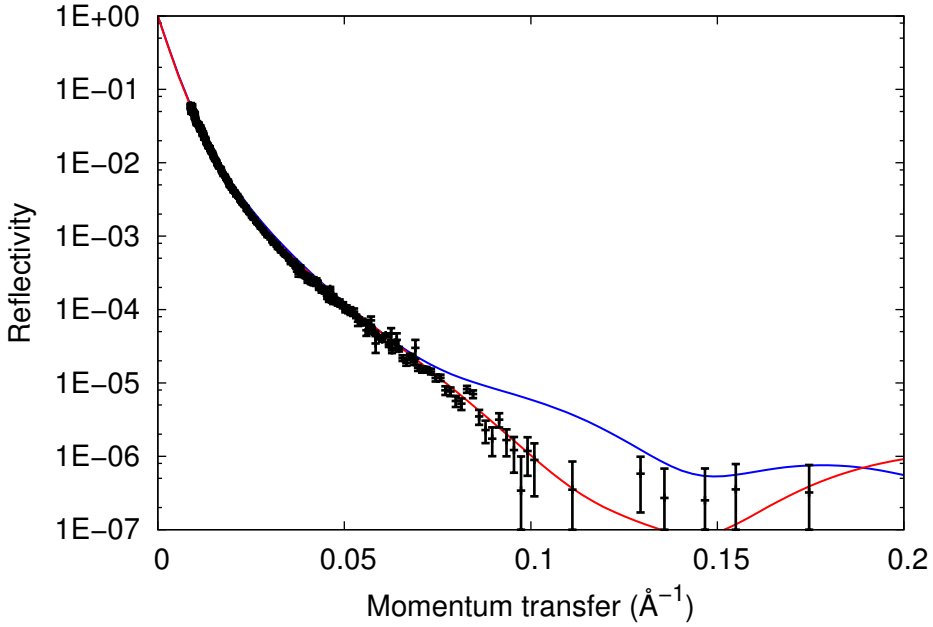

Figure 4.34: Reflectivity profile for hCG introduced to the pre-adsorbed anti-α-hCG/d-HSA mixed film. The red line represents the best fitting model where the hCG is present in both the inner and outer layers, and the blue line represents the best fitting model where the hCG is only present in the outer layer.

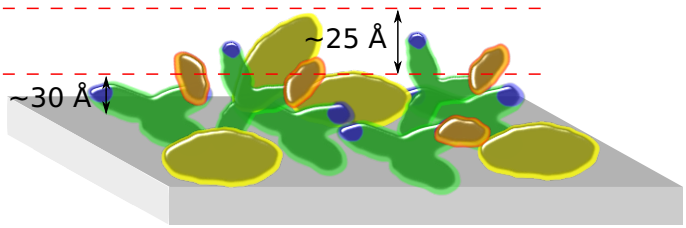

Figure 4.35: Diagram to show how hCG molecules could bind to create an even distribution of hCG molecules in the inner and outer layers.

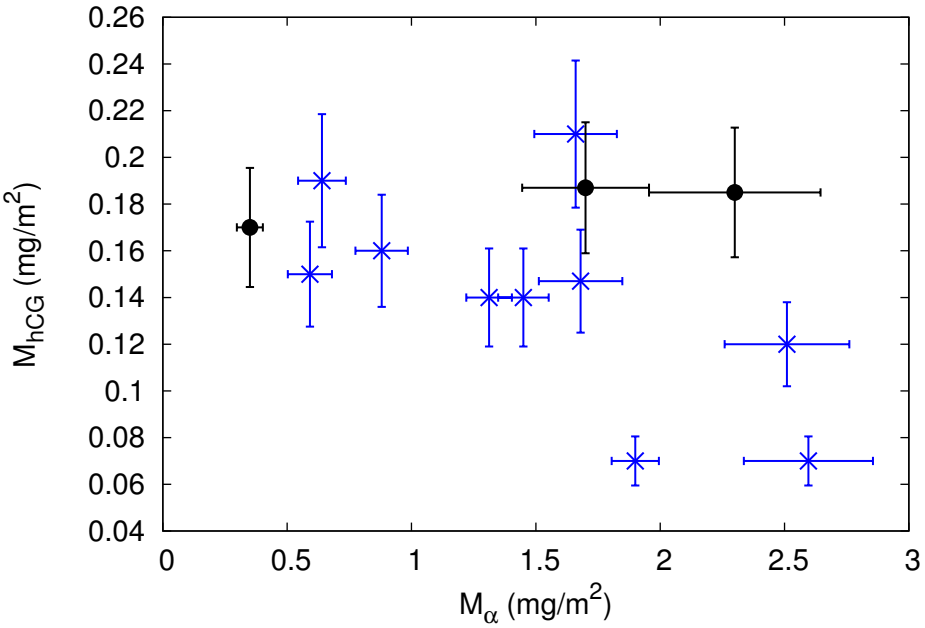

Figure 4.36: hCG surface coverage as a function of anti-α-hCG surface coverage as measured by DPI (blue crosses) and NR (black circles).

so that their long axis is pointed away from the surface and into the outer layer, as shown in Figure 4.35.

4.4.4 Antibody/antigen binding

Figure 4.36 shows that the hCG adsorbed amount was measured to be largely independent of the antibody surface coverage for the DPI and NR experiments. At high, medium and low antibody surface coverage the amount of hCG that was bound to the antibody Fabs remained approximately constant at 0.17 mg/m^2, as seen by Zhao et al for the hPSA antibody and its antigen [68, 126]. However, Figure 4.37 shows that the hCG binding ratio, defined as the number of bound hCG antigen molecules per antibody molecule, can be seen to rapidly decrease with increased antibody surface coverage, even though the antigen was available in excess. These findings suggest that a significant number of antibody Fabs are no longer available to bind to the hCG at higher surface coverages. This phenomenon was previously observed by Xu et al [44] for anti-β-hCG/hCG, who showed that the experimental parameter with the largest effect on the antigen binding ratio was

Table 4.3: Parameters extracted from NR data for an antibody/d-HSA/hCG immunoassay using the best fitting model and the optical matrix method.

Solvent	Sample	Layer no.	Thickness, τ (nm)	SLD, ρ ($\times 10^{-6}$Å^{-2})	Volume fraction, $\phi_\alpha, \phi_{\text{d-HSA}}, \phi_{\text{hCG}}$ ± 0.001	Surface coverage, $M_\alpha, M_{\text{d-HSA}}, M_{\text{hCG}}$ (± 0.05 mg/m^2)	Total surface coverage, M_{total} (± 0.05 mg/m^2)
D_2O	α	1	2.8 ± 0.4	5.40 ± 0.05	0.32, 0, 0	1.33, 0, 0	1.71
		2	2.2 ± 0.4	6.00 ± 0.05	0.12, 0, 0	0.38, 0, 0	
	α, d-HSA	1	2.4 ± 0.4	5.90 ± 0.05	0.32, 0.33, 0	1.33, 1.06, 0	2.83
		2	2.3 ± 0.4	6.03 ± 0.05	0.12, 0.02, 0	0.38, 0.06, 0	
	α, d-HSA, hCG	1	2.9 ± 0.4	5.80 ± 0.05	0.32, 0.33, 0.03	1.33, 1.06, 0.08	3.00
		2	2.6 ± 0.4	5.90 ± 0.05	0.12, 0.02, 0.04	0.38, 0.06, 0.09	
H_2O	α	1	3.8 ± 0.4	0.00 ± 0.05	0.24, 0, 0	1.36, 0, 0	1.69
		2	2.0 ± 0.4	-0.30 ± 0.05	0.11, 0, 0	0.33, 0, 0	
	α, d-HSA	1	2.8 ± 0.4	1.50 ± 0.05	0.24, 0.22, 0	1.91, 0.84, 0	2.64
		2	2.7 ± 0.4	-0.10 ± 0.05	0.11, 0.03, 0	0.33, 0.11, 0	
	α, d-HSA, hCG	1	3.0 ± 0.4	1.60 ± 0.05	0.24, 0.22, 0.04	1.91, 0.84, 0.10	2.84
		2	2.5 ± 0.4	0.02 ± 0.05	0.11, 0.03, 0.05	0.33, 0.11, 0.10	

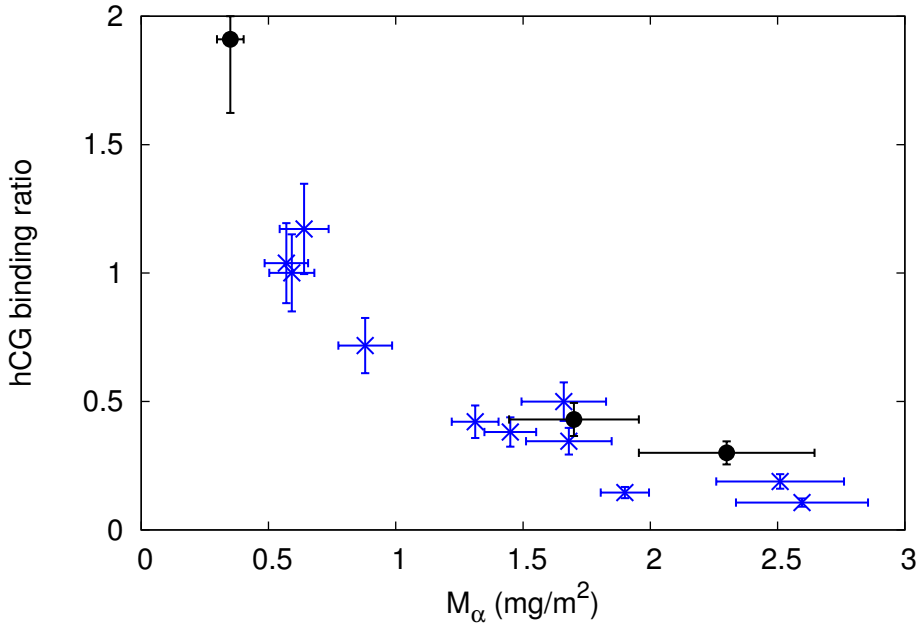

Figure 4.37: hCG binding ratio as a function of anti-α-hCG surface coverage as measured by DPI (blue crosses) and NR (black circles).

the surface packing density of the antibody. The effect was attributed to the antibody Fabs being in such close proximity to other molecules that they were rendered inaccessible to the antigen.

For commercial immunoassays, these findings suggest that there is no advantage in increasing the antibody surface coverage above a certain level. Further adsorption of antibodies is unnecessary as the antibody Fabs are not accessible for the antigen to bind to and, as such, offer no increase in the sensitivity of the immunoassay. Thus, considerable financial savings could be achieved by using only the minimum amount of (often expensive) antibodies necessary to achieve the optimum antibody surface coverage for a given substrate. The antibody history dependence data also show that the amount of time before BSA adsorption has an effect on the structure of the antibody layer. To prevent the formation of antibody clusters, which may reduce the number of Fabs accessible to the hCG molecules, it may be better to adsorb the BSA as quickly as possible after the antibody adsorption step. Further experiments are needed to see what effect this has on the antibody/antigen binding ratio.

4.5 Conclusions

Simplified pregnancy immunoassays were constructed on silica and silicon-oxynitride surfaces and investigated with DPI and NR. DPI showed that both the surface coverage and thickness of the adsorbed anti-α-hCG antibody increased with bulk antibody concentration. For the studied bulk concentrations, the antibody adsorption closely followed the Langmuir adsorption model.

BSA adsorption onto a surface with a pre-adsorbed antibody film was used to investigate the history dependence of the antibody film. It was found that a pre-adsorbed antibody film accelerated the rate of BSA adsorption when compared to BSA adsorption onto an empty surface. This effect was attributed to the formation of antibody clusters on the surface.

Both DPI and NR provided evidence of BSA/HSA insertion into the gaps on the surface between the antibody molecules. This suggests that albumin is an excellent blocking agent. Control experiments also showed that, at sufficient concentrations, BSA can reduce non-specific hCG adsorption to negligible amounts.

The antibody/antigen binding ratio was also investigated with both techniques. It was found that the total amount of adsorbed antigen was independent of the antibody surface coverage and remained constant at approximately $0.17\,\mathrm{mg/m^2}$. However, the antibody/antigen molar binding ratio was dramatically reduced at high antibody surface coverage. This was likely due to the close proximity of the antibody Fabs to other adsorbed molecules, which would have rendered the Fabs inaccessible to the antigen molecules. The results imply that above a certain antibody surface coverage there is no advantage in the adsorption of more antibody molecules, as their Fabs can not be accessed by the antigen molecules.

CHAPTER

FIVE

MAGNETIC TWEEZERS

5.1 Overview

Magnetic tweezers were designed and built to investigate the interaction between the hCG antigen and its antibodies. This chapter offers a detailed discussion of the design of the magnetic tweezers, in particular the pole piece, which was required to produce a homogeneous magnetic field over a viewing area of sufficient size to observe several hundred magnetic beads. The completed magnetic tweezer system was used to estimate the upper and lower values of the binding force between the hCG antigen and its antibodies as well as the interaction length and the dissociation constant.

5.2 Introduction

In Chapter 4 DPI and NR were used to probe the interfacial structure of adsorbed antibodies and the corresponding effects on the antibodies' specific binding with an antigen. However, both DPI and NR are only able to reveal limited information about the interaction dynamics of antibody/antigen binding. Various techniques have been used to fill in these gaps and investigate the specific binding force between antibodies and antigens and other ligand/receptor interactions, which is of great importance to the development of immunoassays and other diagnostics [127]. Such techniques include: flow chambers [128, 129], AFM [49, 130, 131] and micro-pipettes [50]. Although these techniques are exquisitely sensitive they often rely on the measurement of a single molecule, which necessitates numerous repetitions of the experiment in order to obtain satisfactory statistics.

With the relatively new technique of magnetic tweezers, it is possible to perform hundreds of highly sensitive measurements in parallel [132,133]. Useful data can therefore be obtained at a more rapid pace. In a typical magnetic tweezers experiment, ligand/receptor bonds are used to anchor hundreds of small (diameter $< 10\,\mu$m) paramagnetic beads to an optically transparent surface. A microscope and camera are then used to record the movement of beads at the surface as a function of the force experienced by the beads. The

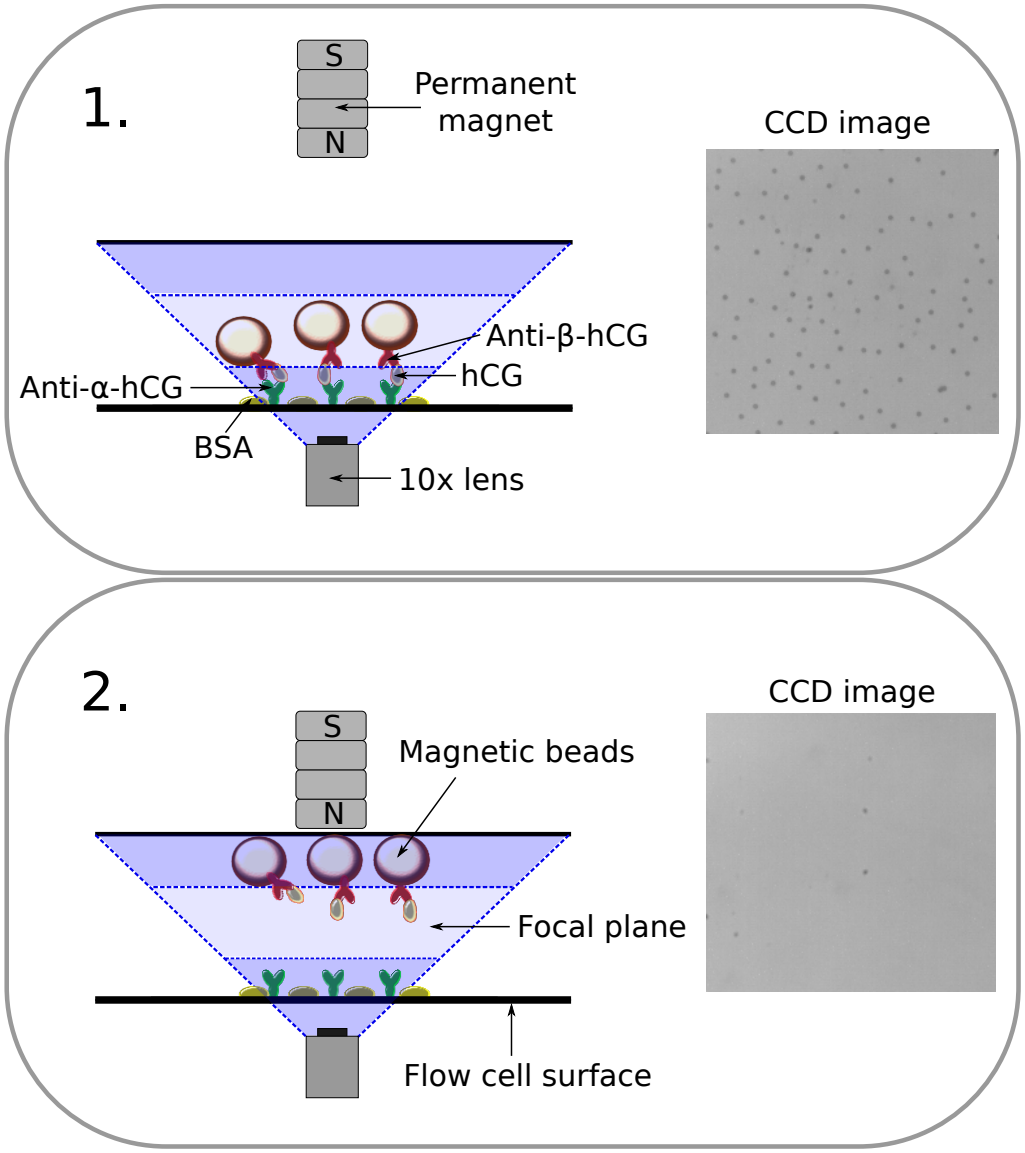

Figure 5.1: Schematic diagram of a magnetic tweezers experiment. **Panel 1.** The antibody/antigen coated beads are allowed to settle and the hCG is bound to the surface adsorbed antibodies to produce a linkage that anchors the bead. The lens is adjusted until the beads are in the focal plane. **Panel 2.** The force on the beads is increased by moving the permanent magnet closer. Eventually the upwards force will become sufficient to overcome the binding force of the antibody/antigen pairs and the immuno-linked beads will be removed from the focal plane. A camera is used to record the number of beads as a function of time and force.

force experienced by the paramagnetic beads is provided by the magnetic field of either a permanent magnet or an electro-magnet [77]. A schematic diagram of a magnetic tweezers system is shown in Figure 5.1. In the depicted experiment antibody coated beads are immuno-linked to an antibody coated surface through hCG antigen molecules.

The information offered by magnetic tweezers is able to complement the antibody/antigen binding data shown in Chapter 4, however, at the time of writing, there were few commercially available magnetic tweezer systems. Instead, a new magnetic tweezer system was designed and constructed. The design and the results obtained are discussed in detail

over the following pages.

5.3 Design

In order to rapidly produce useful data over a large range of forces, the magnetic tweezer apparatus was required to meet the following criteria:

1. Produce a magnetic field large enough to exert a force range of between 0.001 pN and 500 pN on the paramagnetic beads.
2. The force experienced by the paramagnetic beads must be perpendicular to the experimental surface and of high accuracy.
3. The exerted force must be constant for all of the imaged beads over several minutes and must be able to be varied with a high degree of accuracy.
4. Provide parallel imaging of several hundred beads at once in order to provide meaningful statistics.
5. The experimental surface must be optically transparent, to allow for positioning of both magnet and microscope, and able to be reproducibly coated with antibodies and other proteins.

The magnetic tweezer design was built on an Olympus IX 71 inverted microscope. The microscope's condenser pillar was replaced with a new pillar that was custom built to support a ThorLabs LTS150 linear travelling stage (Thorlabs Ltd., Ely, UK), as shown in Figure 5.2. A magnet, used to exert a force on the beads, was mounted on to the travelling stage. The force on the beads was varied by moving the magnet towards and away from the beads by use of the travelling stage, which had a range of 150 mm and a precision of 2 μm.

Although an electromagnet would have allowed for the magnetic field to be varied with current it was found that high currents (>1 A) were required to produce magnetic fields large enough to probe the desired force range. Such high currents were unsustainable for periods of time longer than 1 minute due to the heat produced in the coil. This was not long enough to complete an experiment. Instead, a permanent magnet was selected for the final design. The magnet and pole piece are discussed further in Section 5.3.1.

The imaging was performed by a Photron Fastcam 1024 PCI CCD camera (Photron Europe Ltd., West Wycombe, UK) that was illuminated with a blue LED. A graticule, shown in Figure 5.3, was used to measure the pixel size of the camera. Each pixel was found to have a length of 1.07 ± 0.01 μm, which meant that the total viewing area was 1100×1100 μm, sufficient to view up to 800 beads when viewed with a 10 $\times$ magnification lens.

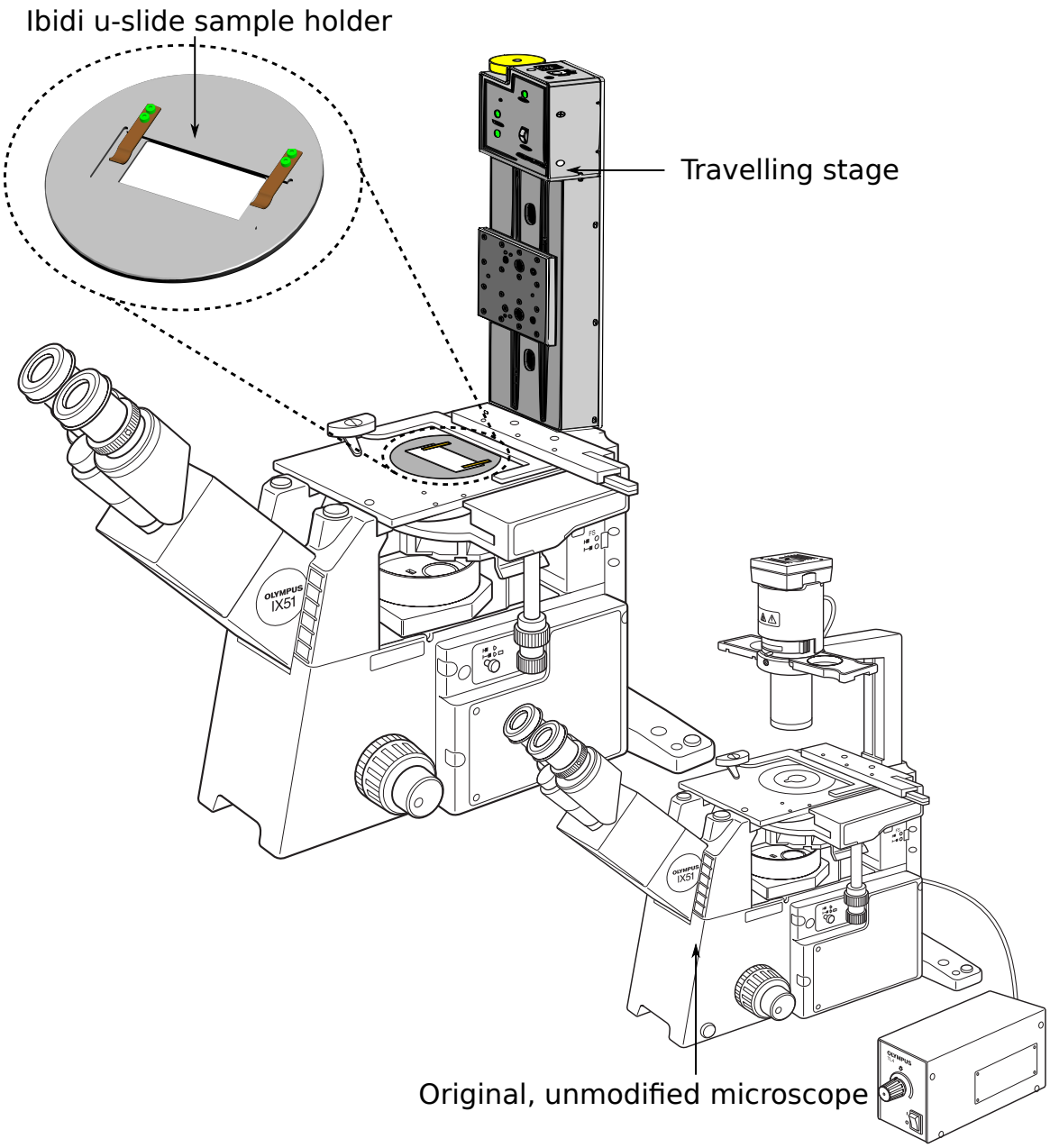

Figure 5.2: Schematic diagram of the magnetic tweezer apparatus. The original condenser pillar was replaced with a custom-built pillar that could support the linear traveling stage.

A sample holder was designed to secure the sample wells above the objective lens. The sample wells were uncoated Ibidi μ-slides (Ibidi GmbH, Martinsried, Germany). The slides were hydrophobic with a contact angle of close to 90° and were made from a polyethylene (PE) derivative. The Ibidi slides were chosen over conventional microscope slides as their inlet and outlet pipes permitted samples and buffers to be easily flowed over their surface. As discussed in Section 5.4, the adsorbed samples required copious amounts of buffer rinsing, this would have been difficult to perform on conventional microscope slides.

M270 Dynabeads (Life Technologies Ltd., Paisley, UK) with carboxylic acid coated surfaces were selected for experimental use. The M270 beads are superparamagnetic

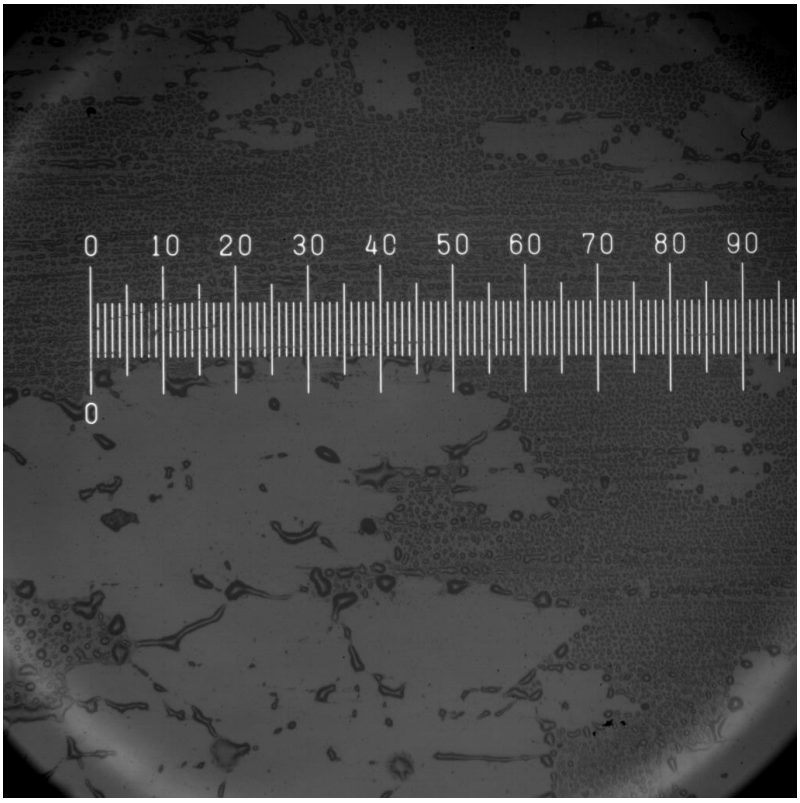

Figure 5.3: Image of graticule through a 10x lens. Each graticule division corresponds to 0.01 mm.

and therefore rapidly magnetise in the presence of a magnetic field. In addition they only saturate at high magnetic field strengths (> 900 mT), meaning that a large range of forces could be exerted on them (since force is proportional to magnetic field strength). Unlike other beads, the M270 beads are highly monodisperse. The manufacturer claim that the beads deviate from the average volume by a maximum of only 3%, which causes only a 3% uncertainty in the force, as calculated by Equation (2.3.1). The beads also have a uniform distribution of superparamagnetic nano-particles [134], which also acts to minimise the uncertainty in the calculated force.

5.3.1 Magnet pole piece

As previously discussed, the magnetic tweezers were required to produce a strong vertical force (> 100 pN) with a constant magnitude over the viewing area. Finite element method magnetics (FEMM) software [135] was used to model different shaped pole pieces and the magnet geometry. Two permanent magnet designs are presented here: a flat pole piece and a pointed pole piece. A pointed pole piece was chosen for consideration, because it was predicted to have a steep magnetic field gradient, and hence be capable of producing a large force, as predicted by Equation (2.3.1). Although a flat pole piece would not be able to produce as large a force as a pointed pole piece, it would produce a more uniform magnetic field and was therefore also considered for the final design.

A 2-dimensional cross section of the two pole piece designs is shown in Figure 5.4.

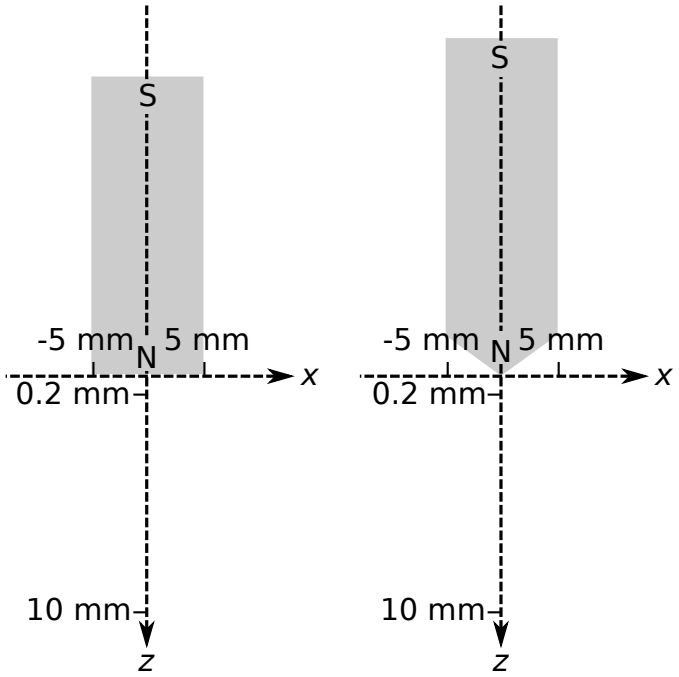

Figure 5.4: 2-dimensional cross-section of the flat (left) and pointed (right) pole pieces with labelled z and x-axes. The y-axis is not shown but is directed into the page. The magnetic flux density was scanned along the z-axis (Figure 5.7) and along the x-axis at $z = 0.2$ mm (Figure 5.9) and at $z = 10$ mm (Figure 5.10).

Each magnet was symmetric about the z-axis with the tip of the pole piece at $z = 0$ mm, $x = 0$ mm. The magnets would be moved along the z-axis towards the sample to vary the force in the z-direction ($\mathbf{F_z}$). The modeled magnets were based on commercially available NdFeB permanent cylindrical magnets of length 20 mm and diameter 10 mm. Since NdFeB is too brittle to shape, the pointed pole piece was formed by attaching a 4 mm long conical mu-metal pole piece to the cylindrical magnet. The FEMM software produced magnetic flux density plots for the pointed and flat pole pieces, as seen in Figure 5.5 and Figure 5.6 respectively.

The z-component of the magnetic flux density ($\mathbf{B_z}$) of each pole piece was calculated at 150 points along the z-axis, between $z = 0$ mm and $z = 30$ mm. The calculated flux densities are shown in Figure 5.7. Although the flat pole piece can be seen to have a greater peak flux density compared to the pointed pole piece (375 mT compared to 320 mT), the pointed pole piece produced a steeper magnetic flux density gradient.

Figure 5.8 shows the calculated vertical force on the M270 beads as a function of magnet distance for the flat and pointed pole pieces. The force was calculated using Equation (2.3.1). The steep magnetic field gradient created by the pointed pole piece was able to create a peak vertical force of 300 pN while the flat pole piece had a peak vertical force of only 120 pN. However, the force produced by the pointed pole piece decreased rapidly with the distance from the magnet when compared to the flat pole piece. Although the two pole pieces are able to probe the same force range, the pointed pole piece can be seen to be more sensitive to the z-position of the magnet and would be required to operate in a smaller z-range. Thus, the pointed pole piece would produce a larger uncertainty in

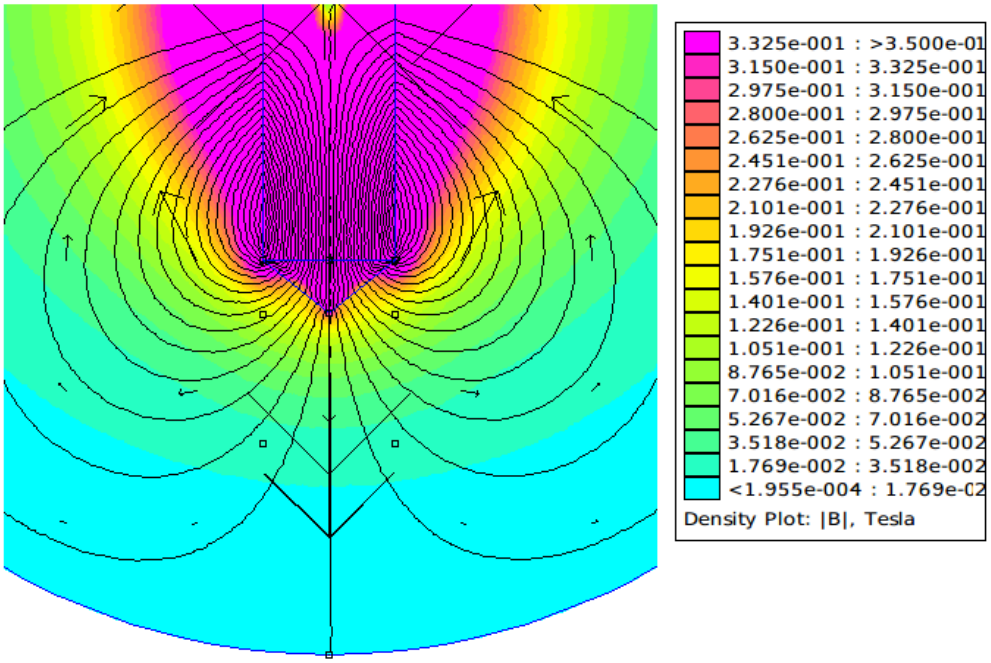

Figure 5.5: Magnetic flux density plot for a 20 mm long neodymium magnet with a pointed mu-metal pole piece. The black lines represent the flux lines and the arrows show the field vectors.

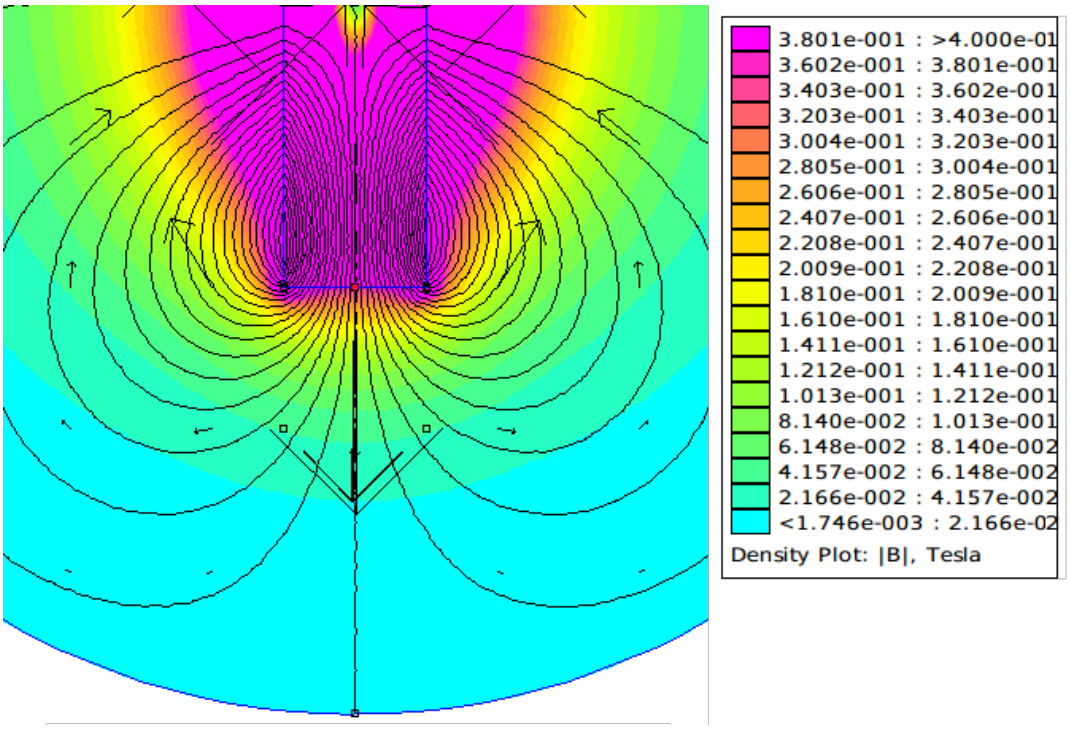

Figure 5.6: Magnetic flux density plot for a 20 mm long neodymium magnet with a flat pole piece. The black lines represent the flux lines and the arrows show the field vectors.

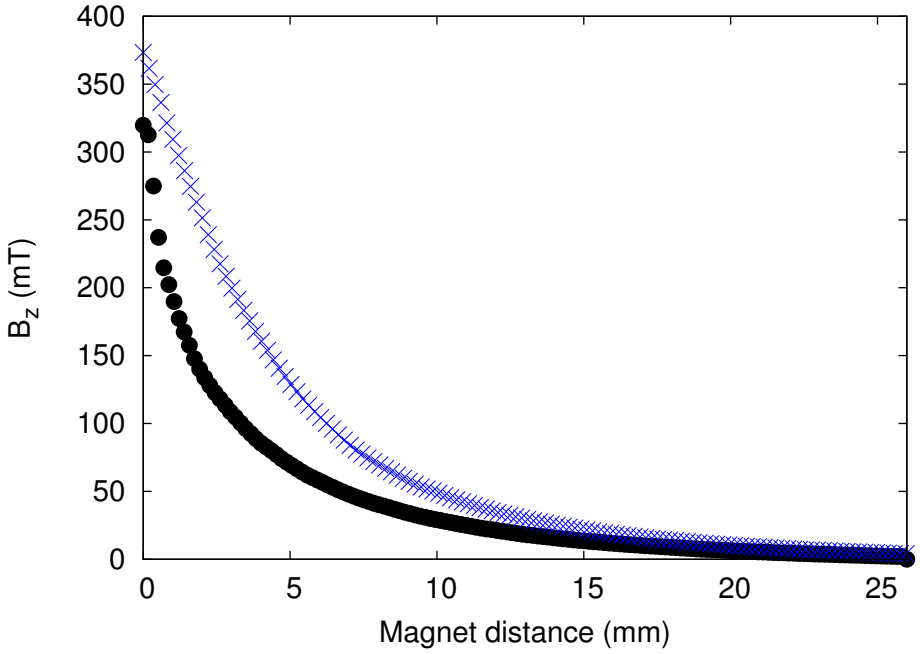

Figure 5.7: Magnetic flux density in the z direction as a function of distance from the magnet. The black circles are for the pointed pole piece and the blue crosses for the flat pole.

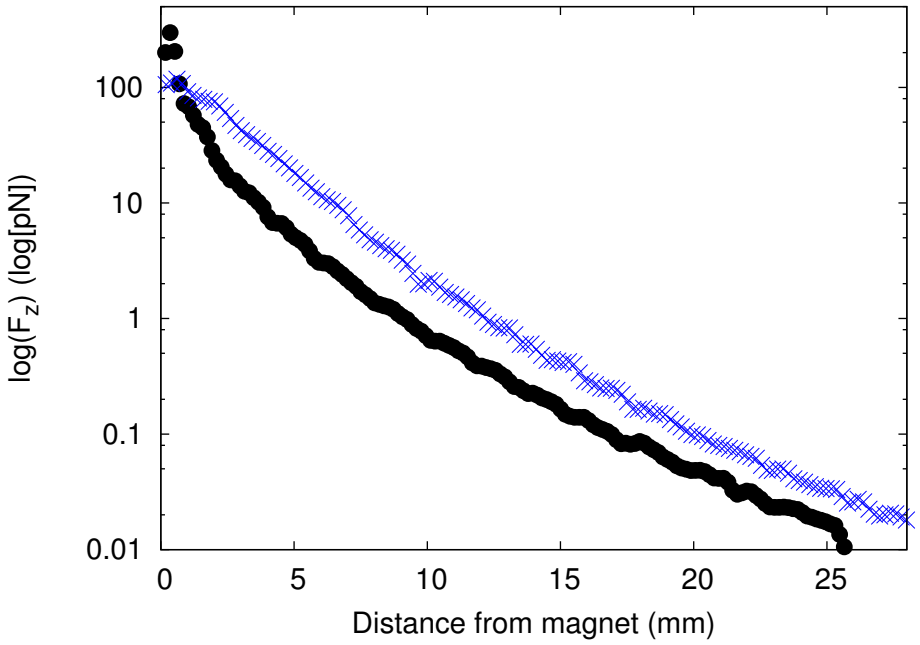

Figure 5.8: Vertical force as a function of distance from the magnet for the pointed pole piece (black circles) and flat pole piece (blue crosses).

the vertical force, $\mathbf{F_z}$.

For the tweezer experiments, beads would be studied in a microscope viewing area of approximately 1 mm^2. The value of $\mathbf{B_z}$ was therefore required to be approximately constant over this area so that a constant force could be applied to the studied magnetic beads. In order to test the uniformity of $\mathbf{B_z}$ along the x-axis, the magnitude of $\mathbf{B_z}$ was

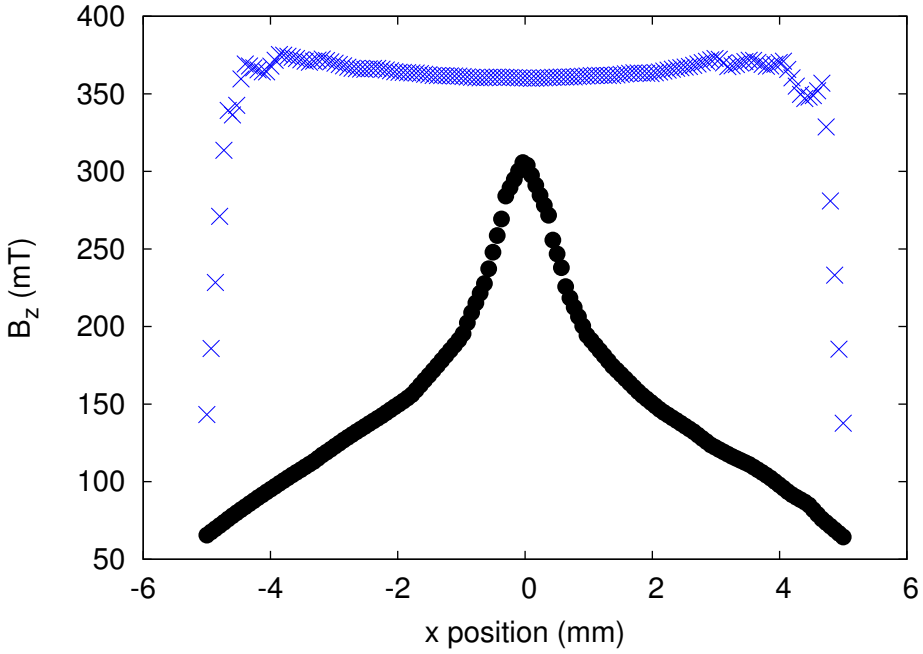

Figure 5.9: Magnetic flux density in the z-direction at different points along the x-axis. The black circles are for the pointed pole piece and the blue crosses for the flat pole. The values were calculated at a distance 0.2 mm from the pole pieces along the z-axis.

calculated along the width of the magnets, between x = -5 mm and x = 5 mm. This was done at z = 0.2 mm and at z = 10 mm, as indicated in Figure 5.4. The results obtained at z = 0.2 mm and at z = 10 mm are shown in Figure 5.9 and Figure 5.10 respectively.

Figure 5.9 clearly shows that the flat pole piece gives a more uniform value of $\mathbf{B_z}$ along the x-axis than the pointed pole piece. Even over a range of 1 mm, which is equal to the length of the viewing area, the pointed pole piece shows a large variation in $\mathbf{B_z}$. The flat pole piece can be seen to remain at approximately 360 mT between x = -4 mm and x = 4 mm, almost the entire diameter of the magnet. The uniformity of $\mathbf{B_z}$ at x = 10 mm over the diameter of the magnet for the flat pole piece can be seen in Figure 5.10 to have been lost and is approximately equal to the uniformity offered by the pointed pole piece. Thus, the flat pole piece loses its main advantage when the magnet/sample separation is increased, although the field strength is still higher than the pointed pole piece.

A final comparison of the pole pieces is shown in Figure 5.11, which shows the modulus of the percentage difference between $\mathbf{F_z}$ at x = 0 mm and $\mathbf{F_z}$ at x = 0.5 mm along the z-axis. The position x = 0.5 mm was chosen as this is equal to the width of the viewing area: 1 mm, which means that magnetic beads at either edge of the viewing area are 0.5 mm from the center of the pole piece. Hence, the percentage difference represents the maximum variation in the force experienced by the magnetic beads. Although the average difference for the pole pieces were found to be similar, $2 \pm 8\%$ for the flat pole and $2 \pm 20\%$ for the pointed pole, the pointed pole showed differences as high as 75% at $z < 2$ mm.

Although the pointed pole piece was able to probe a larger force range than the flat

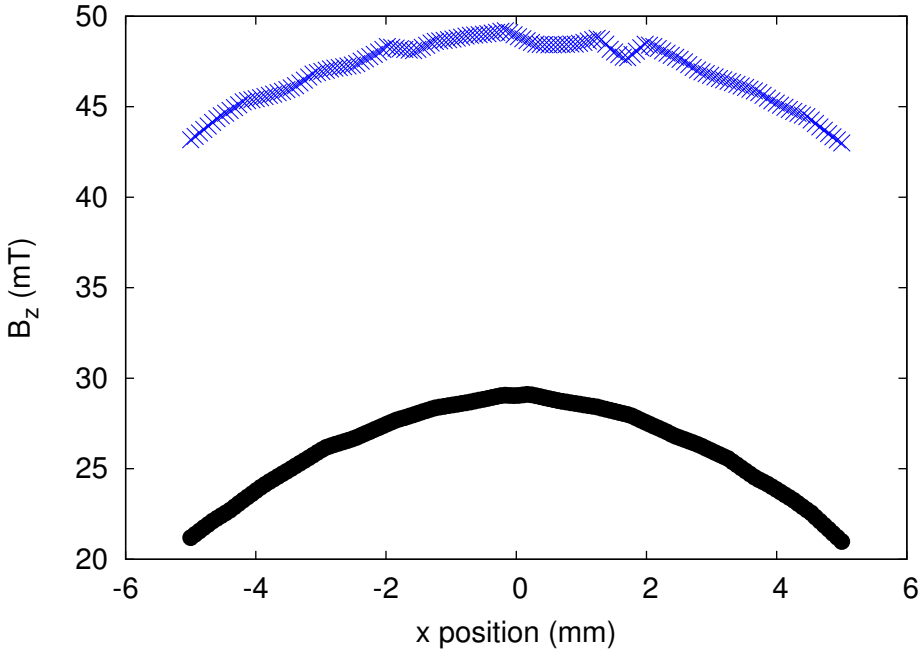

Figure 5.10: Magnetic flux density in the z-direction at different points along the x-axis. The black circles are for the pointed pole piece and the blue crosses for the flat pole piece. The values were calculated at a distance 10 mm from the pole pieces along the z-axis.

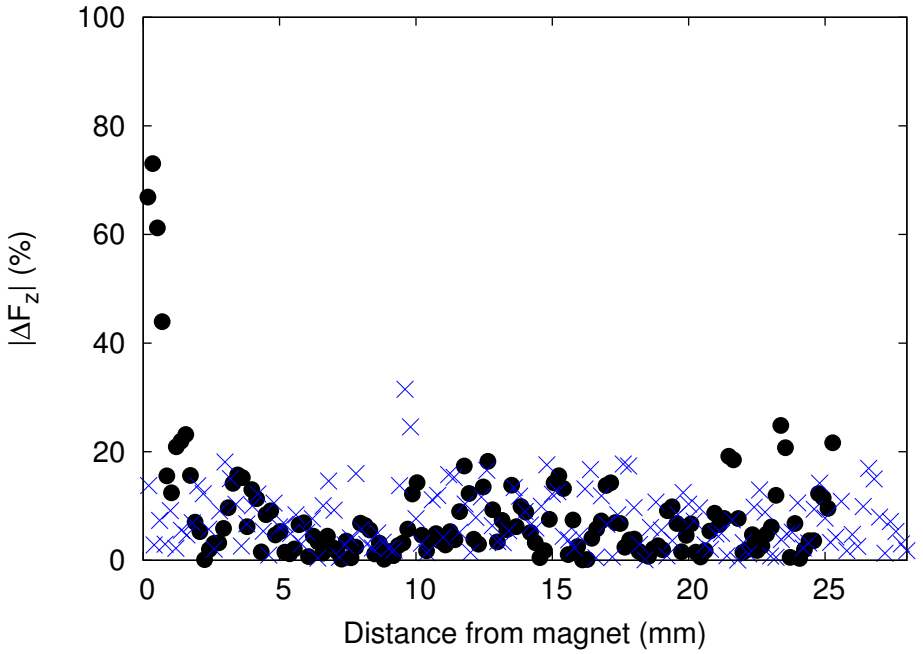

Figure 5.11: Graph to show the percentage difference in vertical force between positions $x = 0$ mm and $x = 0.5$ mm as a function of distance from the magnet for the pointed pole piece (black circles) and flat pole piece (blue crosses).

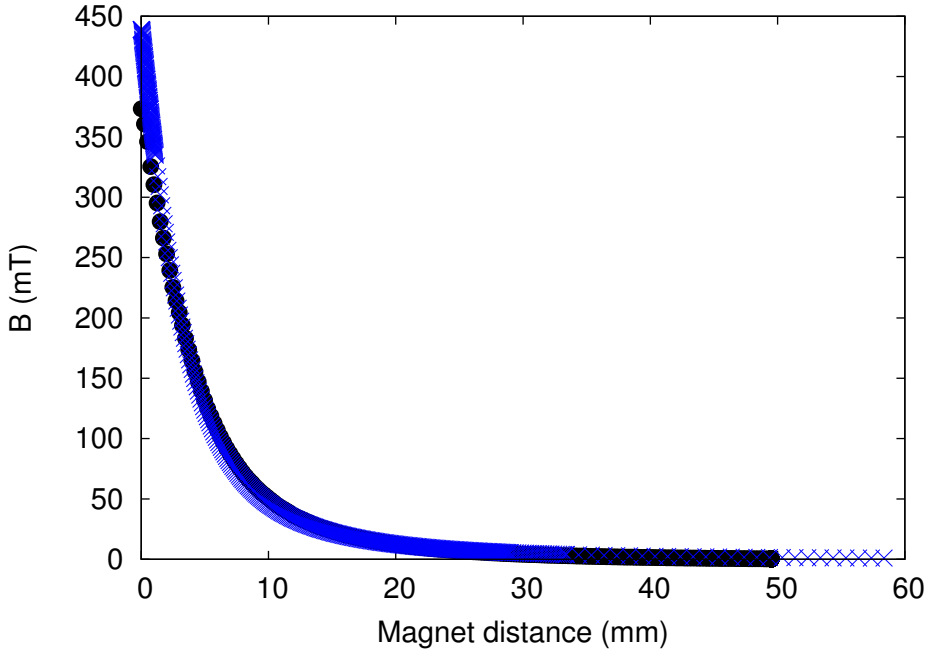

Figure 5.12: B field as a function of distance from the magnet. The blue crosses represent experimental data that were obtained with a GM10 Hall probe and the black circles were obtained by FEMM theoretical analysis.

pole piece, the degree of non-uniformity in $\mathbf{B_z}$ and $\mathbf{F_z}$ along the x-axis was not suitable for the microscope's 1 mm^2 viewing area. Instead, the flat pole piece was selected for the final design as it produced more uniform values of $\mathbf{B_z}$ and $\mathbf{F_z}$ over the viewing area. However, this uniformity came at the expense of a lower magnetic field gradient and peak $\mathbf{F_z}$, compared to the pointed pole piece.

5.3.2 Force calibration

The magnet used for the force spectroscopy experiments detailed in this chapter was constructed from four NdFeB cylindrical magnets. Each magnet was 10 mm in diameter and 5 mm in height. The four magnets were poled and stacked along the z-axis to create a cylindrical magnet 10 mm in diameter and 20 mm in height. Stacking the magnets in this way increased the magnetic field strength at the pole, however, increasing the number of magnets above four offered no further increase in the magnetic field strength.

The magnetic field of the magnet stack was measured at different points along the z-axis in order to calibrate the vertical force applied to the magnetic beads. The results are shown in Figure 5.12, where the black circles represent data obtained from the FEMM analysis and the blue crosses from measurements of the magnetic field with a GM08 gaussmeter (Hirst Magnetic Instruments, Ltd. Falmouth, UK). Good agreement can be seen between the theoretical and experimental data, although the data from the two methods diverge at magnet distances of less than 3 mm. The FEMM analysis predicted a maximum field strength of 373 mT while the maximum field strength was measured to be 439 mT. A possible explanation for this is that the hall probe measured the x, y and z-

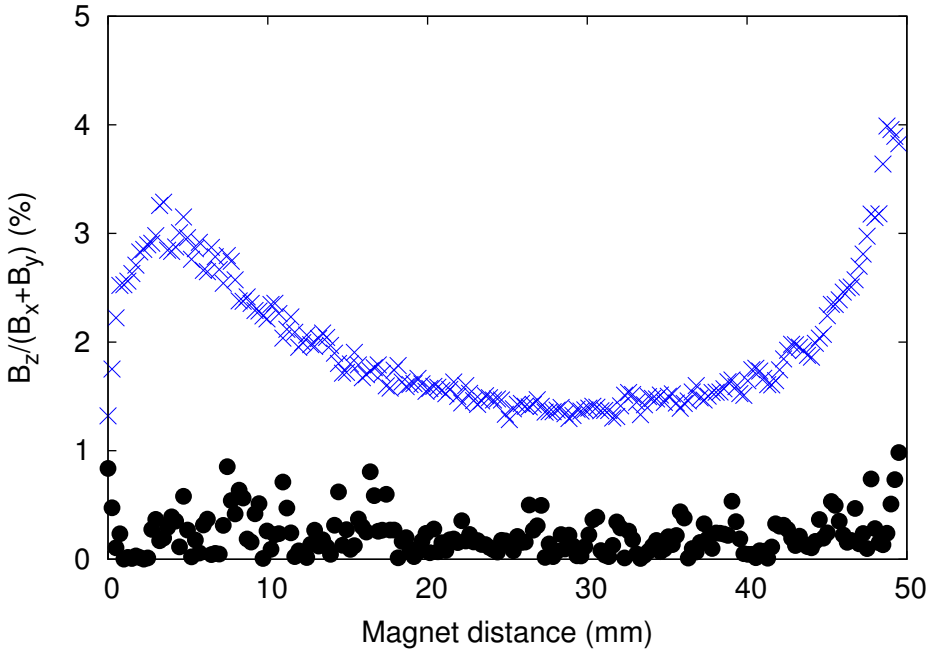

Figure 5.13: Graph to show the percentage of the x and y-components of $\mathbf{B}$ to the z-component along the z-axis. The black circles are for predicted data along the z-axis at $x = 0$ mm and the blue crosses at $x = 0.5$ mm.

components of $\mathbf{B}$, whereas the FEMM analysis only predicted $\mathbf{B_z}$. To test this, $\mathbf{B_{x,y}}$ was measured as a percentage of $\mathbf{B_z}$ along the z-axis. The results are shown in Figure 5.13 and it can be seen that $\mathbf{B_{x,y}}$ is a maximum of 1% of $\mathbf{B_z}$ along the z-axis, a negligible amount. Instead, it is thought likely that differences between the real and predicted magnets, such as imperfections in the real magnets, may be the cause of the differences in the measured magnetic flux density.

Figure 5.13 also shows $\mathbf{B_z}/\mathbf{B_{x,y}}$ as a percentage along the z-axis at $x = 0.5$ mm. It can be seen that the maximum value of $\mathbf{B_z}/\mathbf{B_{x,y}}$ is 4%. $\mathbf{B_{x,y}}$ can therefore be considered negligible throughout the studied z-range, which means that when calculating $\mathbf{F_z}$, $\mathbf{B_{x,y,z}} \approx \mathbf{B_z}$.

The gradients from the magnetic field densities shown in Figure 5.12 were then used to calculate the force on the M270 2.8 μm diameter beads by use of Equation (2.3.1). The calculated vertical forces are shown in Figure 5.14. Although the measured and theoretical values are in good agreement over most of the z-range studied, the experimental values showed a maximum force of 325 pN while the FEMM analysis showed only 120 pN.

The force on a bead is predicted by Equation (2.3.1) to depend on its volume. M270 beads were selected as they are highly monodisperse, which meant that the magnetic force would be expected to remain approximately constant for each bead. In order to test this, the average size of the beads were measured with the microscope as a function of $\mathbf{F_z}$. ImageJ counting software [85] was used to analyse the number of beads in the focal plane. The mean cross-sectional bead area of 1500 beads was measured to be $6.150 \pm 0.005\ \mu\text{m}^2$, in excellent agreement with the manufacturer's value of $6.154\ \mu\text{m}^2$.

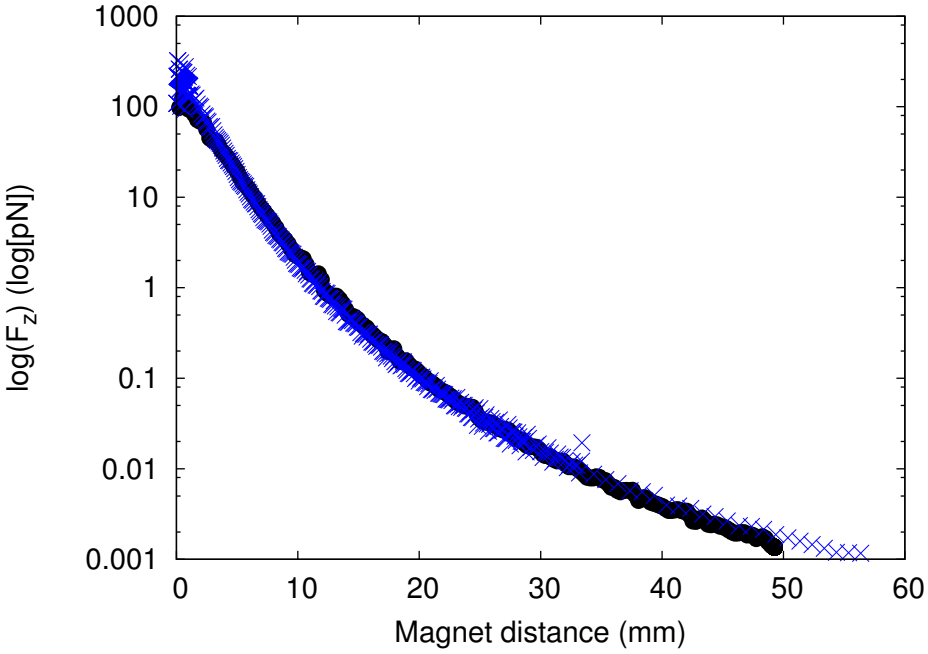

Figure 5.14: Force calibration curve for the magnetic tweezers with M270 2.8 μm diameter beads. The black circles are calculated from the FEMM analysis and the blue crosses from the experimental data.

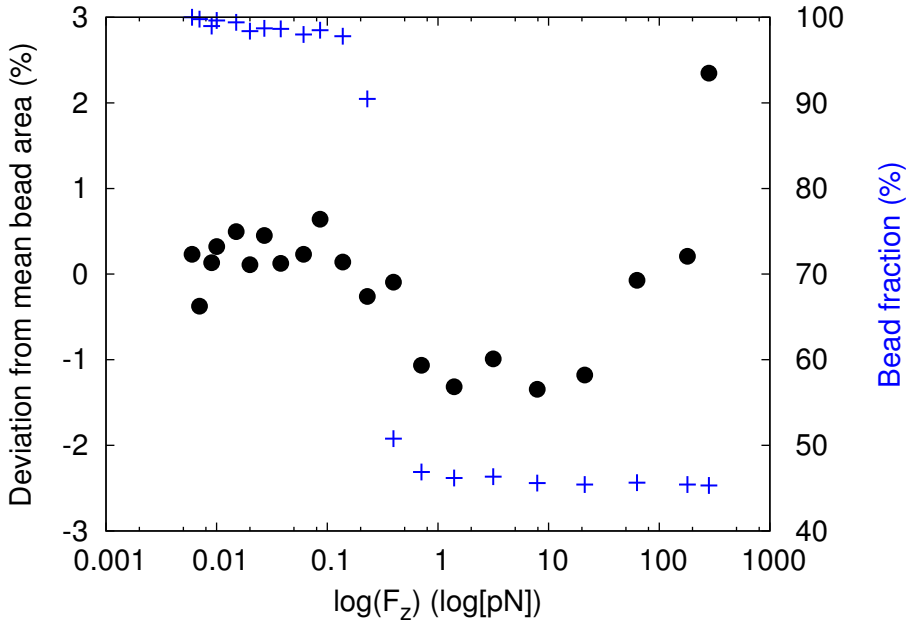

Figure 5.15: Percentage deviation from the mean bead area as a function of force (black circles, left axis). The bead fraction is also shown as a function of force (blue crosses, right axis).

The percentage deviation in bead area from the mean can be seen in Figure 5.15 to be a maximum of approximately 2.5% over the force range 0.005 pN to 250 pN. If the beads were more polydisperse then the average area of the beads would be expected to decrease at higher forces due to the removal of the larger beads, which would experience more force. The 2.5% uncertainty in the bead area implies that the percentage uncertainty in the bead volume, and hence the uncertainty in the force experienced by a bead due to its size, is approximately 5%.

5.4 Experimental method

5.4.1 Effect of buffer ionic strength on bare beads

The M270 beads were prepared by diluting them in 3 ml of PBS (pH 5 20 mM ionic strength). The bead solution was then left to mix in an Eppendorf tube for 20 minutes on a rotating platform. A NdFeB permanent magnet was then used to pellet the beads so that they could be separated from the supernatant with a pipette before another 3 ml of PBS was added to the beads. This washing procedure was repeated 3 times in order to remove the surfactant that the beads were stored in.

After the beads had been thoroughly washed they were placed into 4 Eppendorf tubes, separated from solution and then mixed in either 20 mM, 50 mM, 100 mM or 150 mM ionic strength PBS solutions of pH 7.4.

The prepared beads were presented to the surface of uncoated Ibidi μ-slides and allowed to settle for 30 minutes. The 10x lens was then adjusted until the beads at the slide surface were in the focal plane of the lens. An image was then captured with the CCD camera. The upwards force on the beads was then increased by moving the permanent magnet closer with the traveling stage. After the magnet had been positioned the beads were allowed to equilibrate for 60 seconds before another image was taken. ImageJ counting software was used to count the number of beads at each magnet position.

The effect of buffer ionic strength on bare beads on the hydrophobic Ibidi slide surface can be seen in Figure 5.16. Figure 5.16 clearly shows that increased ionic strength allows a greater proportion of beads to be removed from the surface. This suggests that electrostatic forces between the bead and hydrophobic surface are important. At higher ionic strengths, the salt ions screen the electrostatic interactions between the beads and surface, which means that less force is required to pull the beads from the surface. In order to reduce the interaction between the magnetic beads and the surface, the antibody/antigen force spectroscopy experiments were performed in buffer with an ionic strength of 150 mM.

At least 500 beads were imaged for each experiment and each experiment was repeated at least 3 times. Errors were calculated from the standard deviations of the repeated results.

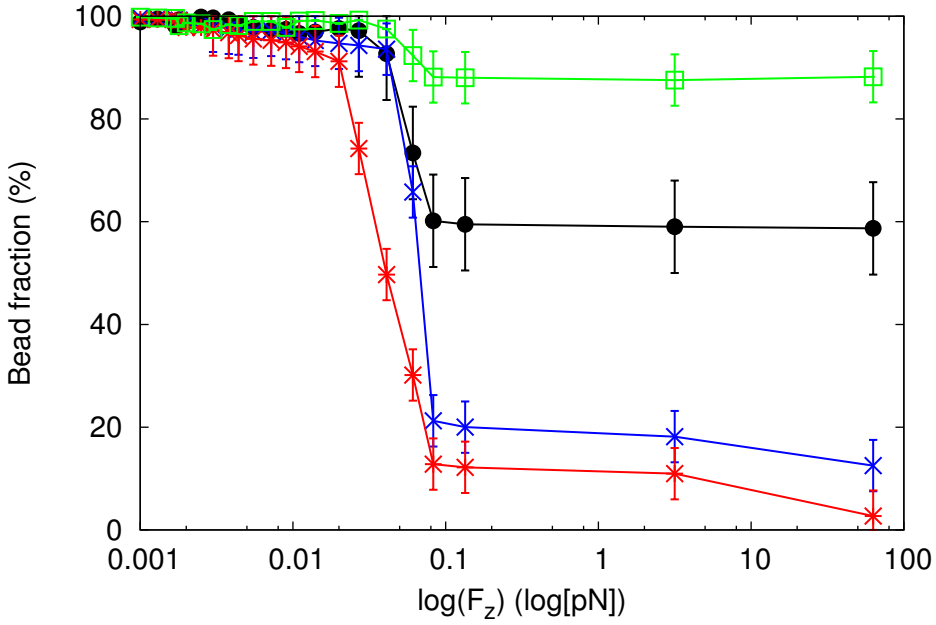

Figure 5.16: Graph to show the percentage of bare beads removed as a function of magnetic force for different ionic strengths: 20 mM (green squares), 50 mM (black circles), 100 mM (blue croses) and 150 mM (red stars). All buffers were set to pH 7.4.

5.4.2 Effect of BSA concentration on BSA coated beads

Washed beads were mixed in a solution of 0.25 mg/ml BSA for 1 hour on a rotating platform. The beads were separated from the solution by use of a magnet and pipette and were washed in 4 ml of PBS, this was repeated 3 times. Ibidi μ-slide surfaces were coated with BSA concentrations of either 0 mg/ml, 0.025 mg/ml or 0.1 mg/ml. Each concentration was allowed to adsorb for 30 minutes before the BSA coated beads were introduced and allowed to settle for 30 minutes.

After the BSA coated beads had settled, the permanent magnet was moved towards the experimental surface in order to vary the magnetic force on the beads. Images were taken at the different forces after waiting 60 seconds for the beads to equilibrate. From Figure 5.17 it can be seen that the BSA coated beads strongly adhere to the bare, hydrophobic surface. Even with a force of 250 pN it was possible to remove only 25% of the coated beads.

The non-specific binding between the coated beads and surface was reduced by coating the surface with BSA. For surfaces coated with 0.025 mg/ml and 0.1 mg/ml the bead fraction was reduced to 50% and 20% respectively at a force of 250 pN. The results suggest that BSA adsorption is required on both surfaces in order to reduce the amount of non-specific binding between the coated beads and surface.

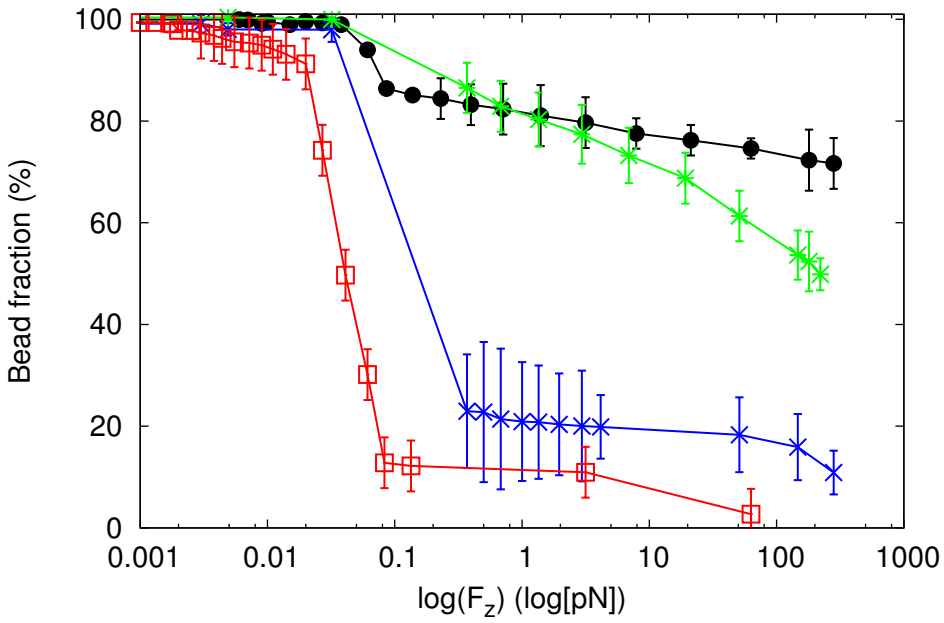

Figure 5.17: Graph to show the percentage of BSA coated beads removed as a function of magnetic force for BSA coated surfaces of 0 mg/ml (black circles), 0.025 mg/ml (green stars) and 0.1 mg/ml (blue crosses). The red squares represent bare beads on a bare surface, as for Figure 5.16. All buffers were set to pH 7.4 and 150 mM ionic strength.

5.4.3 Antibody/antigen force spectroscopy

Each Ibidi slide had 6 experimental capillaries with separate inlet and outlet tubes. The capillaries of the Ibidi μ-slides were coated with 0.1 ml of either 1 mg/ml of anti-α-hCG or 1 mg/ml of anti-β-hCG. The antibodies were allowed to adsorb for 1 hour before the slides were washed with 3 ml of PBS buffer. 0.1 ml of 0.05 mg/ml BSA solution was then added to each capillary in order to block surface areas not coated with antibody. The slides were sealed with parafilm and placed in a 4°C fridge overnight. Before use, each capillary was washed with a further 1 ml of PBS.

Washed beads were placed in an Eppendorf tube with 1 ml solution of either 1 mg/ml anti-α-hCG or 1 mg/ml of anti-β-hCG and mixed on a rotating platform for 1 hour. After mixing, the beads were pelleted with a magnet and the supernatant was removed with a pipette. The pelleted beads were then mixed with 4 ml of PBS on a rotating platform for 20 minutes. The beads were then pelleted and the buffer was removed and replaced with another 4 ml of PBS. This step was repeated twice more in order to remove non-adsorbed antibodies from the bead solution. After the beads were pelleted, all but approximately 50 μl of supernatant was removed from the Eppendorf tube. Thus, after one wash and introduction of 4 ml PBS, the concentration of free antibody in the supernatant was reduced to 0.0125 mg/ml and to a negligible concentration of 0.25 ng/ml after 4 washes. 0.05 mg/ml of BSA was then mixed with the beads and washed in the same way as for the antibodies, in order to block empty spaces on the bead surfaces. Finally, the antibody coated beads were added to a 0.002 mg/ml of hCG antigen. This level of hCG was enough

to almost fully saturate the antibody binding sites on the particle. The hCG was mixed with the beads and washed from solution in the same way as for the antibodies and BSA.

Anti-α-hCG beads were added to the anti-β-hCG coated capillaries and allowed to settle for 30 minutes. The same was done for anti-β-hCG beads and anti-α-hCG capillaries. Two different control experiments were performed. For the first control, anti-α-hCG beads that had not been mixed with hCG were added to the anti-β-hCG coated capillaries, the lack of hCG prevented immuno-links between the beads and surface. The second control introduced anti-β-hCG beads to anti-β-hCG coated capillaries. In this control no immuno-link could be formed between bead and surface as the mono-clonal antibodies both competed for the same hCG epitope. The beads were then viewed with a 10x lens and a CCD camera.

The CCD camera was then used to take images of the settled beads at different magnet positions. Each time the magnet was moved the beads were given 60 seconds to equilibrate before an image was taken. ImageJ counting software was used to count the number of beads in each image. Figure 5.1 shows the bead positions at high and low values of $\mathbf{F_z}$. It can be seen that as the magnet is moved closer, and the vertical force on the beads is increased, the immuno-links between the beads and surface are broken and the beads move out of the focal plane. Repeated experiments were performed on different capillaries of the Ibidi slide in case the specific binding mechanism had been damaged by the previous experiment.

5.4.4 Detachment curves for immuno-linked beads

Additionally, detachment curves were produced with the following method. Anti-α-hCG beads, mixed with hCG, were added to the anti-β-hCG coated capillaries and allowed to settle for 30 minutes. Beads and surfaces were prepared with the same method and with the same concentrations and solutions as discussed in Section 5.4.3.

A constant force of 1 pN was then applied to the settled beads for 10 minutes in order to overcome the buoyant weight (0.04 pN) of, and remove from the surface, any beads that had not been immuno-linked to the surface. The traveling stage was then used to move the magnet to apply a force of 50 pN to the beads and the CCD was used to capture images for 40 seconds at 60 fps. This was repeated for forces of 100 pN and 150 pN. Each experiment was performed on a different capillary and was repeated 3 times.

5.5 Results and discussion

Figure 5.18 shows the percentage of immuno-linked beads on the Ibidi slide surface remaining as a function of $\mathbf{F_z}$. A clear difference between the control experiment and immuno-linked bead experiments can be seen, which confirms that antibody/antigen binding did occur and did increase the force between the surface and beads. The results show that the anti-α-hCG coated beads on anti-β-hCG coated surface required more force to

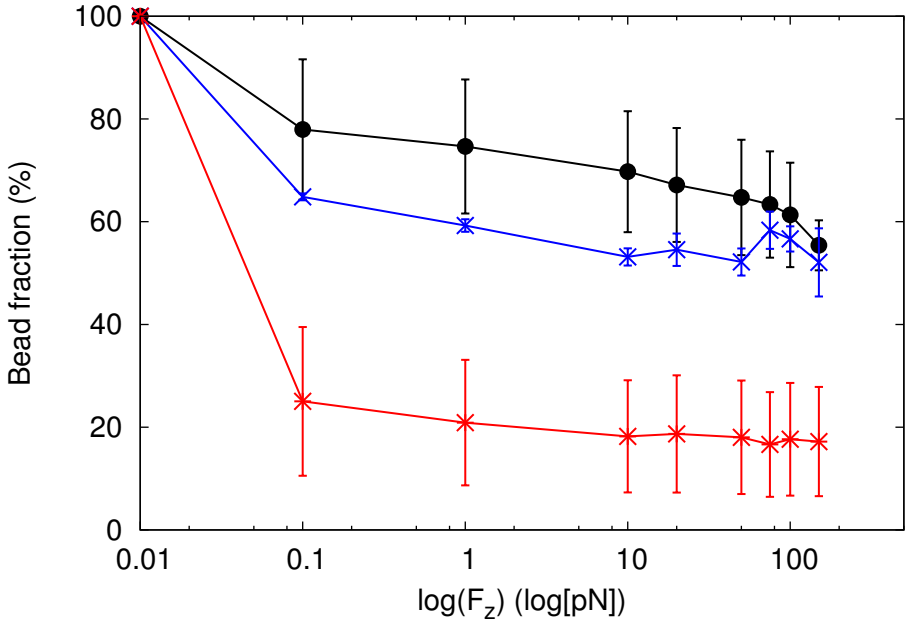

Figure 5.18: Graph to show the percentage of beads removed as a function of magnetic force for immuno-linked beads and control beads (red stars). The black circles represent data from anti-α-hCG coated beads with anti-β-hCG coated surfaces, while the blue crosses represent data from anti-β-hCG coated beads with anti-α-hCG coated surfaces.

pull the beads from the surface than the anti-β-hCG coated beads on anti-α-hCG coated surface. The reasons for this unexpected result are not clear. An anti-α-hCG/hCG/anti-β-hCG bond linked the beads to the surface in each experiment, therefore the beads in each experiment should have been removed from the surface at the same rate. More experiments are required to investigate this result.

In order to approximate the binding force between hCG and its antibodies the following assumptions were made: non-specific adsorption was negligible and that the strength of each antibody/antigen bond was equal and of constant magnitude throughout the experiment. Unlike in previous studies [128, 129], the effects of steric hindrance, caused by the surface packing density of the adsorbed antibody, were not assumed to be negligible. Instead, it was assumed that the antigen surface coverage had a constant value of 0.17 mg/m^2 for each bead. This appeared to be a reasonable assumption as Figure 4.36 showed that the surface coverage of hCG was approximately constant at 0.17 mg/m^2 and was largely independent of antibody surface coverage. As the antigen binding ratio was shown to decrease with antibody surface coverage in Figure 4.37, it was also assumed that the binding ratio for hCG at the surface would be low, most likely as low as 0.05 due to the high concentration of antibody used to coat the Ibidi surfaces. Therefore, the total hCG surface coverage that was available to form an immuno-link between a bead and surface was 0.0085 mg/m^2.

Not every bound antigen on a bead was thought able to bind with an antigen on the surface, as only a small area of the bead was in contact with the surface. The size of this contact area was estimated by assuming that the bead contact area was formed by a

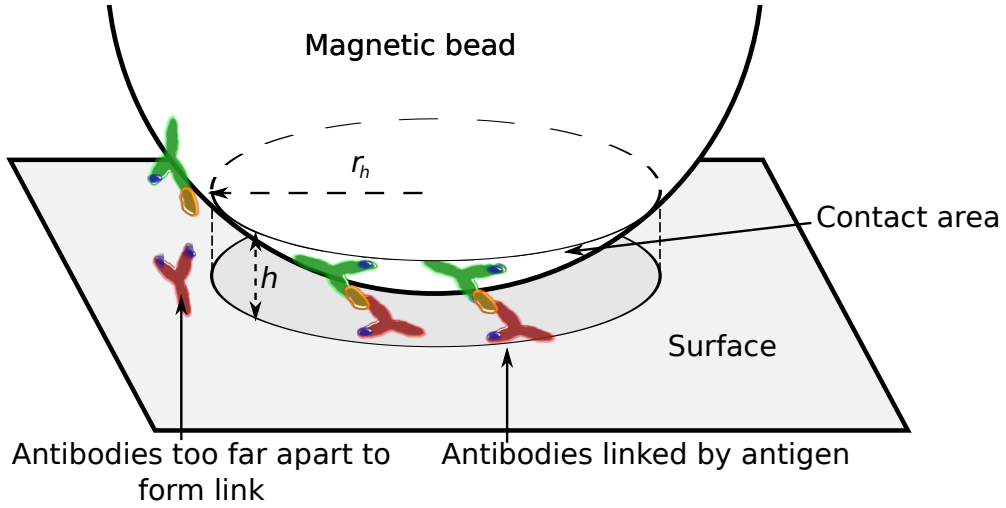

Figure 5.19: The cap of the magnetic bead forms a contact area with the surface. Antibody immuno-links are only possible between antibodies inside the contact area. BSA molecules not shown for clarity.

spherical cap of a height (h) and radius r_h determined by the thickness of the adsorbed antibody/antigen layer. Antibody/antigen pairs outside of this contact area were thought to be too far apart to bind to antibodies on the surface, as shown in Figure 5.19. The surface area of the cap (A_{cap}) was found by use of:

$$A_{cap} = \pi(r_h^2 + h^2) \tag{5.5.1}$$

where r_h is calculated from the bead radius, R,

$$r_h = \sqrt{h(2R - h)}. \tag{5.5.2}$$

A previous study by Gao and Jin [128] used a similar method to calculate the force per antibody/antigen pair. Gao and Jin used the long-axis of their studied antibody (goat anti-human IgG) to determine the value of h. However, the DPI and NR data, Figure 4.17 and Table 4.3 respectively, show that the antibody typically adsorbs in the flat-on orientation and that the antigen binds inside this layer and does not increase the thickness of the film by a significant amount. Therefore upper and lower limits for the value of h were based on the thickness of flat-on adsorbed antibody layers. The upper value of h was set as 8 nm, equal to the flat-on adsorbed thickness of two antibody films, one film on the bead and the other on the surface with half of the antigen inside each layer. The lower value of h was set as 4 nm and it was assumed that after the bead and surface had come into contact, the bead and surface antibody films interlocked to create a dense, mixed layer. From the upper and lower limits of h and the hCG molecular weight of 38 kDa, the minimum and maximum numbers of immuno-links per bead were calculated to be 4 and 11 respectively.

The average force required to remove an immuno-linked bead from the surface was

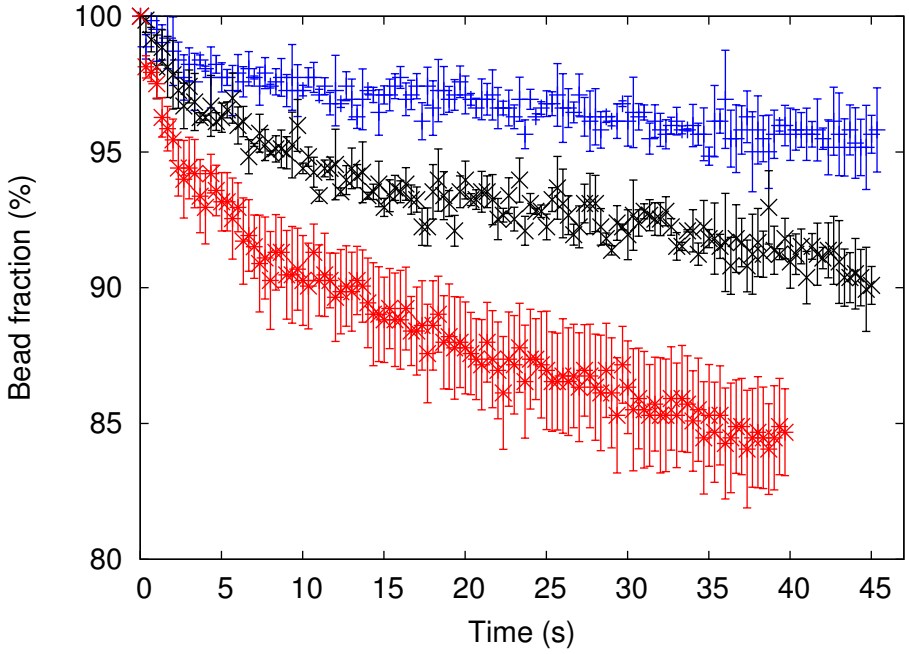

Figure 5.20: Remaining percentage of immuno-linked beads as a function of time for a constant force of 50 pN (blue), 100 pN (black) and 150 pN (red).

defined as the value of $\mathbf{F_z}$ at which 50% of the immuno-linked beads had been removed from the surface. From Figure 5.18 it can be seen that a force of 150 pN was required to remove 50% of the anti-β-hCG coated beads. For the anti-α-hCG coated beads it was necessary to extrapolate from 150 pN to determine the average removal force, which was found to be approximately 175 pN. The force per immuno-link was calculated for the anti-β-hCG coated beads to have an upper limit (4 immuno-links per bead) of 37.5 pN and a lower limit (11 immuno-links per bead) of 13.6 pN. The immuno-links between the anti-α-hCG coated beads and anti-β-hCG coated surface had an upper limit on the strength of adhesion of 43.8 pN and a lower limit of 15.9 pN.

The Bell equation demonstrates that measured force constants critically depend on observation times, a result of non-equilibrium thermodynamics [53]. The constant force generated by the magnetic tweezers allowed the dissociation rate constant ($k_d(F)$) of the anti-α-hCG/hCG/anti-β-hCG complex to be investigated as a function of force. The number of beads on the Ibidi surface was counted as a function of time at $\mathbf{F_z}$ values of 50 pN, 100 pN and 150 pN. Figure 5.20 shows that the rate at which beads were removed from the surface was dependent on the force applied to the beads.

The value of k_d for a single species of intermolecular interaction can be calculated from the number of beads remaining on the surface (N) as a function of time (t)

$$N(t) = N(0)\exp(-tk_d(F)). \tag{5.5.3}$$

Equation (5.5.3) was applied to the experimental data obtained from each force. Figure 5.21 shows that the monoexponential model described in Equation (5.5.3) provided

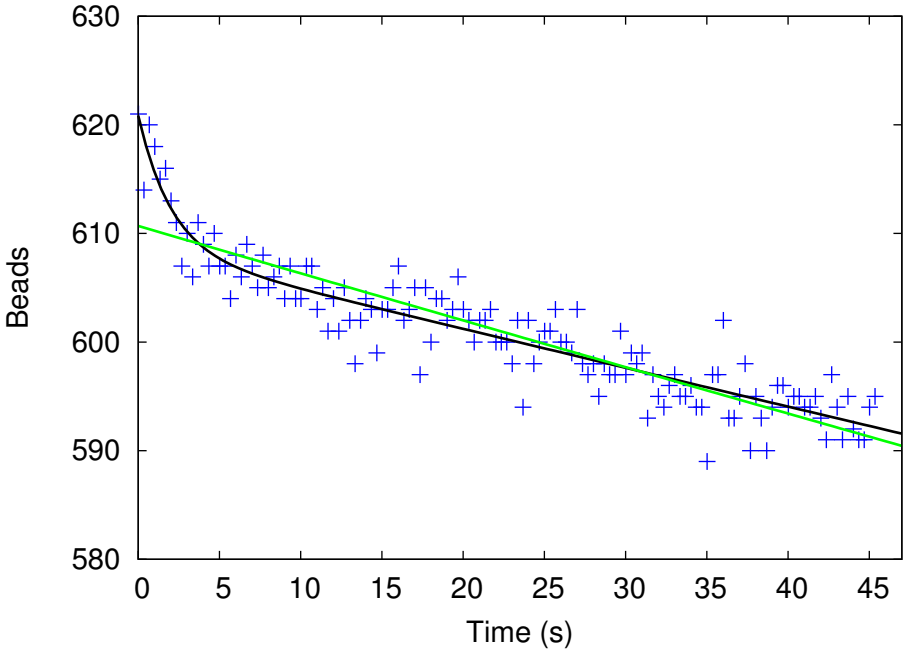

Figure 5.21: Immuno-linked beads as a function of time for a constant force of 50 pN. The best fitting monoexponential is displayed as the green line and the best fitting biexponential as the black line.

a poor fit to the experimental data. The poor fit offered by Equation (5.5.3) suggested that there were multiple species of interactions between the immuno-linked beads and surface. If multiple species of interactions are thought to exist between the beads and surface then N is given by a sum of monoexponentials. For two species of interactions, Equation (5.5.3) becomes a biexponential,

$$N(t) = A\exp(-tk_{d,A}(F)) + B\exp(-tk_{d,B}(F)) \tag{5.5.4}$$

where A and B are the respective number of beads initially bound to the surface by the A and B species of interaction.

The biexponential model provided a far better fit to the 50 pN experimental data than the monoexponential model. The same was true for the 100 pN and 150 pN data, shown in Figure 5.22 and Figure 5.23 respectively. The fitted biexponentials showed that at 50 pN 98% of the interactions were species A and 2% were species B. The percentage of species B increased with force to 5% at 100 pN and 7% at 150 pN. A triexponential model was also fitted to the data to represent a third species of interaction between the bead and surface. However, the triexponential did not provide a significantly better fit than the biexponential and was rejected. Multiple interaction species between ligands and receptors have also been experimentally observed by Shang et al [132] and Danilowicz et al [133].

The value of the dissociation constant at zero force ($k_d(F = 0)$) was calculated for

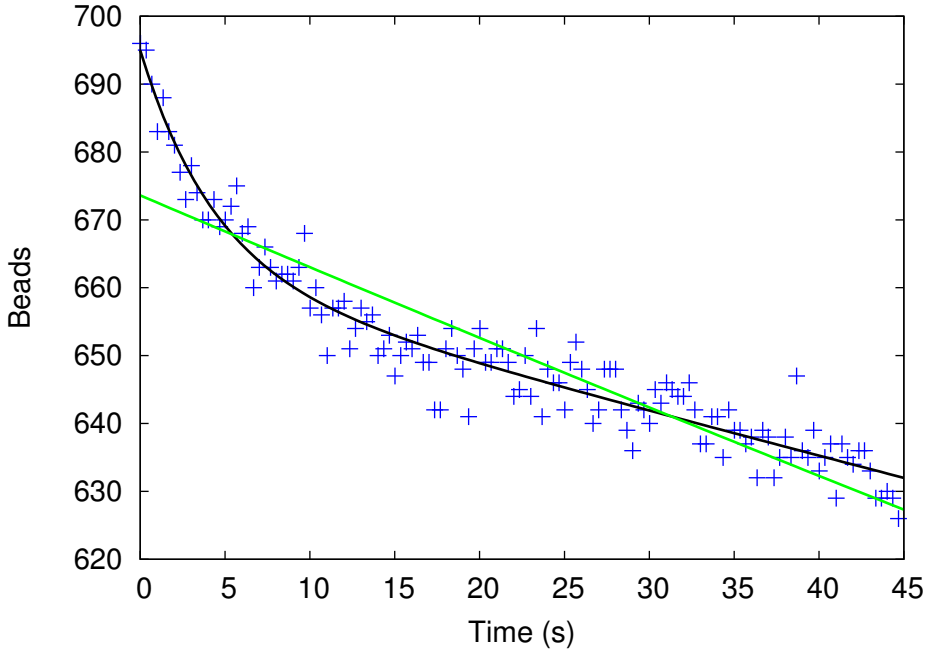

Figure 5.22: Immuno-linked beads as a function of time for a constant force of 100 pN. The best fitting monoexponential is displayed as the green line and the best fitting biexponential as the black line.

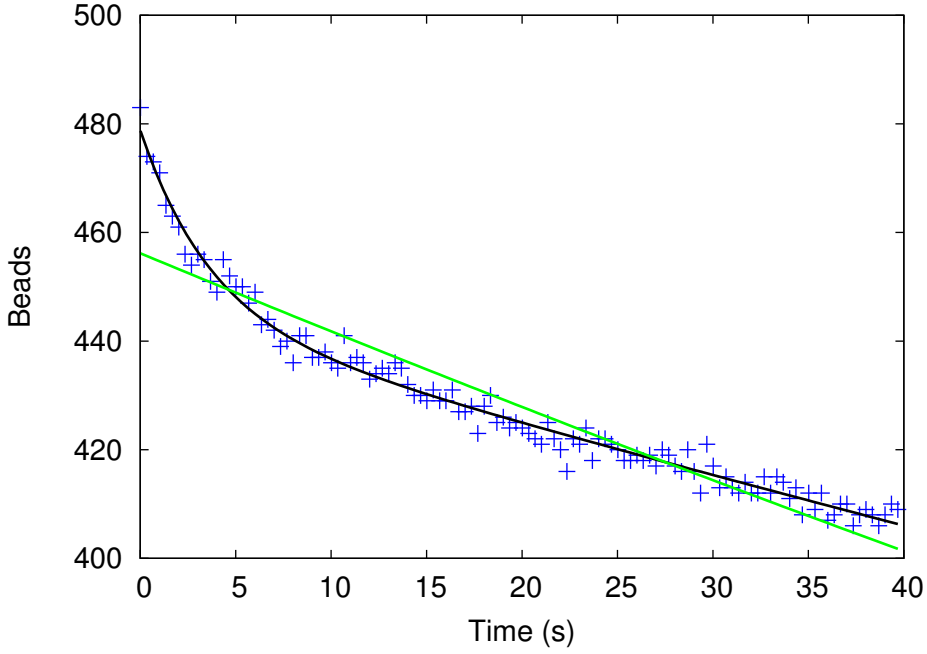

Figure 5.23: Immuno-linked beads as a function of time for a constant force of 150 pN. The best fitting monoexponential is displayed as the green line and the best fitting biexponential as the black line.

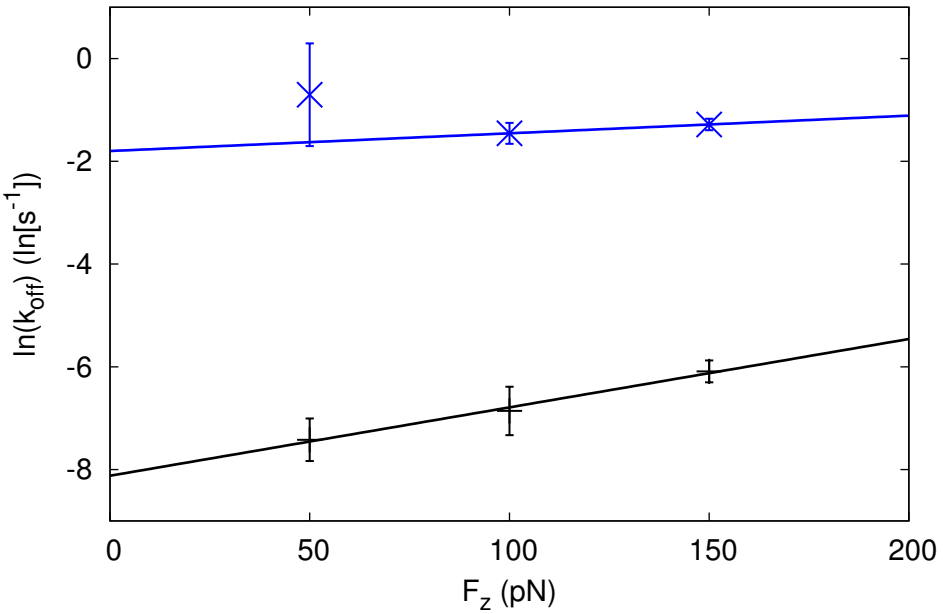

Figure 5.24: The natural logarithm of the measured dissociation rates of interaction species A (black) and B (blue) is shown for the studied forces. The solid lines represent the best fit to the experimental data obtained from Equation (5.5.4). For species B, the model was fit using the lower limit of the 50 pN data point.

each species by use of Equation (1.5.3), rewritten as:

$$\ln[k_d(F)] = \ln[k_d(F=0)] + Fr/k_bT \tag{5.5.5}$$

where r is the effective length of the interaction, k_b is the Boltzmann constant and T is the temperature of the system (291 K). The natural logarithms of the measured values of $k_d(F)$ were plotted as a function of force for each species, shown in Figure 5.24. For species A, $k_d(F=0)$ was found from the intercept of the fitted line to be $(3 \pm 1) \times 10^{-4}\,\mathrm{s}^{-1}$. The interaction length was calculated from the gradient of the fitted line and was found to equal 0.06 ± 0.03 nm. Uncertainties were calculated from differences between the experimental data and fit. Due to the large uncertainty on the measured $k_d(F=50)$ of species B (the second smaller dynamic process) it was not possible to obtain accurate values for x and $k_d(F=0)$. The large uncertainty was due to the small population of beads in species B. For the fit shown in Figure 5.24 only the lower limit of $k_d(F=50)$ was used in order to prevent the calculated k_d from decreasing with force. For species B, $k_d(F=0)$ was calculated to have a value of $0.2 \pm 0.5\,\mathrm{s}^{-1}$ and an interaction length of 0.02 ± 0.04 nm. In comparison, the value of $k_d(F=0)$ for streptavidin/biotin was measured with AFM by Yuan et al to be $1.67 \times 10^{-5}\,\mathrm{s}^{-1}$ [136] with an interaction length of 0.49 nm. However, these values were found to depend on the force loading rate, making direct comparisons between experiments difficult. At a higher loading rate, Yuan et al measured $k_d(F=0)$ to be $2.09 \times 10^{-5}\,\mathrm{s}^{-1}$ with an interaction length of 0.05 nm. A study with micro-pipettes measured the IgG/protein A interaction to be much weaker with a $k_d(F=0)$ of $0.014\,\mathrm{s}^{-1}$

but with a longer interaction length of 0.96 nm [137].

The calculated interaction length of species A ($r = 0.06 \pm 0.03$ nm) appears small when compared to the bond lengths of individual hydrogen bonds ($r \approx 0.2$ nm), covalent bonds ($r \approx 0.2$ nm) or van der Waals interactions ($r \approx 0.4$ nm for $\kappa^{-1} = 0.8$ nm) [53]. This is likely to be a result of the complexity of the antibody/antigen interaction, which will be comprised of a variety of interactions, some of which will be attractive and some of which will be repulsive. The Bell equation gives a simple average of all of these interactions.

5.6 Conclusions

A magnetic tweezer system was designed and built in order to measure the specific antibody/antigen binding force. The magnetic tweezers were constructed from a permanent magnet that was placed on a travelling stage so that the distance, and force, between the magnet and magnetic bead samples could be varied. The magnet and stage were mounted on a microscope so that images of the magnetic beads could be captured with a camera in order to count the number of beads removed from the experimental surface.

A detailed comparison between flat and pointed magnetic pole pieces was carried out with FEMM software. The analysis showed that the pointed pole piece offered a larger force range than the flat pole piece. However, the flat pole piece was selected for the final design as it offered a more homogeneous magnetic field, which was required in order to maximise the number of imaged magnetic beads.

Antibody/antigen force spectroscopy measurements were then performed with the magnetic tweezer system. It was found that the antibodies and antigens formed immuno-links between the magnetic beads and experimental surface. Each bead was calculated to be anchored to the surface by between 4 and 11 immuno-links. The force per immuno-link was estimated to be between 13.6 pN and 43.8 pN.

In addition, bead detachment curves were obtained that revealed two species of interaction between the antibody/antigen linked beads and surface. The dissociation constant of the strong antibody/antigen interaction was found to equal $(3 \pm 1) \times 10^{-4}\,\mathrm{s}^{-1}$ and had an interaction length of 0.06 ± 0.03 nm. The low population of beads bound to the surface by the second, weaker interaction meant that it was not possible to obtain accurate values of the dissociation constant and interaction length of the second weaker interaction.

CHAPTER

SIX

CONCLUSIONS AND FUTURE WORK

6.1 Conclusions

Interfacial adsorption of proteins is fundamental to the development of biocompatible materials and biomedical devices and diagnostics. The work presented in this thesis describes how techniques such as dual polarisation interferometry (DPI) and neutron reflectivity (NR) can be used to measure the interfacial structure of adsorbed protein layers.

BSA is commonly used in biomedical devices as a blocking agent to prevent the non-specific adsorption of proteins to a surface. DPI and NR were used to investigate the effects of pH and protein concentration on BSA adsorption. It was found from both techniques that the adsorbed layer thickness and surface coverage increased the closer the pH was to the isoelectric point of BSA; pH 5. The layer thickness and surface coverage also increased with concentration.

There have been few studies that compare DPI and NR results for protein adsorption on the same surface and in the same buffer conditions. Our results show that DPI and NR provided similar surface coverage data, even when using a two-layer model to fit the NR data. Thus DPI, a relatively inexpensive bench-top technique, can provide reliable protein surface coverage measurements that can be used to complement more expensive NR studies.

DPI is also able to reliably measure the thickness of thin films, a huge advantage over techniques such as ellipsometry. DPI measured thicknesses were compared with NR results that were analysed with both single- and two-layer models. Although the DPI measured thicknesses were close to those obtained by the single-layer NR model, large differences were observed between the DPI and two-layer NR measured thicknesses. Two-layer models were required to adequately fit the NR data above concentrations of 0.1 mg/ml. The uniform-layer model used by DPI was observed to be less sensitive to low density regions than NR.

In addition, the time resolution of DPI was sufficient to obtain kinetic data, which were used to investigate the Langmuir and RSA adsorption models. The Langmuir model was found to fit BSA concentrations of 0.25 mg/ml or less, where the interactions between the

adsorbed proteins were insignificant. Above 0.25 mg/ml the surface coverage was high enough for interactions between the adsorbed molecules to limit the adsorption rate of further proteins. Thus the RSA model proved the better fit to the data above concentrations of 0.25 mg/ml.

At long adsorption times, the RSA predicts an approach to a jamming limit that has a characteristic $t^{-0.5}$ dependency on time (t). For the approximately spherical proteins of BSA and transferrin it was found that their respective approaches to the jamming limit had relationships of -0.5048 ± 0.0007 and -0.4968 ± 0.0006, in excellent agreement with the predicted value. The RSA model could therefore be used to optimise the adsorption times of spherical blocking proteins that are used in immunoassays. This information could be used to reduce the production costs of commercial immunoassays.

DPI and NR were then used to investigate the interfacial structure of a simplified human pregnancy immunoassay. The immunoassay was built in steps so that the adsorption of each protein could be accurately monitored. DPI showed that both the surface coverage and thickness of the adsorbed anti-α-hCG antibody increased with bulk antibody concentration. For the bulk concentration range studied, the antibody adsorption closely followed the Langmuir protein adsorption model.

Both DPI and NR provided evidence of BSA/HSA insertion into the gaps on the surface between the antibody molecules. This suggests that albumin adsorption is an excellent method to reduce the non-specific adsorption of target antigens to the immunoassay test surface. DPI control experiments also showed that, at sufficient concentrations, BSA can reduce non-specific hCG adsorption to negligible amounts.

The antibody/antigen binding ratio was also investigated with both techniques. It was found that the total amount of antigen that specifically bound to adsorbed antibodies was independent of the antibody surface coverage. The amount of bound antigen remained constant at approximately 0.17 mg/m^2. However, the antibody/antigen molar binding ratio was dramatically reduced at high antibody surface coverage, even though the antigen was available in excess. The high surface packing density of molecules at high surface coverage was thought to make the antibody Fabs inaccessible to antigen molecules. The results imply that above a certain antibody surface coverage there is no advantage in the adsorption of more antibody molecules.

Kinetic data from the DPI were also used to measure the rate of BSA adsorption onto a surface pre-coated with antibody. It was found that a pre-adsorbed antibody film accelerated the rate of BSA adsorption when compared to BSA adsorption onto an empty surface. This effect was attributed to the formation of antibody clusters on the surface. Antibody clusters formed when the adsorption time of the antibody was of sufficient duration. Since the antibody surface packing density had a negative impact on the antibody/antigen binding ratio, immunoassays should introduce the BSA as soon as possible after antibody adsorption in order to prevent antibody clustering, which would cause localised areas of high surface packing density.

There have been few studies to investigate the binding force between hCG and its antibodies. To remedy this, a magnetic tweezer system was designed and built in order to measure the specific antibody/antigen binding force. FEMM analysis software was used to compare different pole pieces and it was found that a flat pole piece offered a more homogeneous magnetic field, which was required in order to maximise the number of imaged magnetic beads.

Antibody/antigen force spectroscopy measurements were then performed with the magnetic tweezer system. The antibodies and antigens were used to immuno-link magnetic beads to the experimental surface. Each bead was calculated to be anchored to the surface by between 4 and 11 immuno-links. The force per antibody/antigen immuno-link was estimated to lie between the values of 13.6 pN and 43.8 pN.

In addition, immuno-link detachment as a function of time was investigated at three different forces. It was found that the beads were anchored to the surface by both a strong and a weak interaction. The dissociation constant of the strong antibody/antigen interaction was found to equal $(3 \pm 1) \times 10^{-4}\,\mathrm{s}^{-1}$ and had an interaction length of 0.06 ± 0.03 nm. The low population of beads bound to the surface by the second, weaker interaction meant that it was not possible to obtain accurate values of the dissociation constant and bond length of the second weaker interaction.

6.2 Future work

A recent paper by Giamblanco et al showed that the co-adsorption of fibronectin with HSA caused the fibronectin to be oriented so that specific binding between it and fibrinogen was increased [138]. The co-adsorption of antibody with BSA or HSA could therefore be used to orient the adsorbed antibodies so that their Fabs are more accessible to hCG antigen. This could result in an increased antibody/antigen binding ratio. DPI and NR should be used to investigate this.

The history dependence of antibody adsorption was investigated in Section 4.4.2 and it was shown that adsorbed antibodies form clusters when given sufficient time. Clustered antibodies will produce localised regions of high surface packing density. The findings from Section 4.4.4 suggest that these antibody clusters are therefore likely to have low AgBC compared to evenly distributed antibodies. Thus, the prevention of antibody clustering may help immunoassay manufacturers to increase the AgBC, and hence the sensitivity, of immunoassys. Combined DPI and NR studies should therefore be performed to measure the AgBC of adsorbed antibodies as a function of the antibody adsorption time. Such experiments should be relatively trivial to perform as the history dependence seems to be of the order of several minutes. As the clustering occurs after adsorption, it seems plausible that the clustering will also depend on the surface chemistry of the substrate.

More information about the interaction between antibody and antigen could be obtained from the magnetic tweezers. For example, the magnetic tweezers could be used to

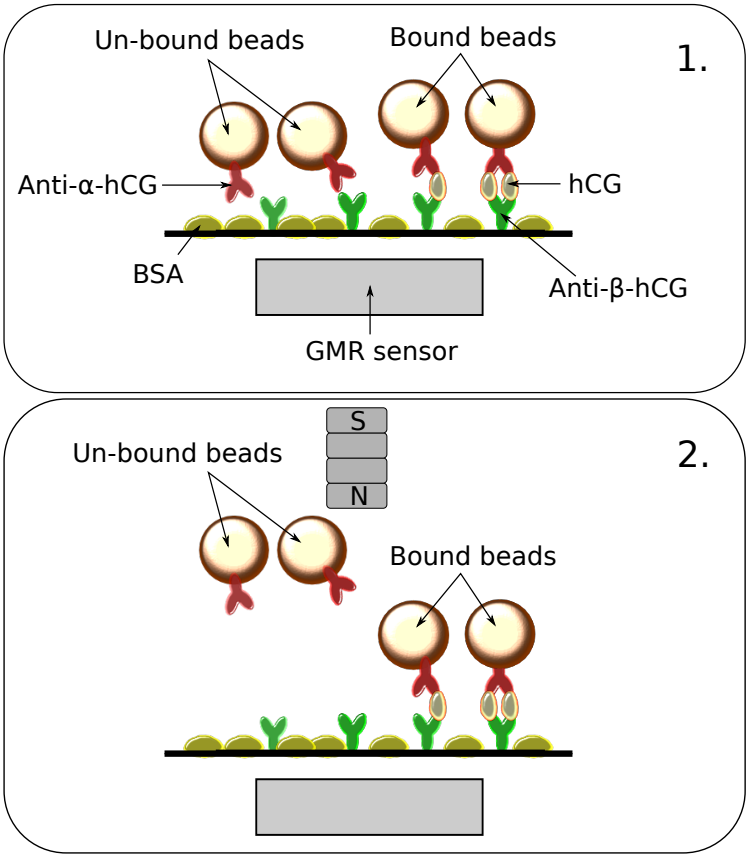

Figure 6.1: Schematic diagram of future assay design. **Panel 1.** The beads are allowed to settle onto the test surface. If hCG is present then beads will become immobilised on the test surface. The number of immobilised beads is proportional to the amount of hCG present. **Panel 2.** The test is exposed to a magnetic field (produced by switching on a solenoid or by introducing a permanent magnet) that is sufficient to remove any un-bound beads from the GMR's sensing range. The GMR sensor will record a magnetic field equal to the permanent magnet's field plus the small fields produced by the magnetised bound beads. Thus, the magnetic field recorded by the GMR sensor is proportional to the amount of hCG.

investigate the effects of repeated breaking and reforming of immuno-links.

The sensitivity of the pregnancy immunoassay could be improved upon. The development of giant magnetoresistance (GMR) sensors means that they will become a viable method of creating new forms of assays. For example, modern pregnancy tests use optical methods to detect the number of latex spheres that become bound to the test strip due to the formation of an hCG/antibody sandwich. By replacing the latex beads with magnetic beads, and applying a weak magnetic field that provides sufficient force to remove only un-bound beads, it would be possible to measure the remaining magnetic field with a GMR. This field would be composed of the magnetism of the bound beads as well as the external field. An example is given in Figure 6.1.

BIBLIOGRAPHY

[1] J. J. Gray. The interaction of proteins with solid surfaces. *Current Opinion in Structural Biology*, 14(1):110 – 115, 2004.

[2] R. A. Latour. Biomaterials: Protein–surface interactions. In G. L. Bowlin and G. Wnek, editors, *Encyclopedia of Biomaterials and Biomedical Engineering*. Marcel Dekker, New York, 2005.

[3] N. Huebsch and D. J. Mooney. Inspiration and application in the evolution of biomaterials. *Nature*, 462:426–432, 2009.

[4] D. Wild. *The Immunoassay Handbook*. Nature publishing group, second edition, 2001.

[5] `http://www.biology-online.org/biology-forum/about4313.html`. Accessed April 4, 2011.

[6] T. A. Waigh. *Applied Biophysics: A Molecular Approach for Physical Scientists*. Wiley, 2007.

[7] D. Bendedouch and S. H. Chen. Structure and interparticle interactions of bovine serum albumin in solution studied by small-angle neutron scattering. *The Journal of Physical Chemistry*, 87(9):1473–1477, 1983.

[8] L. R. S. Barbosa, M. G. Ortore, F. Spinozzi, P. Mariani, S. Bernstorff, and R. Itri. The importance of protein-protein interactions on the pH-induced conformational changes of bovine serum albumin: A small-angle x-ray scattering study. *Biophysical Journal*, 98(1):147 – 157, 2010.

[9] C. E. Giacomelli and W. Norde. The adsorption-desorption cycle. reversibility of the BSA-silica system. *Journal of Colloid and Interface Science*, 233(2):234 – 240, 2001.

[10] T.J. Peters. *All About Albumin: Biochemistry, Genetics, and Medical Applications*. Elsevier Science, 1995.

[11] G. Weber. Energetics of ligand binding to proteins. *Advances in protein chemistry*, 1975.

[12] T. Liping, A. H. Lucas, and J. W. Eaton. Inflammatory responses to implanted polymeric bimaterials: role of surface-adsorbed immunoglobulin G. *The Journal of laboratory and clinical medicine*, 122(3):292–300, 1993.

[13] S. Sugio, A. Kashima, S. Mochizuki, M. Noda, and K. Kobayashi. Crystal structure of human serum albumin at 2.5 Å resolution. *Protein Engineering*, 12(6):439–446, 1999.

[14] L. G. Longsworth and C. F. Jacobsen. An Electrophoretic Study of the Binding of Salt Ions by β-Lactoglobulin and Bovine Serum Albumin. *The Journal of Physical and Colloid Chemistry*, 53(1):126–134, 1948.

[15] A. J. Lapthorn, D. C. Harris, A. Littlejohn, J. W. Lustbader, R. E. Canfield, K. J. Machin, F. J. Morgan, and N. W. Isaacs. Crystal structure of human chorionic gonadotrophin. *Nature*, 369(6480):455–461, 1994.

[16] E. W. Silverton, M. A. Navia, and D. R. Davies. Three-dimensional structure of an intact human immunoglobulin. *Proceedings of the National Academy of Sciences*, 74(11):5140–5144, 1977.

[17] H. Xu, X. Zhao, C. Grant, J. R. Lu, D. E. Williams, and J. Penfold. Orientation of a monoclonal antibody adsorbed at the solid/solution interface: A combined study using atomic force microscopy and neutron reflectivity. *Langmuir*, 22(14):6313–6320, 2006.

[18] W. Norde and C. E. Giacomelli. BSA structural changes during homomolecular exchange between the adsorbed and the dissolved states. *Journal of Biotechnology*, 79(3):259–268, 2000.

[19] T. J. Su, J. R. Lu, R. K. Thomas, and Z. F. Cui. Effect of pH on the adsorption of bovine serum albumin at the silica/water interface studied by neutron reflection. *The Journal of Physical Chemistry B*, 103(18):3727–3736, 1999.

[20] T. J. Su, J. R. Lu, R. K. Thomas, Z. F. Cui, and J. Penfold. The conformational structure of bovine serum albumin layers adsorbed at the silica-water interface. *The Journal of Physical Chemistry B*, 102(41):8100–8108, 1998.

[21] A. Kondo, S. Oku, and K. Higashitani. Structural changes in protein molecules adsorbed on ultrafine silica particles. *Journal of Colloid and Interface Science*, 143(1):214–221, 1991.

[22] W. Norde. The behavior of proteins at interfaces, with special attention to the role of the structure stability of the protein. *Clinical Materials*, 11(1):85–91, 1992.

[23] C. A. Haynes and W. Norde. Globular proteins at solid/liquid interfaces. *Colloids and Surfaces B: Biointerfaces*, 2(6):517–566, 1994.

[24] J. A. Dura, C. A. Richter, C. F. Majkrzak, and N. V. Nguyen. Neutron reflectometry, x-ray reflectometry, and spectroscopic ellipsometry characterization of thin SiO_2 on Si. *Applied Physics Letters*, 73(15):2131–2133, 1998.

[25] K. Kubiak-Ossowska and P. A. Mulheran. What governs protein adsorption and immobilization at a charged solid surface? *Langmuir*, 26(11):7690–7694, 2010.

[26] P Szabelski, A Cavazzini, K Kaczmarski, X Liu, J Van Horn, and G Guiochon. Experimental studies of pressure/temperature dependence of protein adsorption equilibrium in reversed-phase high-performance liquid chromatography. *Journal of Chromatography A*, 950(1-2):41–53, 2002.

[27] C. F. Wertz and M. M. Santore. Effect of surface hydrophobicity on adsorption and relaxation kinetics of albumin and fibrinogen: Single-species and competitive behavior. *Langmuir*, 17(10):3006–3016, 2001.

[28] C. F. Wertz and M. M. Santore. Fibrinogen adsorption on hydrophilic and hydrophobic surfaces: Geometrical and energetic aspects of interfacial relaxations. *Langmuir*, 18(3):706–715, 2002.

[29] P. D. Coffey, M. J. Swann, T. A. Waigh, F. Schedin, and J. R. Lu. Multiple path length dual polarization interferometry. *Opt. Express*, 17(13):10959–10969, 2009.

[30] R. S. Yalow and S. A. Berson. Assay of plasma insulin in human subjects by immunological methods. *Nature*, 184(4699):1648–1649, 1959.

[31] G. Thomas, E. M. El-Giar, L. E. Locascio, and M. J. Tarlov. *Microfluidic Techniques: Reviews and Protocols*. Humana Press Inc., 2005.

[32] M. V. Jacobs, A. J. C. van den Brule, P. J. F. Snijders, T. J. M. Helmerhorst, C. J. L. M. Meijer, and J. M. M. Walboomers. A non-radioactive PCR enzyme-immunoassay enables a rapid identification of HPV 16 and 18 in cervical scrapes after GP5+/6+ PCR. *Journal of Medical Virology*, 49(3):223–229, 1996.

[33] A. Al-Qahtani, S. Muttukrishna, M. Appasamy, J. Johns, M. Cranfield, J. A. Visser, A. P. N. Themmen, and N. P. Groome. Development of a sensitive enzyme immunoassay for anti-müllerian hormone and the evaluation of potential clinical applications in males and females. *Clinical Endocrinology*, 63(3):267–273, 2005.

[34] R. J. Davies, S. S. Eapen, and S. J. Carlisle. *Lateral-Flow Immunochromatographic Assays*. John Wiley & Sons, Ltd, 2008.

[35] R. H. Yolken. Enzyme immunoassays for the detection of infectious antigens in body fluids: Current limitations and future prospects. *Review of Infectious Diseases*, 4(1):35–68, 1982.

[36] D. Knopp and R. Niessner. Biomonitors based on immunological principles. In A. A. F. Kettrup I. Twardowska, H. E. Allen and W. J. Lacy, editors, *Solid Waste: Assessment, Monitoring and Remediation*, volume 4 of *Waste Management Series*, pages 505–537. Elsevier, 2004.

[37] D. S. Aga and E. M. Thurman. *Environmental Immunoassays: Alternative Techniques for Soil and Water Analysis*, chapter 2, pages 1–20. 1997.

[38] T. Chard. Pregnancy tests: a review. *Human Reproduction*, 7(5):701–710, 1992.

[39] E. O. Saphire, P. W. H. I. Parren, R. Pantophlet, M. B. Zwick, G. M. Morris, P. M. Rudd, R. A. Dwek, R. L. Stanfield, D. R. Burton, and I. A. Wilson. Crystal structure of a neutralizing human IgG against HIV-1: A template for vaccine design. *Science*, 293(5532):1155–1159, 2001.

[40] `http://history.nih.gov/exhibits/thinblueline/timeline.html`. Accessed July 21, 2011.

[41] P. Ghalioungui. *Magic and Medical Science in Ancient Egypt*. Hodder and Stoughton, London, 1963.

[42] L. A. Bastian, K. Nanda, V. Hasselblad, and D. L. Simel. Diagnostic efficiency of home pregnancy test kits: A meta-analysis. *Arch Fam Med*, 7(5):465–469, 1998.

[43] J. N. Herron, H. K. Wang, V. Janatova, J. D. Durtschi, and D. A. Christensen. Orientation and activity of immobilised antibodies. In *Biopolymers at interfaces*, New York, USA, 2003.

[44] H. Xu, J. R. Lu, and D. E. Williams. Effect of surface packing density of interfacially adsorbed monoclonal antibody on the binding of hormonal antigen human chorionic gonadotrophin. *The Journal of Physical Chemistry B*, 110(4):1907–1914, 2006.

[45] H. Xu, X. Zhao, J. R. Lu, and D. E. Williams. Relationship between the structural conformation of monoclonal antibody layers and antigen binding capacity. *Biomacromolecules*, 8(8):2422–2428, 2007.

[46] J. Buijs, D. D. White, and W. Norde. The effect of adsorption on the antigen binding by IgG and its F(ab')$_2$ fragments. *Colloids and Surfaces B: Biointerfaces*, 8(4):239–249, 1997.

[47] S. Chen, L. Liu, J. Zhou, and S. Jiang. Controlling antibody orientation on charged self-assembled monolayers. *Langmuir*, 19(7):2859–2864, 2003.

[48] F. Albertorio, S. Daniel, and P. S. Cremer. Supported lipopolymer membranes as nanoscale filters: simultaneous protein recognition and size-selection assays. *J. Am. Chem. Soc*, 128(22):7168–7169, 2006.

[49] S. Izrailev, S. Stepaniants, M. Balsera, Y. Oono, and K. Schluten. Molecular dynamics study of unbinding of the avidin–biotin complex. *Biophysical Journal*, 72(1):1568–1581, 1997.

[50] E. Evans. Probing the relation between force–lifetime–and chemistry in single molecular bonds. *Annual Review of Biophysics and Biomolecular Structure*, 30(1):105–128, 2001.

[51] G. I. Bell. Models for the specific adhesion of cells to cells. *Science*, 200(4342):618–627, 1978.

[52] C. Jarzynski. Nonequilibrium equality for free energy differences. *Phys. Rev. Lett.*, 78(14):2690–2693, 1997.

[53] J. D. Israelachvili. *Intermolecular and Surface Forces*. Academic Press, San Diego, third edition, 2011.

[54] Y. Tie, C. Calonder, and P. R. Van Tassel. Protein adsorption: Kinetics and history dependence. *Journal of Colloid and Interface Science*, 268(1):1 – 11, 2003.

[55] P. Schaaf and J. Talbot. Kinetics of random sequential adsorption. *Phys. Rev. Lett.*, 62(2):175–178, 1989.

[56] J. Talbot, G. Tarjus, and P. Schaaf. Unexpected asymptotic behavior in random sequential adsorption of nonspherical particles. *Phys. Rev. A*, 40(8):4808–4811, 1989.

[57] J. Feder. Random sequential adsorption. *Journal of Theoretical Biology*, 87(2):237–254, 1980.

[58] Z. Adamczyk, J. Barbasz, and M. Cieśla. Kinetics of fibrinogen adsorption on hydrophilic substrates. *Langmuir*, 26(14):11934–11945, 2010.

[59] J. J. Ramsden. Concentration scaling of protein deposition kinetics. *Physical Review Letters*, 71(2):295–298, 1993.

[60] C. Calonder, Y. Tie, and P. R. Van Tassel. History dependence of protein adsorption kinetics. *Proceedings of the National Academy of Sciences*, 98(19):10664–10669, 2001.

[61] J. J. Ramsden. Review of new experimental techniques for investigating random sequential adsorption. *Journal of Statistical Physics*, 73:853–877, 1993.

[62] P. R. Van Tassel, J. Talbot, G. Tarjus, and P. Viot. Kinetics of irreversible adsorption with a particle conformational change: A density expansion approach. *Phys. Rev. E*, 53(1):785–798, 1996.

[63] M. Rabe, D. Verdes, J. Zimmermann, and S. Seeger. Surface organization and cooperativity during nonspecific protein adsorption events. *The Journal of Physical Chemistry B*, 112(44):13971–13980, 2008.

[64] M. Rabe, D. Verdes, and S. Seeger. Surface-induced spreading phenomenon of protein clusters. *Soft Matter*, 5:1039–1047, 2009.

[65] M. Rabe, D. Verdes, and S. Seeger. Understanding cooperative protein adsorption events at the microscopic scale: A comparison between experimental data and Monte Carlo simulations. *The Journal of Physical Chemistry B*, 114(17):5862–5869, 2010.

[66] M. Yaseen, B. J. Cowsill, and J. R. Lu. Characterisation of biomedical coatings. In *Coatings for biomedical applications*. Woodhead.

[67] J. Lyklema. Proteins at solid-liquid interfaces: A colloid-chemical review. *Colloids and Surfaces*, 10(0):33–42, 1984.

[68] X. Zhao, F. Pan, B. Cowsill, J. R. Lu, L. Garcia-Gancedo, A. J. Flewitt, G. M. Ashley, and J. Luo. Interfacial immobilization of monoclonal antibody and detection of human prostate-specific antigen. *Langmuir*, 27(12):7654–7662, 2011.

[69] D. Marcuse. *Theory of dielectric optical waveguides*. Quantum electronics–principles and applications. Academic Press, 1974.

[70] P. D. Coffey. *Interfacial measurements of colloidal and bio colloidal systems in real time*. PhD thesis, School of Physics and Astronomy, The University of Manchester, 2011.

[71] F. L. McCrackin and J. P. Colson. *A Fortran program for analysis of ellipsometer measurements and calculation of reflection coefficients from thin films*. Dept. of Commerce, Washington, 1964.

[72] J. A. De Feijter, J. Benjamins, and F. A. Veer. Ellipsometry as a tool to study the adsorption behavior of synthetic and biopolymers at the air-water interface. *Biopolymers*, 17(7):1759–1772, 1978.

[73] C.H. Henry and Y. Shani. Analysis of mode propagation in optical waveguide devices by fourier expansion. *Quantum Electronics, IEEE Journal of*, 27(3):523–530, 1991.

[74] M. Born and E. Wolf. *Principles of optics*. Oxford: Pergamon, 1970.

[75] A. Nelson. Co-refinement of multiple-contrast neutron/X-ray reflectivity data using *MOTOFIT*. *Journal of Applied Crystallography*, 39(2):273–276, 2006.

[76] T. Strick, J. Allemand, V. Croquette, and D. Bensimon. Twisting and stretching single dna molecules. *Progress in Biophysics and Molecular Biology*, 74(1-2):115–140, 2000.

[77] C. Gosse and V. Croquette. Magnetic tweezers: micromanipulation and force measurement at the molecular level. *Biophysical Journal*, 82(6):3314–3329, 2002.

[78] K. C. Neuman and A. Nagy. Single-molecule force spectroscopy: optical tweezers, magnetic tweezers and atomic force microscopy. *Nature Methods*, 5:491–505, 2008.

[79] I. S. Grant and W. R. Phillips. *Electromagnetism*. Wiley, 1990.

[80] J. P. Jakubovics. *Magnetism and Magnetic Materials*. The Institute of Metals, 1987.

[81] J. D. Krauss. *Electromagnetics*. McGraw-Hill, 1991.

[82] F. H. C. Crick and A. F. W. Hughes. The physical properties of cyto-plasm, a study by means of the magnetic particle method. *Exp. Cell. Res*, 1(1):36–80, 1949.

[83] S. S. Shevkoplyas, A. C. Siegel, R. M. Westervelt, M. G. Prentiss, and G. M. Whitesides. The force acting on a superparamagnetic bead due to an applied magnetic field. *Lab Chip*, 7:1294–1302, 2007.

[84] F. Assi, R. Jenks, J. Yang, C. Love, and M. Prentiss. Massively parallel adhesion and reactivity measurements using simple and inexpensive magnetic tweezers. *Journal of Applied Physics*, 92(9):5584–5586, 2002.

[85] W. S. Rasband. ImageJ. Version 1.6.0 (64-bit).

[86] B. Kasemo. Biological surface science. *Surface Science*, 500(1-3):656–677, 2002.

[87] M. Yaseen, X. Zhao, A. Freund, A. M. Seifalian, and J. R. Lu. Surface structural conformations of fibrinogen polypeptides for improved biocompatibility. *Biomaterials*, 31(14):3781–3792, 2010.

[88] H. Arwin. Ellipsometry on thin organic layers of biological interest: characterization and applications. *Thin Solid Films*, 377-378:48–56, 2000.

[89] R. J. Green, I. Hopkinson, and R. A. L. Jones. Unfolding and intermolecular association in globular proteins adsorbed at interfaces. *Langmuir*, 15(15):5102–5110, 1999.

[90] C. R. Wittmer, J. A. Phelps, W. M. Saltzman, and P. R. Van Tassel. Fibronectin terminated multilayer films: Protein adsorption and cell attachment studies. *Biomaterials*, 28(5):851–860, 2007.

[91] K. Laos, R. Parker, J. Moffat, N. Wellner, and S. G. Ring. The adsorption of globular proteins, bovine serum albumin and β-lactoglobulin, on poly-l-lysine-furcellaran multilayers. *Carbohydrate Polymers*, 65(3):235–242, 2006.

[92] J.R. Lu, T.J. Su, P.N. Thirtle, R.K. Thomas, A.R. Rennie, and R. Cubitt. The denaturation of lysozyme layers adsorbed at the hydrophobic solid/liquid surface studied by neutron reflection. *Journal of Colloid and Interface Science*, 206(1):212–223, 1998.

[93] G. Fragneto, R. K. Thomas, A. R. Rennie, and J. Penfold. Neutron reflection study of bovine beta-casein adsorbed on OTS self-assembled monolayers. *Science*, 267(5198):657–660, 1995.

[94] A. W. Sonesson, T. H. Callisen, H. Brismar, and U. M. Elofsson. A comparison between dual polarization interferometry (DPI) and surface plasmon resonance (SPR) for protein adsorption studies. *Colloids and Surfaces B: Biointerfaces*, 54(2):236–240, 2007.

[95] J. R. Lu, X. Zhao, and M. Yaseen. Protein adsorption studied by neutron reflection. *Current Opinion in Colloid & Interface Science*, 12(1):9–16, 2007.

[96] G. H. Cross, A. Reeves, S. Brand, M. J. Swann, L. L. Peel, N. J. Freeman, and J. R. Lu. The metrics of surface adsorbed small molecules on the Young's fringe dual-slab waveguide interferometer. *J. Phys. D: Appl. Phys.*, 37(1):74–80, 2004.

[97] G. H. Cross, A. A. Reeves, S. Brand, J. F. Popplewell, L. L. Peel, M. J. Swann, and N. J. Freeman. A new quantitative optical biosensor for protein characterisation. *Biosensors and Bioelectronics*, 1(19):383–390, 2003.

[98] N. J. Freeman, L. L. Peel, M. J. Swann, G. H. Cross, A. Reeves, S. Brand, and J. R. Lu. Real time, high resolution studies of protein adsorption and structure at the solid-liquid interface using dual polarization interferometry. *J. Phys.: Condens. Matter*, 16(26):2493–2496, 2004.

[99] M. J. Swann, L. L. Peel, S. Carrington, and N. J. Freeman. Dual-polarization interferometry: an analytical technique to measure changes in protein structure in real time, to determine the stoichiometry of binding events, and to differentiate between specific and nonspecific interactions. *Analytical Biochemistry*, 329(2):190–198, 2004.

[100] A. W. Sonesson, T. H. Callisen, H. Brismar, and U. M Elofsson. Adsorption and activity of thermomyces lanuginosus lipase on hydrophobic and hydrophilic surfaces measured with dual polarization interferometry (DPI) and confocal microscopy. *Colloids and surfaces B Biointerfaces*, 61(2):208–215, 2008.

[101] J. R. Olivieril and A. F. Craievich. The subdomain structure of human serum albumin in solution under different pH conditions studied by small angle X-ray scattering. *European Biophysics Journal*, 24(2):77–84, 1995.

[102] P. G. de Gennes. *Scaling concepts in polymer physics*. Cornel University Press, November 1979.

[103] M. Rubinstein and R. H. Colby. *Polymer Physics*. Oxford University Press, 2006.

[104] F. Kilár and I. Simon. The effect of iron binding on the conformation of transferrin. a small angle X-ray scattering study. *Biophysical Journal*, 48(5):799–802, 1985.

[105] B.R. Ware and W.H. Flygare. The simultaneous measurement of the electrophoretic mobility and diffusion coefficient in bovine serum albumin solutions by light scattering. *Chemical Physics Letters*, 12(1):81–85, 1971.

[106] Y. L. Cheng, S. A. Darst, and C. R. Robertson. Bovine serum albumin adsorption and desorption rates on solid surfaces with varying surface properties. *Journal of Colloid and Interface Science*, 118(1):212 – 223, 1987.

[107] R. García and R. Pérez. Dynamic atomic force microscopy methods. *Surface Science Reports*, 47(6):197–301, 2002.

[108] W. Norde and J. P. Favier. Structure of adsorbed and desorbed proteins. *Colloids and Surfaces*, 64(1):87–93, 1992.

[109] H. Shirahama and T. Suzawa. Adsorption of bovine serum albumin onto styrene/acrylic acid copolymer latex. *Colloid and Polymer Science*, 263:141–146, 1985.

[110] J. R. Lu, E. M. Lee, and R. K. Thomas. The Analysis and Interpretation of Neutron and X-ray Specular Reflection. *Acta Crystallographica Section A*, 52(1):11–41, 1996.

[111] M. J. Swann, N. J. Freeman, and G. H. Cross. *Dual Polarization Interferometry: A Real-Time Optical Technique for Measuring (Bio)Molecular Orientation,Structure and Function at the Solid/Liquid Interface*, volume 1, chapter 33, pages 549–568. Wiley, 2007.

[112] O. Tan and G. H. Cross. Surface anchoring structure of a liquid crystal monolayer studied via dual polarization interferometry. *Phys. Rev. E*, 79:021703, 2009.

[113] W. F. Harrington, P. Johnson, and R. H. Ottewill. Bovine serum albumin and its behaviour in acid solution. *Biochem. J.*, 62(4):569–582, 1956.

[114] D. C. Carter and J. X. Ho. Structure of serum albumin. *Adv. Protein Chem.*, 1994.

[115] P. Viot, G. Tarjus, S. M. Ricci, and J. Talbot. Random sequential adsorption of anisotropic particles. *The Journal of Chemical Physics*, 97(7):5212–5218, 1992.

[116] M. Kosmulski. *Chemical Properties of Material Surfaces*. Dekker, New York, 2001.

[117] R. K. Iler. *The chemistry of silica*. Wiley, New York, 1979.

[118] K. Aoyagi, C. Ohue, K. Iida, T. Kimura, E. Tanaka, K. Kiyosawa, and S. Yagi. Development of a simple and highly sensitive enzyme immunoassay for hepatitis c virus core antigen. *J. Clin. Microbiol.*, 37(6):1802–1808, 1999.

[119] D. A. Healy, C. J. Hayes, P. Leonard, L. McKenna, and R. OâĂŹKennedy. Biosensor developments: application to prostate-specific antigen detection. *Trends in Biotechnology*, 25(3):125 – 131, 2007.

[120] J. Buijs, P. A. W. Van Den Berg, J. W. T. H. Lichtenbelt, W. Norde, and J. Lyklema. Adsorption dynamics of IgG and its F(ab')$_2$ and Fc fragments studied by reflectometry. *Journal of Colloid and Interface Science*, 178(156):594–605, 1996.

[121] F. Höök, J. Vörös, M. Rodahl, R. Kurrat, P. Böni, J. J. Ramsden, M. Textor, N. D. Spencer, P. Tengvall, J. Gold, and B. Kasemo. A comparative study of protein adsorption on titanium oxide surfaces using in situ ellipsometry, optical waveguide lightmode spectroscopy, and quartz crystal microbalance/dissipation. *Colloids and Surfaces B: Biointerfaces*, 24(2):155–170, 2002.

[122] L. Haggerty and A.M. Lenhoff. Analysis of ordered arrays of adsorbed lysozyme by scanning tunneling microscopy. *Biophysical Journal*, 64(3):886 – 895, 1993.

[123] H. Nygren. Nonlinear kinetics of ferritin adsorption. *Biophysical Journal*, 65(4):1508 – 1512, 1993.

[124] S. Ravichandran and J. Talbot. Mobility of adsorbed proteins: A brownian dynamics study. *Biophysical Journal*, 78(1):110 – 120, 2000.

[125] R. K. Thomas. personal communication, 2012.

[126] X. Zhao, F. Pan, L. Garcia-Gancedo, A. J. Flewitt, G. M. Ashley, J. Luo, and J. R. Lu. Interfacial recognition of human prostate-specific antigen by immobilized monoclonal antibody: effects of solution conditions and surface chemistry. *Journal of The Royal Society Interface*, 2012.

[127] H. Gohlke and G. Klebe. Approaches to the description and prediction of the binding affinity of small-molecule ligands to macromolecular receptors. *Angewandte Chemie International Edition*, 41(15):2644–2676, 2002.

[128] B. Gao and G. Jin. Study of interaction force between antigen and antibody using flow chamber method. In *Proceedings of the 2005 IEEE*, 2005.

[129] A. Pierres, D. Touchard, A. Benoliel, and P. Bongrand. Dissecting streptavidin-biotin interaction with a laminar flow chamber. *Biophysical Journal*, 82(6):3214 – 3223, 2002.

[130] L. Li, S. Chen, S. Oh, and S. Jiang. In situ single-molecule detection of antibody-antigen binding by tapping-mode atomic force microscopy. *Analytical Chemistry*, 74(23):6017–6022, 2002.

[131] F. Schwesinger, R. Ros, T. Strunz, D. Anselmetti, H. Guntherodt, A. Honegger, L. Jermutus, L. Tiefenauer, and A. Pluckthun. Unbinding forces of single antibody-antigen complexes correlate with their thermal dissociation rates. *Proceedings of the National Academy of Sciences*, 97(18):9972–9977, 2000.

[132] H. Shang and G. U. Lee. Magnetic tweezers measurement of the bond lifetime - force behaviour of the IgG-protein a specific molecular interaction. *J. Am. Chem. Soc.*, 129(20):6640–6646, 2007.

[133] C. Danilowicz, D. Greenfield, and M. Prentiss. Dissociation of ligandâĹŠreceptor complexes using magnetic tweezers. *Analytical Chemistry*, 77(10):3023–3028, 2005.

[134] G. Fonnum, C. Johansson, A. Molteberg, S. Mørup, and E. Aksnes. Characterisation of Dynabeads by magnetization measurements and mössbauer spectroscopy. *Journal of Magnetism and Magnetic Materials*, 293(1):41 – 47, 2005.

[135] D. C. Meeker. Finite element method magnetics. Version 4.2 (11Oct2010 Build).

[136] C. Yuan, A. Chen, P. Kolb, and V. T. Moy. Energy landscape of streptavidin-biotin complexes measured by atomic force microscopy. *Biochemistry*, 39(33):10219–10223, 2000.

[137] D. A. Simson, M. Strigl, M. Hohenadl, and R. Merkel. Statistical breakage of single protein A-IgG bonds reveals crossover from spontaneous to force-induced bond dissociation. *Phys. Rev. Lett.*, 83:652–655, 1999.

[138] N. Giamblanco, M. Yaseen, G. Zhavnerko, J. R. Lu, and G. Marletta. Fibronectin conformation switch induced by coadsorption with human serum albumin. *Langmuir*, 27(1):312–319, 2011.